MODELING AND ANALYSIS OF TRUCK TIRE-TERRAIN INTERACTION

by
Zeinab El-Sayegh

A thesis submitted to the
School of Graduate and Postdoctoral Studies in partial
fulfillment of the requirements for the degree of

Doctor of Philosophy in Mechanical Engineering

Department of Automotive, Mechanical and Manufacturing Engineering
Faculty of Engineering and Applied Science

University of Ontario Institute of Technology (Ontario Tech University)
Oshawa, Ontario, Canada
April, 2020

THESIS EXAMINATION INFORMATION

Submitted by: **Zeinab El-Sayegh**

Doctoral of Philosophy in Mechanical Engineering

Thesis title:
Modeling and Analysis of Truck Tire-Terrain Interaction

An oral defense of this thesis took place on April 7^{th}, 2020 in front of the following examining committee:

Examining Committee:

Chair of Examining Committee	Dr. Martin Agelin-Chaab
Research Supervisor	Dr. Moustafa El-Gindy
Examining Committee Member	Dr. Yuping He
Examining Committee Member	Dr Haoxiang Lang
University Examiner	Dr. Mohamed Youssef
External Examiner	Dr. Corina Sandu, Virginia Polytechnic Institute and State University

The above committee determined that the thesis is acceptable in form and content and that a satisfactory knowledge of the field covered by the thesis was demonstrated by the candidate during an oral examination. A signed copy of the Certificate of Approval is available from the School of Graduate and Postdoctoral Studies.a

ABSTRACT

One of the key factors for improving the mobility and operating efficiency of trucks is the understanding of the tire-terrain interaction characteristics. Due to the broad range of terrains that trucks may operate over, the understanding process of the tire-terrain interaction is necessary. The terrains for on-road operations are commonly dry or wet surfaces. For off-road operations, a more extensive range of deformable terrains exists, such as dense sand, clayey soil, and gravel. In some cases, vehicles may operate over terrains covered with snow or layers of mixed snow and ice. This research work focuses on modeling and investigating the tire-terrain interaction on several terrains to better predict off-road truck performance.

The truck tire used in this research is the off-road Regional Haul Drive (RHD) size 315/80R22.5 drive tire. The truck tire is built node-by-node using Finite Element Analysis (FEA) technique and is validated using different dynamic and static tests that are compared to the manufacturer's measured data. The terrains are modeled and calibrated using the Smoothed-Particle Hydrodynamics (SPH) instead of the classical FEA technique. Furthermore, two soil moisturizing techniques are presented to model moist soils, the virtually calibrated moist sand is validated against physical measurements.

The in-plane and out-of-plane rigid ring tire model parameters are calculated for the off-road tire running on various terrains. The tire-terrain interaction is performed under several operating conditions and the effect of the operating conditions are investigated. Furthermore, a detailed study of the rolling resistance coefficient prediction over different terrains is presented.

In this research work, the hydroplaning phenomenon is investigated. The hydroplaning speed of the tire is computed under different operating conditions. A novel equation to predict the truck tire hydroplaning speed as a function of several tire operational parameters is developed and validated against an empirical equation.

In addition, the rigid ring tire model is integrated into a highly advanced full vehicle model to predict the truck on-road and off-road performance. Nonetheless, in order to validate the simulation results of the truck tire-terrain interaction obtained in this thesis physical testing was carried out in Gothenburg, Sweden by Volvo Groups Truck Technology.

Keywords: tire-terrain interaction; deformable terrains; terramechanics; moisturizing technique.

AUTHOR'S DECLARATION

I hereby declare that this thesis consists of original work of which I have authored. This is a true copy of the thesis, including any required final revisions, as accepted by my examiners.

I authorize the Ontario Tech University to lend this thesis to other institutions or individuals for the purpose of scholarly research. I further authorize Ontario Tech University to reproduce this thesis by photocopying or by other means, in total or in part, at the request of other institutions or individuals for the purpose of scholarly research. I understand that my thesis will be made electronically available to the public.

ZEINAB EL-SAYEGH

STATEMENT OF CONTRIBUTIONS

Part of the work described in Chapter 2 has been published as:
El-Sayegh, Zeinab, Moustafa El-Gindy, Inge Johansson, and Fredrik Oijer. ”Truck tyre-terrain interaction modelling and testing: literature survey.” International Journal of Vehicle Systems Modelling and Testing 12, no. 3-4 (2017): 163-216.

Part of the work described in Chapter 4 has been published as:
Zeinab El-Sayegh, Moustafa El-Gindy, Inge Johansson, and Fredrik Oijer. “Off-road soft terrain modeling using smoothed particle hydrodynamics technique”. 15th International Conference on Design Education, International Design Engineering Technical Conferences, IDETC 2018-85005, Quebec City, Quebec, Canada. August 26-29, 2018.

Part of the work described in Chapter 5 has been published as:
Zeinab El-Sayegh, Moustafa El-Gindy, Inge Johansson, and Fredrik Oijer. Modelling Tire-Moist Terrain Interaction Using Advanced Computational Techniques. Journal of Terramechanics (review submitted), 2020.

Part of the work described in Chapter 6 has been published as:
Zeinab El-Sayegh, Moustafa El-Gindy, Inge Johansson, and Fredrik Oijer. “development of in-plane rigid ring truck tire model over flooded surface using sph technique”. 15th International Conference on Design Education, International Design Engineering Technical Conferences, IDETC 2018-85006, Quebec City, Quebec, Canada, August 26-29,2018.

Part of the work described in Chapter 6 has been published as:
Zeinab El-Sayegh and Moustafa El-Gindy. Modelling and prediction of tyre-snow interaction using finite element analysis and smoothed particle hydrodynamics techniques. Proceedings of the Institution of Mechanical Engineers, Part D: Journal of Automobile Engineering, 233(7):1783-1792, 2019.

Part of the work described in Chapter 6 has been published as: Zeinab El-Sayegh, Moustafa El-Gindy, Inge Johansson, and Fredrik Oijer. "development of out-of-plane rigid ring truck tire model parameters over flooded surface using fea-sph techniques". 16th International Conference on Design Education, International Design Engineering Technical Conferences, IDETC 2019- 97036, Anahiem, California, USA. August 18-21, 2019.

Part of the work described in Chapter 8 has been published as: El-Sayegh, Zeinab, Moustafa El-Gindy, Inge Johansson, and Fredrik Oijer. "Improved tire-soil interaction model using FEA-SPH simulation." Journal of Terramechanics 78 (2018): 53-62.

Part of the work described in Chapter 8 has been submitted as: Zeinab El-Sayegh and Moustafa El-Gindy. Rolling resistance prediction of off-road tire using advanced simulation and analytical techniques. SN Applied Sciences (under review), 2020.

Part of the work described in Chapter 9 has been published as: El-Sayegh, Zeinab, and Moustafa El-Gindy. "Sensitivity analysis of truck tyre hydroplaning speed using FEA-SPH model." International Journal of Vehicle Systems Modelling and Testing 12, no. 1-2 (2017): 143-161.

Part of the work described in Chapter 10 has been submitted as: Zeinab El-Sayegh, Moustafa El-Gindy, Inge Johansson, and Fredrik Oijer. Development and validation of off-road tire-gravel interaction using advanced computational techniques. Journal of Terramechanics (under review), 2019.

Part of the work described in Chapter 11 has been submitted as: El-Sayegh, Zeinab, Moustafa El-Gindy, Inge Johansson, and Fredrik Oijer. "Development and validation of an off-road rigid ring truck tyre model." International Journal of Vehicle Systems Modelling and Testing 13, no. 3 (2019): 275-294.

I performed the majority of the synthesis, testing of membrane materials, and writing of the manuscripts.

ACKNOWLEDGMENTS

First I would like to thank and offer my sincerest gratitude to my thesis supervisor, Professor Moustafa El-Gindy for his continuous support and motivation throughout this research and for his invaluable advice and encouragement.

I would also like to express my appreciation to Volvo Group Trucks Technology for their financial support of this work and personal appreciation to Frederik Öijer, and Inge Johansson of Volvo Group Trucks Technology for their continued technical support during this course of research. I would also like to express my appreciation for NSERC Discovery Grant for their partial funding of this thesis work.

Furthermore, I would like to thank my colleagues in the lab for their support and encouragement. Special thanks to Kristian Lardner, Brett Russell, Laith Dababneh, Mirwais Sharifi and Fatemeh Gheshlaghi.

Last but not least, I would like to express my genuine appreciation to my family whom without I wouldn't be able to reach my goals. No words can describe my gratitude to my parents for their continuous sacrifice, motivation and unconditional love throughout each stage of my life. My warmest appreciation to my sisters Batoul, Mahassen, and Fatima and my brother Abbass who filled my days with joy and happiness.

TABLE OF CONTENTS

LIST OF FIGURES

LIST OF TABLES

LIST OF SYMBOLS

Symbol	Description	Unit
a	Half contact length between tire and road surface	m
b	Plate width	m
B	Stiffness factor	-
c	Cohesion constant of terrain	kPa
c_{01}, c_{10}	coefficients of Mooney-Rivilin	-
C	Shape factor	-
c_{bx}	In-plane translational damping of sidewall	kNs/m
c_{bz}	In-plane translational damping of sidewall	kNs/m
c_{by}	Out-of-plane translational damping constant	kNs/m
$c_{b\gamma}$	Out-of-plane rotational damping constant	$kNms/rad$
$c_{b\theta}$	In-plane rotational damping of sidewall	$kNms/rad$
c_c	Critical damping constant	kNs/m
c_l	Out-of-plane slip damping constant	kNs/m
c_{vr}	Residual damping constant	kNs/m
d	Tire deflection due to loading	m
D	Peak factor	-
E	Young's modulus of the terrain	MPa
E_t	Tangentail modulus	MPa
f^{α}	External force	N
f_n	Acceleration	m/s^2
f_r	Rolling resistance coefficient	-
$f_{seepage}$	Seepage force	N
F_k	Force on node	N
F_p	Force on particle	N
F_x	Longitudinal (tractive) force	kN
F_y	Lateral force	kN
F_z	Vertical force	kN
G	Shear modulus of the terrain	MPa
I_{ax}	Mass moment of inertia of tire rim about x-axis	kgm^2
I_{az}	Mass moment of inertia of tire rim about z-axis	kgm^2
I_{ay}	Mass moment of inertia of tire rim about y-axis	kgm^2

I_{bx}	Mass moment of inertia of tire about x-axis	kgm^2
I_{bz}	Mass moment of inertia of tire about z-axis	kgm^2
I_{by}	Mass moment of inertia of tire about y-axis	kgm^2
k	Stiffness	kN/m
K	Bulk modulus of the terrain	MPa
k_{bx}	In-plane translational stiffness of sidewall	kN/m
k_{bz}	In-plane translational stiffness of sidewall	kN/m
k_{by}	Out-of-plane translational stiffness	kN/m
$k_{b\gamma}$	Out-of-plane rotational stiffness	$kN.m/rad$
$k_{b\theta}$	In-plane rotational stiffness of sidewall	$kN.m/rad$
k_c	Pressure-sinkage parameter	kN/m^{n+1}
k_{cx}	Longitudinal tread stiffness	kN/m
k_f	Cornering stiffness	kN/rad
k_k	Longitudinal slip stiffness	KN/slip unit
k_l	Lateral slip stiffness	kN/m
k_M	Self-aligning moment stiffness	$kN.m/rad$
k_{tot}	Tire total vertical stiffness	kN/m
k_{vr}	Residual vertical stiffness	kN/m
k_θ	Pressure-sinkage parameter	kN/m^{n+2}
L	Applied vertical load	kN
m	Mass	kg
m_a	Wheel rim mass	kg
m_b	Tire belt mass	kg
m_{tot}	Mass of the tire and rim $(m_a + m_b)$	kg
m_{tread}	Mass of the tread of the tire only	kg
M_x	Overturning moment	$kN.m$
M_y	Rolling resistance moment	$kN.m$
M_z	Vertical or aligning moment	$kN.m$
n	Exponent from terrain values	-
P	Tire inflation pressure	kPa
R	Radius of the inflated tire before loading	m
R_e	Effective rolling radius	m
R_{drum}	Drum radius	m
S_h	Horizontal shift	-
S_v	Vertical shift	-
v, v_{tire}	Tire speed	m/s
v_{drum}	Drum speed	m/s
V	Tire speed	km/h
W	Strain energy function	-
x_n	Position of node	m
X	Slip angle/skid	-
z	Sinkage of disk in Bekker equation	m
σ	Yield stress of the soil	MPa

α	Slip angle	rad
δ	Log decrement	-
$\delta^{\alpha\beta}$	Kronecker's delta	-
γ	Amplitude ratio of the yaw oscillation output	-
γ_w	Sand porosity	-
θ_{ss}	Steady state angle value for rotation	rad
θ_1	First peak angle	rad
θ_2	Second peak angle	rad
ρ	Density of terrain,	kg/m^3
$\tau^{\alpha\beta}$	Shear stress	Pa
τ	System time constant	sec
τ_d	Damped period of vibration	sec
ω	Wheel angular speed	rad/s
ω_d	Damped natural frequency	rad/s
ω_{drum}	Drum angular speed	rad/s
ω_n	Un-damped natural frequency	rad/s
ω_{path}	Path frequency	rad/s
ω_y	Yaw oscillation frequency	rad/s
ψ	Damping ratio	-
τ	Shear stress	MPa
τ_{max}	Maximum shear strength	MPa
ϕ	Angle of internal shearing resistance	deg
ϵ	Critical damping	-

LIST OF ABBREVIATIONS

ANN	Artificial Neural Network
CFD	Computational Fluid Dynamics
FAR	Footprint Aspect Ratio
FEA	Finite Element Analysis
FVM	Finite Volume Method
GA	Genetic Algorithm
MTD	Mean Texture Depth
RHD	Regional Haul Drive
SAE	Society of Automotive Engineering
SPH	Smoothed-Particle Hydrodynamics

CHAPTER 1

INTRODUCTION

1.1 Motivation

The motivation of this research work is to provide researchers in the field, the trucks and tires manufacturers with a better understanding of the off-road truck tires' performance over various terrains at different operating conditions. The terrains include hard and wet surfaces, snow and several sand types. In addition, the operating conditions include inflation pressure, vertical load, and speed. The understanding of tire performance under these conditions will help truck manufacturers and operators to improve the complete vehicle performance as well as its fuel economy.

The off-road trucks usually operate in mining and construction environments under different weather conditions. During rainy days, the vehicle operates over a mixture of soils and water that require the development of an advanced soil moisturizing modeling technique. Thus, these complex terrains were the main cause of developing and presenting two novel soil moisturizing techniques in this research work. These models will help the truck and construction industries to assess the off-road truck's performance under such complex operating conditions.

1.2 Objectives

The objectives of this thesis work include:

- Modeling and calibration of moist soils using two novel soil moisturizing techniques.
- Prediction of the in-plane and out-of-plane rigid ring tire model parameters of truck tires running over different terrains and operating conditions. The terrains include hard and surfaces, snow, sandy loam and sand at different moisture content.

- Determination of the rolling resistance coefficient of the truck tire running over different terrains. Furthermore, investigation of the effect of terrains, inflation pressure, vertical load, and speed on the truck performance.

- Investigation of the hydroplaning phenomenon, and determination of the hydroplaning speeds of truck tires as a function of several operating conditions, such as inflation pressure, vertical load, water and tread depth. Furthermore, the development of a novel equation to predict the hydroplaning speed under various operating conditions is developed using the Genetic Algorithm.

- Integration of the developed rigid ring truck tire model into the full vehicle model to predict the truck performance. The simulated results are validated against physical field tests of a straight truck running on gravelly soil.

1.3 Thesis Outline

In chapter 2, a comprehensive literature review of the most recent work that has been done to the field of tire-terrain interaction is presented. Tire modeling and validation techniques are summarized and presented. Soil modeling and calibration techniques are also presented. FEA and SPH modeling techniques are explained and compared. Later, the tire-terrain interface is discussed, the contact interface algorithm between tire and FEA terrain and tire and SPH terrain are explained and summarized. The research work related to the hydroplaning phenomenon is described. Finally, a review of research related to the modeling and testing of the deformable terrain mixing is presented.

In chapter 3, the truck tire modeling, and validation are presented. The RHD 315/80R22.5 truck tire is modeled using Finite Element Analysis (FEA) technique and several materiel properties. The tire model structure, material, and tire-rim assembly are presented and discussed. Furthermore. the tire validation techniques in static and dynamic response and described and evaluated against measurements data.

In chapter 4, the soft terrain modeling, and calibration research are presented. The soft terrains are modeled using Smoothed-Particle Hydrodynamics (SPH) technique. The calibration techniques including the pressure-sinkage and shear-strength tests are explained. The test procedure and expected outcomes are described. The terrain calibration results are presented, the terrains calibrated includes the dry sand, dense sand, clayey soil, and snow. A sensitivity analysis of the variation of the SPH material properties is performed. The sensitivity analysis includes the shear box displacement speed, equation of state coefficients, yield stress and tangent modulus.

In chapter 5, a novel approach to model the moist soil with different moisture content is explored. In this technique, the water particles are pressurized into sand particles. This process is presented for the first time to simulate moist soil calibration including pressure-sinkage and shear-strength tests. Sensitivity analysis of the terrain moisture content on the terrain value including the sinkage, cohesion, and shear resistance angle is investigated. Results obtained from simulations are validated against laboratory measurements performed at Carleton University, Ottawa.

In chapter 6, the in-plane and out-of-plane rigid ring model parameters of the truck tire over different terrains are presented. The terrains used in this research include flooded surfaces with 0, 25, 50 and 75 % water depth of sidewall height. In addition, a hard surface covered with different snow depth such as 50, 100 and 200 mm. Under these terrain conditions, the in-plane parameters including the vertical stiffness, the longitudinal stiffness, and the rolling resistance coefficient are determined. Also, the out-of-plane parameters including the lateral stiffness, the cornering stiffness, the selfaligning moment stiffness, and the relaxation length are determined.

In chapter 7, the in-plane, and out-of-plane truck tire rigid ring model parameters over the previously modeled and validated sandy loam and moist sand are presented. The technique used in this chapter to determine the in-plane and out-of-plane rigid ring tire model parameters are similar to those presented in chapter 6. Furthermore, the effects of inflation pressure, vertical load, and moisture content are investigated.

In chapter 8, the rolling resistance coefficient of the off-road truck tire running over different terrains are investigated. The first part of this chapter includes the rolling resistance coefficient prediction over dry sand, dense sand and clayey soil. The second part of this chapter includes the development of an Artificial Neural Network (ANN) and Genetic Algorithm (GA) learning algorithm to determine the relationship between the rolling resistance coefficient and the operating conditions of the truck tire running over different terrains.

In chapter 9, a study on the truck tire hydroplaning speed is presented. The tire hydroplaning analysis is performed, analyzed and validated. The effect of vertical load, inflation pressure, water and tread depth on the hydroplaning speeds are investigated. A novel hydroplaning equation to predict the hydroplaning speed as a function of the above-mentioned parameters is developed. This novel equation is based on the genetic algorithm and the R^2 goodness of fit.

In chapter 10, a truck tire-terrain interaction for an 8x4 truck running over gravelly soil is presented. The simulation model is validated against physical measurements performed at Volvo Group Trucks Technology in Sweden. The effect of loading and soil compaction on tire performance characteristics are examined and investigated.

In chapter 11, a detailed study of the full vehicle model implemented in Matlab/Simulink code to predict the truck performance at different maneuvers is presented. The rigid ring model is validated against the simulation results obtained in this research. The rigid ring tire model includes in-plane and out-of-plane parameters for both hard surfaces and soft soil.

Finally, chapter 12 presents the conclusions and future work. In addition, to the major contributions and the list of refereed journal and conference publications are presented.

CHAPTER 2

LITERATURE REVIEW

The need for tires started since the Paleolithic era, round logs were used to move heavy objects more easily [7]. People placed round logs and sled under a heavy object and dragged the sled over one log to next. Sumerian, the first urban civilization in the historical region of southern Mesopotamia, is assumed to be the first who used the solid wheel transportation [8]. In 1839, Charles Goodyear an American chemist [9] discovered the vulcanization process. The vulcanization process is the process of heating raw rubber with sulfur to transform sticky natural rubber to a firm but pliable material. Later, in 1845, a Scottish engineer, Robert William Thomson [10], perceived an idea of air-inflated or pneumatic bicycle tires. Robert expected that the pneumatic tires could overcome the limitation of the solid rubber tires. Following in 1889, a bicyclist brought a punctured bicycle tire to the Michelin brothers, André and Édouard Michelin [11] to fix. Michelin brothers manufactured a detachable pneumatic tire that could save time and effort. The brothers' attempt was accepted and within a few years, the Michelin firm achieved extraordinary growth by serving the early stage of the automotive industry.

As tires are the primary elements connecting the vehicle to the ground, it is significantly important to understand their mechanics. While designing a tire, several factors should be taken into consideration, tires should be able to support the vehicle weight, and provide directional and handling stability. Additionally, tires should cushion the vehicle's ride over rough surfaces.

Considerable types of tires exist depending on the application. The pneumatic tires are widely used for automobile and bicycle applications. A pneumatic tire is defined as an air-inflated structure that can absorb shocks. Pneumatic tires are composed of distinct components such as the carcass, belt plies, tread, under-tread, sidewall, and beads.

In this chapter, a literature review of topics related to tire mechanics, terrain modeling and calibration, tire-terrain interaction, hydroplaning phenomenon, and deformable terrain mixing are presented.

2.1 Tire Modeling and Validation

In this section, various tire modeling techniques including early tires, rigid ring tires, and FEA tire models are presented. In addition, the tire validation procedure in static and dynamic frames are stated and summarized.

The primary step towards tire modeling is the description of the conventional tire axis system, forces, and moments as shown in figure 2.1. The forces applied to the tire are the longitudinal force (F_x), lateral force (F_y), the vertical force (F_z). Similarly, the moments applied are the overturning moment (M_x), rolling resistance moment (M_y), and selfaligning moment (M_z).

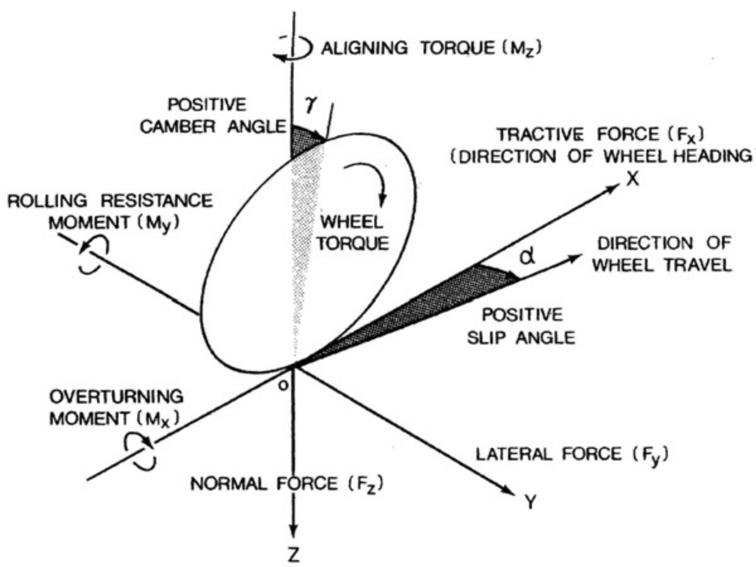

Figure 2.1: Conventional tire forces and moments [1]

The longitudinal force is generated during traction or braking in addition to the rolling resistance force. The rolling resistant force is generated at the tire contact area against the tire rolling direction. The hysteresis in the tire materials and ply is the primary cause of the rolling resistance. The tire operating conditions such as inflation pressure, vertical load and surface condition has an impact on the rolling resistance. The rolling resistance force divided by the vertical tire load represents the rolling resistance coefficient. Generally, for truck tires, the coefficient of rolling resistance varies between 0.006 and 0.01 on a concrete or asphalt road [5]. Higher rolling resistance is usually observed on flooded surfaces than that on dry surfaces. The rolling resistance coefficient at rated inflation pressure and vertical load can be estimated using equation 2.1 [1] for a radial-ply truck tire. Where f_r is the rolling resistance coefficient and V is the tire velocity in km/h.

$$f_r = 0.006 + 0.23 \times 10^{-6} \times V^2 \tag{2.1}$$

As slip occurs between the tire-terrain contact area a longitudinal force develops. The longitudinal force allows the vehicle to accelerate and decelerate. The difference in speed between the tire rolling speed and its traveling speed results in a slip between the tire's tread and the surface. Equation 2.2 and 2.3 describes the slip ratio generated during braking and accelerating, respectively [1]. Where r is the tire rolling radius in m, ω is the wheel angular velocity in rad/s and V is the tire speed in m/s. It should be noted that the slip ratio is 0% in case of pure rolling, while a slip ratio reaches 100% during braking when the wheel locks, and 100% during accelerating when the wheel spins.

$$i_b(\%) = \left(1 - \frac{r\omega}{V}\right) \times 100 \tag{2.2}$$

$$i_d(\%) = \left(1 - \frac{V}{r\omega}\right) \times 100 \tag{2.3}$$

While a vehicle is steered or subjected to cross-wind, lateral forces are generated at the tire-terrain contact patch. The lateral force may also be called cornering force and is a function of the tire slip angle, inflation pressure, and vertical load. When the vertical load is kept constant and the slip angle is increasing, the cornering force also increases. The previous statement is valid until the slip reaches a certain level were the cornering force reaches a saturation level.

Several experimental and analytical studies have been made to measure and estimate the tire-terrain cornering forces as a function of the slip angle.

In 1958, Mercer [12] analyzed the locked wheel skid performance of various tires on the dry road using experimental testing. Furthermore, he investigated the effect of skidding velocity, vertical load and type of road surface on the skid performance. It was found that the coefficient of friction developed between a given tire and road was found to be greater at the higher speeds. Later in 1962, Horne [13] influence the effect of the tire tread pattern and runway surface condition on breaking friction and rolling resistance of modern aircraft tire. It was concluded that the rolling resistance of an aircraft tire increases with increasing forward velocity on dry and contaminated surfaces.

Later in 1968, Gengenbach [14] conducted an experimental investigation on the braking performance of various tires operated over a wet surface. He observed that at a constant tire load, as the inflation pressure increases, the braking and cornering forces increase. In the same year, Grosch and Maycock [15] found that the locked wheel friction coefficient and the cornering friction coefficient decrease with speed. Two years later in 1970, Holmes [16] conducted field testing to measure the braking force and slip over a range of conditions. The effect of tread pattern, tread material, road surface texture, speed, and tire construction was investigated. it was concluded that the braking force versus slip curve rapidly reaches a peak between 7 and 25% braking slip, then remains fairly constant or slowly decrease until about 85% braking slip.

In 1981, Clark [17] found that an increased speed decreases the lateral force of pneumatic tires. He also perceived that the increase in the vertical load and the inflation pressure and the slip angle increases the lateral force. Clark [17], Pacejka [18], and Milliken [19] found that the lateral force increases with the side angle up to a certain value then it starts to slightly decrease for higher values. In 2014, Anupam [20] conducted a study of the cornering maneuvers of a pneumatic tire type size 185/60R15 on asphalt using the FEA technique. Anupam validated his results against the field measurements under similar conditions.

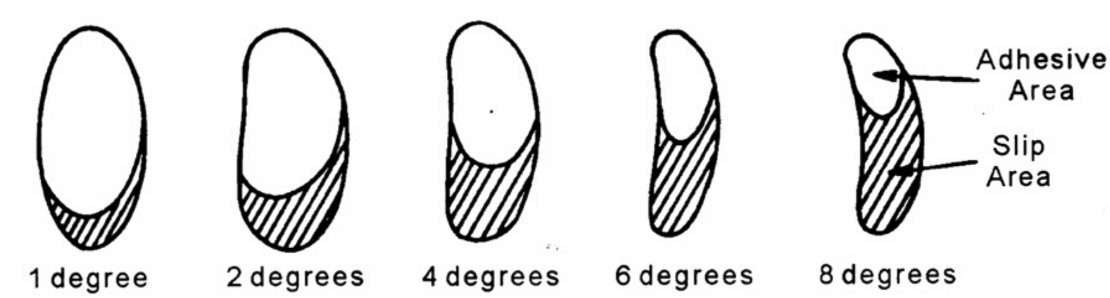

Figure 2.2: Contact area shapes at different slip angles [21]

While applying a cornering force the contact area between the tire and road also appears to change with respect to the slip angle as shown in figure 2.2. In this case, the tire is originally rolling in the direction of the top of the page and is turning left. The adhesive area or so-called effective stationary contact always appears at the leading edge of the contact area, while the slip area appears to the trailing edge of the rolling tire.

The dynamic vertical force at the tire-road contact area was found to reach up to three times higher than a static vertical force, when running over rough surface [5]. This dynamic vertical load should be taken into consideration when tire-terrain interaction is investigated.

The normal pressure distribution at the contact area for a non-rolling stationary tire is shown in figure 2.3a. The tire geometry and boundary conditions are symmetric about the center of the contact area; thus, the normal pressure distribution is also symmetric. Greater normal contact pressures are noticed under the sidewalls and centerline of the tire at rated vertical load and inflation pressure. This is due to higher vertical stiffness in those local areas. Figure 2.3b shows the normal pressure distribution in the contact area for a rolling tire. Unlike the non-rolling stationary state, the boundary conditions and normal pressure are not symmetric about the center of the contact area. In the rolling state, the leading portion of the tire is compressed, and the trailing part of the tire near the contact area is extended.

Due to non-symmetric vertical pressure distribution across the tire width in the contact area, a moment on the tire spindle about the longitudinal axis is formed,

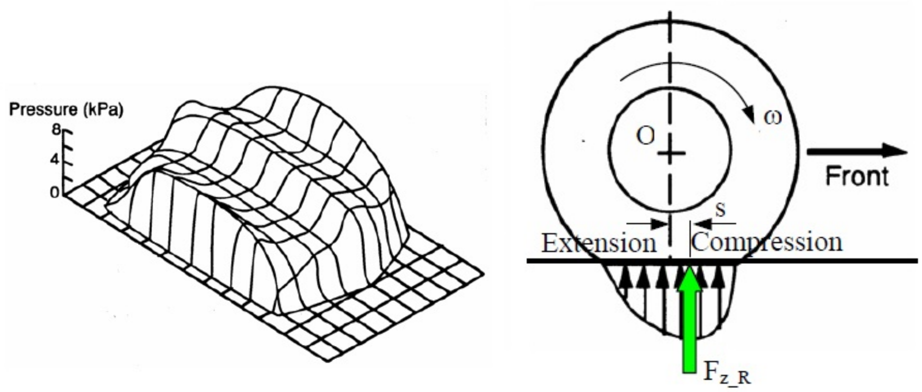

(a) Non-rolling stationary tire (b) Normal contact pressure

Figure 2.3: Normal pressure distributions in the contact area [22]

this moment is the overturning moment. The magnitude and direction of the contact forces are altered across the width of the contact area. Thus, resulting in a slight lateral offset from the non-steered centerline.

As the normal pressure is distributed over the contact area unevenly, the vertical resultant reaction force tends to shift toward the leading edge. Thus, the moment can be developed against the tire rotational direction. This moment is defined as the rolling resistance moment.

The moment about the vertical axis, also known as the selfaligning moment which is defined as the moment acting on the tire center about the vertical axis. The selfaligning moment is determined by the non-symmetric contact force distribution on the tire surface contact plane. The pneumatic trail is a resultant of the cornering force acting on the tire with some offset behind. To restore the tire to its original un-steered orientation a vertical moment is applied. The selfaligning moment increases with the increase of the slip angle until it reaches a peak value at a relatively small slip angle, then reduces as the slip angle increases.

2.1.1 Tire modeling techniques

Tire models and virtual testing has been used since the 1980s. It is important for the tire model to be able to predict the tire response from a dynamic vehicle simulation point of view. Much research is still continuing to optimize the tire modeling process. Figure 2.4 shows the common methods available for the solution of general field problems. The methods are divided into numerical and analytical. The Analytical solution is determined either via an exact solution such as the separation of variables method or approximate method implemented by the Rayleigh-Ritz method. While, the numerical method involves either numerical solution such as the numerical integration and finite differences, or the FEA technique.

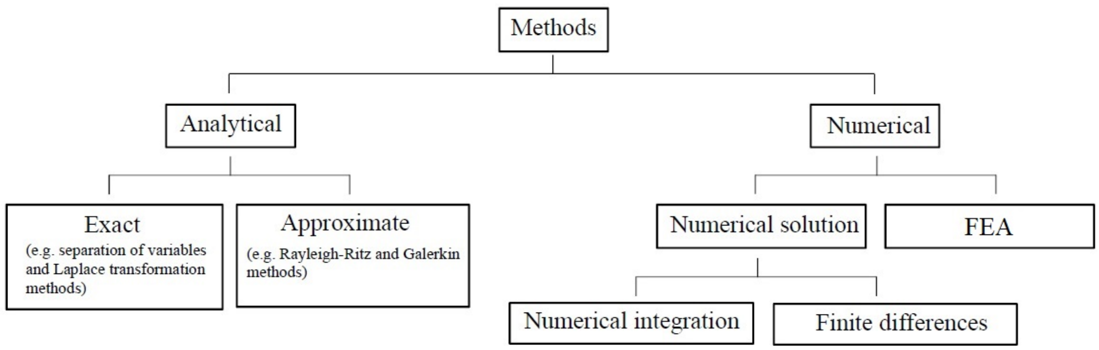

Figure 2.4: Classification of common methods [23]

2.1.1.1 The lumped parameter modeling technique

Ring and string models have been developed since 1950's These early models were based on pre-stressing the tread to string or ring. However, these early models had limitation in accessibility due to the required extensive experiments in order to determine the tire parameters characteristics. Additionally, the validation of these tire models was restricted to a range of parameters, also the domain of validity was not always predicted in advance.

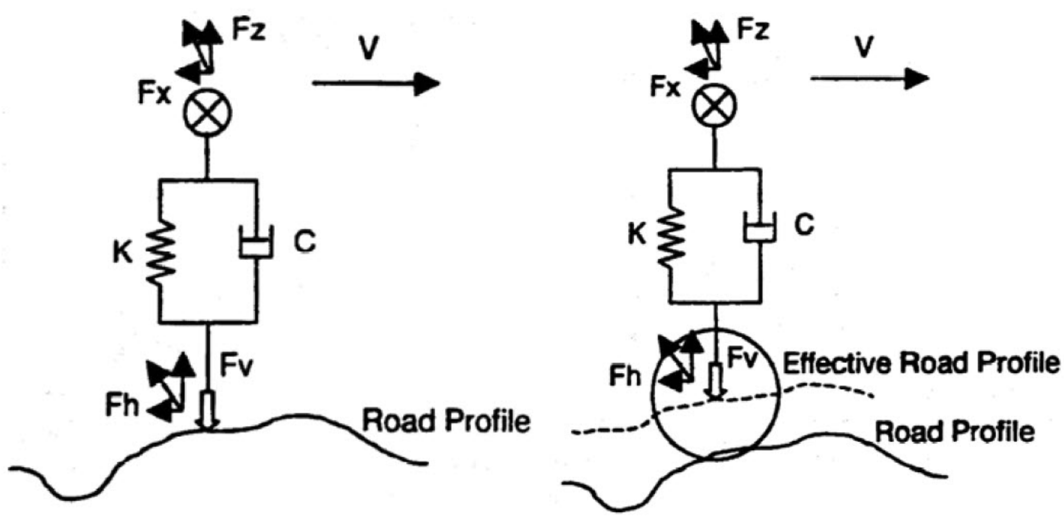

(a) Point contact mechanism (b) Effective road profile mechanism

Figure 2.5: Different tire-road contact mechanisms [24]

During the 1980's and 1990's tire models mostly adopted the point contact mechanism. This mechanism assumes that the tire and road surface are in contact through a single point as shown in figure 2.5a. The point contact mechanism is sensitive to the road ir-regulations, thus it is more useful for longwave road profile inputs. later, the effective road input model was established to overcome the limitations of the point-contact model. Figure 2.5b shows the effective road input model that contributes to more realistic road input.

2.1.1.2 The empirical modeling technique

Bakker et al. [25] predicted cornering forces and selfaligning moment of a tire as early as 1987. In 1997, Pacejka [26] developed an empirical equation to characterize the cornering forces based on the tire measurements called the "Magic Formula". Equations 2.4 and 2.5 shows the basic magic formula equations, where $Y(X)$ represents cornering force, selfaligning torque, or braking effort, and X denotes slip angle or skid. Coefficient B is called the stiffness factor, C the shape factor, D the peak factor, and E the curvature factor. S_h and S_v are the horizontal shift and vertical shift, respectively.

$$y(x) = D\sin\{C\arctan[Bx - E(Bx - \arctan Bx)]\} \tag{2.4}$$

$$\begin{aligned} Y(X) &= y(x) + S_v \\ x &= X + S_h \end{aligned} \tag{2.5}$$

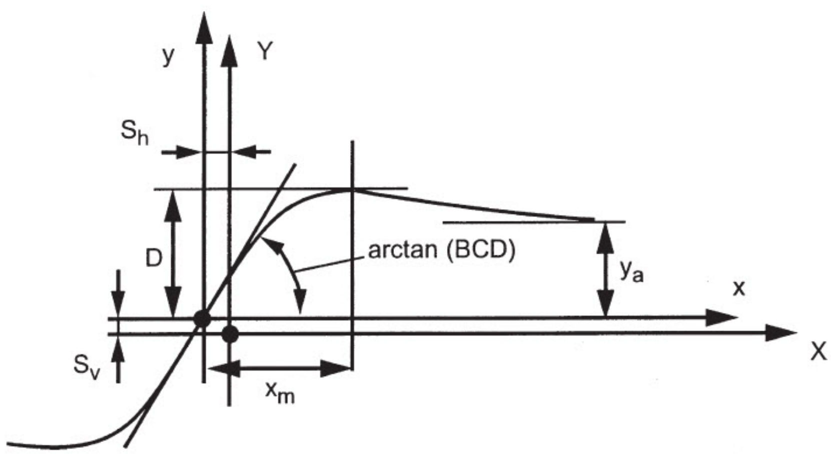

Figure 2.6: Characteristics of the Magic Formula for fitting tire test data [26]

Figure 2.6 shows the characteristics of the Magic Formula for fitting tire test data, in order to complete a set of Magic Formulas, tire measurement data, such as cornering force and selfaligning moment versus slip angle, or brake-traction force versus slip ratio, should be prepared in advance. Thus vast experimental tire measurements are needed to cover a specific range of vertical tire loads. On the other side, to generalize the magic formula, 13 coefficients need to be calculated. These coefficients are computed from the vast and expensive experimental tire measurements at several vertical loads. The magic formula is often criticized due to a large number of coefficients.

2.1.1.3 The semi-empirical modeling technique

In 1997, Zeglaar [27] developed a rigid ring tire model for a passenger car tire. The rigid ring tire model is based on the assumption that the tread and steel belts are modeled together as a rigid ring. Due to this assumption, new parameters were required to describe the deformation of the tire in the contact area, such parameters include the vertical residual stiffness. The tire frequency response on a 2.5 m-diameter rotating drum was measured to determine the rigid ring tire model parameters. Pacejka [28] indicated that the in-plane vibrations are associated with the brake torque fluctuation and the ir-regulation of the road. The rigid ring tire model was used to predict the longitudinal force and the rotational velocity at brake pressure variations. In the same year, Kim [29] implemented the rigid ring model to compute the in-plane contact problem of free rolling pneumatic tires. Figure 2.7 shows the tire model constructed with an elastic ring.

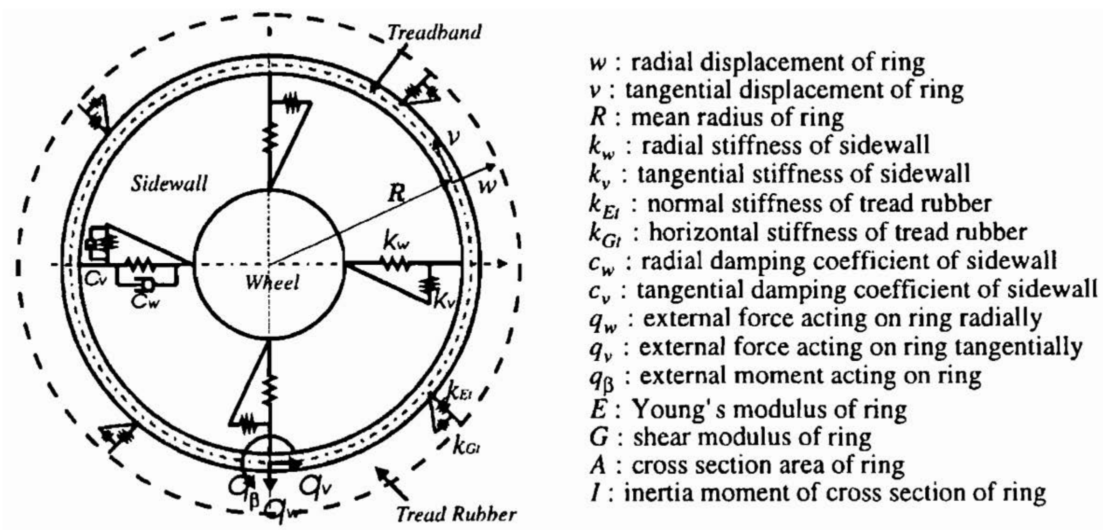

Figure 2.7: Flexible rigid ring tire model [29]

The flexible rigid band and belts of the tire were presented with an elastic ring. Additionally, elastic spring components were introduced to the outer surface of the elastic ring to present the radial and tangential flexibility of the tire tread rubber. In order to complete the rigid ring model the following inputs are required: radial displacement, tangential displacement, mean radius, radial stiffness of sidewall, tangential stiffness of sidewall, normal and horizontal stiffness of tread rubber, radial and tangential damping coefficients of the sidewall, external force acting radially and tangentially on the ring, external moment, young's modulus, shear modulus, cross-section area and inertia moment of cross-section.

In 2004, Yoshida [30] investigated the steering characteristics of a rigid tire over loose sand. Yoshida modeled the driving tire as a function of slip ratio and slip angle, and suggested that the lateral force decreases according to the increment of the slip ratio and increases according to the increment of the slip angle. Later in 2009, Frey [31] developed a rigid ring tire model and compared among various tire models for ride comfort. Frey presented the results of a fixed spindle using point and ring contact followers, in addition to a constant and adaptive footprint model. Frey also developed a quarter vehicle model and analyzed the ride phase results.

In 2012, Tuononen [32] parameterized the in-plane rigid ring tire model using an instrumented vehicle measurements during ABS braking, cleat test, and brake ramp. Tuononen also extracted the vibration modes of the tire using a cleat test, which he then used to define the rigid ring model parameters. Tuononen concluded that it is possible to derive parameters for an in-plane rigid ring tire model from vehicle measurements, however, it is vital to include the vehicle suspension into the model.

In 2014, Chan [33, 34, 35] developed a 3D quasi-steady-state tire model for on-road and off-road vehicle dynamics simulations. Chan implemented the brush tire model for on-road simulation and a simplified off-road tire model capable of reverting back to on-road trend. The on-road tire model is based on empirical data collected experimentally by the National Highway Traffic Safety Administration (NHTSA). Furthermore, the off-road tire model is developed based on observations of experimental data. Then, the research continued to develop an off-road flexible tire model that was later parameterized from test data to acquire static and dynamic friction coefficients, cornering and longitudinal stiffness, as well as camber stiffness.

In 2019, Sandu et al. [36, 37] developed a lumped-mass discretized tire model to better capture the dynamic behavior of tire-soft soil interaction. The research focused on minimizing the computational time of the code and multi-processing. Sandu also examined the contact detection and contact interface model for rigid and defornable terrain.

In 2020, Sandu et al. [38] continued with the developed lumped-mass discretized tire model to investigate parameterization and validation. The Hybrid Soft Soil Tire Model (HSSTM) was then validated against experimental data in lateral and longitudinal dynamic performance.

It should be noted that in the literature there are much more analytical and numerical tire models developed by many researchers in the last decade.

2.1.1.4 The semi-analytical modeling technique

FEA is a numerical method to solve engineering and mathematical problems. In 1909, Ritz [39] established an efficient method for the approximation of problems in the field of deformable solids. Later, in 1943 Courant [40] proposed a particular linear function technique and applied the method to solving torsion problems. The combination of both Ritz method and Courant modification is similar to the FEA method. However, the FEA method was later proposed by Clough [41] in 1960. Clough was the first to introduce the term "finite element" in the paper "The finite element method in plane stress analysis". A significant contribution was carried into Finite Element Method (FEM) expansion by the papers of Argyri [42], Turner [43], Martin [43], and Hrennikov [44].

Significant use of the FEA technique is done in the domain of terramechanics. The FEA technique has been very useful in solving several problems in Terran mechanics. In 1978, Yong et al. investigated the performance of off-road pneumatic tires using the FEA technique [45]. Yong performed various tests to determine the tire stiffness and tractive forces as a function of the tire inflation pressure. In 1985, Noor [46] studied the two-dimensional shell models of the tire, the study was based on shell theory with transverse shear deformation.

In 1990, Eskinazi [47] investigated the possibility of predicting the relative belt edge endurance for a car tire using the FEA technique. it was concluded that the two-dimensional analysis can lead to inaccurate conclusions and thus a three-dimensional analysis under static vertical loading was performed. In 1997, Hiroma [48] implemented the FEA method to predict the tractive forces and pressure distributions beneath a rolling wheel. Hiroma compared the FEA prediction to those from measurements and found that the predictions were reasonable. Hiroma concluded that under small slip conditions, FEA methods could be used to predict traction force. In 1998, Koishi [49] computed the tire cornering characteristics using Pam-Shock an explicit FEA software. A three-dimensional FEA tire model was built and the effect of inflation pressure, belt angle and rubber modulus were investigated.

FEA uses the meshing methodology is used to establish numerical models of a physical structure with smooth and realistic discretization and representation of the boundary conditions. In recent years, Pam-Crash, the virtual environment software has been extensively adopted to built FEA tire models. Pam-Crash also implements the principle of explicit time integration which advances the solution along the time axis. The explicit solution method expresses the equilibrium equation at time t_n as shown in equation 2.6 [3].

$$m\frac{d^2x_n}{dt^2} + kx_n = f_n \tag{2.6}$$

Where m is the mass, x_n is the position at node n, k is the stiffness, and f_n is the acceleration. The advantage of the explicit method is that only the mass, m, appears in the denominator, however, the requirement for stability puts an upper limit on the time step.

In 2006, Chae [5] modeled the Goodyear's 295/75R22.5 drive tire for tractor semi-trailers. The drive tire is a radial ply tire with rim diameter of 22.5 inches. The truck tire-rim assembly model includes 27 different material definitions with 4200 solid elements, 1680 membrane elements, and 120 beam elements. The section width of the truck tire is 315 mm, and the aspect ratio is 75-percent. The off-road tire and components are shown in figure 2.8.

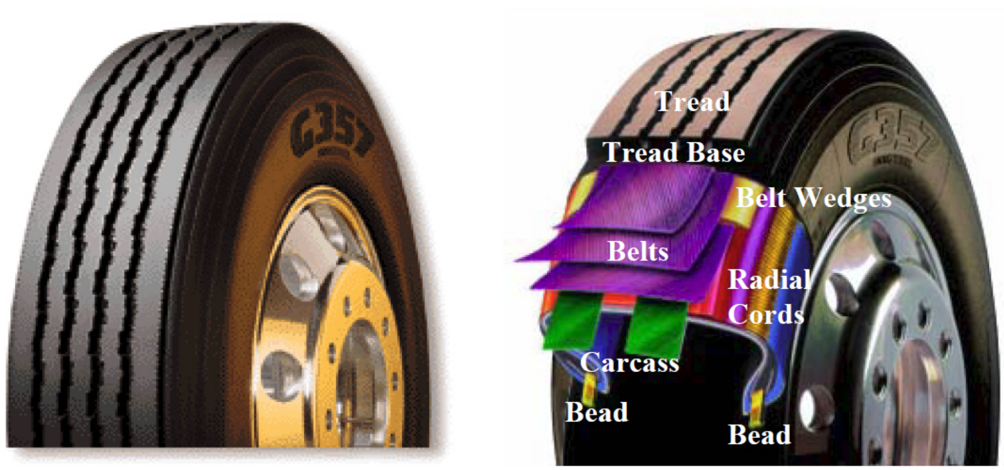

(a) 295/75R22.5 Truck tire (b) Components of the tire

Figure 2.8: Radial truck tire size and components [5]

Later, Slade [2] modified the tire model built by Chae to represent the Goodyear off-road size 315/80R22.5 with four grooves. The cross-section was built node by node and then rotated about the tire axle axis in 6-degree increments to create the full tire with 60 equal pieces. This tire model is built using 9200 nodes, 1680 layered membrane elements, 120 beam elements, 27 material definitions, and one rigid body definition. The rim is defined as a rigid body for the simplicity of the model because the deformation of the rim is negligible.

The rubber material used in modeling the tire was first developed by Mooney [50] in 1940, the rubber material was isotropic and strain energy function, W was used to represent the elastic behavior. The strain energy function, W shown in figure 2.9 can be written in terms of three extension ratios, λ_1, λ_2,and λ_3.

The strain energy function, W can be written in terms of the strain invariants, I_1, I_2 and I_3 as shown in equation 2.7.

$$W = \sum_{i=0}^{n}\sum_{j=0}^{n}\sum_{k=0}^{n} C_{ijk}(I_1-3)^i(I_2-3)^j(I_3-1)^k(n=1,2,3,...,\infty) \tag{2.7}$$

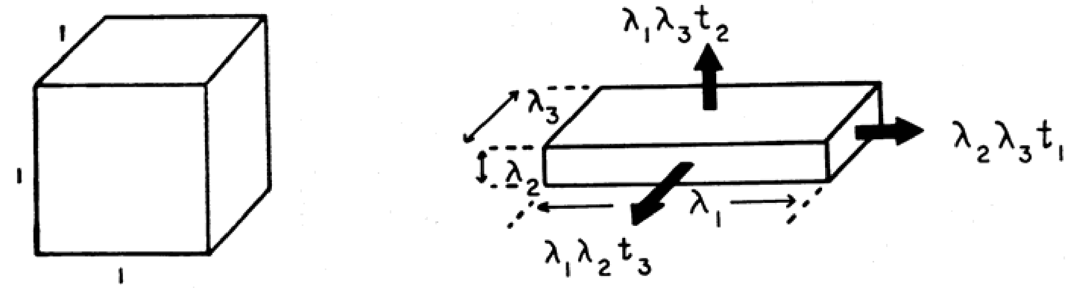

Figure 2.9: Undeformed and deformed states of element [5]

equation 2.7 can be reduced as shown in equation 2.8. Where C_{10} and C_{01} are constants that are experimentally determined.

$$W = C_{10}(I_1 - 3) + C_{01}(I_2 - 3) \tag{2.8}$$

Typical Mooney-Rivilin tensile test can be seen in figure 2.10 on natural rubber vulcanizates. The coefficient C_{10} is the intercept at extension ratio of 1 within the low strain range, and the constant C_{01} is the slope of the line. The two constants, C_{10} and C_{01}, of the Mooney-Rivlin equation are determined in the low strain range because engineering applications usually fall within the low strain ranges.

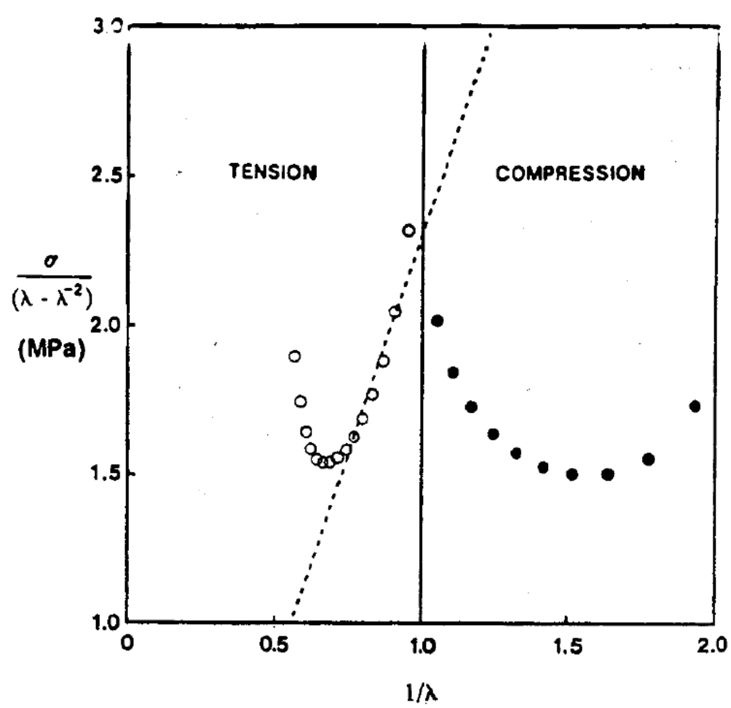

Figure 2.10: Coefficients of Mooney-Rivlin for tensile and compression tests [51]

In most truck models, Mooney-Rivlin material is used to model tread, under-tread, shoulder and bead filler.

2.1.2 Tire model validation techniques

The validation of tire models is performed statically and dynamically through measurements and simulations.

2.1.2.1 static validation techniques

In 1988, Ford [52] extensively investigated the heavy-duty truck tire, the study emphasized on three major elements in the field of heavy-duty tires; tire design factors, performance properties, and application requirements of commercial truck tires. Ford updated the design factors of a tire to include the cross-sectional shape since radial-ply tires became more popular.

In 2002, [53] validated a passenger car tire model using the in-plane vibration modes, the standing waves, traction friction coefficient, vertical static stiffness, and contact patch. Later in 2006, Chae [5] validated the truck tire model in both static and dynamic responses. The static response is verified by vertical stiffness and static footprint tests. The dynamic drum-cleat test validates the dynamic response of the tire.

The vertical stiffness test allows for the calculation of the tire's spring rate. During the vertical stiffness test the tire is constrained in all directions except for the vertical direction. The free motion in the vertical direction allows the tire to move on the vertical axis as shown in figure 2.11. The tire is subjected to a ramp load which causes the tire to deform. The resultant deflection is then recorded for the corresponding vertical loads, and the relationship between vertical load and the deflection is considered.

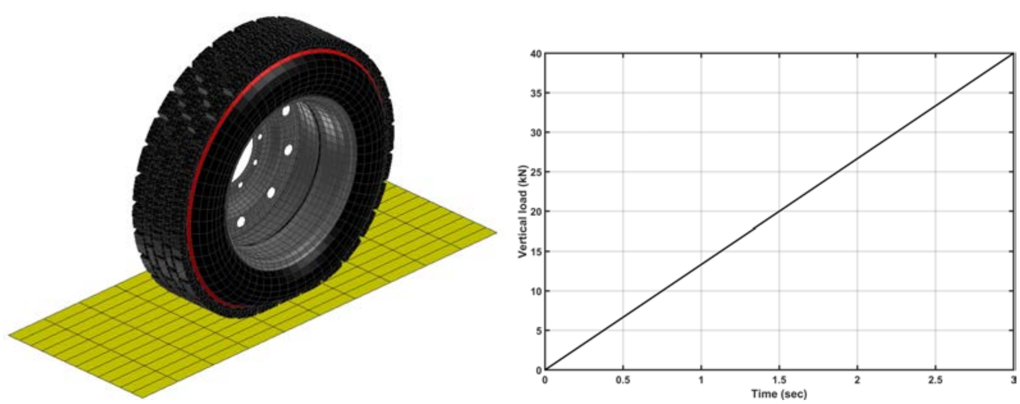

(a) Schematic of Vertical test

(b) Applied ramp load

Figure 2.11: FEA Vertical stiffness test under a ramp loading upto 40 kN (9000 lbs)

The static footprint test is the second validation test applied to validate the tire. The contact patch of a tire is affected by the inflation pressure and vertical load. In the static footprint test, the same procedure of the vertical stiffness test is applied. However, in this case, the contact patch area is recorded instead of the deflection.

2.1.2.2 dynamic validation techniques

Later in 1991, Yap [54] measured the cornering characteristics of a radial truck tire over the dry surface. The tire used was 11R22.5 and the tread design effect on the cornering characteristics was investigated. In 1997, Davis [55] performed physical testing to determine the mechanical properties of an aircraft tire under several conditions. The study focused on measuring the quasi-static characteristics and comparing them to the dynamic response of the tire.

In 2006, Chae [5] stated that a significant amount of the tire mass is concentrated near the tread. The rolling tire radius is not constant due to the radial deflection. However, the stiffness of the tire is affected by the inflation pressure and the material properties. During this test, a 10 mm-radius semicircular cleat test is virtually simulated with a 2.5 m diameter drum to excite the tire vertically and cyclically as the drum rotates.

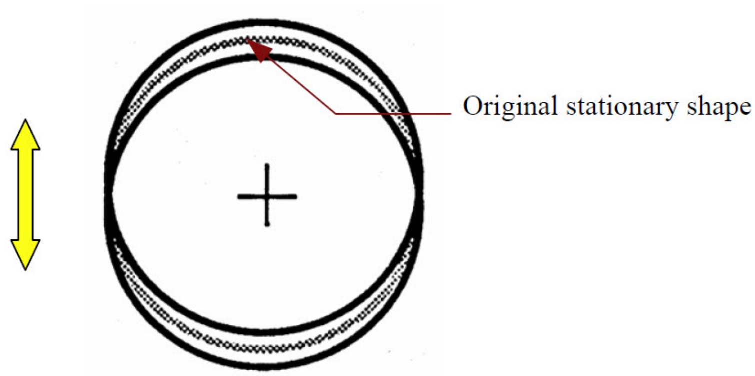

Figure 2.12: FEA drum-cleat test and vibration mode [5]

Figure 2.12 shows the illustration of the vertical first mode of vibration where the entire tread band vibrates vertically without distortion about the vertically fixed rim. Due to the movement of the tread band, the force associated with the resonance is transmitted to the wheel and axle.

The tire is first inflated to the desired inflation pressure, then the tire is loaded by applying the vertical load. The drum center is constrained in all translational directions and free in the rotational direction, while the tire center is constrained in all translational directions to detect the transmitted vertical force. Anangular velocity is then applied to the center of the drum to enable free rolling of the tire at 50 km/h speed. The rotation of the drum allows the cleat to excite the tire vertically, and the vertical reaction force along with the in-plane free vibration mode is determined. The vertical and longitudinal reaction forces are measured and converted from a time domain to a frequency domain using the Fast Fourier Transformation (FFT) algorithm as demonstrated in figure 2.13. Tire's Sidewall damping is calculated using equation 2.9 [5]. Where α is sidewall damping, $\epsilon = 5\%$, is 5-percent critical damping effect, and ω is considered as the first mode of vibration frequency.

$$\alpha = \epsilon 2\omega \tag{2.9}$$

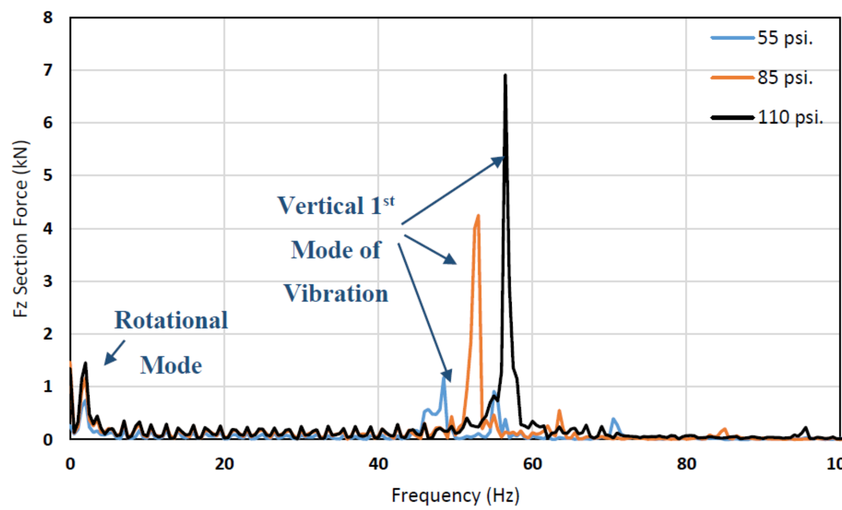

Figure 2.13: FFT result of vertical reaction force at tire spindle [56]

In 2017, Lardner [56] predicted the first mode of vibration of a truck tire at different inflation pressure. Lardner concluded that as the inflation pressure increases the first mode of vibration increases as well. She concluded that the first mode of vibration of this specific tire ranges between 46 and 57 Hz depending on the inflation pressure. Lardner also predicted the sidewall damping of the tire to be 29, 33 and 36 for an inflation pressure of 380, 586, and 758 kPa, respectively.

In 2006, Chae [5] used the cornering test to validate the tire dynamic response. During this test the tire is subjected to a lateral deflection caused by a lateral force, the cornering force is computed at different slip angles ranging between 0 and 12°. The cornering force versus slip angle is plotted and compared to measured data provided by the University of Michigan Transportation Research Institute (UMTRI). Additionally, the aligning moment is also computed from this test and plotted against slip angle the validated against data provided by UMTRI.

Figure 2.14 shows the variation of the cornering force as a function of slip angle for both the FEA tire model and the measurements. The applied vertical loads

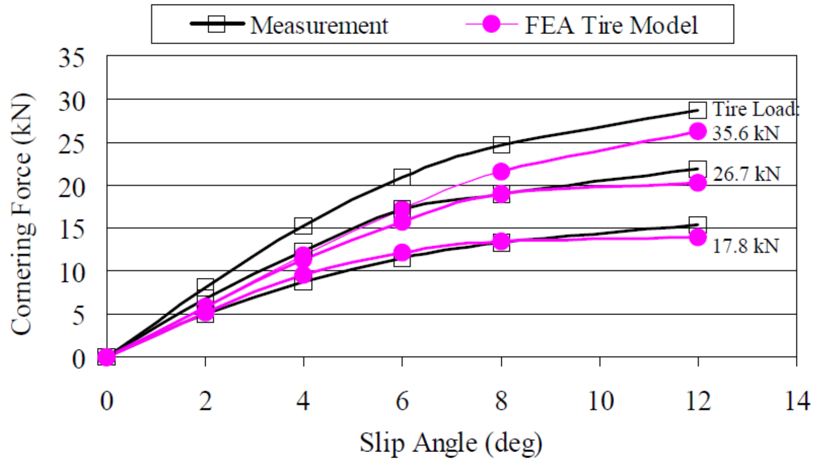

Figure 2.14: Cornering force as a function of slip angle for FEA tire model and measurements [5]

are 17.8 kN (4000 lbs), 26.7 kN (6000 lbs), and 35.6 kN (8000 lbs). The predicted cornering forces and slopes at slip angle 0°, cornering stiffness, are generally in good agreement with the measurements, especially for the two cases of lower vertical loads, 17.8 kN (4000 lbs) and 26.7 kN (6000 lbs).

2.2 Terrain Modeling & Calibration

Terrain calibration methods presented in the literature are significantly depending upon the laboratories and equipment available. Several approaches for measuring soil properties exist including the bevameter, the cone penetrometer, Triaxial apparatus, and the traditional civil engineering techniques. For vehicle applications, the penetrometer and the bevameter are frequently used. In 1964, Onafeko and Reece [57, 58] measured the radial and tangential stresses beneath a tire under driven and towed conditions over a range of longitudinal slip/skid ratios. Later in 1967, Wong and Reece [59, 60] formulated the radial and tangential stress distributions underneath a rolling tire as functions of the tire sinkage and slip/skid ratio.

Bekker developed the bevameter machine shown in figure 2.15 in the 1950s. The bevameter measures soil characteristics by applying pressure-sinkage and shear-strength test. The pressure-sinkage test also known as plate penetration test is performed with a plate on top of the soil and normal stress is measured. The shear-strength test is conducted with a finned plate being twisted within the soil, and the shear stress is measured [61].

Triaxial Apparatus shown in figure 2.16, is an equipment to measure the mechanical properties of deformable solids and soils. During the test, a cylindrical

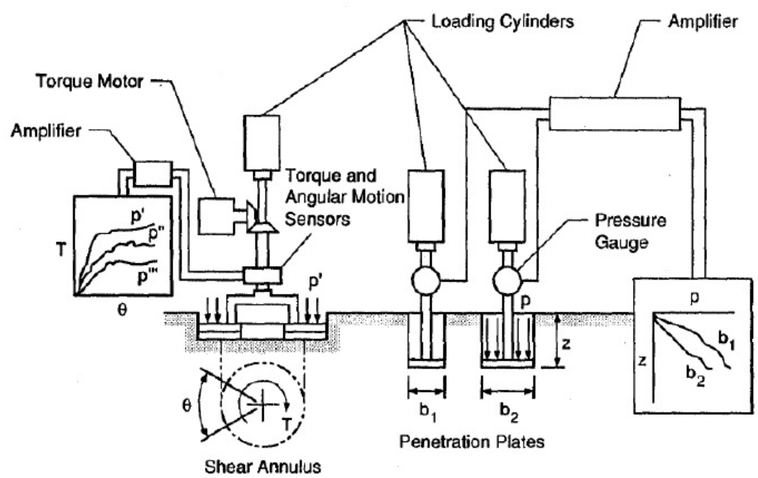

Figure 2.15: Bevameter equipment [1]

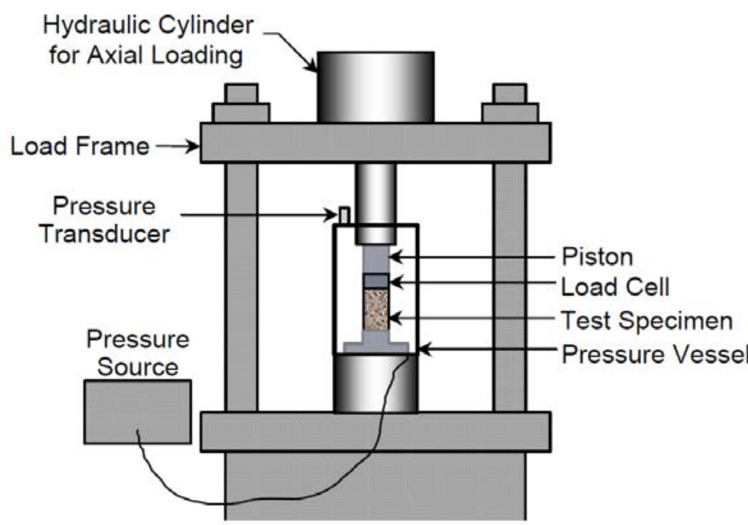

Figure 2.16: Schematic of a triaxial apparatus used to measure soil properties [62]

specimen of soil is subjected to hydrostatic pressure and axial load. The triaxial apparatus features a measurement feedback control system that can simulate idealized states such as hydrostatic and triaxial compression as well as uniaxial strain loading/unloading. This feature is essential for characterizing compressibility, shear strength and unloading behavior of soil [63].

Figure 2.17 shows the direct shear strength box used to measure the shearing characteristics of soils. The direct shear test includes the testing of a square of soil that is laterally restrained and sheared along a mechanically involved horizontal plane while being subjected to pressure applied along a plane normal to the shearing plane [64]. The direct shear test outputs the angle of shearing resistance

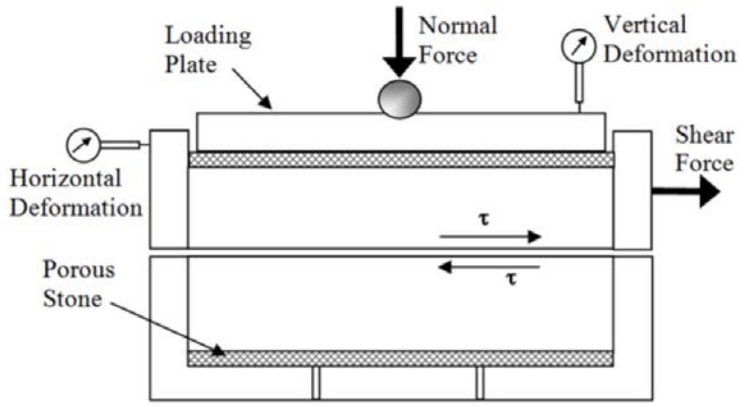

Figure 2.17: Schematic of the sear box [62]

in addition to the cohesion, which is used during the soil calibration.

In 2019, He et al. [65] reviewed the terramechanics models and their applicability to real-time applications. The review included a comprehensive literature related to the parameterization of fundamental terramechanics models. . The review documented and summarized the modeling approaches that may be applicable to real-time applications of terramechanics in simulation, as well as in controller design.

2.2.1 Numerical terrain modeling

In 2005, Sandu et al. [66] modeled terrain profiles and soil parameters using stochastic analysis. This technique captures the uncertain nature of this running support and the corresponding vehicle response. The study modeled various uncertain soil parameters, such as change with environmental conditions using the uniform or normally distributed random variables. In 2007, Li et al. [67] modeled and simulated 2D Auto-Regressive Moving Average (ARMA) terrain models for the vehicle dynamics application. The terrain model deploys the ARMA series method to model a two-dimensional terrain profile. The developed terrain was analyzed in the frequency domain, in addition to the International Roughness Index (IRI)/Ride Number (RN) terrain/road standards.

In 2014, Naranjo et al. [68] developed an off-road soil model and validated using experimental testing. The off-road soil tire model was developed using a semi-analytical tire model for soft soil that utilizes tire construction details which parallel commercially available on-road tire models. The models were validated against data collected from full vehicle testing. In 2012, Lee et al. [69, 69] developed a dynamic model for tire-rail contact friction. The model estimates the coefficient of friction using a mass-spring-damper system to simulate the basic wheel-rail dynamics. It was concluded that the model is capable of capturing the coefficient of friction extremes and nonlinear behavior.

In 2013, Li et al. [70, 71] modeled 1D and 2D terrain profiles using a polynomial chaos approach. Li utilized mathematical tools to investigate the impact of uncertainties in the terrain profile on vehicle mobility, and to auto-correlate the terrain profiles by solving the eigenvalues and eigenvectors of the autocorrelation function. Li suggested that the developed tool used to simulate the terrain profile for on-road and off-road vehicle dynamics or robotic applications. In 2014, Sandu et al. [36, 37] developed and implemented a Hybrid Soft Soil Tire Model (HSSTM). The developed model can be easily linked with multi-body dynamics software packages to simulate vehicle performance on deformable terrains. It was concluded that the proposed model was superior in comparison to other lumped parameter models currently available.

In 2016, Motamedi et al. [72] analyzed the rubber-road contact using physics based theory and indoor experiments. The study performed two-dimensional parameterization using one-dimensional profile measurements. It was concluded that the correlation between the simulation and the experimental results were in good agreement.

In 2017, Motamedi et al. [73] characterized the road profiles based on fractal properties and contact mechanics. they study utilized the a non-contact profilometer to measure the macro-and micro-texture of several different road surfaces. The research found a good correlation between the wet friction measurements and friction prediction results.

In 2019, He et al. [74, 75] developed a systematic tests to study the tractive performance on soft soil. The study consisted of two parts, first collection of experimental data and second the parameterization of the model. The experimental part presented herein produces parameterization and validation data. The parameterization part presented herein that can be used to develop tire off-road dynamics models.

2.2.2 FEA and SPH terrain modeling

In 1997, Heroma [48] adopted the FEA modeling technique to represent soil. The soil model was considered to be viscoelastic with certain moisture content. The tractive forces acting on the contact area between the tire and soil were investigated at various slip angles.

Later in 2006, Shoop [76] modeled soil using the viscoelastic model to investigate the tractive performance of a wheel moving on soft ground. The model was validated with pressure sinkage lab and field testing. In 2008, Hambleton and Drescher [77] investigated soils rutting using FEA elastic-plastic soil models implemented in ABAQUS. It was concluded that the effects of indentation are insignificant for clayey and significant for sands. Figure 2.18 shows an example of soil rutting. It was further concluded that the rutting process of a rolling wheel is steady, meaning the analytical model is able to predict sinkage under steady-state conditions.

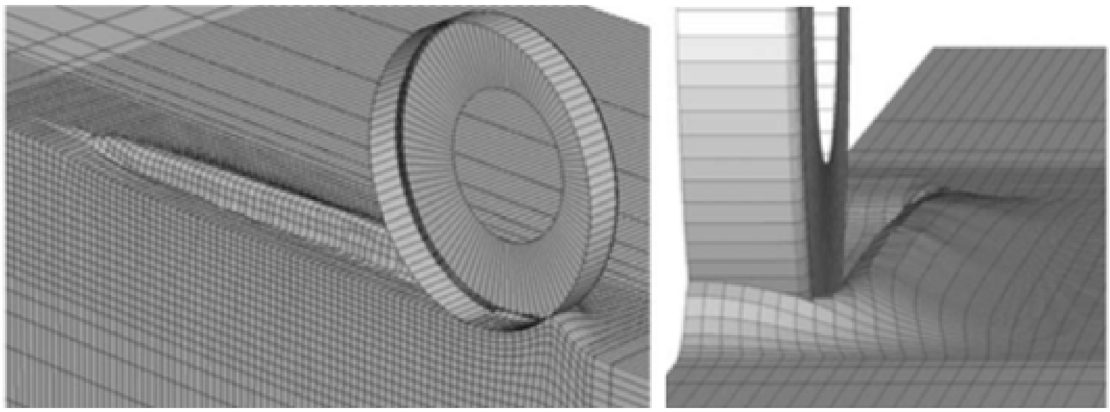

Figure 2.18: Side and front illustration of rut formation in FEA soil [77]

In 2009, Slade [2] modeled sandy loam soil using FEA technique. However, the hysteresis and damping effects were not part of the defined elastic-plastic soil model. The elastic-model itself has the limitation of behaving like springs at stresses lower than that of the yield stress and deforming at stresses higher than that of the yield stress. Due to software limitations using FEA techniques the Mohr-Coulomb failure criterion was not being implemented. Slade recommended the investigation of SPH techniques to improve the soil model's accuracy.

SPH is defined as a sphere centered on the particle center of mass, and a radius r as shown in figure 2.19. Each SPH particle has an associated mass, velocity and stress state which evolve according to the discretized conservation equations. Each SPH also has 3 Degrees of Freedom (DOF), the center of mass, the volume, and the domain of influence [3].

SPH is composed of a finite collection of particles; these particles are created from an FEA mesh as shown in figure 2.20. SPH is modeled from FEA elements which are defined as a rigid body, the center of every FEA square is taken to be one SPH particle.

SPH element part card definition implements several control parameters that influence the behavior of the soil model apart from the material properties. Pam-Crash defines SPH restriction such that each particle is not allowed to exceed 10% of the internal energy. The neighboring distance between each two consecutive SPH particles is specified by the smoothing length, while the minimum and maximum smoothing lengths are governed by the equation 2.10, where h_0 is the initial smoothing length. An option of the dynamic neighborhood is introduced in Pam-Crash within a sphere of influence which updates automatically by the solver algorithm.

$$H_{min} \times h_0 \leq CSLHh(t) \leq H_{max} \times h_0 \tag{2.10}$$

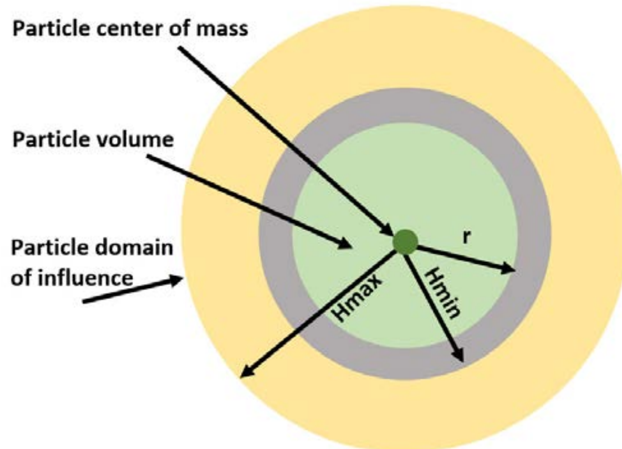

Figure 2.19: SPH particle with ratio 1.5

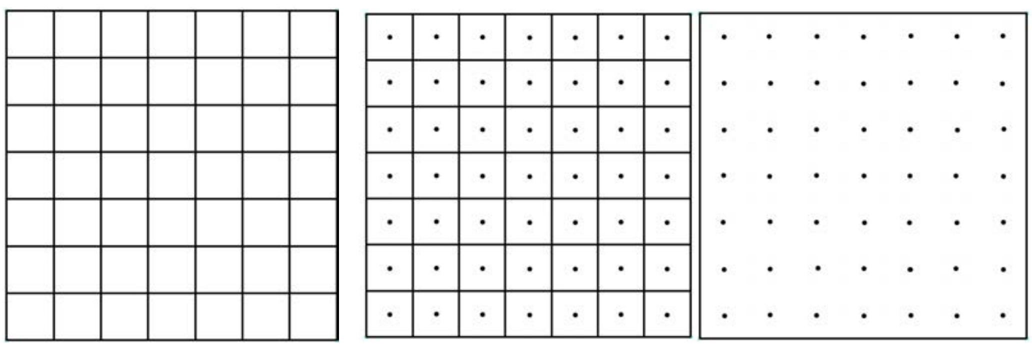

(a) FEA mesh (b) FEA to SPH (c) SPH

Figure 2.20: FEA to SPH conversion for a 100 mm by 100 mm square

SPH part definition requires the definition of a ratio which is the particle smoothing length to radius ratio, and it is recommended within the range 1.8-2. H_{min}, which is the minimum smoothing length and is defined by default to be zero. H_{max}, which is the maximum smoothing length and it is a user input with a range of 0 to 100. The Anti-Crossing force (ETA) is defined using equation 2.11, where ϵ is the relative strength which is usually smaller than 0.5. The artificial viscosity parameters (ALPHAmg, BETAmg) has a defaults of 0.04 and 0.01, respectively and based on research these value are suitable for most fluids.

$$\frac{dr_i}{dt} = u_i + \epsilon \sum_j m_j \frac{u_j - u_i}{\frac{1}{2}(\rho_i + \rho_j)} W_{ij} \tag{2.11}$$

In 2010, Lescoe [78] modeled soil using FEA and SPH techniques in Pam-Crash for dense sand, and solved the equation of state to find the pressure-volume relationship for elastic materials. Also, Lescoe classified terrain materials according to The Idaho Association of Soil Conservation Districts [79] as shown in figure 2.21. In 2013, Dhillon [80] validated different FEA and SPH soil models through Pam-Crash using pressure-sinkage and shear-strength tests for various soils including dry sand and clayey.

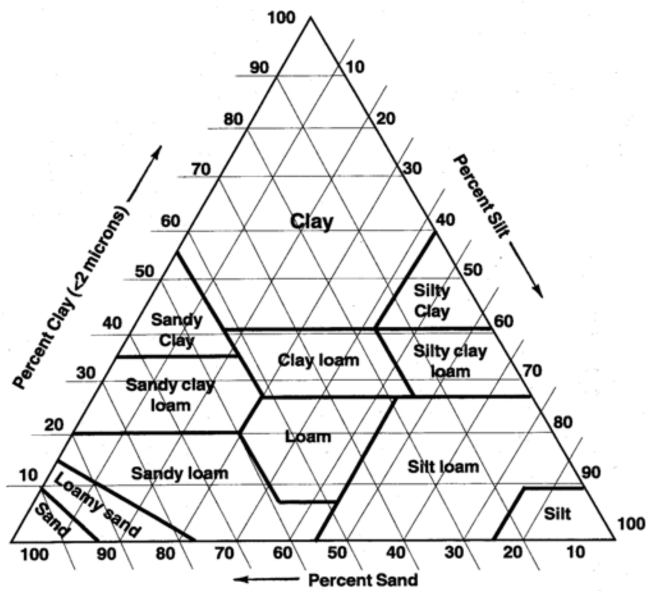

Figure 2.21: Soil composition ratios [79]

In 2016, Marjani [81] optimized soil models using FEA and SPH methods, and compared FEA and SPH results for the pressure-sinkage test in Pam-Crash. Also, Marjani developed a new modeling combination which reduces the computational time, combining hybrid FEA-SPH soil models for an optimized tire-soil interaction process. In 2017, Shahram [63] developed soil models using LS-Dyna using the material for soil and foam. Shahram developed and validated several soil models including high-density clayey sand, low-density dry sand, high-density wet sand, and high density flooded sand. Later in 2017, Lardner [56] utilized Marjani models to predict the tire-terrain interaction of a truck tire running over loose sand.

2.3 Tire-Terrain interaction

Tire-terrain interaction is considered a vital task towards an accurate interaction model. Contact is considered very important in engineering applications as well as in human life. It is impossible to grab or hold objects for using them without frictional contact. Modeling tire and terrain in a virtual environment requires virtual and numerical contact definition. Computational contact problem has been found since 1960s [82, 83, 84]. Preliminary, the contact condition was defined using simple boundary conditions due to computational limitations. Later, solution algorithms were adopted in computational contact mechanics.

The contact algorithm includes contact search, contact pair match, and two important methods for contact force calculation. Figure 2.22 shows the contact-impact simulation methods. The contact search algorithm can be divided in to node-to-node proximity search and node-to-segment correspondence search. While the contact interaction algorithm can be divided into penetration detection method and imposition of contact-impact conditions.

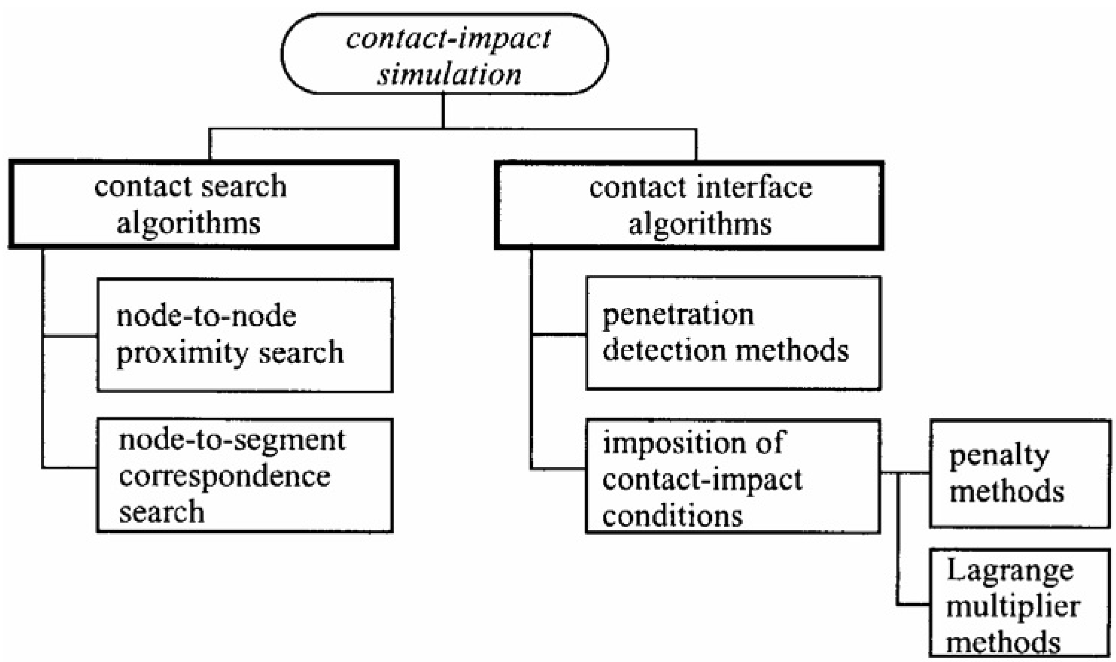

Figure 2.22: Contact-impact simulation methods [3]

The computational contact solution algorithm defines the contact events between two objects. The algorithm explores for contact prone parts and applies the contact condition after contact has been detected. Without the contact algorithm employed in computational simulations, no contact will occur. The computational contact problem resolution is to detect penetration between two objects. After the penetration is encountered a suitable response that eliminates, minimizes, or reduces the penetration is computed.

In 2015, Taheri et al. [85] performed a technical survey related to the terramechanics models for tire-terrain interaction. The study provided two summary tables for three groups of models in which the overall features of each model are reviewed and compared. These tables can be used to understand the general picture of the available techniques, and facilitate selecting the appropriate model for future applications.

2.3.1 Contact interaction algorithm with FEA terrain

Two important terms should be defined during interaction the master-slave contact and self-contact. The master-slave contacts require the definition of two surfaces: slave and master sides. Each node of the slave side is checked for penetrations to the segments-edges of the master side. The self-contact involves the definition of one slave surface only. Each node-edge of the slave side is checked for penetrations to the segments-edges of the slave side. In 1990, Benson [86]recognized a search technique that subdivides the contact body into three-dimensional cubic buckets and restricts the search to the bucket that contains a slave node and to all neighboring buckets.

The contact search algorithm evaluates which part of the structure is likely to contact a rigid wall, another part of the structure, or itself. The contact search algorithm can be subdivided into two major methods, node-to-node proximity search and node-to-segment correspondence search. The node-to-node proximity is given by their spatial distance. In this vicinity, the nodes of a structure are organized according to their distance along a given search direction for a fast and efficient search algorithm [3]. The search algorithm performs pairing of the contact proximity and node-to-segment contact.

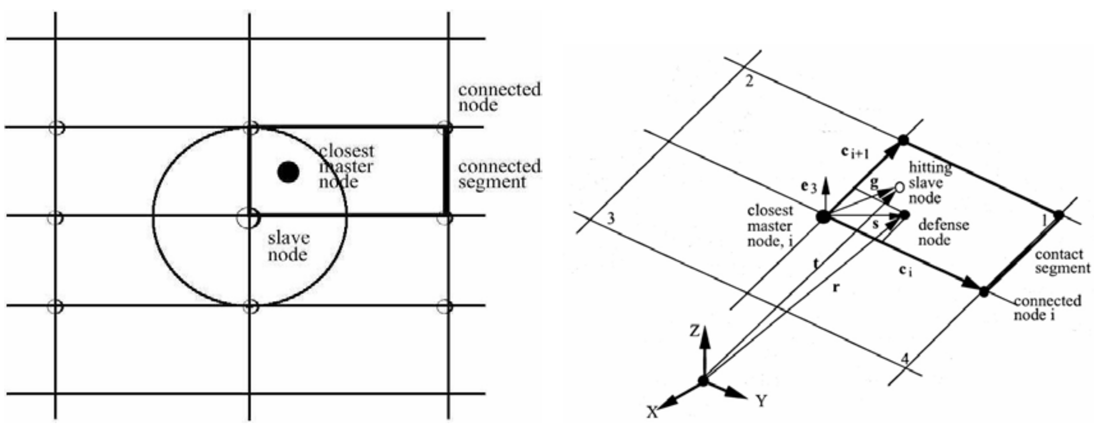

(a) Search radius (b) Node-to-segment correspondence search

Figure 2.23: Search technique implemented in Pam-Crash [3]

Figure 2.23a shows the searching radius scheme for the contact search algorithm. First, the master node closest to a slave node within its contact sphere is to be located. Then, the segment to which this master node is connected and which the slave node is likely to hit is to be determined. Based on equation 2.12, the contact segment s can be determined from neighboring elements around the closest master node [87].

$$s \;=\; g - (g \times e_3)e_3 \tag{2.12}$$

$$
\begin{aligned}
e_3 &= \frac{c_1 c_2}{\mid c_1 c_2 \mid} && (2.13)\\
(c_1 \times s)(c_1 \times c_2) &> 0 && (2.14)\\
(c_1 \times s)(s \times c_2) &< 0 && (2.15)
\end{aligned}
$$

Figure 2.23b defines the node-to-segment correspondence search parameters implemented in equation 2.12. The vector, g, initiates from the closest master node to the slave node above the master surface. While the vector, s, is determined from the closest master node to the projection node of the slave node on the master surface. The unit vector normal to the master surface near the closest master node is called e_3. Vector e_3 can be determined using the equation 2.13, where c_1 and c_2 are defined in figure 2.23b. Vector s should also satisfy the following two constraints in equation 2.14 and 2.15 to guarantee that the slave node projects onto contact segment 1.

After the contact nodes and contact, segments have been matched using the contact search algorithm. The conditions of contact are implemented whenever the contacting slave node penetrates the surface of the contact segment. The contact interaction algorithm is then processed, the interaction algorithms include the Lagrange multiplier method and the Penalty method.

2.3.2 Contact interaction algorithm with SPH terrain

In 1985, Hallquist [87] established comprehensive two-and-three-dimensional contact algorithms to computationally solve static and dynamic impact problems. Later in 1990, Benson and Hallquist [86] examined the behavior of a shell structure after it buckled. They specified that when a structure collapsed completely, a single surface might buckle enough to encounter itself.

In 2001, Hirato [88] performed computational contact simulations of elastic solids using an implicit FEA approach. Hirato developed a new penalty FE formulation based on the concept of material depth. This penalty represented the distance between a particle inside an object and the object's boundary. The new algorithm was implemented in their in-house implicit FE program for static and quasi-static analysis of nonlinear viscoelastic solids.

In 2006, Rabczuk [89] reviewed several novel methods used for coupling meshfree particle methods including the element-free Galerkin (EFG) method. The master-slave approaches are widely used, the coupling can be achieved by fixing the particles to the FE nodes. The force that acts on the FE nodes and particles is indicated in equation 2.16, F_K denotes the force on the FE node and F_P denotes the force on the particles.

$$F_K = m_K a_k; F_P = m_P a_P \qquad (2.16)$$

The acceleration of the node and the corresponding particle is computed using equation 2.17, $a_{K,coupling}$ is the acceleration of the FE node and $a_{P,coupling}$ is the particle acceleration.

$$a_{K,coupling} = a_{P,coupling} = \frac{F_K + F_P}{m_k + m_P} \tag{2.17}$$

Another possibility exist in the fixing of the particles rigidly to the element, this will allow for the agreement between arbitrary nodes. The location of the particle is found using equation 2.18.

$$x = \sum_{J=1}^{N} N_I \left(\xi_C, \eta_C, \pm 1\right) x_I \tag{2.18}$$

The velocities of the point at anytime are shown in equation 2.19.

$$v = \sum_{J=1}^{N} N_I \left(\xi_C, \eta_C, \pm 1\right) v_I \tag{2.19}$$

In 2014, Thiyahuddin [90] analyzed the fluid-structure interaction of vehicle and barrier impact using the SPH-FEA coupling. The barriers were filled with water and placed on the roadside to separate the moving traffic from the work-zone. The study focused on the fluid-structure interaction under vehicular impact using several methods,

In 2016, Hermange [91] developed a coupling strategy for violent fluid-structure interaction between SPH and FEA elements as shown in figure 2.24. The study focused on the implicit schemes for structures to preserve the coupling stability and reduce the computational time. Hermange Introduced different coupling strategies though the treatment of deformable bodies and the Conventional Parallel Staggered (CPS). The study concluded that the proposed coupling strategy can be used for any kind of SPH or FEA method.

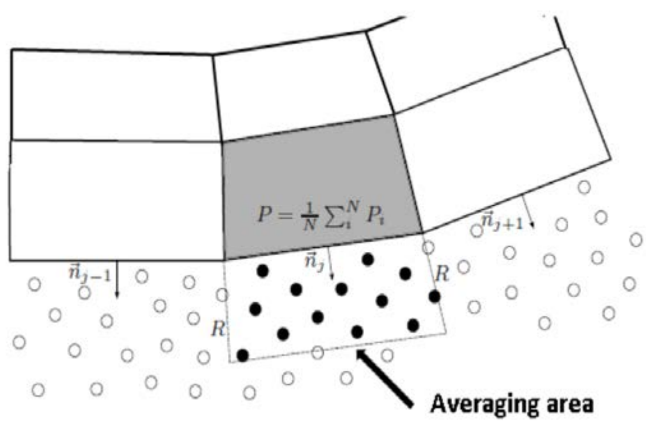

Figure 2.24: Averaged pressure calculation on a wet body panel j [91]

In the same year, Aimin [92] performed a numerical simulation of hyper-velocity impact of FEA and SPH algorithm based on large deformation of material. The study focused on the research and application of the FEA and SPH methods, in addition to the algorithms to overcome the defect instability of the smooth particle tensile. The study described the coupling of SPH and FEA calculation using node-particle consolidation as shown in figure 2.25a. The study also described the contact force between the SPH particles and the finite element contact as shown in figure 2.25b. The time step calculation was suggested using the renew mass-velocity-position-energy of the SPH particle or the renew of the displacement of finite element nodes.

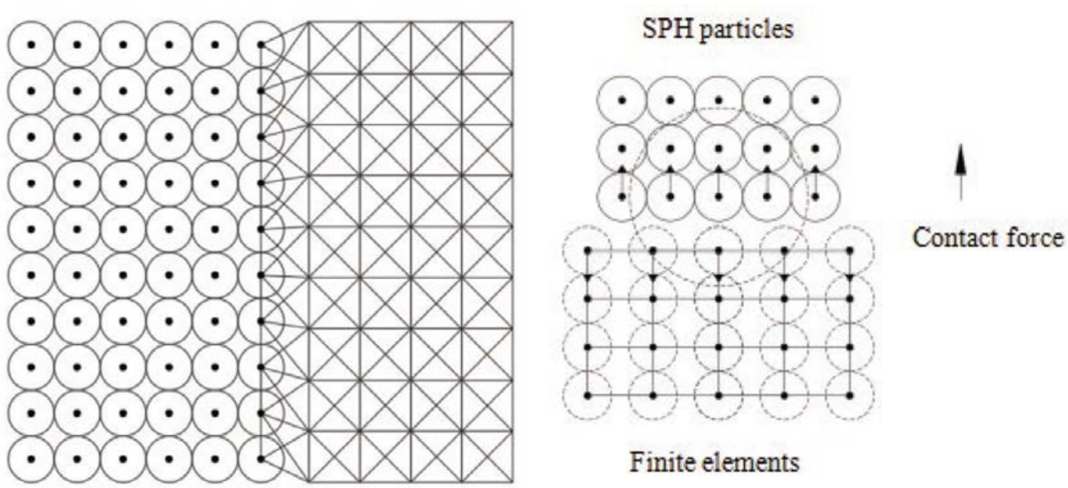

(a) Particles and element nodes (b) Particle and finite element

Figure 2.25: Different Connection schematics [92]

2.4 Hydroplaning Phenomena

Hydroplaning is the loss of tire-road surface contact due to hydrodynamic lift force of water. In other words, water layers build under the rubber tires of the vehicle and the road surface, which leads to loss of traction [93]. The contact forces between the tire and road decrease as the tire speed increases, this results in the decrease of the driving controllability of the vehicle [94]. This phenomenon was first noticed and demonstrated experimentally during a tire treadmill study in 1957 [95]. Several manifestations were accredited with the hydroplaning phenomenon, these manifestations are mentioned by [93]. Some of these manifestations are the detachment of tire footprint, hydrodynamic ground pressure, spin-down of the wheel, suppression of tire bow ware, loss of breaking and loss of tire directional stability.

Since the 1960s many researchers tend to employ an analytical or numerical method to investigate the hydroplaning problem. In 1966, Martin [96] considered the total dynamic hydroplaning problem by applying the potential flow theory and conformal mapping techniques. Later in 1967, Moore [97] modeled a rubber sliding on a 2D smooth sinusoidal asperity by a thin fluid film. In the same year, Eshel [98] divided the tire-water contact area into three zones based on the amount of the inertial and viscous effects and utilized a different method for each zone.

In 1972, Browne [99] studied hydroplaning phenomenon using Navier-Stokes equations and proposed a 2D treatment for a 3D tire deformation model. In 1972, Leland [100] reported that in shallow water around a thickness of 1 mm, tread grooves are highly effective in delaying the occurrence of hydroplaning. In 1974, Sinnamon [101] concluded that hydroplaning speed varies inversely with water depth, thus lower water depth decelerates the onset of hydroplaning phenomena.

In 1996, Gogger [102] investigated the tire velocity field and the pressure distribution of a deformable automobile tire without rotation during hydroplaning. One year later in 1998, Panagouli [103] perfumed investigation on pavement textures which indicated that pavement macrotexture is a function of aggregate size, shape, spacing, and distribution of coarse aggregates.

Later in 2000, Seta [94] used an FEA to model the tire and (Finite Volume Method) FVM to model the water to simulate tire hydroplaning. One year later, Janajreh [104] used Computational Fluid Dynamics (CFD) to determine the drag force, which indicates the fluid evacuation around the tread pattern. In 2005, Fwa established a numerical simulation model for hydroplaning prediction using CFD techniques implemented by Fluent to investigate the effect of several factors such as groove width, depth and spacing of pavement on hydroplaning speed of smooth passage car tire [105]. In 2007, Ong [106] established a numerical simulation model for hydroplaning prediction using CFD techniques implemented by Fluent to investigate the effect of different factors such as groove width, depth and spacing of pavement on hydroplaning speed of smooth passage car tire. Moreover, Oh [107] adopted two separate mathematical models to simulate hydroplaning. One year later, Jenq [93] implemented a hydroplaning model for a tire using Ls-Dyna, the model accounted for the water viscous effect. In 2012, Choi [108] estimated a wet road braking distance for vehicles equipped with Anti-lock Braking System (ABS).

To describe the hydroplaning phenomena, researchers developed a "Three-Zone" concept. This concept was first applied by Gough [109] in 1954 and then developed further to cover the rolling tire case by Moore [97] in 1967. Figure 2.26 shows a schematic of the three-zone concept.

Zone A is the squeeze-film zone which is governed by the Elastohydrodynamic lubrication (EHL), in this district water wedge penetrates in the backward direction. In this section, the frictional forces depend on the viscosity and velocity gradient in the lubricant film. Zone B is the transition zone where tire elements penetrate the squeeze-film commence to drape about the asperities of the road

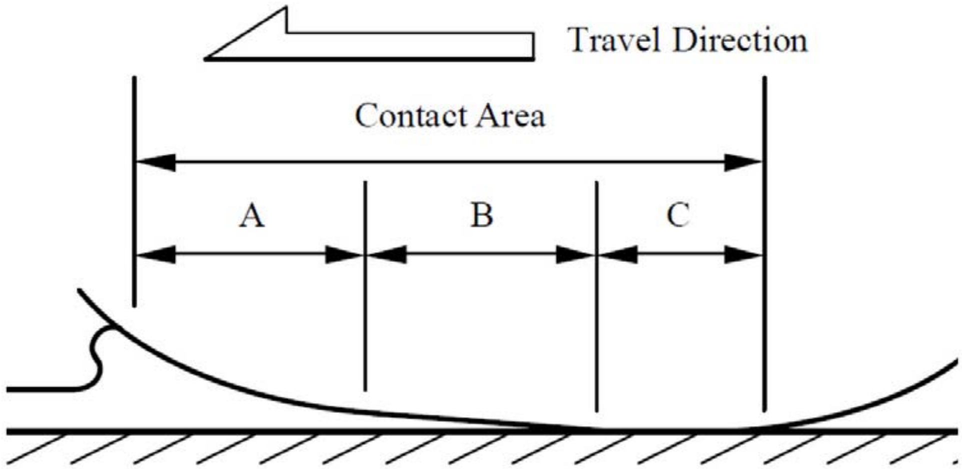

Figure 2.26: Schematic of three-zone concept [93]

surface. When driving at ordinary speeds, the uplift forces produced in this zone are not great enough to produce a full dynamic hydroplaning. Zone C is the traction zone; this is the rear part of the contact area, it starts at the beginning of the end of the transition zone. In this zone, the lubricated water film is considerably removed, and the vertical equilibrium of the tread elements is attained. Depending on the tire speed the length of this zone may vary.

2.4.1 Hydroplaning speed prediction

Different equations have been developed to predict the minimum hydroplaning speed.

2.4.1.1 NASA equation

In 1965, Horne [110] proposed the NASA hydroplaning equation according to aircraft tire experiments at NASA Langley Research Center. NASA equation is shown in equation 2.20, where p is the tire inflation pressure in kPa and v is the minimum hydroplaning velocity km/h.

$$v = 6.36\sqrt{p} \tag{2.20}$$

Equation 2.20 can be implemented if the water depth exceeds the tire tread depth or if the tread pattern is smooth.

2.4.1.2 Horne's equation for truck tires

Later in 1986, Horne [111] developed an equation that predicts hydroplaning speed for truck tires. Horne developed equation 2.21; the equations relate the hydroplaning speed with the tire Footprint Aspect Ratio (FAR) and the inflation pressure.

$$v = 23.3p^{0.21}\left(\frac{1.4}{FAR}\right)^{0.5} \tag{2.21}$$

2.4.1.3 Gallaway's equation

In 1979, Gallaway [112] developed another equation to predict the tire hydroplaning speed. Gallaway's equation involves the spin down %, tire inflation pressure, tread depth, water film thickness, mean texture depth of pavement surface. Equation 2.22 presents Gallaway equations, and equation 2.23 shows the parameter A. Where, SD is the spin down %, t_w is the water film thickness in in, MTD is the mean texture depth in, in, TD is the tire tread depth in, $1/32in$.

$$v = SD^{0.04}p^{0.3}(TD+1)^{0.06}A \tag{2.22}$$

Where A is:

$$A = max\left[\left(\frac{10.409}{{t_w}^{0.06}} + 3.507\right), \left(\frac{28.952}{{t_w}^{0.06}} - 7.819\right)MTD^{0.04}\right] \tag{2.23}$$

2.4.1.4 Wambold's equation

In 1984, Wambold [113] developed an equation that predicts hydroplaning for low-pressure tires based 10% SD a 165 kPa tire inflation pressure.

$$v = 3.5k_1\left[\left(\frac{TD}{25.4} + 1\right)^{k_2} MTD^{k_3}\left(\frac{k_4}{{t_w}^{k_5}} + 1\right)\right] \tag{2.24}$$

Equation 2.24 shows Wambold equation, t_w is water film thickness in mm, MTD mean texture depth mm, TD tire tread mm, and k_s are empirical coefficients. The empirical coefficients k_1, k_2, k_3, k_4 and k_5 are typically 0.05, 0.01, 1.8798, 0.01, respectively.

2.5 Soil Moisturizing Techniques

Soil mixing was first introduced by Intrusion-Prepakt, Inc. of Cleveland Ohio [114] in the 1950s as "Intrusion Grout Mixed-in-Place Piles". The Swedes used a mixed-in-place lime stabilization process in the late 1960s and early 1970's [115]. Since the 1970s, the Japanese and Scandinavians continue to refine the soil mixing technology in various foundation applications.

In 2001, Andromalos [116] used soil mixing for providing stabilization of soft or loose soils, he indicated that the use of soil mixing is considered a modern technology in the United States. In 2004, Fervers [117] recognized a flexible tire model and applied it to study tire-soil interaction using finite element.

In 2007, Bui [118] simulated the water-sand interaction using the SPH technique as shown in figure 2.27, in addition to the soil erosion via a water jet. The frictional boundary conditions were investigated through different numerical equations. The SPH model was validated through numerical analysis of dry sand collapse tests and erosion processes providing stable results. It was determined that SPH is able to simulate large deformations during soil collapse, and different terrain interaction.

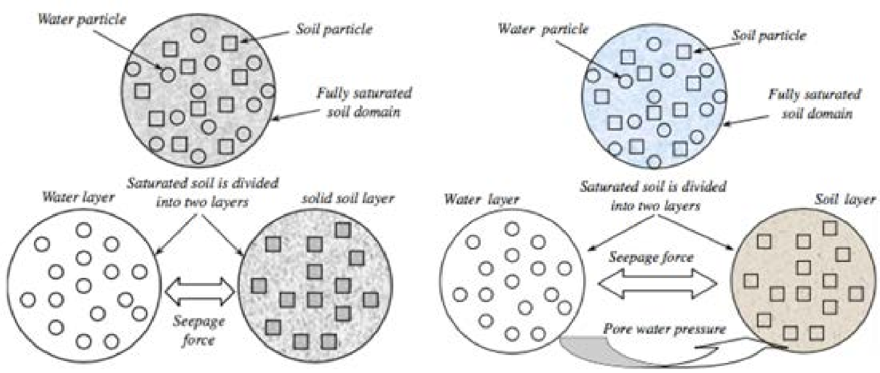

Figure 2.27: Saturated SPH soil schematics with seepage force and pore water pressure [118]

Later in 2010, Nakashima [119] established soil-tire contact model based on dynamic finite element-discrete element method. In 2011, Xia [120] layered FEA soil to predict soil characteristics better. The top layer of soil is assumed to exhibit elastoplastic mechanical behavior and modeled using Drucker-Prager-Cap design. The bottom layer soil is relatively stiffer and is assumed to deform elastically. Xia simulated the footprint and predicted the soil compaction on agricultural soil. Also, Xia computed the frictional coefficient of the tire-terrain interaction.

Soil mixing is used in several applications as a more economical or enhanced performance alternative to some traditional and other geosystem methods. Besides, soil mixing is used in settlement control of soft soils supporting embankments. Soil mixing is achieved using either a single shaft or various shaft drilling equipment. For off-road vehicle design, excellent tire maneuverability and little compaction on terrain are always strongly desired. It is reported that simulations to demonstrate how the tire-terrain interaction model can be used to predict soil compaction and tire maneuverability in the field of terramechanics [120]. The majority of the research effort was focused on field tests [121, 122].

The performance of tire mobility is directly related to the inflation pressure, tire contact area, soil properties, tire/terrain interaction properties, and vehicle load. Operating any off-road vehicle on natural terrain generates soil compaction. Soil compaction is a mechanical mechanism by which soil particles are pressed together by the momentary application of loads through rolling tires or wheels and eventually increases the bulk density of soils. Soil properties are a critical parameter in predicting tire-soil interaction. In off-road application, terrain may be a mixture of several soils, on a rainy day the off-road terrain could be wet sand or wet clayey. It is thus important to accurately model mixed soil situations. SPH soil mixing is new research that has not been done before for the purpose of tire-terrain interaction.

2.6 Summary

The literature review covered the following aspects; tire modeling and validation, terrain modeling and calibration, tire-terrain interaction, hydroplaning phenomena and soil moisturizing techniques.

The tire modeling and validation section included the description of the tire forces (longitudinal, lateral, vertical) and moments (selfaligning moment, rolling resistance moment, overturning moment) using the conventional axis system. The tire modeling techniques described including the lumped parameter modeling technique and the semi-analytical modeling technique. The FEA tire models described included different element types used in modeling along with material properties and Mooney-Rivilen material. Then the tire validation techniques were reviewed using both static and dynamic responses to compute the first mode of vibration, vertical stiffness and static footprint.

In the terrain modeling and calibration section, the physical methods including the Bevameter, Triaxial apparatus and cone penetrometer to measure the soil characteristics were reviewed. The terrain numerical and FEA modeling since 1997 were described and the limitations of FEA techniques were explained. Then, the fundamentals of the SPH modeling technique were described including the equations of motions and viscosity. Later, the SPH terrain model was reviewed along with the hydrodynamic-elastic-plastic equation of state.

In the tire-terrain interaction section, a review of the previous contact impact simulation methods were presented. The contact interaction algorithm used with FEA terrains was then described including the contact search algorithm and the contact interaction algorithm. Later, the contact interaction algorithm with SPH terrain review was performed and included a previous attempt to model the interaction between FEA and SPH elements since 1985.

The hydroplaning phenomena were reviewed as well. The hydroplaning was first defined and the fundamentals of hydroplaning including the different types, sings, and previous studies were explained. Then the three-zone concept was reviewed and each zone was described. Finally, the hydroplaning minimum speed prediction was reviewed and previous equations to predict the minimum hydroplaning speed were described including the NASA, Horne, Wambold and Gallaway equations.

Finally, the previous attempts to physically moisturize soils were reviewed and presented. Furthermore, the seepage force implementation to saturate SPH soil was described and the performance of tire mobility was reviewed.

CHAPTER 3

TIRE MODELING AND VALIDATION

A three-groove Finite Element Analysis (FEA) truck tire, was originally developed by Chae in 2006 [5]. The truck tire is a radial-ply size 295/75R22.5, and it was modeled on Pam-Crash. Later in 2009, Slade [2] modified Chae tire to represent the Goodyear's four-groove off-road RHD 315/80R22.5 drive tire. The advantages of this tire model are mainly related to its computational efficiency and proven stability.

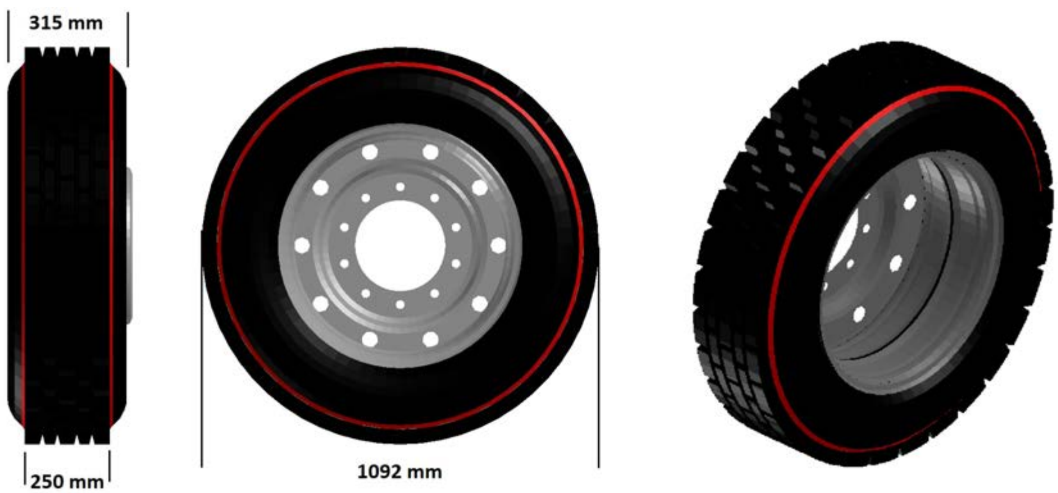

Figure 3.1: Goodyear RHD 315/80R22.5 drive tire basic dimensions

Figure 3.1 shows the basic dimensions of the RHD 315/80R22.5 truck drive tire used in this research. The tire has a diameter of 1092 mm, a tread width of 250 mm, and an overall width of 315 mm. The rim width is 229 mm and it has a weight of 34.8 kg, while the overall weight of the tire is 106.8 kg. The static loading radius is around 505 mm, and the tread depth is 27 mm. The tire single inflation is 850 kPa (123 psi) and maximum dual inflation is 850 kPa (123 psi). In addition, the rated speed is 120 km/h and the dual maximum load is 3350 kg.

This chapter presents the modeling and validation of the Goodyear RHD tire.

The material properties, parts, elements, and tire-rim assembly are presented. Finally, the different tests performed to validate the tire model are presented and discussed.

3.1 RHD Tire Modeling

In this section the basic tire structure and materials are discussed, in addition, the tire-rim assembly technique is demonstrated.

3.1.1 FEA tire structure

The tire model is created by constructing half a 3D cross-section, the section is then mirrored about the tire's longitudinal axis to create one full cross-section as shown in figure 3.2. The cross-section is then rotated about the tire axis in 6-degree increments to create the full tire with 60 equal pieces.

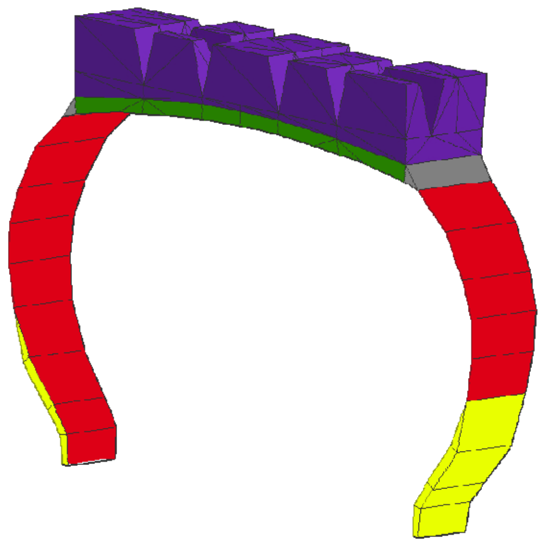

Figure 3.2: A single cross-section of the FEA tire model [2]

The RHD tire has a asymmetric tread pattern to help prevent the tire from holding stones into the tread. The tread design was simplified to contain the fundamental elements while minimizing modeling and simulation processing time [2]. Straight edges were utilized to replace curves for the shape of the lugs and the grooves between the lugs. Each lug was created using a rectangular with angled sides, and the grooves between lugs are simple V shapes. The tread depth is accurately modeled to 27 *mm* as specified by Goodyear's technical data. Solid tetrahedron (TET4) elements with Mooney-Rivlin material properties were chosen for the tread based on previous research work [5].

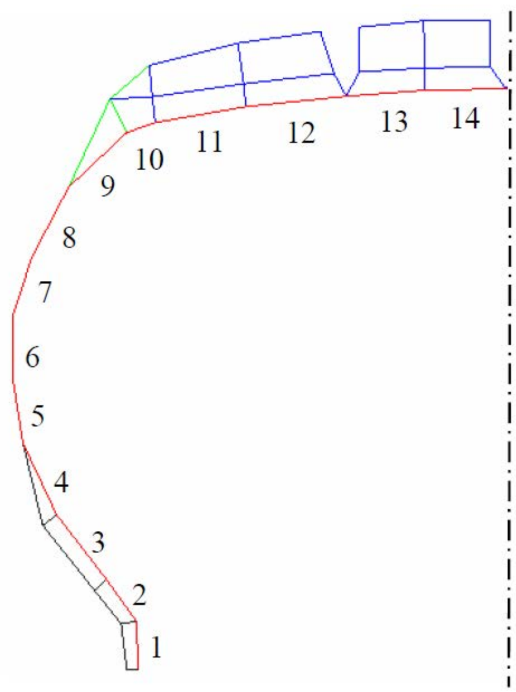

(a) Layered membrane elements

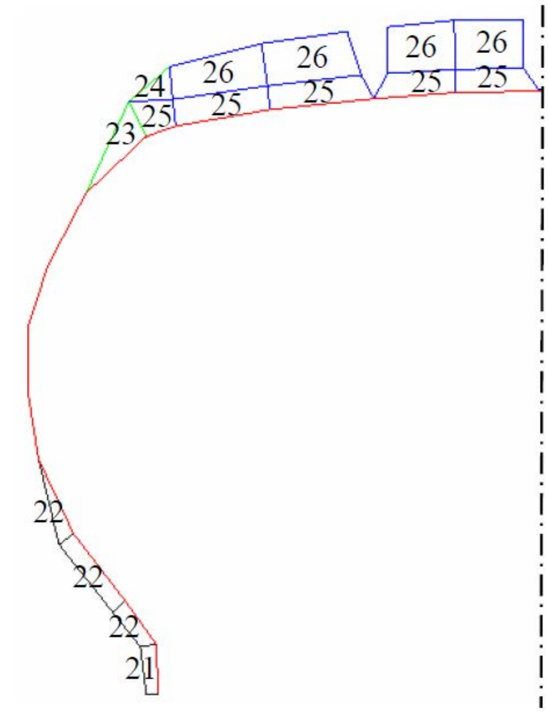

(b) Solid elements

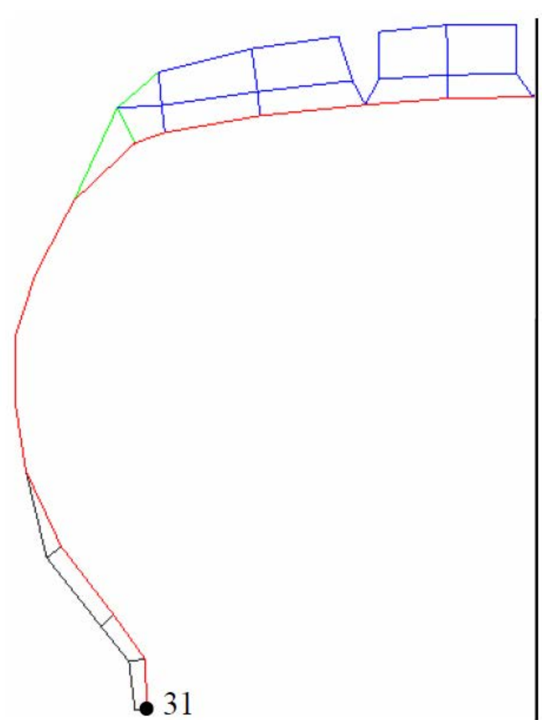

(c) Beam elements

Figure 3.3: Location of different element types with their part I.D numbers [5]

Figure 3.3 shows the different types of elements used to model the tire with their part I.D numbers. The carcass and belts are modeled using elastic, three-layered membrane elements that consist of two layers, the cords controlled in two directions, and a single layer of isotropic matrix. The radial cord ply in the carcass is modeled using layer 1 and the belt plies are modeled using layer 2. The radial-ply cords are embedded in the carcass from one bead to the other. The zero cord angle from the R-axis show in figure 3.4 is input in the Layer 1 to represent the radial cord because the radial direction coincides with the R-axis. Figure 3.3a shows the location of the layered membrane elements used in the tire model.

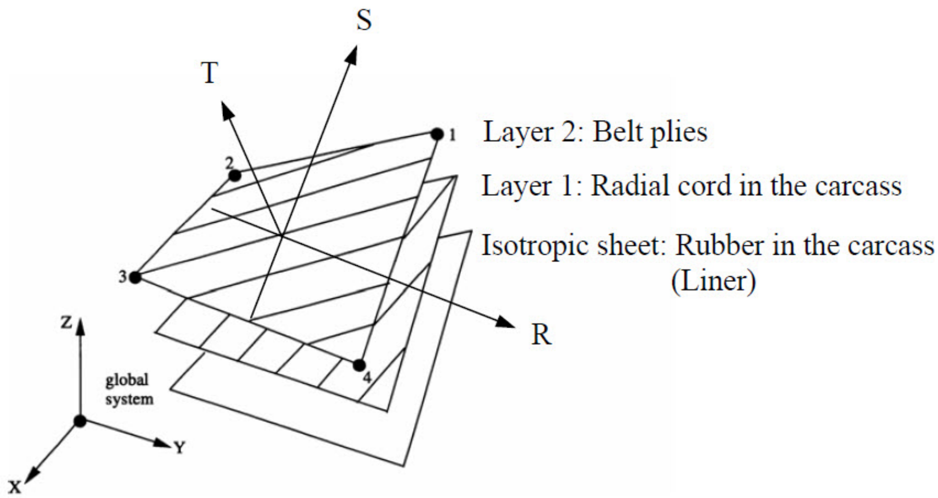

Figure 3.4: Three-layered membrane element [3]

Furthermore, figure 3.3b shows the tire elements modeled using a solid element. The solid elements are used to model the tread, under-tread, tread shoulders and bead fillers. Since these parts are made of relatively thick rubber material and experience shear stresses and sudden changes of curvature during operation, three-dimensional solid elements are utilized to model those parts. Moreover, rubber materials exhibit hyperelastic behavior during loading and unloading, the behavior is described by a constitutive law obtained from Mooney-Rivlin's strain energy density function, W, which is deployed for solid elements.

Figure 3.3c shows the parts of the tire modeled using beam elements. The beam elements are know for the capability to transmit axial forces, shear forces, bending, and torsion moments. It should be noted that in the tire model only the beads are modeled using beam elements.

3.1.2 FEA tire materials

The 21 different elements that form the full truck tire are associated with 31 different material properties. Table 3.1 shows the material properties of the 14 layered elements. It should be noted that the Young's moduli of Layer 2 from material I.D.s 10 to 14 are very high compared to the others in the layer to represent the belt layers at 90° from the radial R-axis as shown in figure 3.4.

Table 3.1: Material properties of layered membrane elements [5]

Tire component	Radial-ply and rubber liner of the carcass				
Material I.D	1	2	3	4	5
Density (ton/mm^3)	7.63E-10	7.64E-10	7.63E-10	7.33E-10	7.21E-10
Thickness (mm)	6.75	4.5	3.75	3.75	3.75
Isotropic parent sheet Young's modulus (MPa)	28	24	22	12	7
Isotropic parent sheet Poisson's ratio	0.3	0.3	0.3	0.3	0.3
Layer 1 Young's modulus (MPa)	365	315	498	429	406
Layer 1 Shear modulus (MPa)	0.0001	0.0001	0.0001	0.0001	0.0001
Layer 1 Angle of fibers with R-axis	0°	0°	0°	0°	0°
Layer 2 Young's modulus (MPa)	0.0003	0.0003	0.0003	0.0003	0.0003
Layer 2 Shear modulus (MPa)	0.0001	0.0001	0.0001	0.0001	0.0001
Layer 2 Angle of fibers with R-axis	90°	90°	90°	90°	90°
Material I.D	6	7	8	9	10
Density (ton/mm^3)	7.23E-10	7.19E-10	7.25E-10	7.44E-10	8.73E-10
Thickness (mm)	3.75	3.75	3.75	3	3.75
Isotropic parent sheet Young's modulus (MPa)	7	7	7	9	12
Isotropic parent sheet Poisson's ratio	0.3	0.3	0.3	0.3	0.3
Layer 1 Young's modulus (MPa)	392	180	193	207	155
Layer 1 Shear modulus (MPa)	0.0001	0.0001	0.0001	0.0001	0.0000
Layer 1 Angle of fibers with R-axis	0°	0°	0°	0°	0°
Layer 2 Young's modulus (MPa)	0.0003	0.0003	0.0003	0.0003	0.0003
Layer 2 Shear modulus (MPa)	0.0001	0.0001	0.0001	0.0001	0.0001
Layer 2 Angle of fibers with R-axis	90°	90°	90°	90°	90°
Material I.D	11	12	13	14	
Density (ton/mm^3)	1.07E-09	1.07E-09	1.06E-09	1.06E-09	
Thickness (mm)	3.75	4.5	3.75	3.75	
Isotropic parent sheet Young's modulus (MPa)	14	14	14	14	
Isotropic parent sheet Poisson's ratio	0.3	0.3	0.3	0.3	
Layer 1 Young's modulus (MPa)	202	200	155	198	
Layer 1 Shear modulus (MPa)	0.0001	0.0001	0.0001	0.0001	
Layer 1 Angle of fibers with R-axis	0°	0°	0°	0°	
Layer 2 Young's modulus (MPa)	0.0003	0.0003	0.0003	0.0003	
Layer 2 Shear modulus (MPa)	0.0001	0.0001	0.0001	0.0001	
Layer 2 Angle of fibers with R-axis	90°	90°	90°	90°	

The solid elements shown in figure 3.3b have material properties as shown in table 3.2. As mentioned previously, the coefficients of Mooney-Riviln, C_{10} and C_{01} are adopted and the method of determination is mentioned in section 2.1.1.4 of chapter 2.

Table 3.2: Material properties of solid elements [5]

Tire component	bead filler		tread shoulder		tread	tread cap
Material I.D	21	22	23	24	25	26
Density (ton/mm^3)	8.82E-10	8.81E-10	8.69E-10	6.93E-10	5.96E-10	6.93E-10
1st Mooney-Rivlin coeff. (C_{10})	0.392	0.392	0.41	0.67	0.51	0.67
2nd Mooney-Rivlin coeff. (C_{01})	1.268	1.268	1.44	2.46	1.86	2.46
Poisson's ratio	0.499	0.499	0.499	0.499	0.499	0.499

Table 3.3 shows the beads material properties. It should be noted that, a very high number for the yield stress is artificially input in the model [5].

Table 3.3: Material properties of bead element [5]

Tire components	Beads
Material I.D	31
Density (ton/mm^3)	4.26E-08
Young's modulus (MPa)	92.1
Poisson's modulus (MPa)	0.4
Yield stress (MPa)	1E20
Cross section description	solid circular section
Cross section circular radius (mm)	2.5

3.1.3 Tire-rim assembly

The developed tire has a total of 9200 nodes, 1680 layered membrane elements, 4200 solid elements, 120 beam elements, and 1 rigid body definition. The rim is defined as a rigid body in order to simplify the model, this assumption is based on the negligence of the rim deformation. This assembly is considered very secure for the transmission of load, traction, and braking efforts when the slip at tire rim strips-rim contact is not of interest and ignored.

The rim is model is newly designed for the truck tire-rim assembly. The rim dimensions are standardized by The Tire and Rim Association [123] for size and contour. It should be noted that the load and cold inflation pressure imposed on the rim must not exceed the rim manufacturers' recommendations even though the tire may be approved for a higher load or inflation pressure. Table 3.4 shows the 15°drop center rim contour dimensions. The notations used in table 3.4 are shown in figure 3.5.

Table 3.4: 15°Drop center rim contour dimensions [5]

Rim size	H min		h min		L min		M max		P min	
D (in)x A (in)	*mm*	*in*	*mm*	*in*	*mm*	*in*	*mm*	*in*	*mm*	*in*
22.5 × 8.25	30	1.17	10	0.394	28	1.10	74	2.90	36	1.42

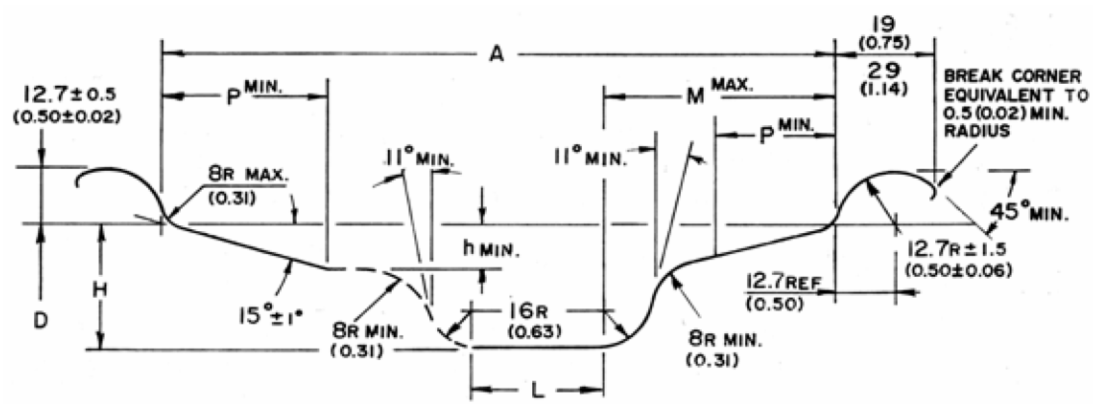

Figure 3.5: 15°drop center rim contour [123]

When the tire is inflated, it sits tightly inside of the rim and is constrained by the tire-rim contact. The rim contact is extremely important to pressurize the air sealed by the contact. The sealing should always be secured during normal vehicle operations. In addition to air sealing, traction and braking efforts are transmitted only through the tire-rim contact. The rim is made of steel and it weighs around 32 kg.

3.2 RHD Tire Validation

Several tire characteristics must be matched closely to achieve the appropriate tire response. The FEA tire model is statically and dynamically validated. The static response is verified by vertical deflection and footprint tests. The dynamic response is verified using the drum-cleat and cornering tests. The results obtained from simulations are verified against available measurements of a truck tire.

3.2.1 Static validation tests

The static validation tests are performed to calculate the static footprint and vertical stiffness at different inflation pressure and vertical load. The results obtained from simulations are compared with manufacturer data.

3.2.1.1 static footprint

A static footprint test is utilized to validate the tire contact area on a hard surface at different inflation pressure and vertical load. The footprint is virtually computed by loading the tire model against a flat road and defining the contact area.

In this procedure, the tire is first inflated to the desired inflation pressure, then a constant vertical load is applied to the center of the tire and the tire is allowed to settle on the surface. The length and width of the contact patch are recorded for each inflation pressure and load, then the simulation results are compared to manufacturer-provided data [2]. Figure 3.6 shows the contact area between the tire model and the surface at 586 kPa (85 psi) inflation pressure and 27 kN (6000 lbs) vertical load.

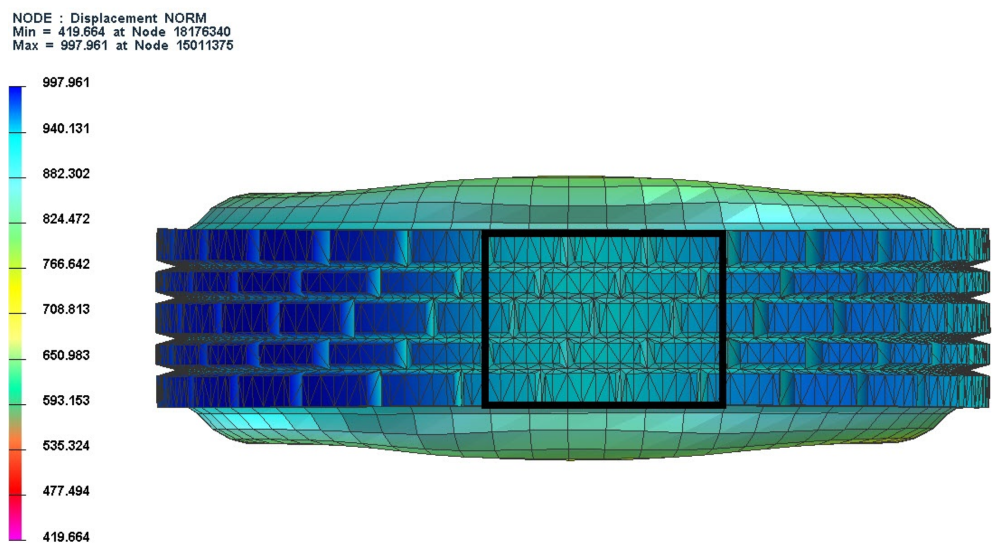

Figure 3.6: Normal nodal velocity acting on the tire-road contact area at 27 kN vertical load and 586 kPa inflation pressure

Figure 3.7 shows the relationship of the contact area as a function of the vertical load for measured data provided by Goodyear, 3-groove, and the RHD tire models. The blue curve represents the 3-groove truck tire model, which is based on the data provided by Goodyear (yellow curve), and the red curve represents the RHD tire.

It is seen that the trend of the curves is very similar for all of the tires, and the RHD tire appears to have a larger contact area than the other two tires for an equal load. It should be noted, however, that the provided measurements from Goodyear are for the 3-groove tire and not the RHD tire model, however, both tire exhibits a similar trend as a function of load.

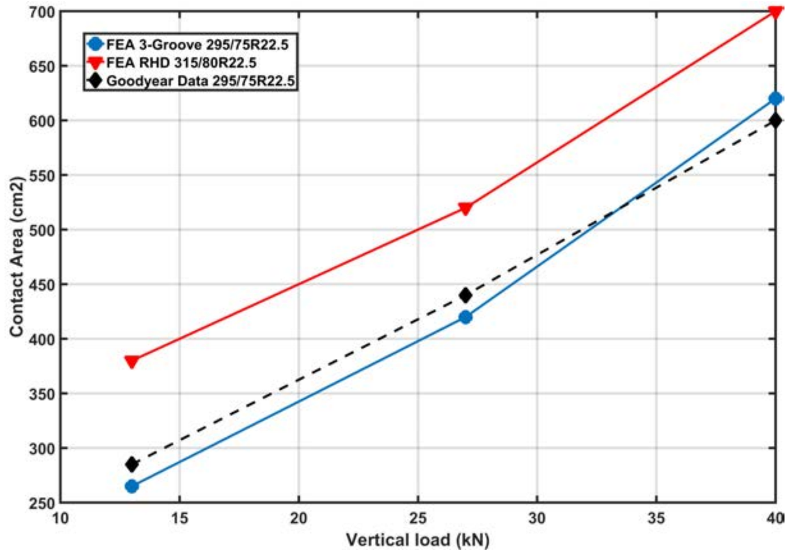

Figure 3.7: Contact area as a function of vertical load at 758 kPa inflation pressure, for the 3-groove tire, RHD tire, and measurements data

3.2.1.2 vertical deflection test

The vertical stiffness test was implemented by Chae [5], Slade [2], and Mehrsa [81]. The vertical stiffness test is shown in figure 3.8 allows for the calculation of the tire's spring rate.

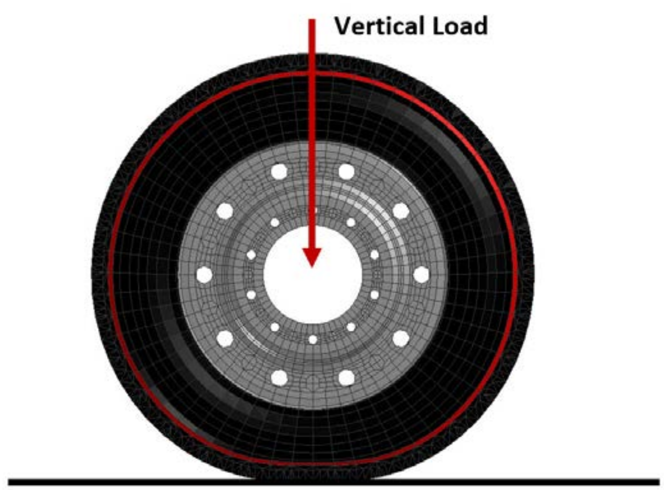

Figure 3.8: Schematic of the vertical stiffness test setup

During the vertical stiffness test, the tire is constrained in all directions except for the vertical direction. The tire is first inflated to the desired inflation pressure, then the tire is subjected to a low rate ramp loading (quasi-static) which causes the tire to slowly deform. The resultant deflection is then recorded for the corresponding vertical loads, and the relationship between vertical load and the deflection is considered.

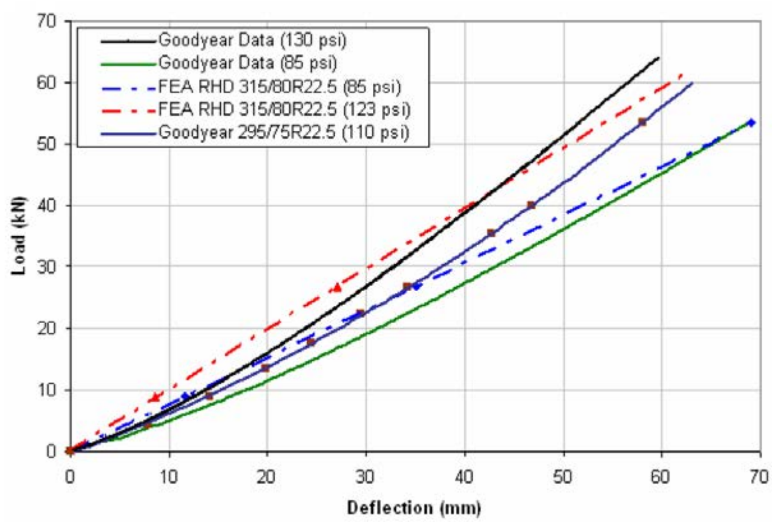

Figure 3.9: Load as a function of deflection for RHD tire model and other similar tire measurements [2]

Figure 3.9 shows the static deflection curves from actual tire data provided by Goodyear and the simulation results using the RHD tire model over a wide range of loads and inflation pressures. It is observed that all curves have a similar trend, as the vertical load increases the deflection increase as well. Furthermore, the results obtained for the RHD tire at 848 kPa (123 psi) and those obtained from Goodyear at 896 kPa (130 psi) are in good agreements. It is concluded that the tire model exhibits a similar trend as that of the actual Goodyear tire.

3.2.2 Dynamic validation test

The dynamic validation tests include the drum-cleat test to determine the first mode of vibration and the cornering test to determine the lateral force versus slip angle at different vertical loads. The results are compared with available measurements of a truck tire.

3.2.2.1 drum-cleat test

The first model of vibration is predicted using the drum-cleat test. A significant amount of tire mass is concentrated near the tread. The rolling tire radius is not constant due to the radial deflection. However, the stiffness of the tire is affected by the inflation pressure and the material properties. During this test, the drum-cleat is virtually simulated to determine the first mode of vibration by exciting the tire over a cleat on a rigid circular drum [5]. Vertical forces acting on the center of the tire are translated due to the vibrations. These vertical forces are measured and converted from a time domain to a frequency domain using a Fast Fourier Transformation (FFT) algorithm [3].

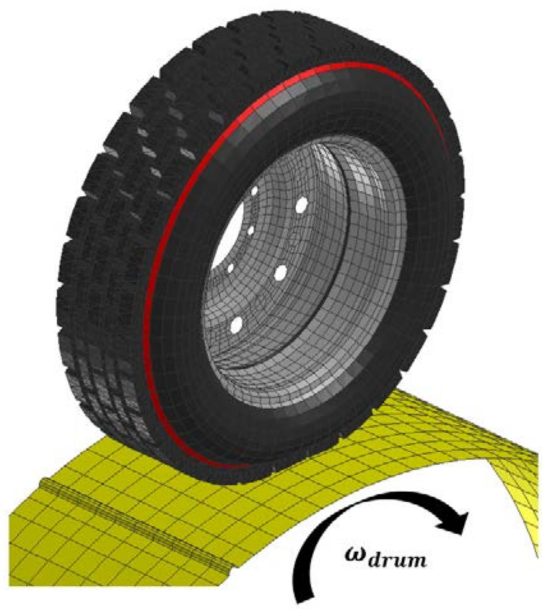

Figure 3.10: Schematic of drum-cleat test setup

Figure 3.10 shows the schematic diagram of the drum-cleat test setup. The drum has a diameter of 2.5 m, while the semicircular cleat has a radius of 10 mm. The tire is first inflated to the desired inflation pressure, then the desired vertical load is applied to the center of the tire. After loading the tire, a constraint in all three translational directions is applied to detect transmitted vertical force on the center and to be free only in the rotational direction. Angular velocity is then applied to the center of the drum to enable free rolling of the tire at a translational speed corresponding to 50 km/h. As the drum rotates, the cleat on the drum vertically excites the tire. Since the tire center is constrained vertically, the vertical reaction force due to the cleat excitation is then computed at the tire center. Furthermore, the in-plane free vibration mode is obtained by applying an FFT algorithm to the predicted vertical force as a function of time history output as shown in figure 3.11.

Figure 3.11a shows the variation of the vertical section force as a function of the frequency for different inflation pressures at 27 kN (6000 lbs) vertical load. The vertical first mode of vibration is observed between 48 and 57 Hz, while the

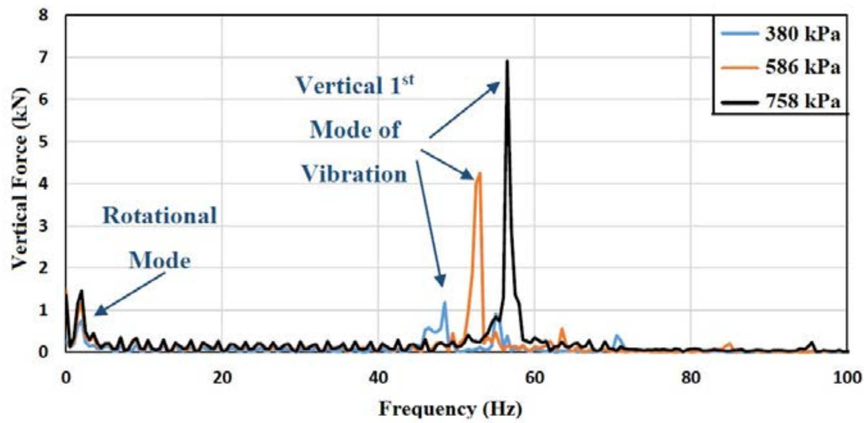

(a) Vertical first mode of vibration

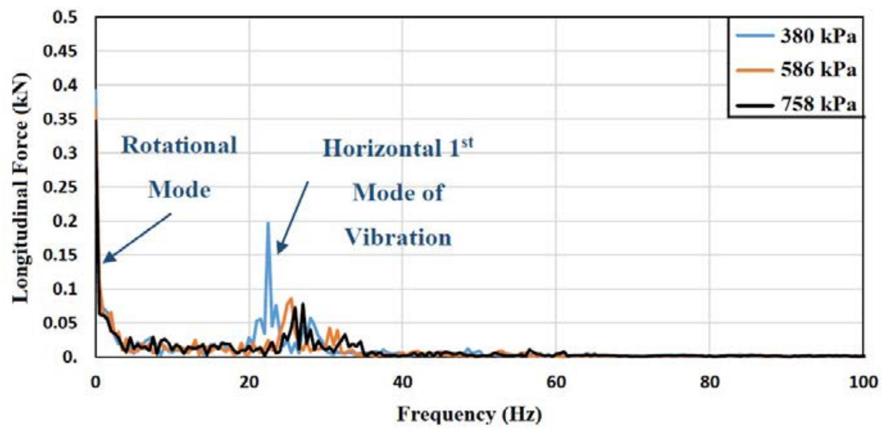

(b) Horizontal first mode of vibration

Figure 3.11: Vertical and longitudinal section force as a function of frequency for different inflation pressures at 27 kN (6000 lbs)

horizontal first mode of vibration is observed between 20 and 30 Hz, depending on the inflation pressure. It is noticed that as the inflation pressure increase, the first mode of vibration increase as well.

It should be noted that for passenger car tire the vertical first mode of vibration is between 60 and 80 Hz, and the horizontal first mode of vibration is between 40 and 50 Hz [53]. In the case of off-road tires, both horizontal and vertical modes of vibration are lower due to the thickness of the lugs. This conclusion is in agreement with published measured data for 16R20 Michelin XZL off-road tire [124], and published simulation results for 12R20 XML TL 149J [125]

3.2.2.2 cornering test

Another important dynamic validation test to be taken into consideration is the cornering test. The cornering test is virtually performed to examine the cornering characteristics of the tire model as shown in figure 3.12. The tire model is pre-steered to the desired steering angle (slip angle, α) up to 12°before the start of the simulation. The tire model is first inflated to the desired inflation pressure, and the desired vertical load is applied to the center of the tire. Later, a 10 km/h longitudinal speed is applied to the ground, and the tire is kept freely rolling until a steady-state condition is satisfied.

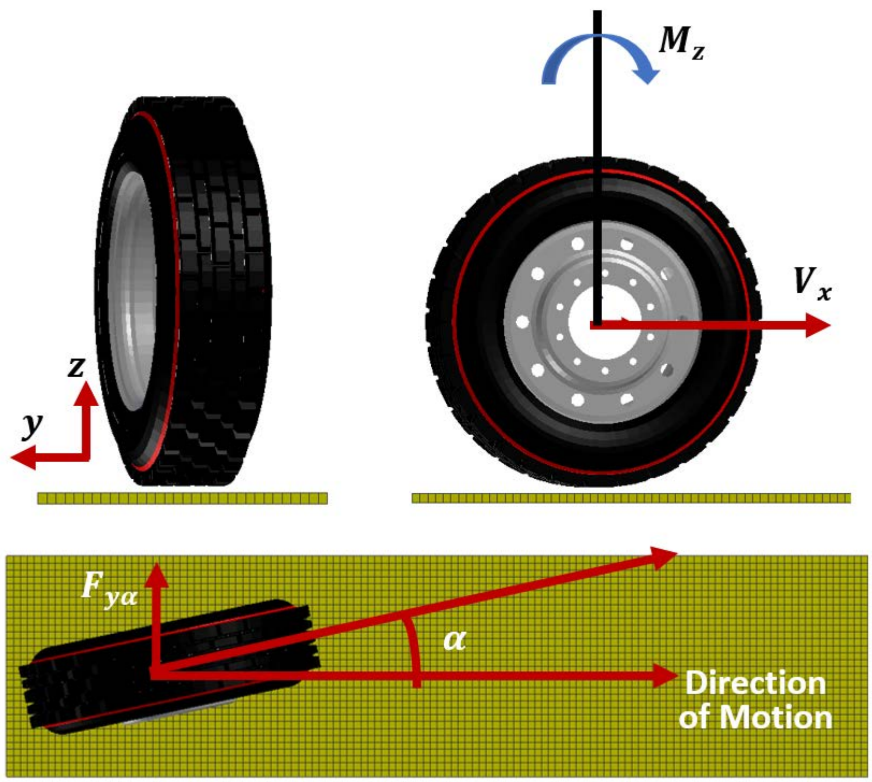

Figure 3.12: Schematic of the cornering test model setup

Figure 3.13 shows the cornering force as a function of the slip angle at 758 kPa (110 psi) inflation pressure and various loads for simulated and measured data. The measured data are obtained from the University of Michigan Transportation Research Institute (UMTRI) for the 3-groove truck tire. The measured data are used to compare the trend of the cornering characteristics of the RHD tire due to the lack of availability of measured cornering characteristics.

The applied vertical loads are 18 kN (4000 lbs), 27 kN (6000 lbs), and 36 kN (8000 lbs). The trend of predicted cornering forces as a function of slip angle is in good agreement with measurements especially at low vertical loads such as 18

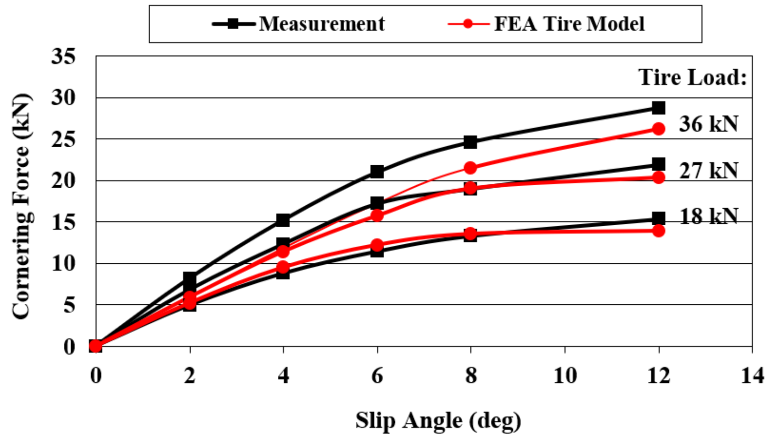

Figure 3.13: Cornering force as a function of slip angle at different vertical loads for measurement [5] and simulations

kN(4000 lbs), and 27 kN (6000 lbs).

3.3 Summary

In this chapter, the FEA tire model and validation were presented. The Goodyear's off-road RHD 315/80R22.5 drive tire model was discussed, the modeling technique including the structure, material properties, and dimensions was presented. The developed tire has a total of 9200 nodes, 1680 layered membrane elements, 4200 solid elements, 120 beam elements, and 1 rigid body (rim) definition. Furthermore, the 15°drop center rim contour dimensions, in addition to the tire-rim assembly were presented.

The FEA tire model was then verified in static and dynamic response against measured truck tire data. The static response was verified using the static footprint and vertical deflection tests. The dynamic response was verified using the drum-cleat and the cornering tests. The tests were repeated at different operating conditions including vertical load and inflation pressure. It was concluded that the static and dynamic test results are in good agreement with previously measured truck tire data.

CHAPTER 4

SOFT TERRAIN MODELING AND CALIBRATION

In this chapter, soft terrains are modeled using Smoothed-Particle Hydrodynamics (SPH) technique. The terrain models include dry sand, dense sand, clayey soil and snow. The modeled terrains are calibrated using pressure-sinkage and shear-strength tests, and compared with published terramechanics data.

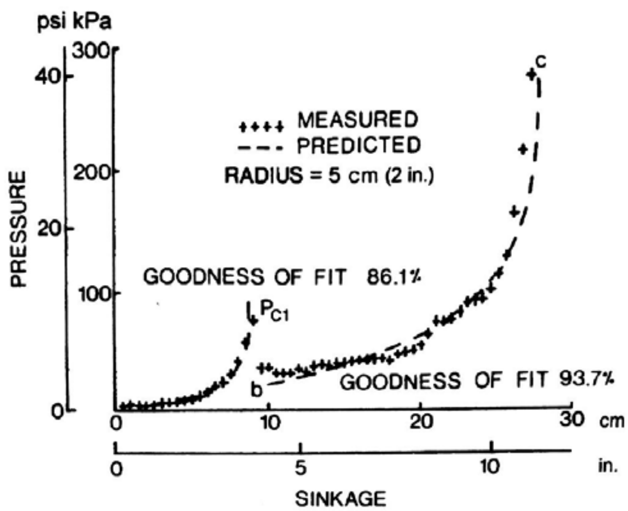

Figure 4.1: Pressure-sinkage relationship for snow collected from measurement for a plate radius of 5 cm [1]

Figure 4.1 presents the pressure-sinkage behavior of snow measured from physical terrain properties for a plate of radius 5 cm. The snow surface of the physical test is covered in an open area with subsequent snowfall on the top of the crusts. This leads to ice layer forming in the snow test. Additionally, resistance in the sinkage is observed after reaching a critical pressure of around 100 kPa. The resistance is due to snow deformation zone in the lower boundary when the plate reaches the ice layer. Thus, the pressure increases rapidly with a minimal increase in the sinkage after reaching a critical pressure [1].

4.1 Calibration Techniques

The SPH material properties are indicated in table 4.1 for various terrains. The performed two tests to calibrate the terrains are; the pressure-sinkage test, and the shear-strength test. The purpose of these tests is to validate the computational terrain models and to simulate a virtual testing simulation for parametrization.

Table 4.1: Material properties for various soils [126]

Material Type	E MPa	K MPa	G MPa	σ MPa	ρ ton/mm^3
Dense Sand	22	15	9	0.016	1.6E-9
Loose Sand	17	11	7	0.004	1.44E-9
Clayey Soil	54	133	23	0.025	2.01E-9
Sand and gravel	121	80	48	0.024	1.92E-9
Snow	1	10	1	0.001	1E-10

The pressure-sinkage and direct shear-strength tests are applied to calibrate the terrain in the normal and shear stress directions.

4.1.1 Pressure sinkage test

A rectangular soil domain of $800 \times 800 \times 800$ mm dimensions is filled with SPH terrain particles. A rigid circular plate of a 150 mm radius is placed on top of the box. The plate is then subjected to a range of pressures between 0 kPa and 200 kPa. The pressure is applied in a step change going directly into the desired pressure, the duration of the test is 0.4 sec, as it only takes a part of a second for the sinkage to reach steady state. The sinkage of the plate is then measured as an output for various pressures, and a curve is fitted to present the pressure-sinkage relationship. Figure 4.2 shows the pressure-sinkage initial and final states.

The pressure-sinkage theoretical results are found in published terramechanics data [1] for terrain materials, and the equations for pressure-sinkage relationships are also provided. Since soil is homogeneous terrain, thus it may be characterized by the following equation proposed by Bekker [127]:

$$p = (\frac{k_c}{b} + k_\theta)z^n \tag{4.1}$$

The pressure-sinkage simulation results are compared with the results obtained from equation 4.1 that contains measured terrain parameters show in table 4.2 [1]. Where p is the pressure in kPa, b is the smaller dimension of the contact patch, that is the width of a rectangular contact area or the radius of a circular

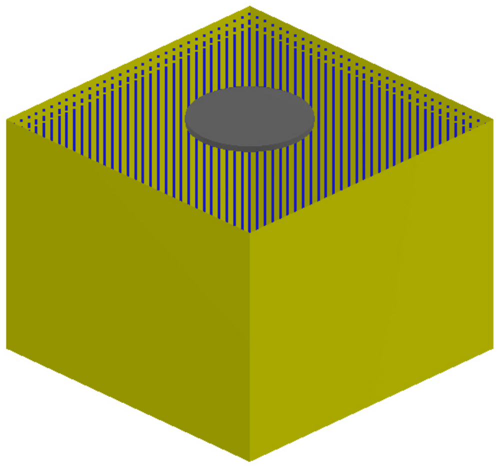

(a) Initial state

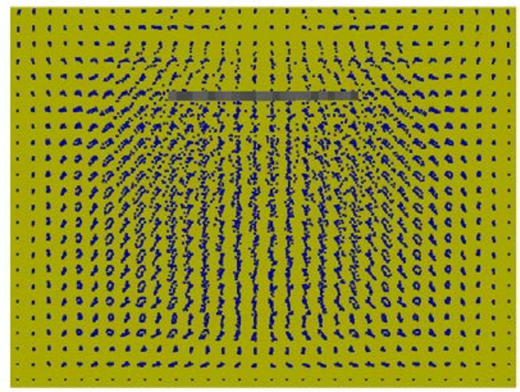

(b) Final state

Figure 4.2: Pressure-sinkage test with SPH terrain

Table 4.2: Terrain properties of modeled soils [1]

Soil name	n	k_c kN/m^{n+1}	k_θ kN/m^{n+2}	c kPa	ϕ deg
Dry sand	1.1	0.99	1528.43	1.04	28
Dense sand	0.7	5.27	1515.04	1.72	29
Clayey soil	0.7	16.03	1262.53	2.07	10
Snow Sweden	1.44	10.55	66.08	6	20.7
Snow U.S.	1.6	4.37	196.72	1.03	19.7

contact area in mm, z is the sinkage of the plate in mm, and n, k_c, and k_θ are pressure-sinkage terrain parameters.

Finally, the process is repeated several times for different SPH material parameters until the best fitting of pressure-sinkage results is obtained.

4.1.2 Direct shear-strength test

The shear-strength test is performed by constructing a rectangular box of $400 \times 200 \times 240$ mm size filled with SPH soil particles, shown in figure 4.3 [1]. The box is made of three parts the top plate in which pressure is applied on, the upper which is the sliding plate and the lower plate which is constraint from moving in all directions. A known pressure ranging between 0 kPa and 200 kPa with an increment of 50 kPa is applied to the top plate of the box, then a small ramp displacement is applied to the upper and the top plates at a rate of 10 mm/s. The shear force is computed until the top box displacement reaches 100 mm.

The shear stress is calculated and plotted against the shear-stress displacement relation described by the exponential function proposed by Janosi and Hanamoto in equation 4.2 [127]. The results are compared with Bekker's shear-strength relation shown in equation 4.3 [1]. The test is repeated for different SPH material properties until the best fitting results are obtained.

$$\begin{aligned}\tau &= \tau_{max}\left(1-e^{(-j/k)}\right) \\ &= (c+p\tan\phi)\left(1-e^{(-j/k)}\right)\end{aligned} \tag{4.2}$$

The maximum shear τ_{max} can be determined through the Mohr-Coulomb failure criterion in equation 4.3.

$$\tau_{max} = c + p\tan\phi \tag{4.3}$$

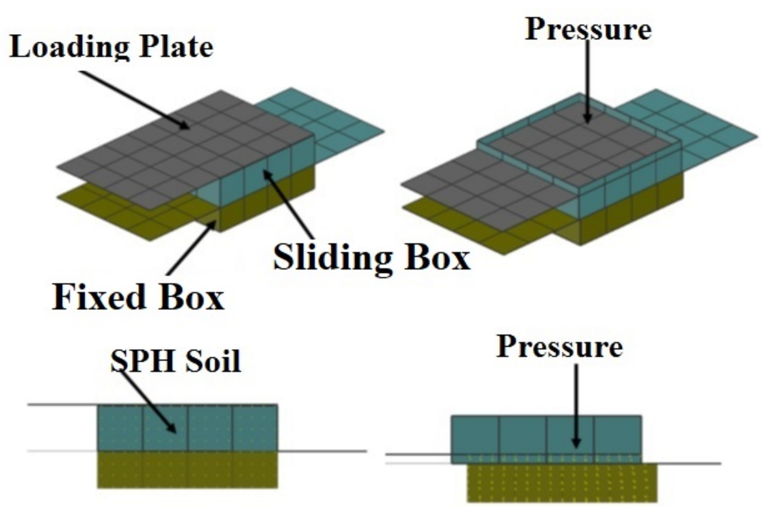

Figure 4.3: Shear-strength test with soft terrain

It should be noted that both the pressure-sinkage and shear-strength tests must be simulated using identical SPH material properties to get optimal behavior for both tests. During the calibration process, the SPH material parameters are continuously adjusted, and both tests are continuously repeated until the best agreement is reached between the simulation and experimental results. The pressure-sinkage and shear-strength simulations are repeated several times, the number of repetition of the test varies from one terrain to another and could vary between 10 to 30 repetitions.

4.2 Terrain Calibration Results

The material properties mentioned in table 4.1 were preliminary used to calibrate the terrain properties. The pressure-sinkage and shear-strength tests are performed and the results are compared with the terrain values mentioned in table 4.2.

4.2.1 Dry sand

Dry sand is found in most countries and consists of non-homogeneous granular particles with various material properties. It behaves like a fluidic flow when disturbed since there is no moisture present in it. Figure 4.4a presents the pressure-sinkage relationship results for both simulated and measured cases. It is shown that the two lines corresponding to simulation and measured are close.

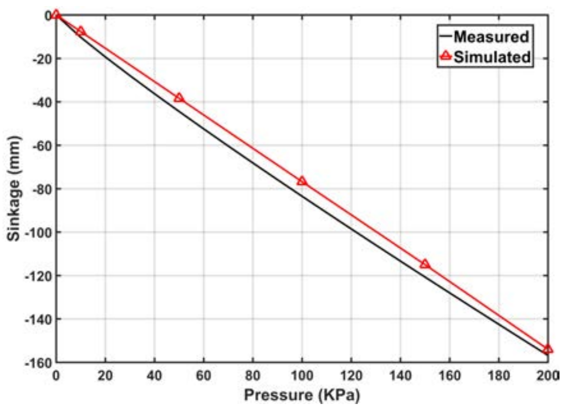

(a) Pressure-sinkage

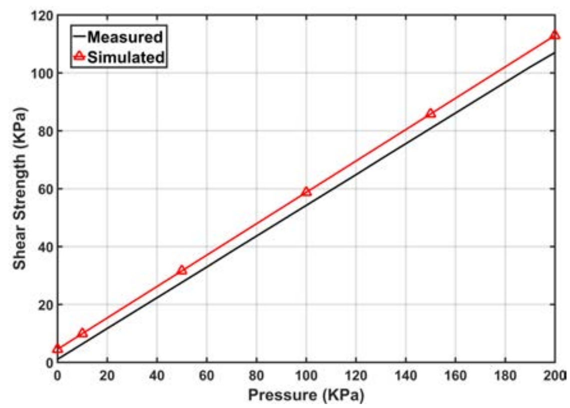

(b) Shear-strength

Figure 4.4: Pressure-sinkage and shear-strength relationship for dry sand simulation and measurement

The simulated sinkage at 200 kPa is determined to be 157 mm, while the measured one is 156.8 mm. Figure 4.4b presents the shear-strength relationship results for dry sand. The slope of the shear-strength curve is known as the $\tan\phi$ and the y-intercept of the shear-strength curve is known as the soil cohesion shown in figure 4.4b. The cohesion simulated is determined to be 4.5 kPa, while the one measured is 1.04 kPa. The simulated internal friction angle is determined to be 28.4°while the measured one is 28°. These results are close to the physical measurements and within a minimal range. Thus, this dry sand model is proven to be consistent, and adopt the same physical behavior in normal and shear stresses.

4.2.2 Dense sand

Dense sand or sandy loam is another type of soil; it is mostly composed of sand particles and a small amount of clay. The moisture content is around 15% which makes it suitable for gardening and drainage. The same analysis procedure is performed on the dense sand. The two tests are implemented, and the results are compared with the measurements. Figure 4.5a and 4.5b presents the results of the pressure-sinkage and the shear-strength for both simulated and measured cases.

The pressure-sinkage relationship for dense sand is fitted as a second-degree quadratic equation which takes the parabolic shape. The simulated sinkage at 200 kPa is determined to be 56.66 mm, while the measured one is 53.64 mm. The shear-strength parameters are determined for the curves, the cohesion coefficient simulated is determined to be 9.8 kPa, and the measurement is 1.72 kPa. The internal friction simulated is determined to be 29.4°, and the measurement is 29°. The pressure-sinkage test and the shear-strength test show similar behavioral results.

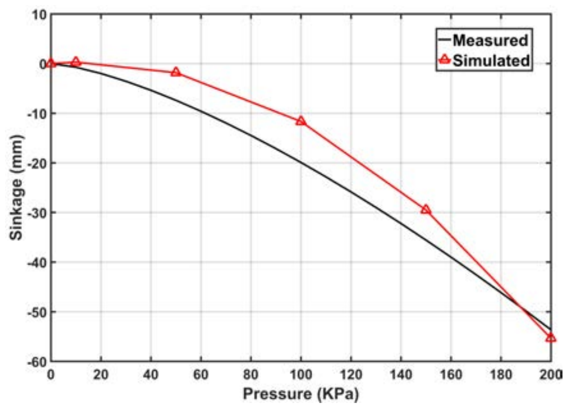

(a) Pressure-sinkage

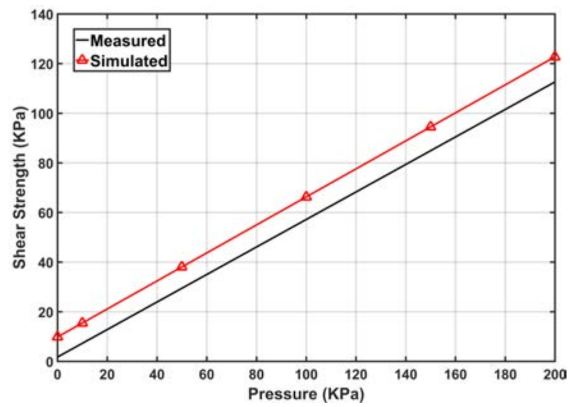

(b) Shear-strength

Figure 4.5: Pressure-sinkage and shear-strength relationship for dense sand simulation and measurement

4.2.3 Clayey soil

Clayey soil and its counterpart from Thailand consist of clay minerals and relatively high moisture content, resulting in a more cohesive type of soil than sand. The same analysis is applied to clayey soil from Thailand. Figures 4.6a and 4.6b shows the pressure-sinkage and shear-strength results. The simulated cohesion is determined to be 15.7 kPa; the measured one is 2.07 kPa. The simulated internal friction is determined to be 12°; the calculated one is 10°. The results show a difference between the simulations and the measured, as clayey properties may vary depending on the sample collection and the material properties. It is noted that the SPH technique doesn't accurately capture the shear characteristics of the clayey soil behavior completely due to its hardness in comparison to the dense sand and dry sand.

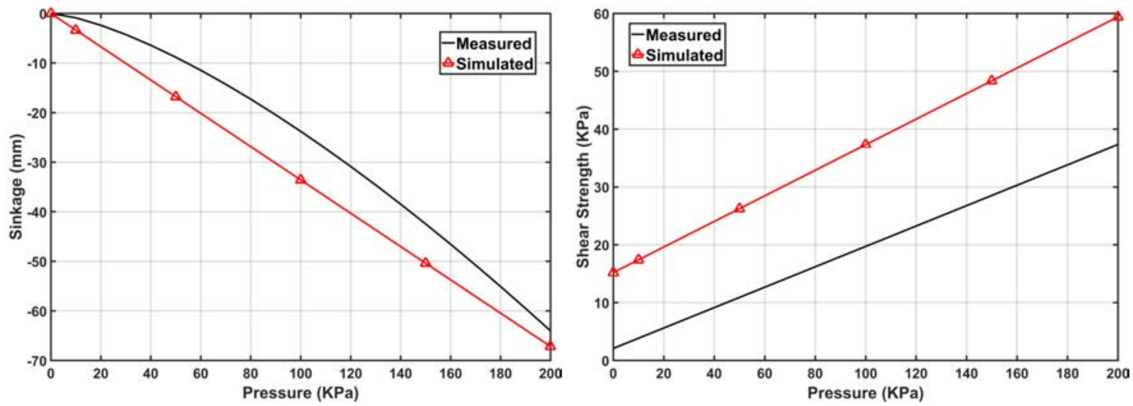

(a) Pressure-sinkage (b) Shear-strength

Figure 4.6: Pressure-sinkage and shear-strength relationship for clayey soil simulation and measurement

4.2.4 Snow

The SPH snow model presented in this section is considered to be a first attempt to model snow using SPH technique.

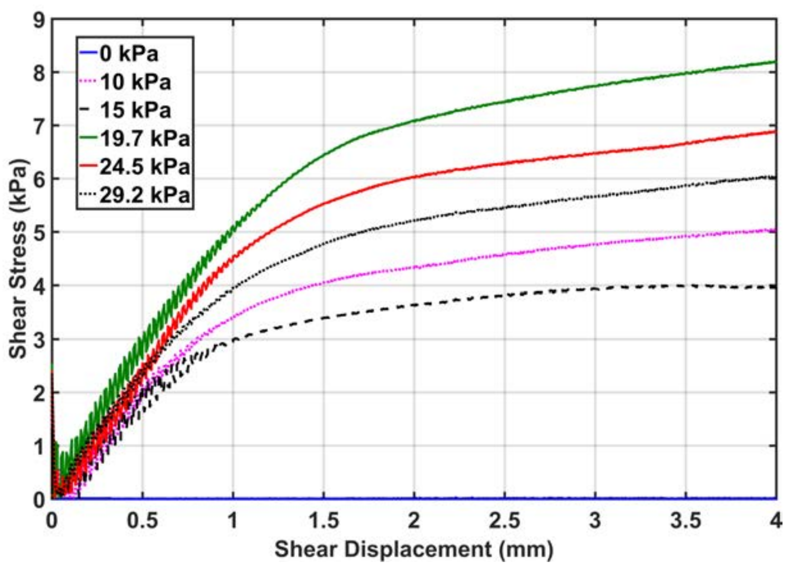

Figure 4.7: Shear stress as a function of shear displacement obtained from shear-strength test for snow at different applied pressure

The snow is calibrated using the above two mentioned tests. SPH snow is calibrated against snow from Sweden collected from literature [1]. Sweden snow has considerably a high cohesion in comparison to that of sand. In a comparison of the Sweden snow to snow from the U.S., Sweden snow has the lowest index n and the highest cohesion which is 6 kPa. Figure 4.7 shows the shear-stress in kPa as a function of the shear displacement in mm for various pressures between 0 and 29.2 kPa. The figure shows a rapid increase and some oscillations at the beginning of displacement curve, the curve then continues in an approximately steady state motion. The curves can be compared with those obtained from physical measurements [1]. The results show similarity in shape and slope.

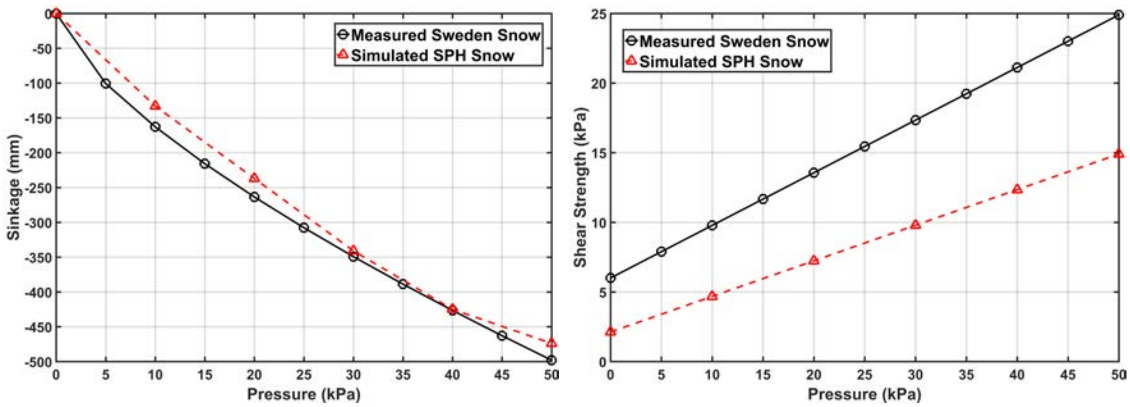

(a) Pressure-sinkage

(b) Shear-strength

Figure 4.8: Pressure-sinkage and shear-strength relationship for simulated snow and measurement

Figures 4.8a and 4.8b shows the pressure-sinkage and shear-strength relations, respectively. It can be concluded from figure 4.8a, the SPH snow modeled is in good agreement with that from Sweden, at 50 kPa pressure the SPH snow has a sinkage of 473 mm while the Sweden snow has a sinkage of 498 mm. It is noted that this test is only done for a pressure up to 50 kPa due to the limitation of snow during pressure.

Furthermore, the SPH snow and Sweden snow are in good agreement in shear-strength behavior as well. The internal friction angle known as the tangent of the shear-strength line is calculated from simulations to be 20.7°and that from Sweden snow to be 16.2°. The cohesion known as the y-intercept is calculated from simulation to be 1 kPa and that of Sweden snow is 6 kPa.

It should be noted that the snow model may vary significantly depending on the desired terrain properties and the environmental conditions. The snow model presented is obtained from various calibrations and simulations.

4.3 Sensitivity Analysis of SPH Material

The SPH terrain behavior is highly dependent on the material parameters being used. The material parameters have consequences on the property change in the pressure-sinkage and shear strength relationships. In this section, sensitivity analysis for various parameters is conducted. The effect of these parameters on the material behavior is investigated. The parameters studied include shear box displacement speed in the shear-strength test, tangent modulus, yield strength, the coefficient of the pressure-volume equation of state.

4.3.1 Shear box displacement speed

The shear box displacement speed is the speed at which the box is being pulled. This parameter is relevant when performing the direct shear box test. It defines how fast the SPH particles are moving, and thus how quickly will the particles react to the change in speed.

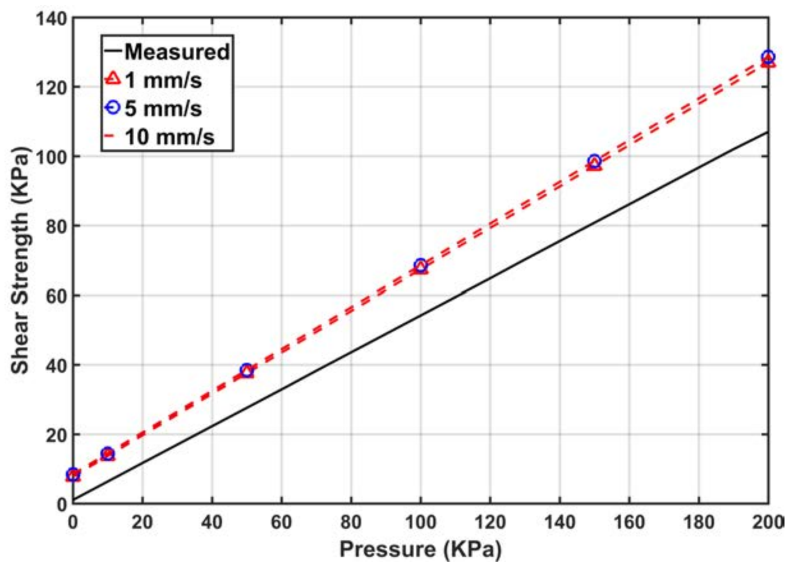

Figure 4.9: Shear-strength as a function of pressure for several shear displacement speeds

Three different speeds are tested under constant material conditions. All material and SPH control parameters are kept constant while changing the speed of shear box displacement. The total displacement of 10 mm is required to finish this test. Thus, the box with speed of 10 mm/s ran for 1 sec, the box with speed of 5 mm/s ran for 2 sec, and the box with speed 1 mm/s ran for 10 sec.

Figure 4.9 shows the results of the three different displacement speed of the shear box from simulation and the measurement at 1 mm/s. Table 4.3 summarizes the parameters required to compare the results. It was concluded, the speed of the box has a minimal effect on the shear strength relationship. As the speed varies 10 times slower between 10 mm/s to 1 mm/s, the cohesion changes between 8.48 kPa and 7.77 kPa which is only 8%. Note that a speed difference of 10 times also means approximately 10 times more computational time to reach the same displacement.

Table 4.3: Shear-strength properties for several simulated displacement speed

Terrain properties	Measurement 1 mm/s	10 mm/s	5 mm/s	1 mm/s
c (kPa)	1.04	8.48	8.41	7.77
ϕ (deg)	28	30.99	30.95	30.8

4.3.2 Equation of state coefficient

The second parameter studied is the coefficient of the pressure-volume equation of state c_1, and it is calculated by solving the pressure-volume equation of state. This parameter affects both pressure-sinkage and shear-strength relationships. Similar to the previous test, all parameters are kept constant, and only c_1 is being changed. The box is moving at a constant speed of 5 mm/s for 10 seconds. Three different values of c_1 were selected 2.5, 5 and 11 MPa for dry sand. Figures 4.10a and 4.10b shows the results for the pressure-sinkage and shear-strength respectively.

Table 4.4 presents a summary of the results of both tests, and the sinkage is calculated at 200 kPa pressure. The sinkage of the soil is highly affected by the value of c_1. As c_1 increases from 2.5 MPa to 11 MPa the sinkage decreases between 157 mm and 139 mm.

Table 4.4: Terrain properties summary for various simulated c_1 coefficients and measurement for dry sand

Terrain properties	Measurement	2.5 MPa	5 MPa	11 MPa
Sinkage (mm)	156.8	157	147	139
c (kPa)	1.04	8.31	8.41	8.47
ϕ (deg)	28	27.29	30.95	34.2

For the shear- strength test, as c_1 increases between 2.5 and 11 MPa, the cohesion increases between 8.31 and 8.47 MPa. Similarly, for the internal friction angle, it also increases between 27.29°and 34.2°. The coefficient c_1 affects the stiffness of the material, for example; having a smaller value will give a softer material resulting in more sinkage. The best result is obtained when c_1 is equal to 2.5 which is close to the measurement sinkage. The effect over the shear-strength is similar to that over sinkage as c_1 increases so does the internal friction that increases the shear force. As c_1 increases the material becomes denser and thus the plate sink less. In this case, the best value of c_1 is taken to be 2.5 MPa.

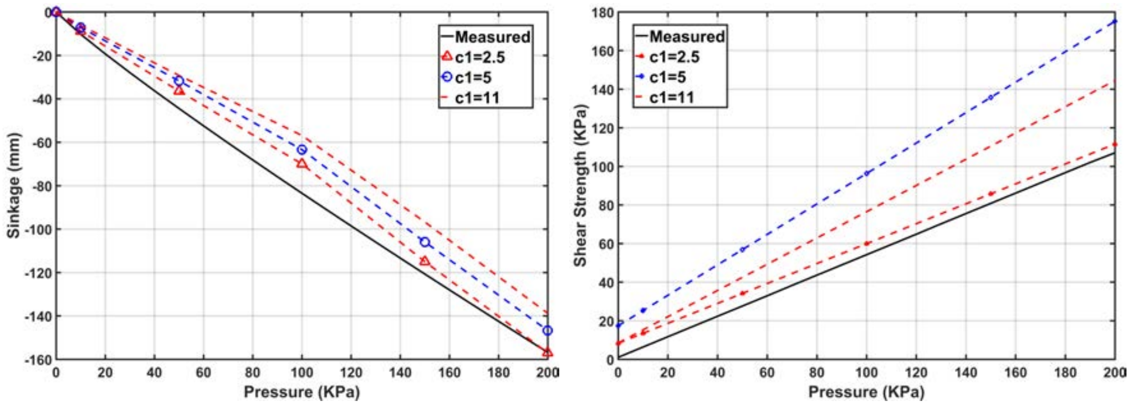

(a) Pressure-sinkage (b) Shear-strength

Figure 4.10: Calibration results for various c_1 coefficients of 2.5, 5 and 11 MPa versus measurement for dry sand

4.3.3 Yield strength

The third parameter studied is the yield strength (SIGMAy). The yield stress presents the value of the stress at the yield strength. Stress higher than the yield strength will lead to a permanent deformation also known as plastic deformation. After performing several simulations on the shear box test, it was concluded that the yield strength has a minimal effect on the shear-strength relationship. However, it has a significant effect on the pressure-sinkage relationship. During this test, all parameters were kept constant, and only yield strength is changed to 0.01, 0.016, and 0.025 MPa.

Figure 4.11 presents the pressure-sinkage relationship for various yield strengths. The effect of yield strength is similar to that of the coefficient of the equation of state. As the yield strength increases between 0.01 and 0.025 MPa, the sinkage decreases between 64.03 and 39.7 MPa. Thus, as the yield strength increases, resulting in a denser material. In this case, the best value of the yield strength is the nearest one to the measurement which is 0.01 MPa.

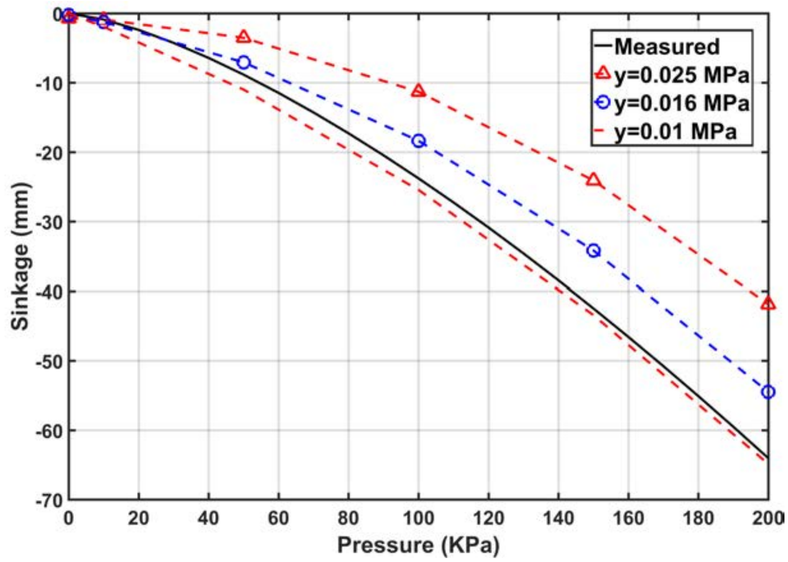

Figure 4.11: Pressure-sinkage relationship of various yield strength of 0.01, 0.016, 0.025 MPa versus measurement for clayey soil

4.3.4 Tangent modulus

The last parameter considered is the tangent modulus (E_t). Tangent modulus is defined as the slope of the stress-strain curve at a point of interest and is known as Young's Modulus when the point of tangency falls within the linear range of the stress-strain curve. Tangent modulus is useful in defining material behavior since it quantifies the softening of the material when determining the modulus in the plastic range of the material stress-strain curve.

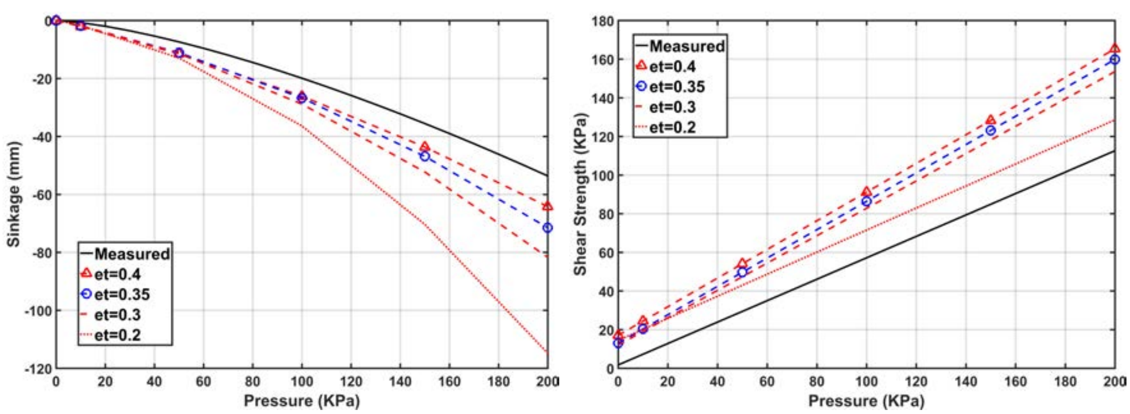

(a) Pressure-sinkage (b) Shear-strength

Figure 4.12: Calibration results of various tangent modulus for dense sand

In this test, all parameters are kept constant, and the tangent modulus is varied. This test was done for dense sand at a constant displacement speed of 5 mm/s for 10 sec. Different tangent modulus of 0.4, 0.35, 0.3, and 0.2 MPa magnitude are tested. Figures 4.12a, and 4.12b presents the results of the pressure-sinkage and shear-strength tests respectively. As the tangent modulus increases between 0.2 and 0.4 MPa, the sinkage decreases between 115.13 and 53.64 mm. The increase in the tangent modulus results in a stiffer soil. In this case, the optimal modulus based only on the sinkage test is 0.4 MPa. On the other side, as the tangent modulus increases between 0.2 and 0.4 MPa, the cohesion increases between 9 and 14.1 kPa. The increases result in a greater cohesion than the measured value. Similarly, internal friction increases between 30°and 37.3°. The best tangent modulus according to the shear-strength relationship only is 0.2 MPa.

The tangent modulus affects both pressure-sinkage and shear-strength tests inversely. However, the optimal soil properties should include only one tangent modulus regardless of the test performed. Thus, all parameters should be consistent for both tests. In this case, a compromise should be made while choosing the tangent modulus. The compromises could include choosing a mean value for E_t and then making soil stiffer by changing the equation of state constant c_1.

Note that the tangent modulus affects the slope of the shear force versus shear displacement. As the tangent modulus increases the slope of the curve increases, resulting in a non-steady curve. It is recommended to keep tangent modulus low to have a stable shear test.

4.4 Summary

This chapter focused on three main aspects of soft terrain modeling and calibration. First, calibrating three soil types that are highly used in the vehicle-terrain industry the soils included the dry sand, dense sand, and clayey soil. Second, attempt to model snow using the SPH technique and published terramechanics data for snow from Sweden. Third, studying the effect of various parameters on the soil behavior, the parameters included the shear box displacement speed, equation of state coefficients, yield strength, and tangent modulus.

The terrains were modeled using the SPH technique and the hydrodynamics-elastic-plastic material. Then the terrains were virtually calibrated by performing pressure-sinkage, and shear-strength tests. The results obtained from the simulation were compared with published terramechanics measurement data. The calibration procedure was repeated several times until the desired behavior was obtained. The cohesion and angle of shear resistance were calculated using Mohr-Columb failure criteria and validated against physical terramechanics published parameters. It was concluded that the modeled dry sand and dense sand is in a good agreement with that from the measurement. In the case of clayey soil, the pressure-sinkage characteristics and the angle of shear resistance were captured correctly. Moreover, the SPH technique doesn't accurately capture the cohesion of the clayey soil behavior completely due to its hardness in comparison to the dense sand and dry sand.

Furthermore, snow was modeled using preliminary material parameters obtained from the literature. Physical measurements were reported in the literature for various snow models from the U.S. and Sweden. The snow was also modeled using the SPH technique and hydrodynamic-elastic-plastic material. The snow simulated represents a first attempt to model snow using the SPH technique for coupled FEA-SPH applications. It was concluded that the snow model well captures the normal stresses, however further investigation is needed for the shear stresses.

Sensitivity analysis for various parameters including the yield strength and tangent modulus was performed. The results showed a minimal influence of the yield strength on the shear box test and a high impact on the pressure-sinkage relationship. It was reported that as the yield strength increases the sinkage decreases making the soil stiffer. The tangent modulus affects both tests and is considered the most difficult parameter to calibrate, as it has an inverse effect on the pressure-sinkage and shear strength relationships. It was reported that the tangent modulus should be kept low for a stable shear box test. Another parameter that affects both tests is the c_1 which was computed by solving the pressure-volume equation of state. This parameter affects the behavior of both pressure-sinkage and shear strength, as c_1 increases the material behaves more stiffly. The speed of the shear box displacement was investigated, and it was reported that the effect of the speed is minimal when kept between 1 and 10 mm/s.

CHAPTER 5

MOIST TERRAIN MODELING AND CALIBRATION

This chapter explores two novel approaches to model moist terrains. The first approach deploys linear interpolation onto published terramechanics research to compute moist terrain values. The moist terrain values are then used to calibrate new terrain models using pressure-sinkage and shear-strength tests.

The second approach pressurizes water particles into sand particles by implementing sand-water interaction. This process is presented for the first time to simulate moist terrain calibration including pressure-sinkage and shear-strength tests. The sand is modeled by several layers of an individual type of particles created in the bottom of a terrain box; the sand is considered to be hydrodynamic elastic-plastic material, the Mohr-Coulomb failure criterion is used to model the stress state of the sand. The water is modeled by several layers of an individual type of particles created on top of the sand in the terrain box; the water behavior is captured using the Murnaghan equation of state. The second moisturizing technique is examined using pressure-sinkage and shear-strength simulation tests and validated against physical measurement carried out in a laboratory under similar terrain conditions and bulk density. Finally, the effect of moisture content on terrain characteristics is discussed and investigated.

5.1 Analytical Two-Phase Terrain Model

The SPH principles used to model water and terrain are summarized in this section. Additionally, the modeling of water and terrain using the SPH technique is explained. Finally, the two-phase interaction between water and terrain is examined using Darcy's law.

5.1.1 Principles of SPH

The SPH method is based on interpolation which allows any function to be exposed regarding its values at a set of disordered points. In 1977, Gingold and Monaghan introduced the SPH idea [128]. The integral interpolant also is known as the "kernel estimate" of any function $A(r)$ is defined in equation 5.1, where r and r' are contained in the integration domain; and h is the smoothing length defining the influence domain $A(r)$ [129].

$$A(r) = \int A(r')W(r - r', h)dr' \tag{5.1}$$

W, is an interpolating kernel also known as the smoothing function and should satisfy the three properties in equations 5.2, 5.3 and 5.4 [130]. Equation 5.2 is the normalization condition of the function W; equation 5.3 is the Delta function property when the normalization length, h, approaches zero. Equation 5.4 is the compact condition; κ defines the domain of $A(r)$ and is a constant related to the smoothing function for point at r as shown in figure 5.1.

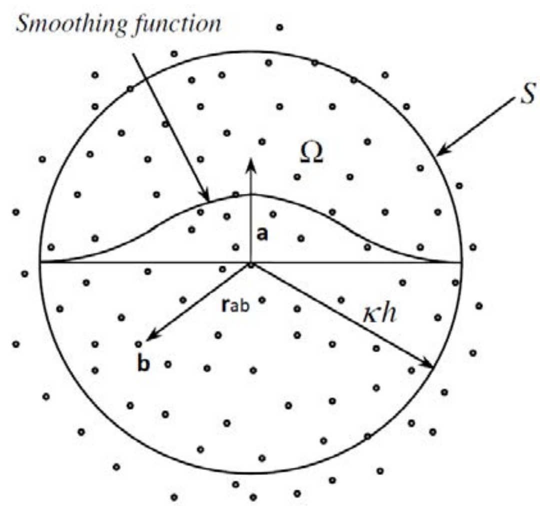

Figure 5.1: Particle interpolation using particles within the influence domain of W for particle a [118]

$$\int W(r - r', h)dr' = 1 \tag{5.2}$$

$$\lim_{h=0} W(r - r', h) = \delta(r - r') \tag{5.3}$$

$$W(r - r', h) = 0 \text{ when } | r - r' | > \kappa h \tag{5.4}$$

Originally in 1977, Monaghan and Gingold [130] used Gaussian kernel which is defined in one-dimensional. A kernel based on splines has demonstrated to be computationally efficient. However, to find physical interpolation of an SPH equation, it is always best to assume the kernel is a Gaussian. For the purpose of this research the cubic spline interpolation function introduced by Monaghan

[131] is implemented. The cubic spline function is defined in equation 5.5 for three different x conditions, where x is the relative distance between r and r'.

$$W(x,h) = \alpha_d \times \begin{cases} 1.5 - x^2 + 0.5x^3 & 0 \le x < 1 \\ \frac{(2-x)^3}{6} & 1 \le x < 2 \\ 0 & x \ge 2 \end{cases} \tag{5.5}$$

α_d is a function defined in one-dimensional space as $\frac{1}{h}$, in two-dimensional space as $\frac{15}{7\pi h^2}$ and in three-dimensional space as $\frac{3}{2\pi h^3}$. The spatial derivative of a vector quantity $\nabla A(r)$ is derived by substituting $A(r)$ with $\nabla A(r)$ in equation 5.1, equation 5.6 shows the spatial derivative after applying the compact condition.

$$\nabla A(r) = -\int A(r')\nabla W(r - r', h)dr' \tag{5.6}$$

For numerical analysis the integral interpolant is approximated by a summation interpolant, and thus $A(r)$ is written in summation interpolant, where b denotes a particle label, and the summation is over all the particles. Particle b has a position r_b, mass m_b, and density ρ_b. A_b denotes the value of any quantity A at r_b. Consecutively, the particle approximation of the spatial derivative of the function at point a can be written as shown in equation 5.7 and the function $\nabla_a W_{ab}$ is the gradient of $W(r_a - r_b, h)$ taken with respect to the coordinates of particle a [132].

$$\nabla A_a(r) = \sum_b m_b \frac{A_b}{\rho_b} \nabla_a W_{ab} \tag{5.7}$$

5.1.2 SPH water model

Navier-Stoke equations are known as the governing equations for fluid flow. The conservation of mass and moment stated by the Lagrangian description are shown in equation 5.8 and 5.9, respectively [132]. Where α, β are used to express the coordinate directions, $\sigma^{\alpha\beta}$ is the total stress tensor, and f^α is the component of acceleration caused by external force.

$$\frac{D\rho}{Dt} = -\rho \frac{\partial v^\alpha}{\partial x^\alpha} \tag{5.8}$$

$$\frac{Dv^\alpha}{Dt} = \frac{1}{\rho}\frac{\partial \sigma^{\alpha\beta}}{\partial x^\beta} + f^\alpha \tag{5.9}$$

The stress tensor $\sigma^{\alpha\beta}$ is defined in equation 5.10 and it consists of two parts the isotropic pressure p and the viscous shear stress $\tau^{\alpha\beta}$. Where $\delta^{\alpha\beta}$ is the Kronecker's delta, which is equal to 1 if $\alpha = \beta$ and zero otherwise.

$$\sigma^{\alpha\beta} = -p\delta^{\alpha\beta} + \tau^{\alpha\beta} \tag{5.10}$$

Water is considered a Newtonian flow and thus the viscous shear stress is proportional to ϵ the shear rate through the viscosity μ as shown in equation 5.11.

$$\tau^{\alpha\beta} = \mu \left(\frac{\partial v^{\beta}}{\partial x^{\alpha}} + \frac{\partial v^{\alpha}}{\partial x^{\beta}} - \frac{2}{3} \left(\frac{\partial v^{\gamma}}{\partial x^{\gamma}} \right) \delta^{\alpha\beta} \right) \tag{5.11}$$

The equation of state is additionally used to determine the above Navier-Stokes relationships. The equation of state is adopted to estimate the change in pressure of SPH water particles. Murnaghan equation of state [130] is used for liquids with artificially expanded compressibility. Equation 5.12 is used to perform a particular class of hydrodynamic simulations where the flow velocity remains entirely below the physical speed of sound.

$$p = p_o + B \left(\left(\frac{\rho}{\rho_0} \right)^{\gamma} - 1 \right) \tag{5.12}$$

$$B \geq 100 \rho_0 \frac{{v_{max}}^2}{\gamma} \tag{5.13}$$

Equation 5.12 presents the relation between the pressure and the density rations. Where γ is a constant parameter that is equal to seven in most cases, ρ_0 is the initial density and B is a parameter that depends on the problem conditions and establishes a boundary to the maximum variation in density. The parameter B can be determined using equation 5.13, where v_{max} is the maximum water speed.

5.1.3 SPH terrain model

The behavior of terrain is modeled in a similar way to that of water. The conservation equation of mass and moment, nevertheless utilized to predict the density and motion of terrain particles. The main difference between the terrain and water model is the stress tensor. As mention in section 5.1.2, the water adheres to the Murnaghan equation of state, while in the case of terrain the pressure and the stress-strain behavior are considered to be hydrodynamic elastic-plastic. Unlike water, the stress tensor of the modeled terrain shown in equation 5.14 consists of two parts; the deviatoric shear stress, s and the isotropic pressure, p [3].

$$\sigma^{\alpha\beta} = -p\delta^{\alpha\beta} + s^{\alpha\beta} \tag{5.14}$$

The pressure is commonly calculated using the “equation of state” which is a function of the density change and internal energy. The equation of state used in this research is that of a hydrodynamic elastic plastic material as shown in equation 5.15. Where c_0 to c_6 are material constants, $\mu = \rho/\rho_0 - 1$ is the ratio of current over initial mass density, and E_i denotes the internal energy.

$$p = c_0 + c_1\mu + c_2\mu^2 + c_3\mu^3 + (c_4 + c_5\mu + c_6\mu^2)E_i \tag{5.15}$$

The solution of equation 5.15 depends on the terrain being modeled and a calibration procedure is required to obtain the proper material behavior, further research on different material properties can be found in a previous publication.

$$s_{max} = c + p \tan\theta \tag{5.16}$$

The shear stress components should be limited to the failure of the surface which happens when the plastic flow commences. The Mohr-Coulomb criterion is implemented to determine the plastic flow region shown in equation 5.16. Where c is the cohesion constant, p is the applied pressure, and θ is the angle of internal shearing resistance [1]. It is noted that c, and θ are considered terrain properties and are determined experimentally through the direct shear test.

5.1.4 Two-phase interaction

The conservation equations developed in sections 5.1.2 and 5.1.3 are only for one flow phase, to model the interaction between two phases (in this case sand and water) the seepage force is introduced. The gravitational and seepage forces emerge on the sand particles and are added to the momentum equations for both sand and water as an external force. Equation 5.17 is based on Darcy's law [133], where the unit weight of water is denoted by γ_w, n is the porosity and k is the dry sand permeability which is selected from literature in this case to be 5 $cm/hour$ for dry sand [134].

$$f_{seepage} = \frac{\gamma_w n}{k}\left(v_{water} - v_{soil}\right) \tag{5.17}$$

The movement of SPH particles on sand and water is computed independently using each material SPH governing equations. The governing equations are superimposed, and the interaction connecting the two-phases is reflected through the seepage force. The pressure exerted on the sand due to water is allowed to contribute to the sand pressure throughout the overlapping method.

5.2 Moist Terrain Interpolation Technique

The moist terrain interpolation technique is applied to the sandy loam. Sandy loam is a terrain composed mostly of sand (50 to 70 % sand) and a small amount of clayey and silt [62]. Unlike dry sand, sandy loam exist with different moisture content depending on the environment and weather conditions. The advantage of using sandy loam for tire-terrain interaction includes the ability to predict the effect of moisture content on tire operational performance. Wong [62] published experimental data representing a wide range of mean terrain values characterizing the pressure-sinkage and shear-strength relationships of various upland sandy loam as shown in tables 5.1 and 5.2, respectively. The terrain values presented in tables

5.1 and 5.2 are then used to generate the best linear fit between sandy loam terrain values and moisture content. Once the terrain values are identified for each moisture content, the calibration procedures are implemented and new terrains with moisture content are modeled.

Table 5.1: Pressure-sinkage terrain properties of sandy loam with different moisture content [62]

n	k_c kN/m^{n+1}	k_θ kN/m^{n+2}	Wet density kg/m^3	Moisture content, %
1.10	74.6	2080	1557	51.6
0.97	65.5	1418	1542	49.2
1	5.7	2293	1570	49.1
0.74	26.8	1522	1519	44.3
1.74	259	1643	1696	50.0
0.85	3.3	2529	1471	28.6
0.72	59.1	1856	1592	34.3
0.77	58.4	2761	1559	35.1
1.09	24.9	3573	1716	31.2
0.7	70.6	1426	1470	27.3
0.75	55.7	2464	1526	32.6

Table 5.2: Shear-strength terrain properties of sandy loam with different moisture content [62]

Cohesion, c kPa	Angle of shear resistance ϕ, deg	Wet density, ρ kg/m^3	Moisture content %
2.2	39.4	1468	49.4
3.3	33.7	1549	50.1
2.8	33.4	1497	62.2
1.1	33.5	1479	53.9
3.4	24.1	1646	54.2
2.6	29.1	1641	58.1
5.1	25.6	1445	34.0
4.3	22.7	1459	39.3
2.7	26.1	1441	41.3
2.5	28.2	1384	30.0

5.2.1 Identification of terrain values

Figure 5.2 shows different terrain values as a function of moisture content for sandy loam.

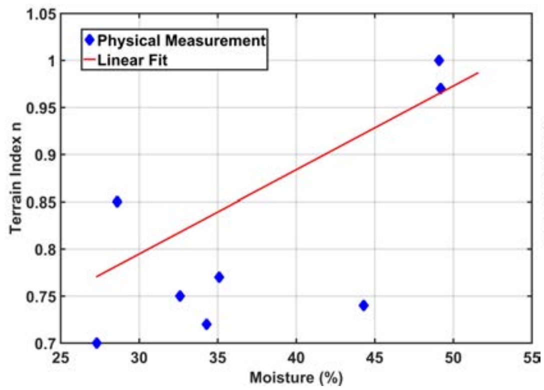

(a) Terrain index, n

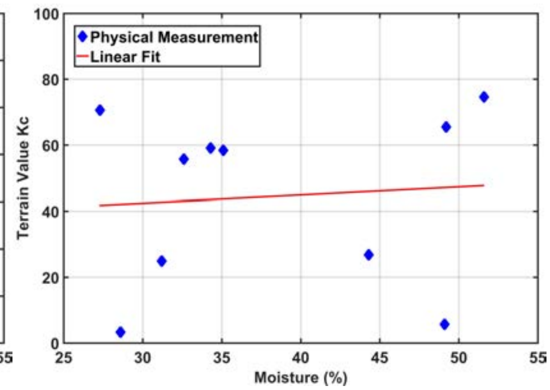

(b) Terrain value, k_c

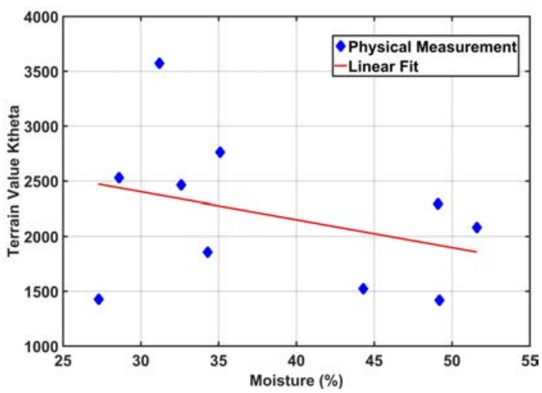

(c) Terrain value, k_θ

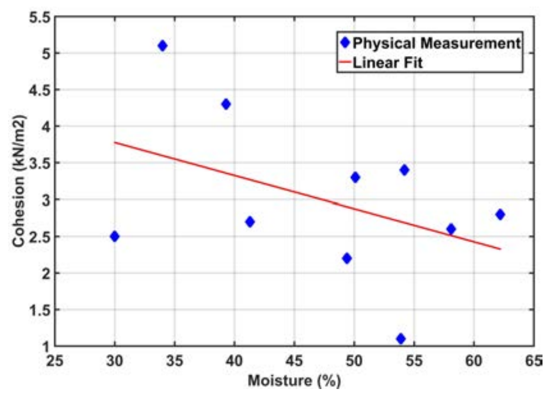

(d) Cohesion, c

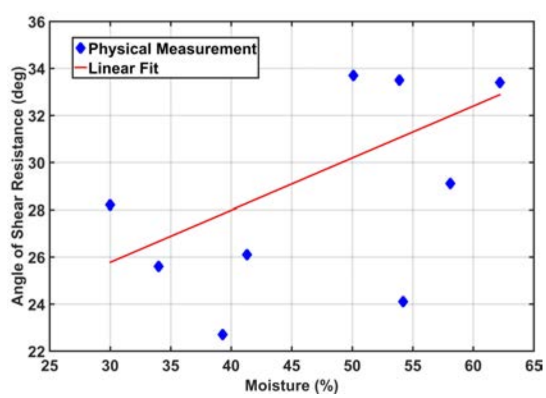

(e) Angle of shearing, ϕ

Figure 5.2: Pressure-sinkage and shear-strength terrain values of sandy loam as a function of moisture content

In order to interpolate between different moisture content, a linear fit between each terrain value and moisture content was chosen based on the best linear fitting criteria. It was observed that the index n increases as the moisture content increases and ranges between 0.7 and 1 for moisture content between 25 and 50 %. Additionally, the terrain value, k_c, was highly varying with respect to the moisture content, for a moisture content between 25 and 50 %, k_c, varies between 3 and 80 kN/m^{n+1}. On the other side, k_θ was noticed to decrease as moisture content increase and it ranged between 1418 and 3570 kN/m^{n+2}. The terrain values, n, k_c, and k_θ are used in Bekker's relationship shown in equation 4.1 to predict the pressure-sinkage characteristics.

The cohesion of the terrain reduced with the increase of moisture content and it ranged between 1 and 5 kPa. While the angle of shear resistance increase as the moisture content increase and ranged between 22°and 34°. It should be noted that the cohesion and angle of shear resistance are used in the Mohr-Coulomb failure criterion in equation 4.3 to predict the shear-strength characteristics of the terrain. The terrain values at desired moisture content were then calculated and recorded in table 5.3.

Table 5.3: Computed sandy loam pressure-sinkage and shear-strength terrain values at various moisture content

n	k_c kN/m^{n+1}	k_θ kN/m^{n+2}	Cohesion, c kPa	Angle of shear resistance, ϕ,deg	Moisture content,%
0.62	37.53	2908.4	4.67	21.36	10
0.75	41.2	2529.2	4	24.67	25
0.84	43.64	2276.4	3.55	26.88	35
0.98	47.31	1897.2	2.88	30.19	50
1.08	50.25	1593.9	2.34	32.84	62

The terrain values computed in table 5.3 were then used to calibrate SPH sandy loam terrains with different moisture content. The calibration was done in the same methodology mentioned in section 4.1 using pressure-sinkage and shear-strength tests and both tests were repeated until a good agreement is obtained with the computed terrain values.

5.2.2 Sandy loam with 25-percent moisture

Figure 5.3a shows the pressure-sinkage relationship for sandy loam with 25% moisture content for both simulations and computed terrain values. At a 200 kPa pressure the sandy loam sinks around 27 mm while the measured one is computed to be 29 mm. Thus the values are close and the sinkage behavior is considered to be captured correctly. Figure 5.3b shows the shear-strength relationship for sandy loam with 25% moisture content. The angle of shear resistance predicted from simulation is 23.7°, while that measured is 24.7°, thus the predicted and measured shear-strength versus pressure are considered in good agreement.

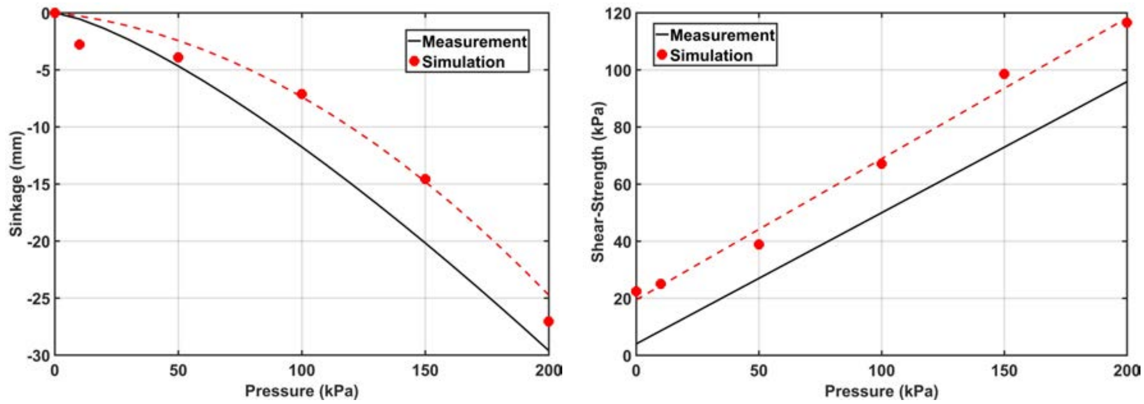

(a) Pressure-sinkage (b) Shear-strength

Figure 5.3: Pressure-sinkage and shear-strength relationship for sandy loam with 25% moisture content

5.2.3 Sandy loam with 50-percent moisture

Figure 5.4a shows the pressure-sinkage relationship for sandy loam with 50% moisture content for both simulations and computed terrain values.

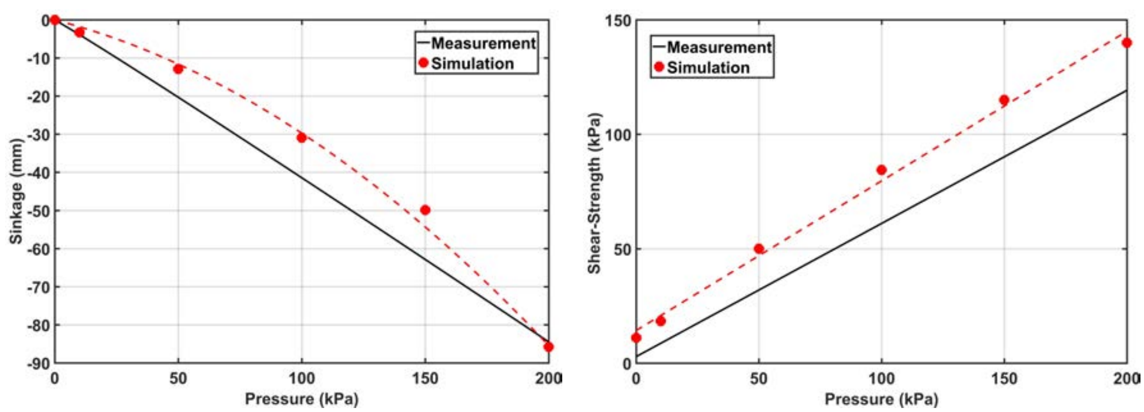

(a) Pressure-sinkage (b) Shear-strength

Figure 5.4: Pressure-sinkage and shear-strength relationship for sandy loam with 50% moisture content

At a 200 kPa pressure the sandy loam the plate sinkage is about 85.8 mm, while the measured sinkage is computed to be 84.5 mm. Thus the simulated and computed pressure-sinkage are considered to be in good agreement.Figure 5.3b shows the shear-strength relationship for sandy loam with 50% moisture content. The predicted angle of shear resistance is 33.2°, while that measured angle is 30.2°, thus the shear test results are also considered to be in good agreement with measurement.

5.2.4 Sandy loam with 62-percent moisture

Figure 5.5a shows the pressure-sinkage relationship for sandy loam with 62% moisture content for both simulations and computed terrain values. At a 200 kPa pressure the sandy loam sinks around 124.64 mm while the measured one is computed to be 122.5 mm, these values are very close and the sinkage behavior is considered to be captured correctly.

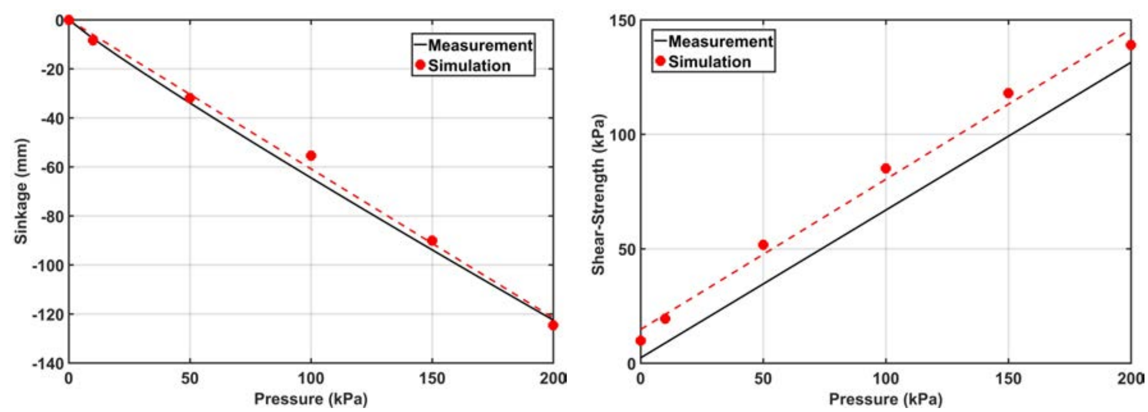

(a) Pressure-sinkage

(b) Shear-strength

Figure 5.5: Pressure-sinkage and shear-strength relationship for sandy loam with 62% moisture content

Figure 5.5b shows the shear-strength relationship for sandy loam with 62% moisture content. The angle of shear resistance predicted from the simulation is noted to be 33.26°, while that computed from terrain values is 32.84°, thus the shear resistance behavior is also considered to be in agreement.

5.3 Terrain Moisturizing Technique

This technique is applied to moisture the dry sand. The technique adopts the theory of pressurizing the water particles into the sand particles in a terrain box. Additionally, the calibration techniques used to calibrate terrains including the pressure-sinkage and shear-strength tests are presented. The type of sand used in this moisturizing technique is considered to be dry sand and is modeled and calibrated previously in chapter 4.

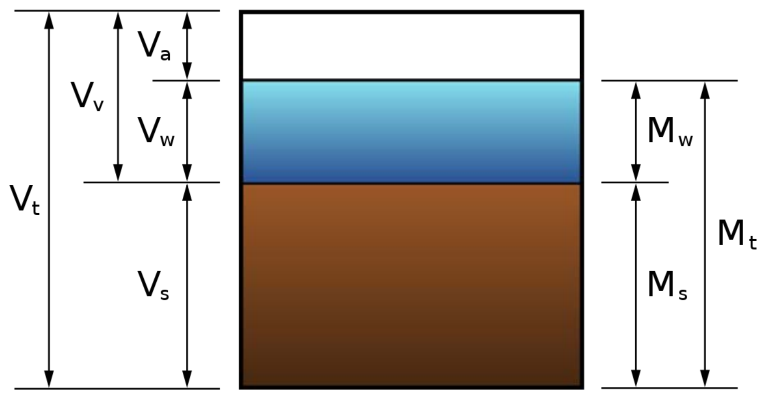

Figure 5.6: Terrain composition by volume and phase of sand, water and total [135]

The depth of sand and water are defined by a ratio of terrain volume and the volumetric water content percentage, w is computed as shown in equation 5.18 and figure 5.6 [135].

$$w = \frac{V_w}{V_{wet}} * 100 = \frac{V_w}{V_s + V_w} * 100 \tag{5.18}$$

Where, V_w, is the volume of water and V_{wet} is the volume of the sand and water added. For the purpose of this research, the water content percentage will be used and referred to as the moisture content and the sand-water model will be referred to as moist sand. Another way to define the water content also using figure 5.6 is by using the gravimetric water content percentage, u described in equation 5.19.

$$u = \frac{m_w}{m} * 100 \tag{5.19}$$

Where m_w is the mass of the water and m is the mass of the sample that is the mass of the dry sand and water combined.

5.3.1 Pressure-sinkage test

As previously mentioned the terrain moisturizing technique is examined using the pressure-sinkage test. The sand is modeled by several layers of an individual type of particles created in the bottom of a terrain box, and the water is modeled by several layers of an individual type of particles created on top of the sand. The effect of pressure and displacement on the moist sand is computed by permitting the pressure of the water to contribute to the pressure of the sand. Figure 5.7

shows the pressure-sinkage procedure for moist sand with 30% moisture content. The pressure-sinkage test is performed by applying a known pressure to a circular plate with a 150 mm radius placed on top of a box ($600 \times 800 \times 600$ mm) filled with the SPH terrain particles [1]. The SPH particles are subjected to a range of pressure between 0 kPa to 200 kPa, and the sinkage of the plate is measured. The relationship between the pressure applied to the circular plate and the circular plate sinkage is computed.

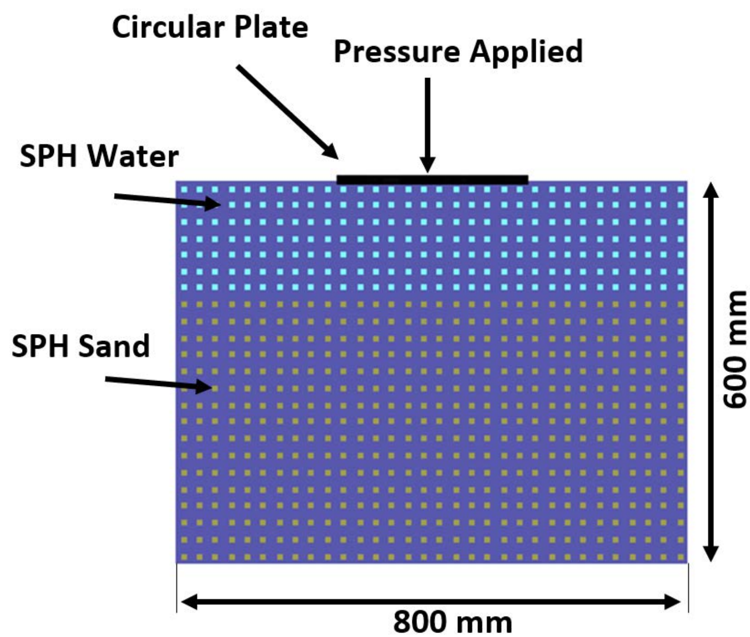

Figure 5.7: Pressure sinkage test condition for 30% moist sand

It is noted that in the case of moist sand, the water particles are pressurized into the sand particles and allowed to settle. This step is performed before the pressure-sinkage simulation procedure starts.

The pressure-sinkage simulation results are fitted in equation 5.20 known as Bekker's equation [1]. Where p is the pressure in kPa, b is the radius of the circular plate in mm, z is the sinkage of the plate in mm, and n, k_c, and k_θ are terrain values.

$$p = (\frac{k_c}{b} + k_\theta)z^n \tag{5.20}$$

5.3.2 Direct shear-strength test

The shear-strength test presented in figure 5.8 is performed by constructing a rectangular domain of $400 \times 200 \times 240$ mm size filled with SPH terrain materials [1]. Similar to the pressure-sinkage the terrain consists of water layered on top of the sand in the terrain box and pressurized into the sand. The shear box is composed of three parts the top plate which pressure is applied on, the upper box which is the sliding box and the bottom box which is constraint from moving in all directions.

A pressure ranging between 0 kPa and 200 kPa is applied to the top plate of the shear box, then a small ramp displacement is applied to the upper box and the top plate at a rate of 10 mm/s. The shear force is computed until the upper sliding box displacement reaches 100 mm. The results are fitted to Mohr-Coulomb failure criteria shown in equation 5.21 [1]. Where c and θ are previously defined terrain values in section 5.1.3.

$$\tau_{max} = c + p \tan \theta \tag{5.21}$$

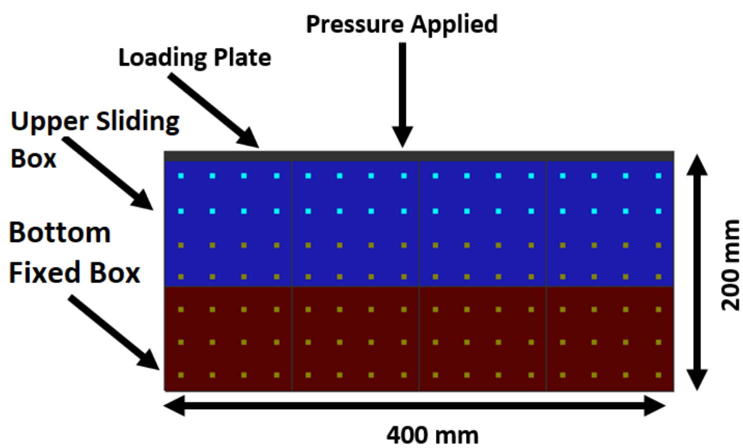

Figure 5.8: Shear-strength test condition for sand with 30% moisture

5.4 Laboratory Testing

The test sand used in the experiment is classified as poorly-graded and non-plastic sand in accordance to the Unified Soil Classification System (USCS) [136]. The maximum dry density, $\rho_{d,max}$ and optimum moisture content of the terrain, w_{opt} were measured at 1850 kg/m^3 and 10% respectively according to Standard Proctor test [137]. The ASTM standard [137] was used to determine the particle size distribution for the sand, furthermore the terrain contained approximately 5% fines passing through 0.075 mm sieve.

The shear-strength testing was carried out in the Minto Centre for Advanced Studies in Engineering at Carleton University, Ottawa, Canada in accordance with ASTM D3080/D3080M-11. Figure 5.9b shows the equipment used to perform the shear test for moist sand at different moisture content, the equipment consists of two boxes and a pressure plate in addition to two sensors to measure the lateral and vertical displacement of the terrain.

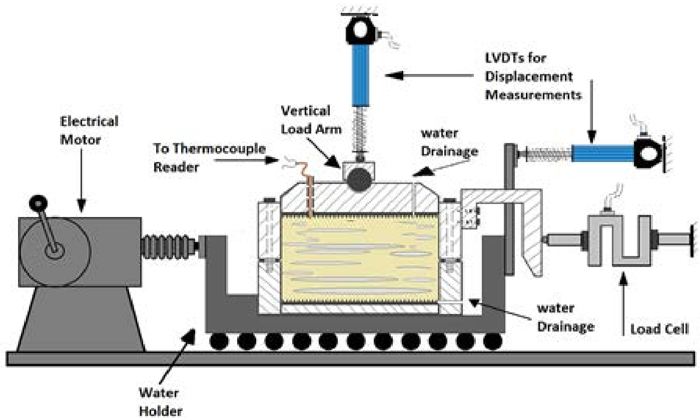

(a) Schematic of the direct shear test

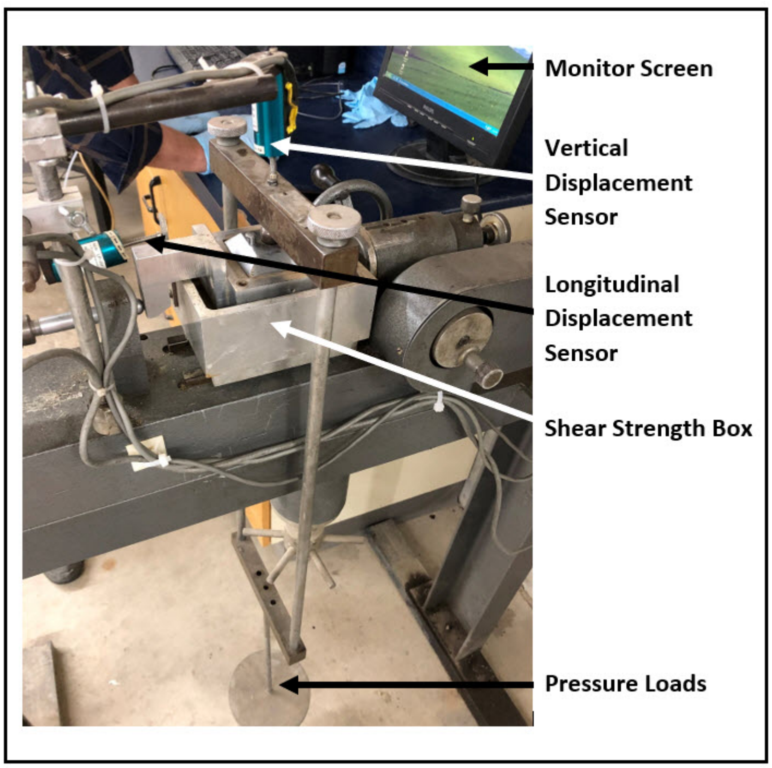

(b) Direct shear test equipment

Figure 5.9: Shear-strength test equipment used during testing (courtesy of Carleton University, Ottawa, Canada) [4]

The direct shear-strength test apparatus consists of an electrical motor that produces a constant displacement rate to the lower part of the shear box as shown in figure 10.3b. A digital load cell is attached to the upper part of the shear-strength box to restrain its movement parallel to the shear plane.

The apparatus is featured with a gearbox that controls the motion of the electrical motor and enables adjustment of the shear velocity. The horizontal and vertical displacements were measured through a Linear Variable Differential Transducers (LVDT). The LVDT was connected to a digital logging station using LabView software. The apparatus frame facilitates applying normal stress to the top of the test specimen by incorporating a steel bearing arm. For terrain shear testing, a regular coupling shear box was used. This shear box had inner plan-view dimensions of 60 mm by 60 mm and depth of 40 mm .

Each test is repeated 3 times at different applied pressure to obtain one angle of shear resistance and one terrain cohesion at a specific moisture content, thus to obtain terrain characteristics at six different moisture contents at least 18 samples were required.

Table 5.4: Sand sampling and properties specification

	Dry density (kg/m^3)	Moisture content (%)	Bulk density (kg/m^3)	Mass (g)
1	1300	0	1300	196.56
2	1300	5	1365	206.39
3	1300	15	1430	216.216
4	1300	25	1625	245.7
5	1300	35	1755	265.36
6	1300	50	1950	294.84

Table 5.4 shows the dry and bulk density for each sample in addition to the mass and the volume of the shear box. The test was repeated for 6 different samples with different moisture contents and the bulk density of each condition was calculated using equation 5.22 and controlled throughout the test.

$$\rho = \rho_d \left(1 + \frac{w}{100}\right) \tag{5.22}$$

Where ρ is the bulk density, ρ_d is the dry density and w is the water content percentage. It should be noted that the sample mass calculated in table 5.4 is the mass of the water and sand together, thus using equation 5.19 the mass of each of the water and sand can be calculated. Table 5.5 summarizes the mass of the water and sand in addition to the water content percentages.

To prepare the test samples, the respected mass of the dry sand and water were weighed and then mixed thoroughly to achieve a homogenous mixture. The mixture was then compacted into the shear box to reach the corresponding bulk

Table 5.5: Water content and mass distribution

Moisture content (%)	Sample mass (g)	Water mass (g)	Sand mass (g)
0	196.56	0	196.56
5	206.39	10.32	196.07
10	216.22	21.62	194.59
25	245.7	61.42	184.27
35	265.35	92.87	172.48
50	294.84	147.42	147.42

densities. The shear box was then mounted on the direct shear test apparatus and the desired normal stress was respectively applied on top of the sample using a predefined dead load. The shear tests were conducted under a controlled strain rate where the loading was applied at a constant linear velocity of 0.01 mm/sec. For each water content, shear-strength properties including the cohesion and angle of shear resistance were determined under several normal loading ranging between 16 and 100 kPa as shown in table 5.6.

Table 5.6: Normal stress and load during the shear strength test

Normal stress (kPa)	Normal mass (kg)	Steel holder mass (kg)	Normal load needed (kN)
16	5.87	5.7	0.073
50	018.35	5.8	12.55
100	36.7	5.8	30.91

Figure 5.10a shows the variation of the shear stress as a function of the shear strain at three different pressure for a sand with 50% moisture content. It can be seen that the shear stress increases as the shear strain increases for a shear strain ranging between 0 and 2%. Afterwards the shear stress reaches steady state as the shear strain keep on increases until 10%.

It is also noticed that the maximum shear strength is recorded at the highest pressure, for a 50% moist sand at an applied pressure of 100 kPa the maximum shear strength is recorded to be around 70 kPa.

On the other side dry sand, for example, experienced strain-softening after showing well-defined peak strength especially under the high normal stress of 100 kPa. This could be attributed to the initial volume contraction which densified

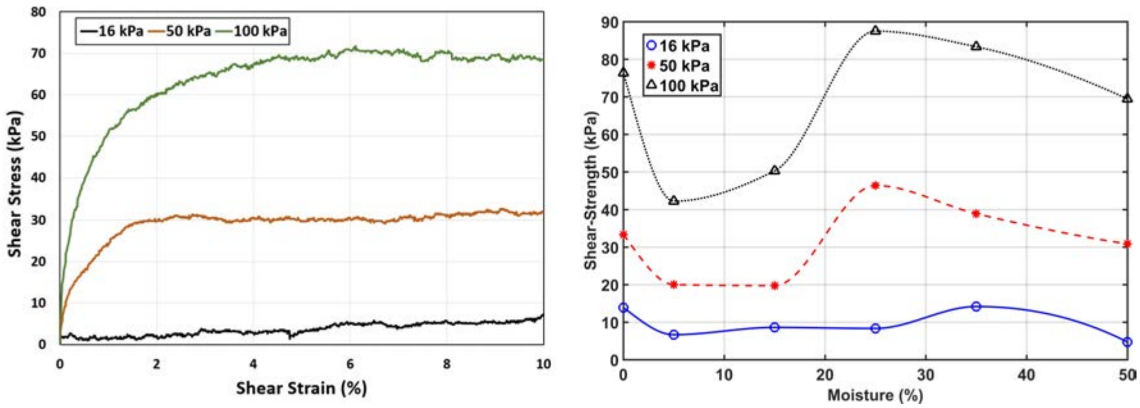

(a) Sample of the shear stress measurements

(b) Shear-strength as a function of moisture content

Figure 5.10: Sample of the shear stress experimental results [4]

the terrain and resulted in higher strength, however, and as the loading progresses, the terrain sample dilated and peak strength slightly decreased.

Figure 5.10b shows the variation of the shear-strength as a function of the moisture content for the different applied loads. The shear-strength is calculated from the shear-strength versus shear-strain curve at a steady state. The relationship between the shear-strength and moisture content is not linear and reaches a peak value of around 25% moisture content. Additionally, the shear-strength increases as the applied pressure increases. For a low applied pressure such as 16 kPa, the shear-strength is less affected by the moisture inc comparison to the 100 kPa pressure which is highly affected by the change in terrain moisture.

5.5 Results and Discussions

In this section, the results of the pressure-sinkage and shear-strength tests for the terrain moisturizing technique are presented. Furthermore, the effect of terrain moisture content on terrain characteristics is investigated.

5.5.1 Validation of terrain moisturizing technique

To validate the results obtained using the novel moisturizing technique the shear-strength results at different moisture content are discussed. It should be noted that the sand tested has similar characteristics to that simulated, however, it has slightly different angle of shear resistance, due to the limitations in the available sand for testing, this sand type was selected. The simulated sand was calibrated based on published terramechanics research [62].

Figure 5.11 shows the shear-strength results of the dry sand for the simulated, measured, and published terramechanics results. The modeled terrain was calibrated based on published terramechanics research due to the limitation of results and the wide change of terrain characteristics from one sand to another. The angle of shear resistance and cohesion are determined using the shear-strength line fitting. The angle of shear resistance is computed using the slope of the line, while the cohesion is computed as the y-intercept which is, in this case, the intersection of the shear-strength line with the shear axis.

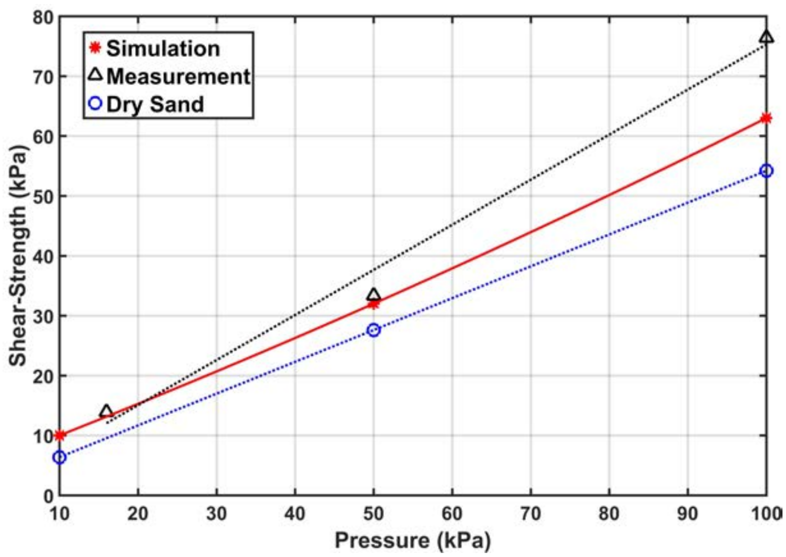

Figure 5.11: Shear-strength as a function of pressure for dry sand

In the case of sand with 0% moisture content, the measured cohesion is about 0.45 kPa while the simulated on is around 1 kPa. The measured angle of shear resistance is recorded to be 36°while the simulated on is 33°. In comparison between the simulated and published terramechanics results the published cohesion is 1.04 kPa and the angle of shear resistance is around 28°.

Similarly, for sand with 50% moisture content both measured and simulated curves exhibit similar trends. The measured cohesion is recorded to be 7.6 kPa while the simulated one is around 4.5 kPa, the measured angle of shear resistance is recorded to be 32°while the simulated on is 25°.

5.5.2 Moist sand with different moisture content

Figure 5.12a shows the variation of the sinkage as a function of the pressure applied to the plate for different moisture contents. At 0% moisture content the sand is completely dry and the box is filled with several layers of sand particles, the maximum sinkage recorded is 157 mm at 200 kPa plate pressure. It can be concluded that as the moisture content increases the sinkage of the plate increases as well causing the terrain to be diluted. However, the increase in sinkage is not linearly depended on the increase in moisture content.

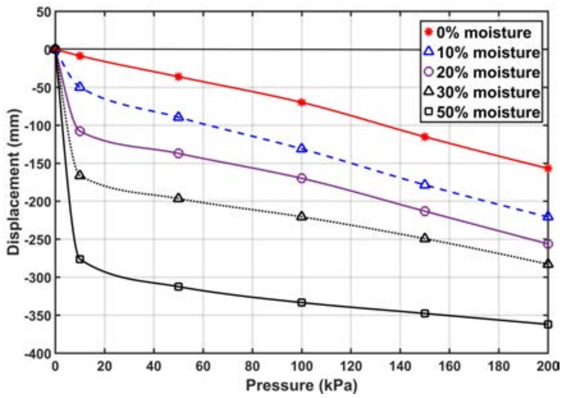

(a) Pressure-sinkage

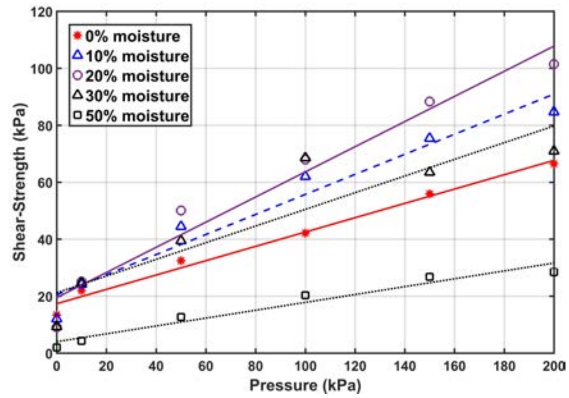

(b) Shear-strength

Figure 5.12: Pressure-sinkage and shear-strength relationship for moist sand at different moisture content

Figure 5.12b shows the variation of the shear-strength as a function of pressure for different moisture content. The terrain cohesion known as the component of shear strength of terrain that is independent of inter-particle friction is regarded to as the y-intersect in the shear-pressure line, and the slope of the shear-pressure line is known to be the internal shear friction of the terrain. It is observed that as the moisture content increases the cohesion of the terrain reduces, and so does the internal shear friction. This indicates that the terrain with 100% moisture content had the lowest cohesion and internal friction angle and the terrain with 0% moisture content has the highest cohesion and friction angle. In a similar methodology different moist sand are modeled depending on the desired moisture content. These results are in good agreement with the results obtained from shear-strength physical testing.

5.5.3 Effect of moisture content on sinkage characteristics

Figure 5.13 shows the variation of the terrain sinkage at 100 and 200 kPa pressure as a function of terrain moisture, these results are in good agreement with previously measured data [138]. It is observed that as the moisture content increases the sinkage increases at a given pressure. It can also be seen that the rate of increases of sinkage as a function of that of moisture is almost linear at a given pressure. It should be noted that the sand at 0% moisture content in the dry sand that has been previously modeled and calibrated and has a plate sinkage of 157 mm at 200 kPa pressure.

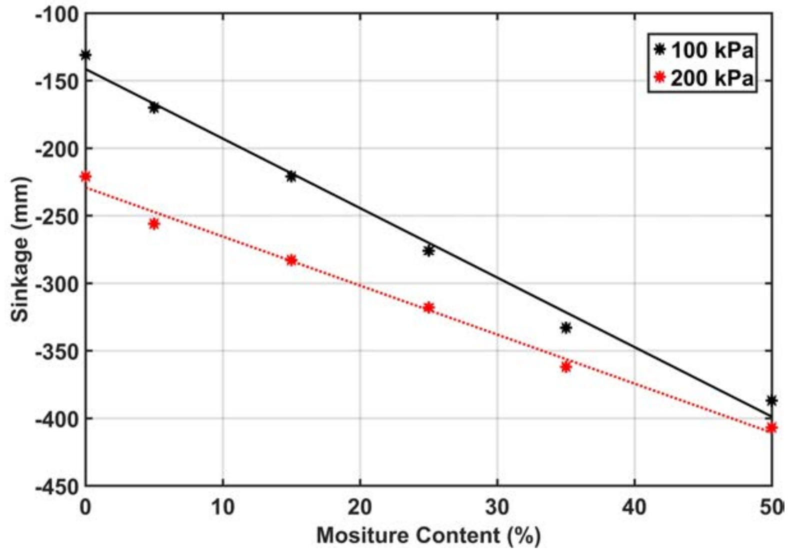

Figure 5.13: Sample of simulation results for pressure-sinkage characteristics at different moisture content

Furthermore, the rate of change of sinkage as a function of moisture content is dependent on the applied pressure. For instance, the lower the applied pressure is the higher the effect of moisture content on sinkage. This observation is derived from the slope of sinkage versus moisture content line at different pressures.

Analysis of the simulation animation shows that the sand and water particles are being compressed due to pressure exerted on the plate, also the water particles are exerting pressure on the sand as well. Additionally, water particles are being trapped under the plate and thus mixed with the sand particles, the water particles on top of the box are forced to expand outside the box due to the increase of pressure around the plate. The output of this test allows computing the pressure-sinkage characteristics of the moist sand at different moisture content and different pressures.

5.5.4 Effect of moisture content on shearing characteristics

Figure 5.14a shows the angle of shear resistance as a function of moisture content for both measurement and simulated.

It is observed that although the measurement and simulation results are not equal they exhibit a similar trend. As the moisture content increases the angle of shear resistance increases until a peak is reached at around 25% moisture. After the peak, the angle of shear resistance reduces as the moisture content continues to increase. Both the measurement and simulated results show a similar trend in variation with respect to moisture content and show a peak at the same moisture content. Further, the angle of shear resistance varies between 42 °and 23 °for

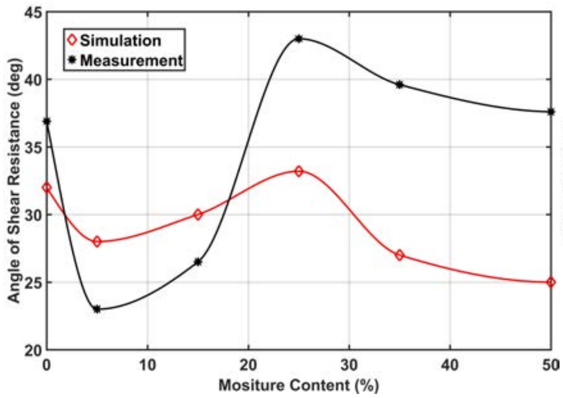

(a) Angle of shear resistance

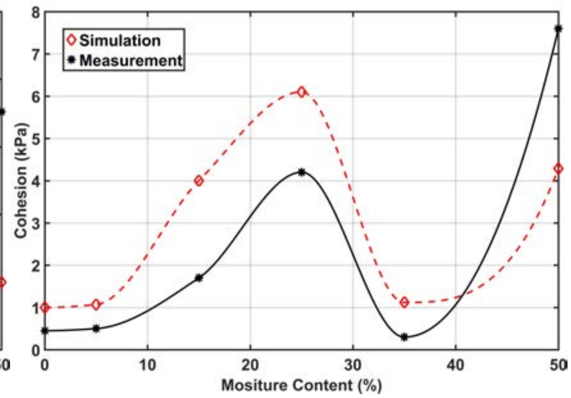

(b) Cohesion

Figure 5.14: Shearing characteristics for different moisture content for sand at different moisture content

measurements, while for angle varies between 34 °and 25 °for simulations. It is noticed however that the rate at which the angle of shear resistance is varying with respect to the moisture content is almost the same for both measurement and simulation.

Figure 5.14b shows the variation of the terrain cohesion as a function of moisture content for both measurements and simulations. It is noticed that as the moisture content increases the terrain cohesion increases until a peak is reached at a moisture content of 25%. Afterward, as the moisture content increases the cohesion exhibits a parabolic relationship. The cohesion ranges between 0.45 kPa and 7.6 kPa for a moisture content ranging between 0 and 50 %.

The sand behavior is attributed to the role of water in sand particle arrangement and the terrain fabric. As water content increases from 5% to 25%, water may have acted as a lubricant between the particles leading to denser terrain and more compact fabric. For higher water contents, the water-filled pore voids of the terrain leading to slightly loose fabric.

Analysis of the simulation animation showed that the sand and water particles are first compressed due to a pressure exerted on the loading plate. Then the particles start moving due to the displacement applied on the top and sliding plate, the displacement is applied until 10 seconds. It is shown that the sand and water particles interact together and move together causing a shear between particles.

5.6 Summary

In this chapter, two different terrain moisturizing techniques were presented. The first technique consists of using terramechanics published data to interpolate terrain values of sandy loam at different moisture content, and then modeling and calibrating the terrains using pressure-sinkage and shear-strength tests. The terrains modeled include sandy loam with 10%, 25%, 35%, 50% and 62% moisture content. The second technique consists of layering water on top of previously modeled and calibrated dry sand in chapter 4 and pressurizing the water particles into the sand. This technique was used to model moist sand with moisture content ranging from 10% to 60% with a 10% increment. The results were validated against measurements obtained from physical testing performed in a laboratory.

The effect of moisture content on the terrain characteristics was investigated. It was concluded that both sandy loam and moist sand becomes loose when moisture content increase which allows for more sinkage of the plate in the terrain. Additionally, as the moisture content increases the terrain cohesion reduces for both sandy loam and moist sand. However, the angle of shear resistance exhibits opposite trends. In the case of sandy loam as the moisture content increases the angle of shear resistance increases, while for moist sand as the moisture content increases the angle of shear resistance reduces.

Furthermore, the angle of shear resistance for sand with 5% moisture content was around 23 °and increased as water content increased to 15% and 25%. The maximum angle of shear resistance was measured at around 43 °for the sand sample tested at 25% moisture content. After this moisture level, the angle of shear resistance slightly drops for the sand with 35%and 50% moisture content.

CHAPTER 6

TIRE-TERRAIN INTERACTION

This chapter focuses on the determination of the in-plane and out-of-plane rigid ring tire model parameters using the previously developed FEA the RHD truck tire running over different SPH terrains. The terrains included in this chapter are the flooded surface and snow. The terrain independent in-plane and out-of-plane rigid ring tire model parameters such as rotational stiffness and damping of the sidewall, residual vertical stiffness, and damping, out-of-plane rotational stiffness and damping are determined in chapter 11.

The terrain dependent in-plane rigid ring model parameters include the longitudinal tire and tread stiffness, the vertical stiffness, and the rolling resistance coefficient. The out-of-plane rigid ring model parameters include the lateral stiffness, cornering stiffness, selfaligning moment stiffness, and relaxation length.

6.1 Tire-Flooded Surface Interaction

The in-plane and out-of-plane rigid ring tuck tire model parameters over the flooded surface are discussed in this section. The effect of several operating conditions including the inflation pressure, vertical load and water depth over the tire-flooded surface interaction are investigated. Three different inflation pressures are examined (379, 586 and 758 kPa); three different vertical loadings are discussed as well (13, 27 and 40 kN) and four different water depth are used to model wet surface and 25, 50 and 75% of sidewall height.

6.1.1 Determination of the in-plane rigid ring model parameters

The test procedure and results of the in-plane rigid ring model parameters are described and discussed. The in-plane rigid ring model parameters shown in figure 6.1 are obtained by performing rolling resistance, longitudinal and vertical virtual testing at different conditions.

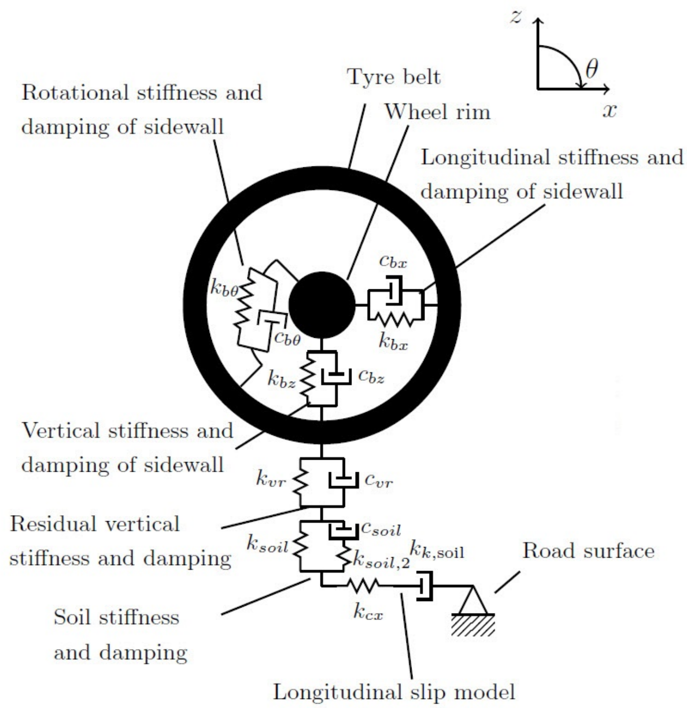

Figure 6.1: Off-road in-plane rigid ring tire model parameters

6.1.1.1 longitudinal tire and tread stiffness

The longitudinal tire stiffness of the truck tire is defined as the tire's ability to recover maximum traction after experiencing 100% slip conditions through the application of a rapid angular acceleration to the tire's center. The longitudinal slip is calculated using equation 11.20, where s is the longitudinal slip, v and ω are the longitudinal and rotational velocities at the center of the tire, respectively, and r is the effective rolling radius of the tire.

$$s = \left(1 - \frac{v}{r\omega}\right) * 100 \tag{6.1}$$

The model setup is shown in figure 6.2, the tire is first inflated to the desired inflation pressure; then the desired vertical load is applied to the center of the tire. Rapid angular acceleration ($\dot{\omega}$) is then applied to the tire's center until the desired steady-state speed is reached. Due to the quick angular acceleration, the tire experiences 100% slip conditions at the beginning of the simulation. The longitudinal and angular velocities at the center of the tire, in addition to the longitudinal force at the contact patch, are computed. The simulation results are used to analyze the longitudinal force against the longitudinal slip ratio. From the relationship between the longitudinal force, f_x, and slip, s, the tire longitudinal stiffness, $k_k\big(\frac{\partial F_x}{\partial s}|_{s=0}\big)$. and the peak coefficient of adhesion, μ_p, is determined.

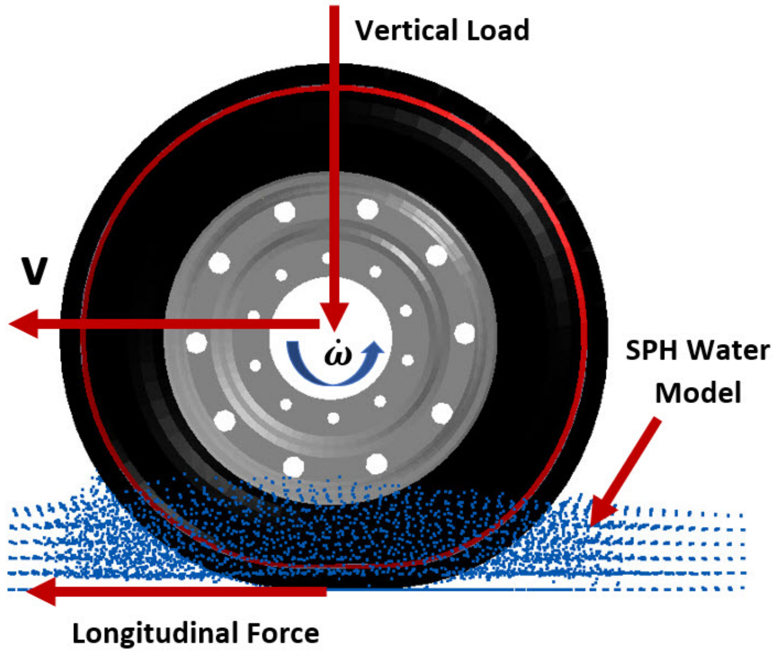

Figure 6.2: Schematic of the longitudinal tire stiffness simulation model

The longitudinal force as a function of the longitudinal slip for several applied vertical loads and inflation pressures are shown in figures 6.3a and 6.3b, respectively.

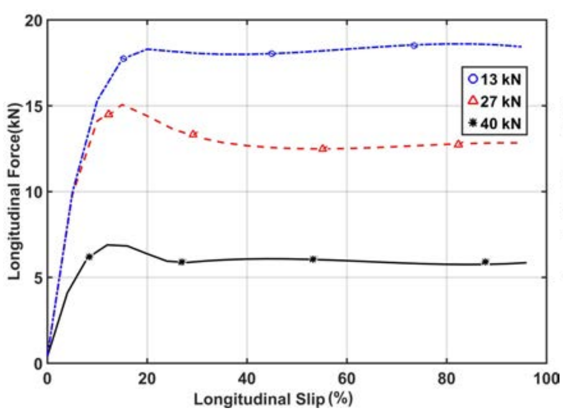

(a) Effect of vertical load at 586 kPa (85 psi) inflation pressure

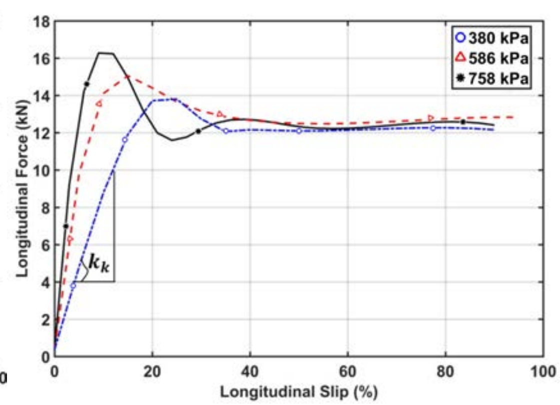

(b) Effect of inflation pressure at 40 kN (9000 lbs) applied vertical load

Figure 6.3: Longitudinal force as a function of longitudinal slip for several applied vertical load and inflation pressure over a wet surface

Figure 6.3a indicates that the longitudinal force reaches a maximum value for a longitudinal slip between 15% and 40% depending on the water depth. The longitudinal force increases as the applied vertical load increases and the longitudinal force reach its peak earlier for a higher vertical load.

On the other side, figure 6.3b shows that the peak longitudinal force is slightly affected by the inflation pressure, as the inflation pressure increases the peak longitudinal force decreases. This is due to the fact that the higher the inflation pressure, the lower the contact area is. The previously discussed results are for wet asphalt surface and stand true for all flooded surface cases.

Furthermore, the effect of the water depth on the longitudinal force is observed in figure 6.4. The results are restricted to 0-10% longitudinal slip as this is considered the linear part of the curve. The simulations are performed at different water depth as a percentage of the sidewall height. This figure shows that all three curves intersect at 5% longitudinal slip, at 0% slip the 50% sidewall water depth has the highest longitudinal force meaning it has the highest rolling resistance. As the longitudinal slip increases beyond 5% the longitudinal force increases for all water depths. However, at a longitudinal slip greater than 5% the longitudinal force increases as the water depth decrease.

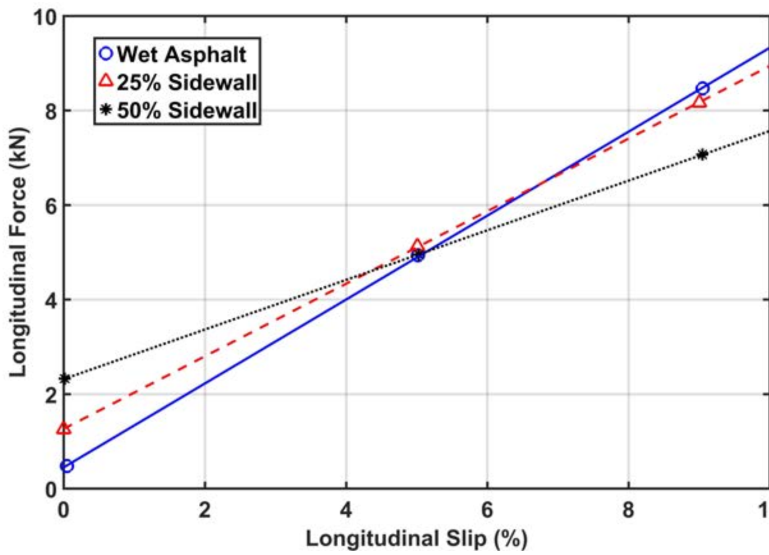

Figure 6.4: Longitudinal force as a function of longitudinal slip for several water depth at 586 kPa (85 psi) and 40 kN (9000 lbs) vertical load

Figure 6.5a shows the variation of the longitudinal stiffness, k_k, as a function of water depth at 586 kPa (85 psi) inflation pressure and 0 kN (9000 lbs) vertical load. The trend shows that an increase in the longitudinal tire stiffness as the water depth increases. This indicates that the tire produces lower forces at higher water depth.

The longitudinal tread stiffness, k_{cx}, is determined by dividing the tire stiffness by half of the contact length, a, of the tire which is 0.0625 m [1]. Figure 6.5b shows the longitudinal tread stiffness as a function of water depth for 586 kPa (85 psi) inflation pressure and different vertical loads. The longitudinal tread stiffness decreases as the water depth increases, this trend is proven for all inflation pressures and applied vertical loads.

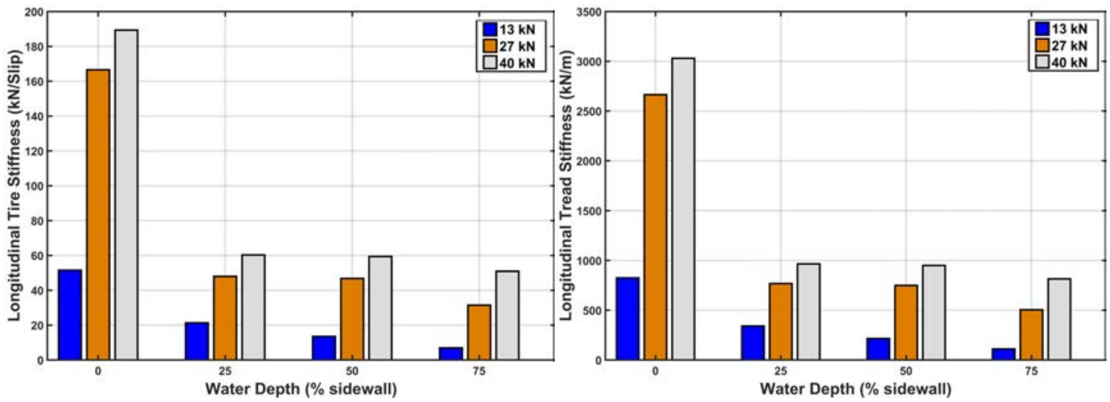

(a) Longitudinal tire stiffness

(b) Longitudinal tread stiffness

Figure 6.5: Longitudinal tire and tread stiffness as a function of water depth at 586 kPa (85 psi) and different vertical loads

6.1.1.2 tire vertical stiffness

The tire vertical stiffness test is implemented to represent the tire model's ability to resist deformation in the vertical directions from a known applied vertical force. A simple static loading test is employed to determine the vertical stiffness. The test setup is shown in figure 6.6, the tire model is inflated at the specified inflation pressure, and a slow ramp vertical load is gradually applied to the center of the tire. The deflection of the center of the tire tire is recorded and a plot of vertical contact force as a function of the tire deflection is produced, the slope of the trends is regarded as the vertical stiffness, k_z. The simulation is repeated at different inflation pressures and water depth.

Figure 6.7b shows the variation of the vertical stiffness as a function of the water depth for different inflation pressures. It is shown that the lines are parallel to the x-axis and thus the variation of the vertical stiffness is insignificantly affected by the water depth. This proves that the tire vertical stiffness is an internal characteristic and is almost insensitive to the water depth. Figure 6.7a shows the variation of the vertical load as a function of the tire deflection for several inflation pressures. The results show that for a specific vertical load the deflection increases as the inflation pressure decreases.

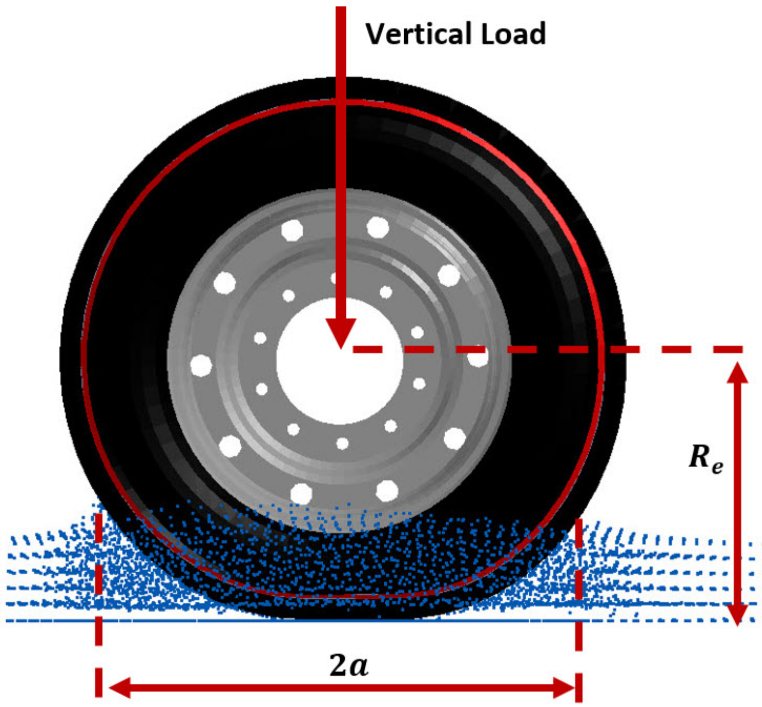

Figure 6.6: Schematic of the vertical stiffness simulation model

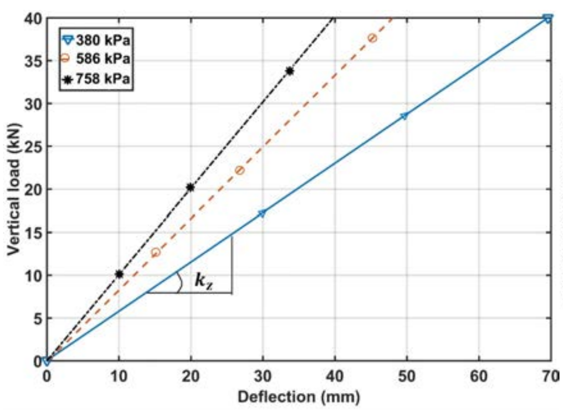

(a) Vertical load as a function of the tire deflection

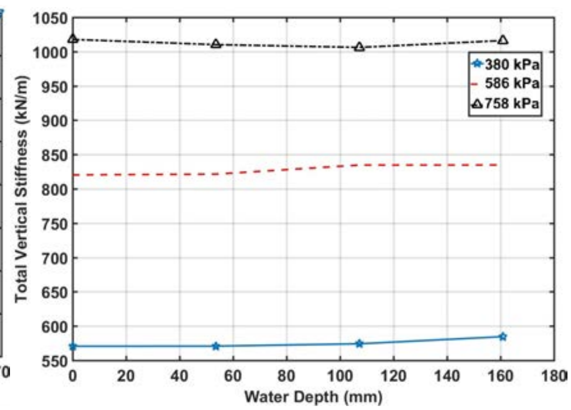

(b) Vertical stiffness as a function of water depth

Figure 6.7: Vertical load and stiffness at various inflation pressures

6.1.1.3 rolling resistance coefficient

Figure 6.8 shows a schematic of the main forces acting on a free rolling tire; the forces include the applied vertical force and the rolling resistance force.

In this simulation, the tire is first inflated to the desired inflation pressure, and

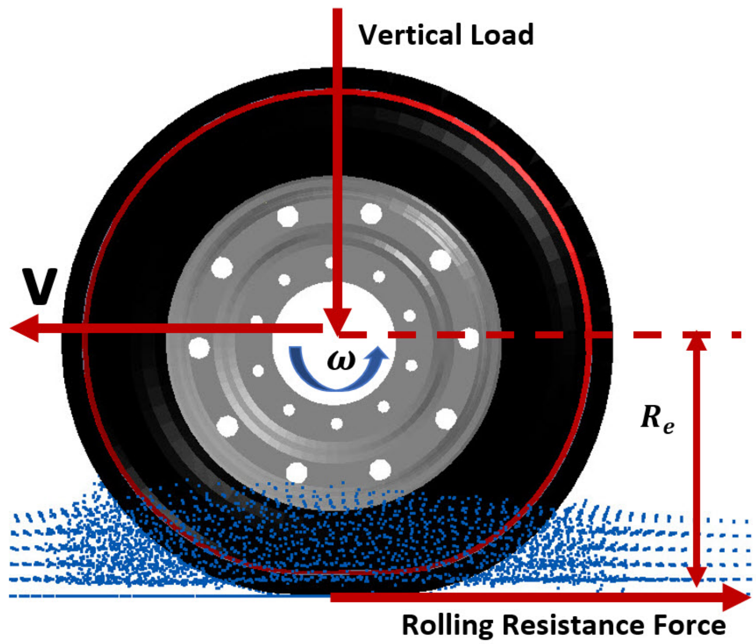

Figure 6.8: Schematic of the main forces acting on a free rolling tire

then the tire is loaded on the flooded surface by applying the desired vertical load. After allowing the tire to settle, a constant linear longitudinal velocity is applied at the center of the tire. The simulation runs until the vertical and longitudinal contact forces reach a steady state. It should be noted that constant longitudinal velocity is applied at the center of the tire as shown in figure 6.8. However, the angular velocity of the free-rolling tire may change depending on the water depth, inflation pressure, and applied vertical load. The change in angular velocity even without applying driving torque is due to the sinkage of the tire in the water while it's towed with constant linear longitudinal velocity. Therefore, the predicted rolling resistance may not be under a pure free rolling condition as it is the case on the hard surface. The variation of the angular velocity at constant linear longitudinal velocity results in longitudinal slip which is found to be between 4-13%.

Simulations were performed to determine the rolling resistance of a tire running over the flooded surface at several inflation pressures and vertical loads. The vehicle fuel efficiency is directly related to the rolling resistance. Figure 6.9a shows the variation of the rolling resistance coefficient as a function of the water depth at 758 kPa (110 psi) inflation pressure and different vertical loads at given speed of 10 km/h. It is concluded that the rolling resistance coefficient decreases as the vertical load increases at a given speed and inflation pressure. In addition, the rolling resistance coefficient increases as the water depth increases. It is noted that the variation of the angular velocity at constant linear longitudinal velocity results in longitudinal slip which indicates that the rolling resistance is not calculated at a freely rolling tire. The method used to predict the rolling resistance of a tire running over a flooded surface is commonly used in physical testing.

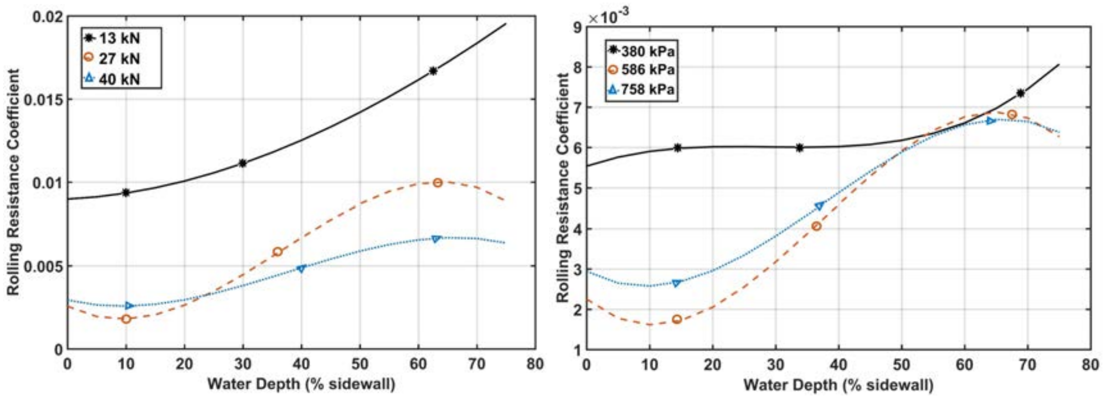

(a) Rolling resistance coefficient at 758 kPa (110 psi) inflation pressure

(b) Rolling resistance coefficient at 40kN vertical load

Figure 6.9: Rolling resistance coefficient as a function of water depth at different operating conditions

To further understand the relationship between the rolling resistance coefficient and the tire operating conditions figure 6.9b is presented. Figure 6.9b shows the variation of the rolling resistance coefficient as a function of the water depth at a given vertical load of 40 kN (9000 lbs) and different inflation pressures at given longitudinal speed of 10 km/h. It is shown from this figure that as the inflation pressure increases the rolling resistance coefficient decreases at given water depth and vertical load. This result is due to the fact that the increase of the inflation pressure decreases the contact area between the tire and the surface leading to lower resistance forces. The same conclusion mentioned in the previous paragraph is also noticed here. The rolling resistance coefficient increases as the water depth increases at a given vertical load and inflation pressure. This relationship is due to the fact that the contact area between the tire and the surface increases as the water depth increases.

The parameters of the in-plane rigid ring tire model of the RHD tire running over flooded surface are provided in appendix A.1.1

6.1.2 Determination of the out-of-plane rigid ring model parameters

The out-of-plane rigid ring model parameters of the tire over flooded surface shown in figure 6.10 are explained and the required test procedure and results are discussed and investigated in this section.

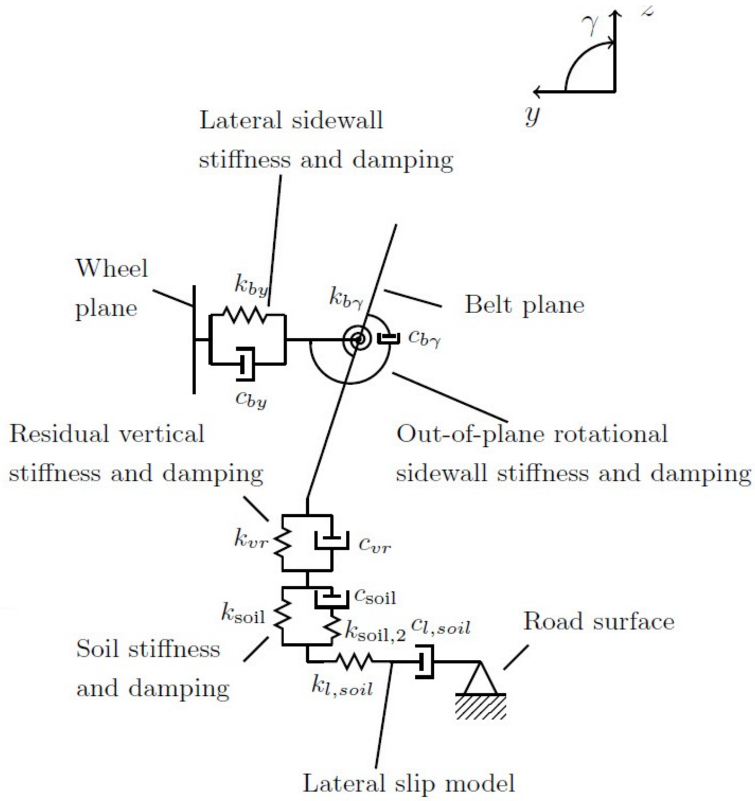

Figure 6.10: Off-road out-of-plane rigid ring tire model parameters

6.1.2.1 lateral tire stiffness and damping

The lateral characteristics of a tire includes the lateral stiffness, k_l, and the lateral damping, c_l. Figure 6.11 shows the free body diagram of the lateral force acting on the tire.

The test starts by inflating the tire to the desired inflation pressure then apply the desired vertical loading. A lateral force of 5 kN is then applied to the center of the tire and then rapidly removed allowing the tire carcass to resonate. The tire center lateral displacement as a function of the tire is computed and the first three peaks are recorded. The lateral stiffness, k_l is described in equation 6.2, which is simply the ratio of the lateral force to the lateral displacement.

$$k_l = \frac{\text{lateral force}}{\text{lateral displacement}} \tag{6.2}$$

Moreover the total lateral stiffness, k_{ltot} is determined using equation 6.3 and it is depending on the lateral stiffness over the flooded surface and that over rigid

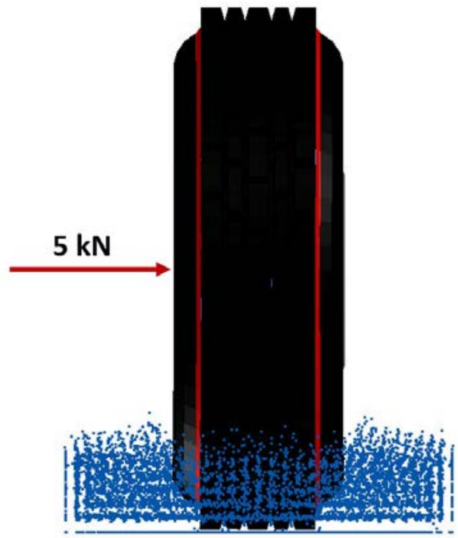

Figure 6.11: Schematic of the lateral stiffness test simulation setup

surface as well.

$$\frac{1}{k_l} = \frac{1}{k_{ltot}} - \frac{1}{k_{l,rigid}} \tag{6.3}$$

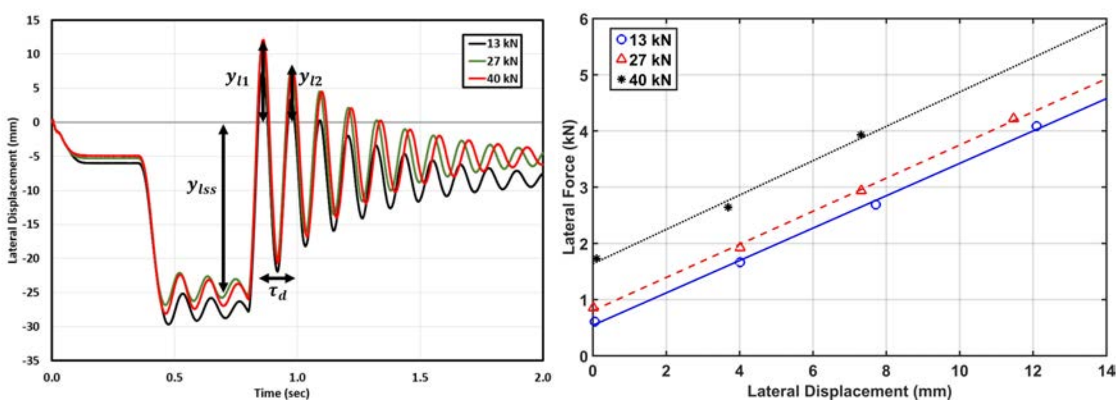

(a) Lateral displacement as a function of time (b) Lateral force as a function of displacement

Figure 6.12: Lateral force and displacement at 586 kPa (85 psi) and different vertical loads

Figure 6.12 shows sample of the lateral test outputs at 586 kPa (85 psi) and different vertical loads for tire running over wet surface. Figure 6.12a shows the variation of the lateral displacement at the center of the tire as a function of tire for a wet surface at 586 kPa (85 psi) and several vertical loads. The first three amplitudes are used to determine the lateral damping constant, c_l. Equations 6.4

to 6.8 are used to determine the critical damping constant, c_c, which is then used determine the lateral damping constant, c_l as shown in equation 6.10.

$$\delta = \ln \frac{y_1}{y_2} \tag{6.4}$$

$$\xi = \frac{\delta}{\sqrt{4\pi^2 + \delta^2}} \tag{6.5}$$

$$\tau_d = t_2 - t_1 \tag{6.6}$$

$$\omega_n = \frac{2\pi}{\tau_d \sqrt{1 - \xi^2}} \tag{6.7}$$

$$\omega_d = \frac{2\pi}{\tau_d} \tag{6.8}$$

$$c_c = 2 m_{wheel} \omega_n \tag{6.9}$$

$$c_l = \xi c_c \tag{6.10}$$

Figure 6.13a shows the variation of the lateral stiffness as a function of applied vertical load on a wet surface for different inflation pressures. The lateral stiffness slightly increases as the vertical load increase and then reduces after that, for the simplification of the results a trend-line is added. Similar nonlinear behavior was noticed on a hard surface for a passenger car tire using experimental testing [139]. The nonlinear behavior may be attributed to the contact area between the tire and the ground at different vertical loads. Additionally, the lateral stiffness increases as the inflation pressure increase at a given vertical load. The same trend was observed using experimental testing for passenger car tire [139]. Generally, for a wet surface, the lateral stiffness ranges between 200 and 305 kN/m.

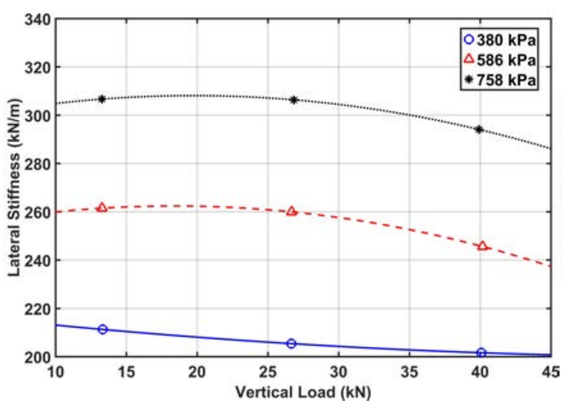

(a) Lateral stiffness as a function of vertical load

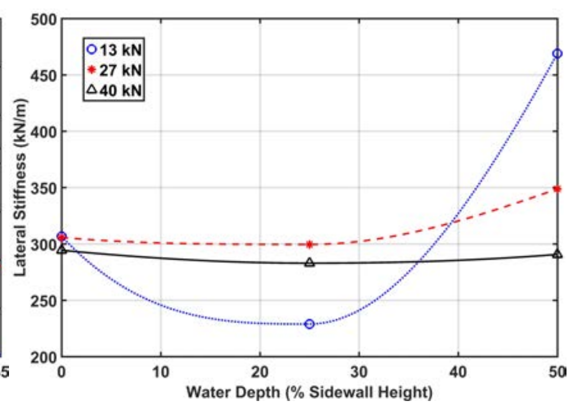

(b) Lateral stiffness as a function of water depth

Figure 6.13: Lateral stiffness as a function of vertical load and water depth at different operating conditions

Figure 6.13b shows the variation of the lateral stiffness as a function of water depth for rated inflation pressure of 379 kPa (55 psi) and different vertical loads.

The lateral stiffness increases as the water depth increase at a given vertical load and inflation pressure. For high vertical loads such as 40 kN, the effect of the water depth becomes negligible. For lower vertical loads such as 13 kN, the effect of water depth becomes crucial, when the water depth increases from 0% to 50% sidewall height the lateral stiffness increase 53%. The increase in lateral stiffness is attributed to the increase in the contact area as the water depth increases.

6.1.2.2 cornering stiffness

The cornering characteristics determined in this section include the cornering stiffness, selfaligning moment and relaxation length. Figure 6.14 shows the free body diagram of the cornering test procedure with the forces and moments acting on the tire at 25% sidewall height water depth.

The cornering stiffness, k_f is defined as the ability of the tire to resist deformation in the shape while a vehicle is undergoing a cornering operation, furthermore cornering stiffness can be determined from the lateral force applied on the contact area, equation 6.11 defines the cornering stiffness relationship to the slip angle and the lateral force. For a small slip angle, the cornering stiffness is considered linear, while for a slip angle greater than 2°the relationship can be highly nonlinear. The cornering stiffness concept is used to approximate the interaction between side and circumferential tire forces as shown in figure 6.15.

$$k_f = \frac{F_l}{\alpha} \tag{6.11}$$

Figure 6.15 indicates that the cornering force appears to be approximately linear under 2°steering and increasing after that. The increase in slip angle increases the cornering force as well. Additionally, as the vertical load increases at given surface condition, inflation pressure and steering angle the cornering force increases as well.

The tire is first inflated to the desired inflation pressure, then the vertical load is applied to the center of the tire. A constant longitudinal speed of 10 km/h is then applied to the center of the tire and the model is kept running for 2 sec. The contact forces are computed on the contact patch between the tire-ground and tire-water. The tire is pre-steered to several slip angles ranging between 0°and 12°, this will allow examining the influence of slip angle on tire operational performance.

Figure 6.16a shows the variation of the cornering stiffness, k_f, as a function of vertical load for several inflation pressures over the wet surface. The cornering stiffness increases as the vertical stiffness increases at given inflation pressure. Moreover, the cornering stiffness also increases as the inflation pressure increases at a given vertical load. The increase in loading increase the tire ability to resist deformation while cornering which results in the increase of cornering stiffness. Additionally, when the inflation pressure increases the contact area of the tire

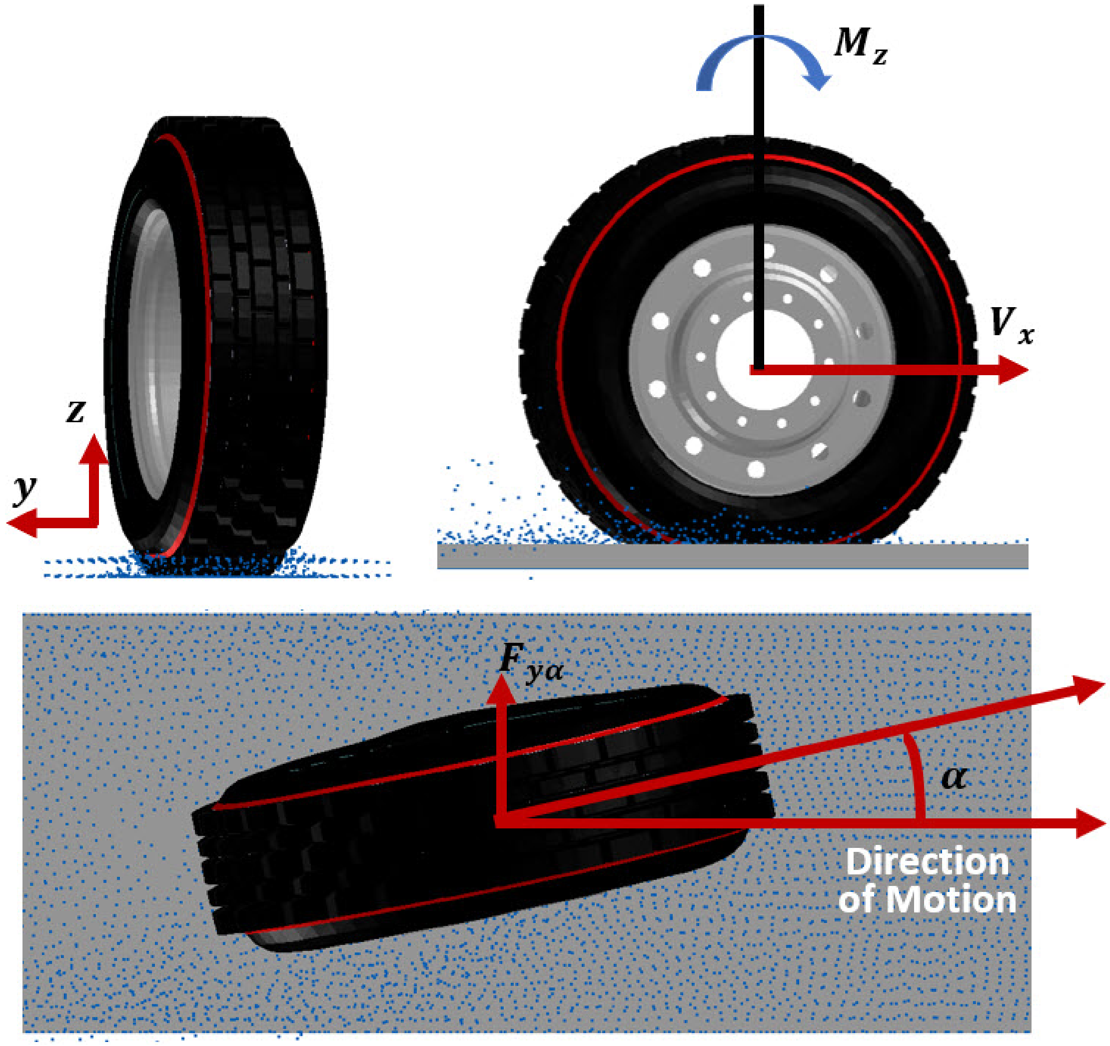

Figure 6.14: Schematic of the cornering test of the truck tire over flooded surface simulation setup

increase as well and thus the cornering force per unit area reduces which leads to an increase in the cornering stiffness. It is noted that the relationship between the rate of change and vertical load change is not linear and is dependent on other operating conditions at the same time, this is unlike the relationship between the lateral stiffness and vertical load rate of change.

Figure 6.16b shows the variation of the cornering stiffness, k_f as a function of the water depth at rated inflation pressure of 586 kPa (85 psi) and different vertical loads. The cornering stiffness reduces as the water depth increases at given vertical load and inflation pressure. The rate of reduction in cornering stiffness with respect to water depth is dependent on the vertical load as well. For low tire loading the cornering stiffness is highly sensitive to the water depth, while for higher loading

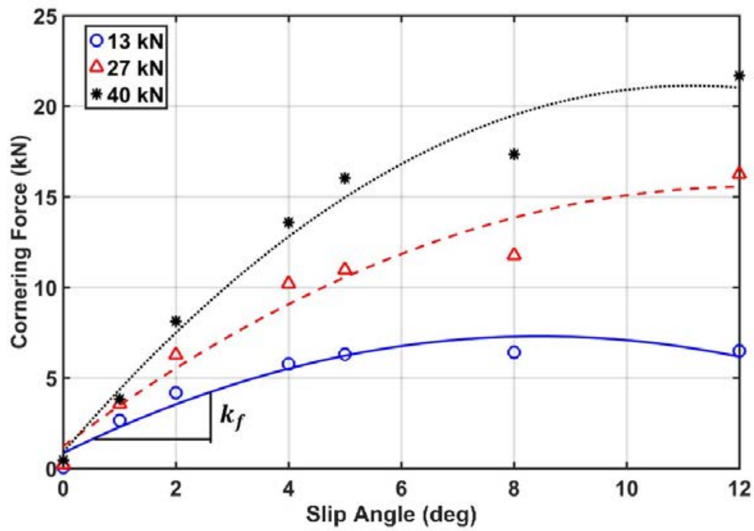

Figure 6.15: Cornering force as a function of slip angle for 586 kPa (85 psi) inflation pressure and different vertical loads on wet surface

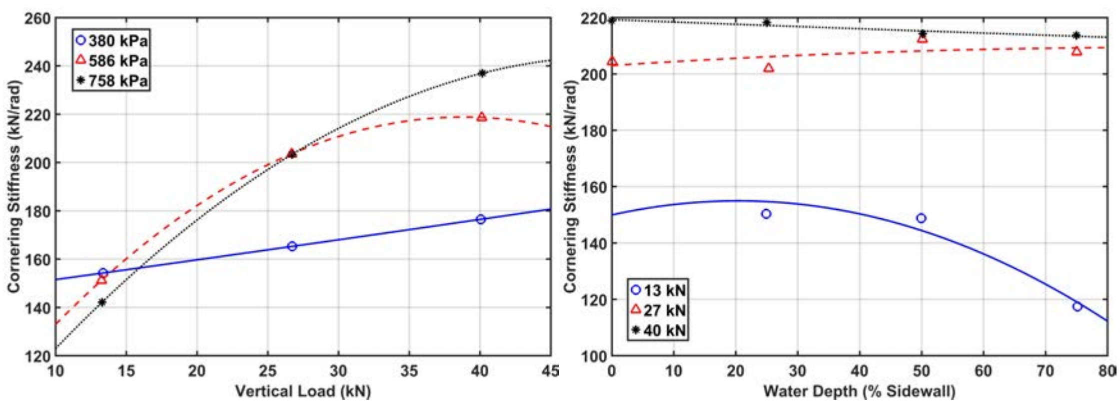

(a) Cornering stiffness as a function of vertical load

(b) Cornering stiffness as a function of water depth

Figure 6.16: Cornering stiffness as a function of vertical load and water depth at different operating conditions

(40 kN) the cornering stiffness is less affected by the water depth. Generally, for a rated inflation pressure of 586 kPa and 13 kN vertical load the cornering stiffness ranges between 155 kN/rad and 120 kN/rad for a water depth ranging between 0 and 70% of sidewall height.

6.1.2.3 Selfaligning moment stiffness

The selfaligning moment, M_z is the torque created by the tire while undergoing a cornering maneuver. The selfaligning moment stiffness, k_m is another parameter used to determine the cornering operational performance of a tire , the relationship between the selfaligning moment, slip angle and the selfaligning moment stiffness is shown in equation 6.12 and equation 6.17.

$$k_m = \frac{\partial M_z}{\partial \alpha}|_{\alpha=0} \tag{6.12}$$

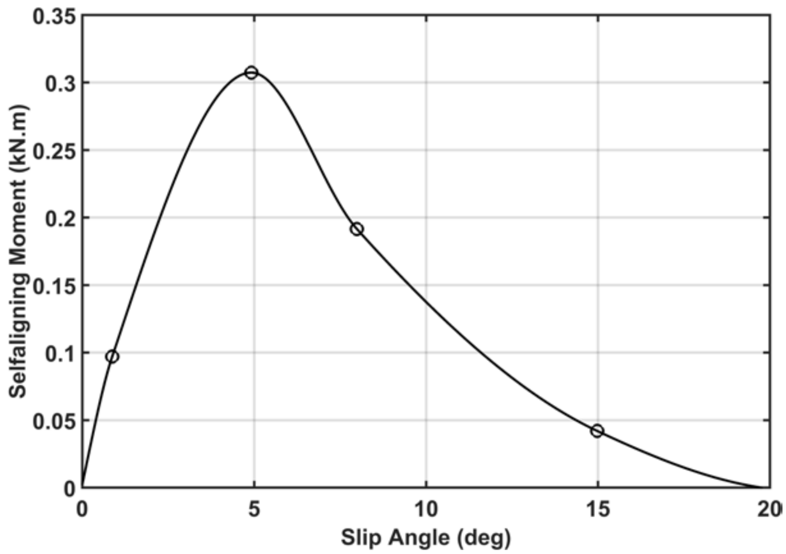

Figure 6.17: Selfaligning moment as a function of slip angle for 586 kPa (85 psi) inflation pressure and 27 kN (6000 lbs) vertical load on wet surface

The selfaligning moment stiffness, k_m, as a function of the water depth for rated inflation pressure of 586 kPa (85 psi) and several vertical loads is presented in figure 6.18. It is observed that the selfaligning moment stiffness increases as the water depth increases for a specific load and inflation pressure.

The rate of increase of the selfaligning moment with respect to the water depth at a specific inflation pressure is minimally dependent on the vertical load. Additionally, the selfaligning moment stiffness increase as the vertical load increase as well at given water depth and inflation pressure. It is noticed that the relationship between the selfaligning moment stiffness and the inflation pressure is not linear at given water depth and vertical load.

6.1.2.4 relaxation length

The relaxation length is defined as the length required by the tire to travel in order to overcome an initial resistive force and achieve steady-state again. The

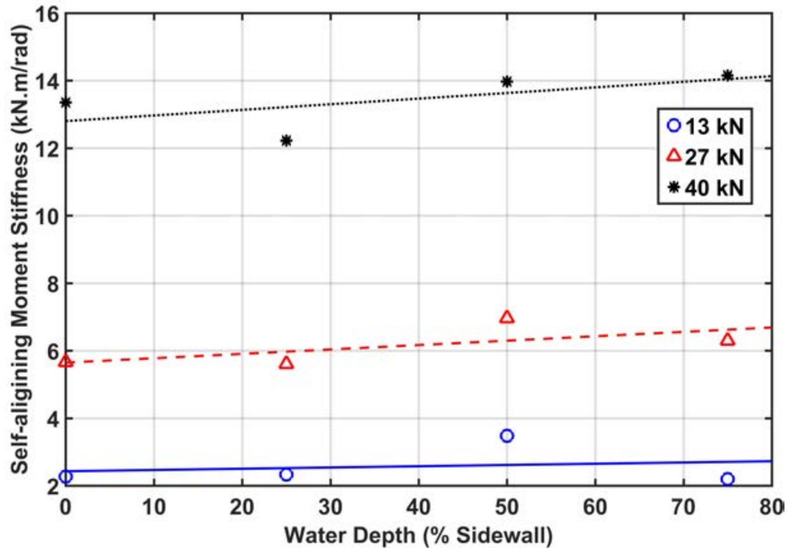

Figure 6.18: Selfaligning moment stiffness versus water depth for an inflation pressure of 586 kPa (85 psi) and different vertical loads

relaxation length σ is known as the ration of the cornering stiffness to the total equivalent lateral stiffness as shown in equation 6.13.

$$\sigma = \frac{k_f}{k_{ltot}} \tag{6.13}$$

The relaxation length, σ, as a function of the water depth for rated inflation pressure of 586 kPa and several vertical loads is presented in figure 6.19. The relaxation length reduces as the water depth increases at given inflation pressure and vertical load. Additionally, the relaxation length increases as the vertical load on the tire increase at given water depth and inflation pressure. When the water depth increases the distance to overcome a constant initial resistive force reduces, this is due to the fact that the increase in water depth increases the contact area between the tire and the terrain and thus reduces the pressure on the tire (reduction in the force per unit area). Moreover, as the inflation pressure increases the relaxation length reduces at given vertical load and water depth. The increase in inflation pressure increases the contact area and thus reduces the force per unit area which leads to a reduction in the distance to overcome a resistive force (relaxation length).

It is noticed that the relaxation length rate of change with respect to water depth is higher at low vertical loads and lower on higher vertical loads. Generally, the relaxation length ranges between 0.2 and 0.9 m for a water depth between 0 and 75% water depth of sidewall height.

The parameters of the out-of-plane rigid ring tire model of the RHD tire running over the flooded surface are provided in appendix A.1.2.

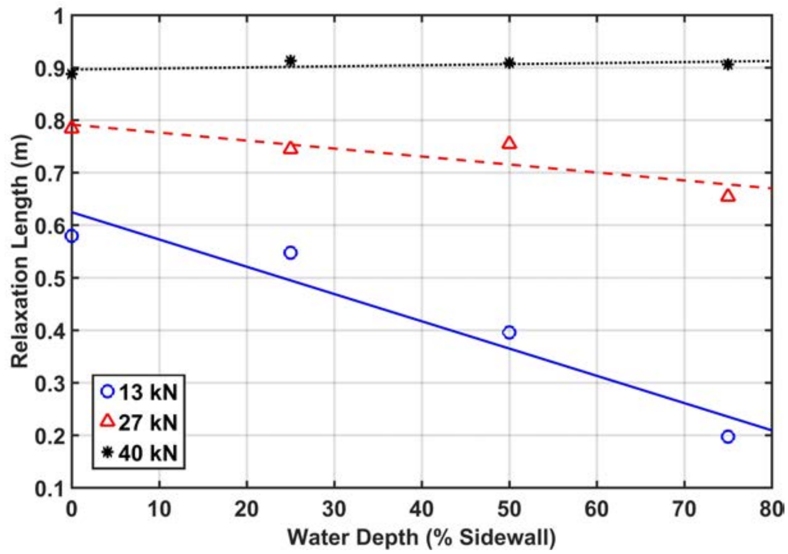

Figure 6.19: Relaxation length versus water depth for an inflation pressure of 586 kPa (85 psi) and different vertical loads

6.1.3 Verification of tire-flooded surface interaction

In order to verify the trends of the obtained results, comparisons were made with some published data. The previous study has demonstrated that the rolling resistance coefficient for a truck tire running over flooded surface ranges between 0.008 and 0.02 depending upon the water depth and tire operational parameters. The rolling resistance coefficient obtained in these simulations falls within the range mentioned in the previously published study.

Figure 6.20 shows the variation of the rolling resistance coefficient as a function of water depth for P225/60R16 [140]. This figure shows that the rolling resistance coefficient increases as the water depth increases, this trend is in agreement with the simulation results shown in figures 6.9a and 6.9b.

The tire traction force, f_x, as a function of the longitudinal slip of a truck tire is shown in figure 6.21 [141]. The traction force is an indication of the force required to accelerate the tire under certain operational conditions. It is noticed that the tractive force increases as the applied load increases for a certain longitudinal slip. Furthermore, the peak of the tractive force is delayed as the applied load increases. The obtained results from this reference verify the trend of the variation of the longitudinal force vs longitudinal slip as shown in figure 6.3a.

The measured vertical stiffness of the RHD tire at an inflation pressure between 379 kPa (55 psi) and 758 kPa (110 psi) are determined to be 575 and 995 kN/m, respectively [56]. This indicates that the tire used in these simulations has the same vertical stiffnesses (slope of the lines in figure 6.7a) as measured in the previous studies.

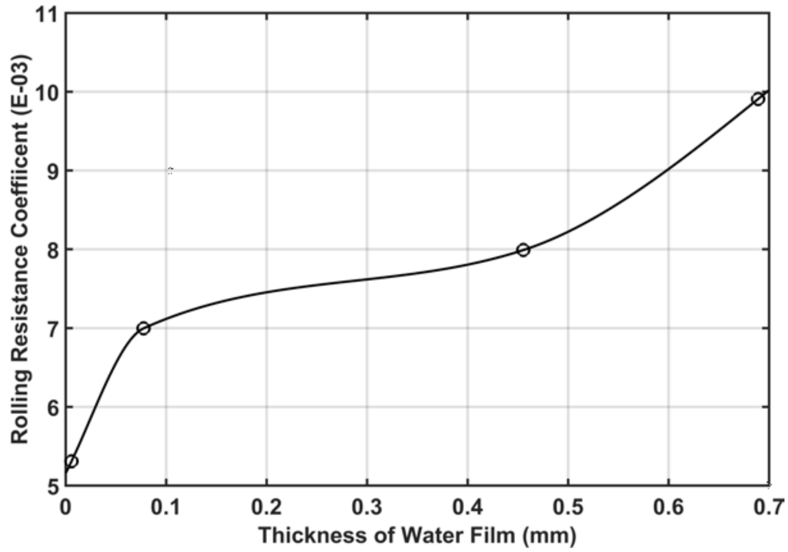

Figure 6.20: Variation of rolling resistance coefficient as a function of water depth for a P225/60R16 tire [140]

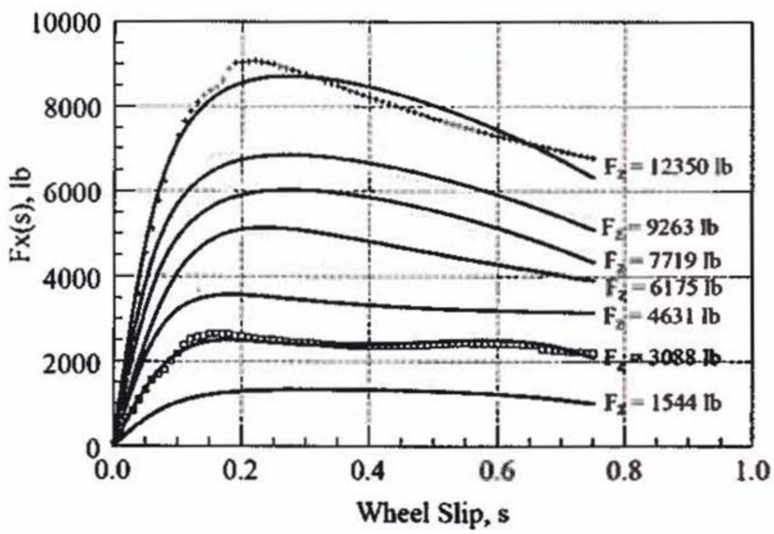

Figure 6.21: Measured traction forces for a 295/75R22.5 truck tire at different normal forces [141]

6.2 Tire-Snow Interaction

The SPH snow model used in this section is previously modeled and validated in section 4.2.4. The same in-plane and out-of-plane rigid ring model parameters computed for the tire-flooded surface interaction are computed in this section as well. The operating conditions examined in this section are the inflation pressure, vertical load, snow depth, and tire speed.

6.2.1 Determination of the in-plane rigid ring model parameters

In this section, the in-plane rigid ring model parameters are computed for tire running over snow with different inflation pressure, vertical load and snow depth.

6.2.1.1 longitudinal tire stiffness

Figure 6.22 shows the longitudinal force as a function of the longitudinal slip of a truck tire running over 50 mm snow depth at 758 kPa (110 psi) inflation pressure and different vertical loads. It is observed that as the vertical load increase the peak longitudinal force increases as well, at given snow depth and inflation pressure. Additionally, the longitudinal slip at which the peak longitudinal force occurs increases as the vertical load increases as well at given snow depth and inflation pressure.

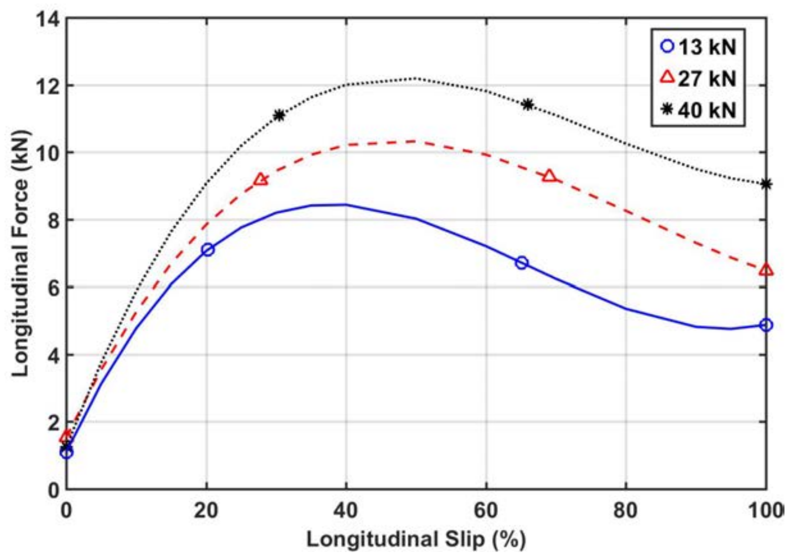

Figure 6.22: Longitudinal force as a function of longitudinal slip for truck tire running over 50 mm snow depth and 758 kPa (110 psi) inflation pressure for different vertical loads

The longitudinal tire stiffness is computed in the same manner mentioned previously (the slop of the linear portion of the longitudinal force versus longitudinal slip curve). Figure 6.23a shows the variation of the longitudinal tire stiffness as a function of the inflation pressure for truck tire running over snow with different depth at 27 kN (6000 lbs) vertical load. The longitudinal tire stiffness decreases as the inflation pressure increases at given vertical load and snow depth, for instance if the inflation pressure is doubled the longitudinal tire stiffness, k_k, reduces by 60% for a 200 mm snow depth and 27 kN (6000 lbs) vertical load. Additionally, the longitudinal tire stiffness increases as the snow depth on the ground increases at given vertical load and inflation pressure, for instance if the snow depth increases from 50 mm to 100 mm the longitudinal tire stiffness increases by around 20% for a rated inflation pressure of 586 kPa (85 psi) and a vertical load of 27 kN.

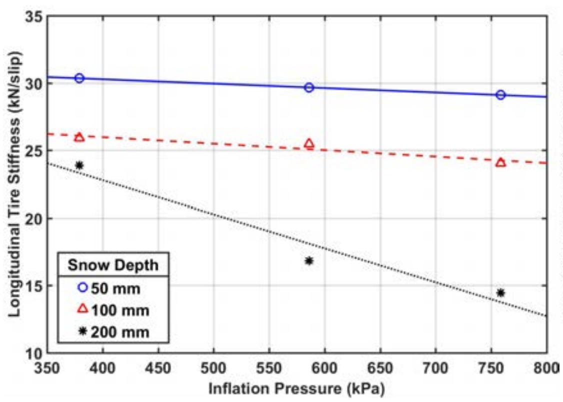

(a) Longitudinal tire stiffness as a function of inflation pressure

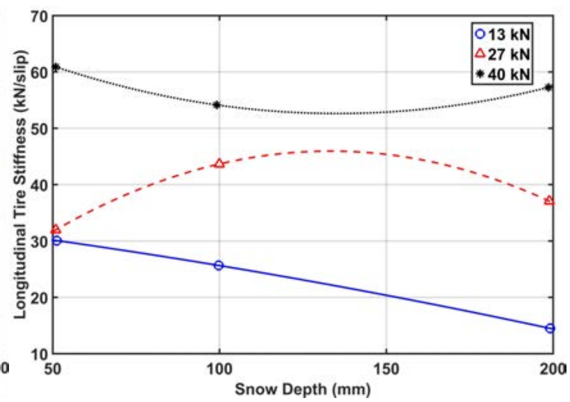

(b) Longitudinal tire stiffness as a function of snow depth

Figure 6.23: Longitudinal tire stiffness as a function of inflation pressure and snow depth at different operating conditions

To further investigate the effect of snow depth on longitudinal tire stiffness figure 6.23b is used. Figure 6.23b shows the variation of the longitudinal tire stiffness, k_k, as a function of the snow depth at 379 kPa (55 psi) inflation pressure and different vertical loads. The longitudinal tire stiffness generally decreases as the snow depth increases which is the same conclusion mentioned above in regards to figure 6.23a. However, for higher vertical loads a nonlinear trend is observed as a function of snow depth. Additionally, the longitudinal tire stiffness increases as the vertical load increases at given snow depth and inflation pressure, for instance, if the vertical load is doubled the longitudinal tire stiffness increases by about 25%. Generally, the longitudinal tire stiffness varies between 15 and 60 $kN/slip$ depending on the snow depth, inflation pressure, and vertical load.

6.2.1.2 tire vertical stiffness

Figure 6.24 shows the variation of the total vertical stiffness as a function of the snow depth at different inflation pressures. It is noticed that as the inflation pressure increases the vertical stiffness increases as well at given snow depth, this conclusion was also noticed in the case of the flooded surface. Additionally, the vertical stiffness adheres to a nonlinear relationship as a function of the snow depth at given inflation pressure. The total vertical stiffness slightly increases when the tire is running at a snow depth between 50 and 100 mm and then decreases as the snow depth increase between 100 and 200 mm. This nonlinearity in the trend could be due to the contact between the tire and snow at different snow depth.

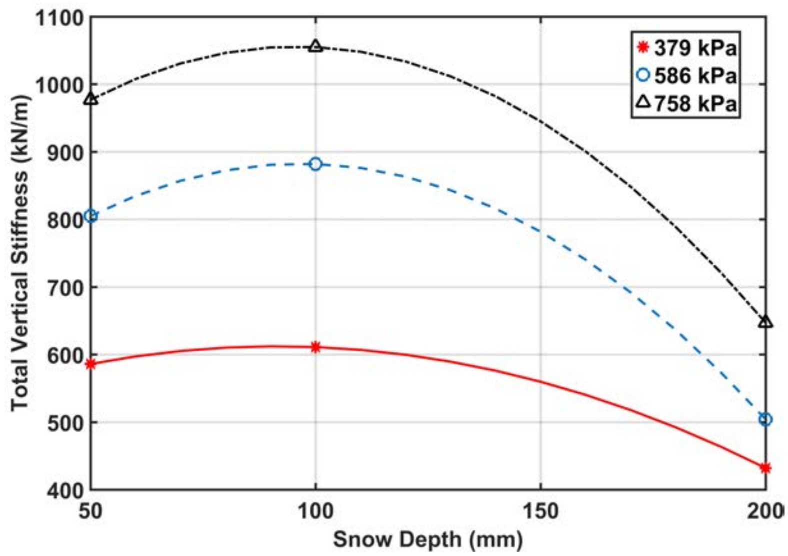

Figure 6.24: Variation of the vertical stiffness as a function of the snow depth for different inflation pressures

It is observed that the tire running on snow is different than that of a tire running over water in terms of the vertical stiffness characteristics. The tire-water vertical stiffness is constant as a function of water depth, unlike that of snow. The tire-snow vertical stiffness is regarded as that of the tire-soil one since the vertical stiffness changes with the snow depth which is a similar trend to that of tire running over soil.

6.2.1.3 rolling resistance coefficient

Figure 6.25 shows the rolling resistance test set up and forces at 200 mm snow depth.

The rolling resistance procedure is repeated for various truck tire operating parameters such as; inflation pressures; applied vertical loads; constant linear longitudinal speed of 10, 25, 50 and 75 km/h; and snow depth of 50 mm, 100 mm and 200 mm.

Figure 6.26 shows the simulation setup of the tire-snow model to predict the rolling resistance coefficient (motion resistance coefficient) of the free-rolling truck tire at 586 kPa (85 psi) inflation pressure, 27 kN (6000 lbs) applied vertical load, 200 mm snow depth and constant longitudinal speed of 10 km/hr. The contour used in this case is the displacement in the vertical direction.

Figure 6.26a shows the simulation at the start of running the tire over the snow where the snow particle has a zero displacement due to the fact that in the

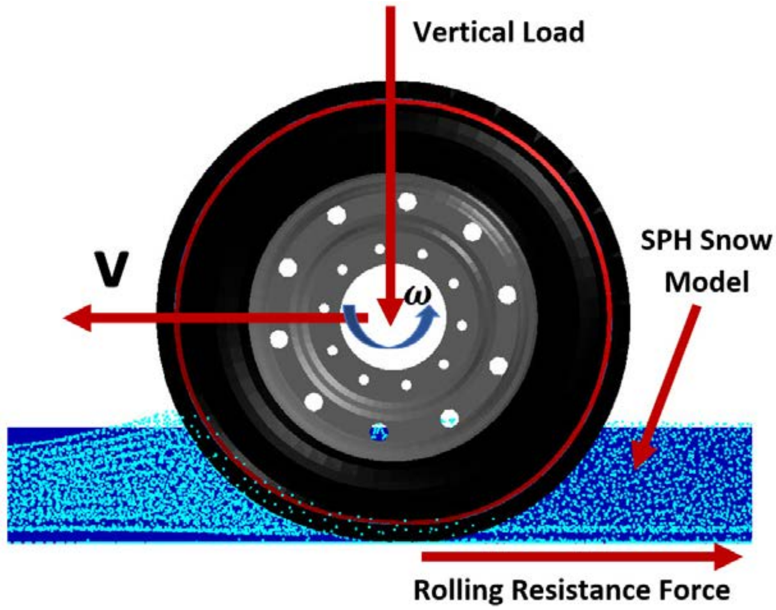

Figure 6.25: Forces acting on a free-rolling tire over 200 mm of snow depth

beginning, the snow is not moving. While figure 6.26b shows the compaction of the snow (residual rut) in the vertical direction due to running the tire over the snow at a given linear longitudinal velocity of 10 km/h. It can be shown that the snow normal displacement increased over the portion where the tire is running and in front of the tire as well.

Figure 6.27a presents the relationship between the rolling resistance coefficient and the tire loading at different inflation pressures and constant snow depth of 200 mm. The rolling resistance coefficient reduces as the load increases, for example an increase of loading from 13 kN (3000 lbs) to 27 kN (6000 lbs) which is doubling the loading the rolling resistance coefficient reduces by 57% for an inflation pressure of 758 kPa (110 psi). The same pattern was obtained by for a truck tire over flooded surface.

Generally, the rolling resistance coefficient ranges between 0.32 and 0.13 at a rated inflation pressure of 586 kPa (85 psi) and 200 mm snow depth for a vertical loading between 13 kN (3000 lbs) and 40 kN (9000 lbs). Figure 6.27b presents the relationship between the rolling resistance coefficient and the tire longitudinal speed at the rated inflation pressure 586 kPa (85 psi) and loading of 27 kN (6000 lbs), for different snow depth. The longitudinal speed of the tire was set constant through the simulation, and the simulation was repeated at different longitudinal speed (10, 25, 50, 75 km/h) and snow depth (50, 100, 200 mm). It can be concluded that as the tire speed increases at given inflation pressure, loading and snow depth the rolling resistance coefficient increases. Additionally, as the snow becomes deeper on the road the rolling resistance coefficient increases

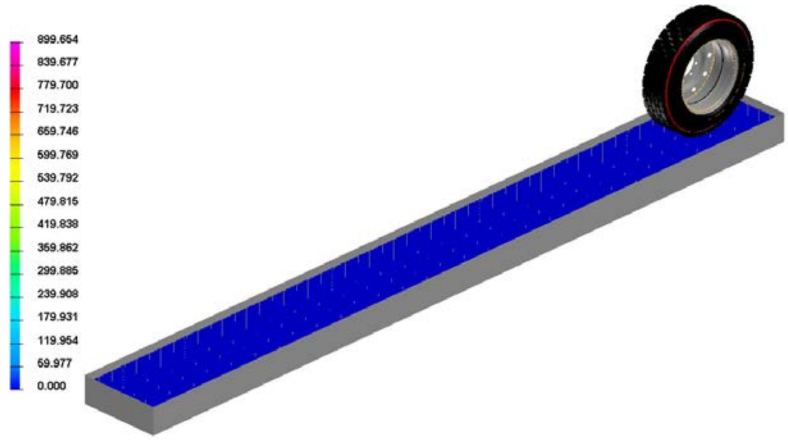

(a) Start of simulation

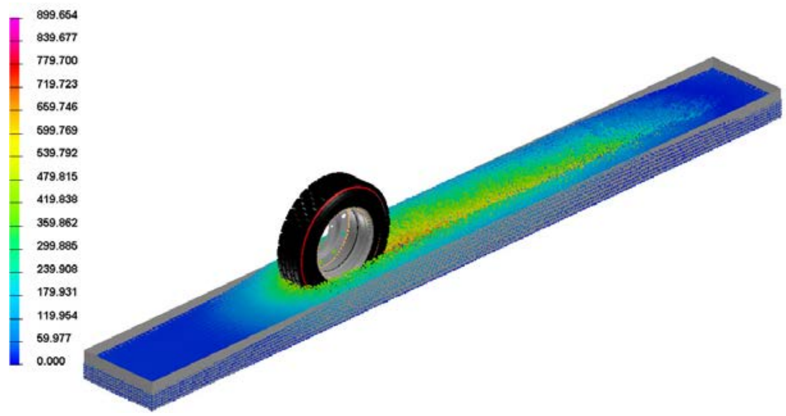

(b) End of simulation

Figure 6.26: FEA Tire- SPH snow model setup at 586 kPa (85 psi) inflation pressure, 27 kN (6000 lbs) loading and snow depth of 200 mm

for constant speed, inflation pressure, and loading; this is the same observation mentioned in the effect of snow depth section. For a speed change from 10 and 75 km/h which is about 7.5 times more the rolling resistance coefficient increases around 6 times from 0.0179 to 0.114.

As mentioned in the rolling resistance test procedure the tire is considered free rolling as no driving or braking torque is applied to the center of the tire, however, during the free-rolling, the angular velocity may vary depending on the snow depth and operating conditions. The change in the angular velocity of the tire is due to the sinkage in the snow. The variation of the angular velocity at constant linear longitudinal velocity will results in a longitudinal slip as shown in figure 6.28a.

Figure 6.28b presents the relationship between the rolling resistance coefficient and snow depth at 586 kPa (85 psi) for different loadings. It is concluded that as the snow depth increases the rolling resistance coefficient increases for all loadings.

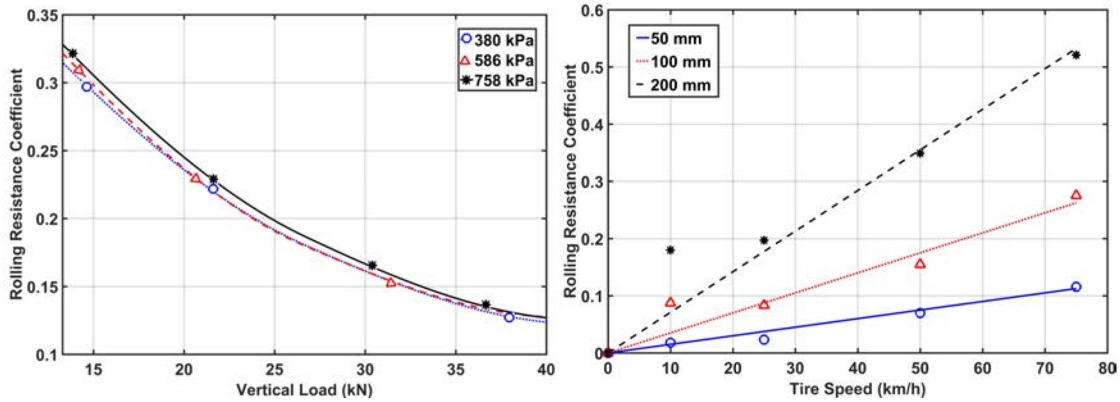

(a) Rolling resistance coefficient versus vertical load

(b) Rolling resistance coefficient versus tire longitudinal speed

Figure 6.27: Rolling resistance coefficient as a function of vertical load and speed a different operating conditions

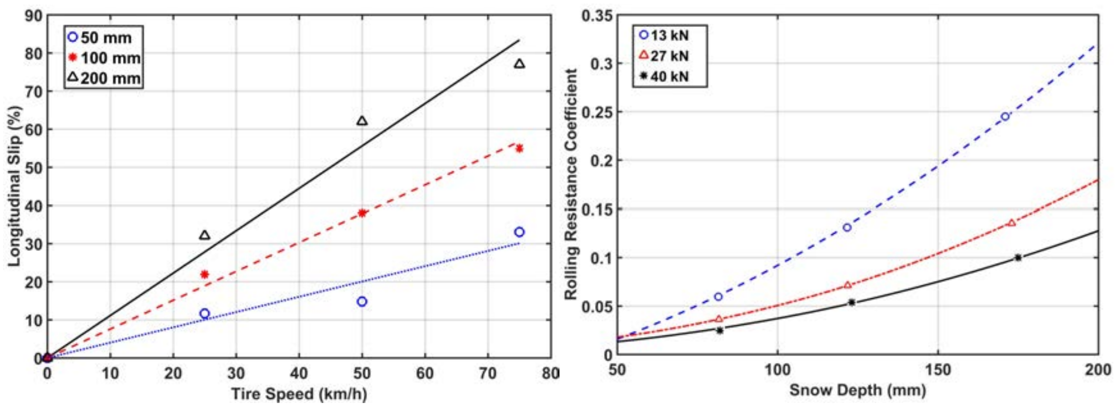

(a) Longitudinal slip as a function of tire longitudinal speed

(b) Rolling resistance coefficient versus snow depth

Figure 6.28: Rolling resistance characteristics of the free-rolling tire at different operating conditions

However, the rolling resistance coefficient does not linearly increase with respect to the snow depth but rather parabolically. It is noticed that at a snow depth of 50 mm the rolling resistance coefficient of 13 kN (3000 lbs) and 27 kN (6000 lbs) is almost the same, and as the snow depth increases the difference in rolling resistance coefficient becomes more clear. For instance, if snow depth is doubled from 100 to 200 mm, the rolling resistance coefficient increase by 350% at 13 kN (3000 lbs) vertical load. As snow depth increases the tire-snow contact area increases as well resulting in a higher rolling resistance coefficient. Additionally, the increase in snow depth increases the tire rolling resistance due to the bulldozing effect. This trend is similar to that observed by [76] and mentioned in figure 6.34. Also, figure 6.33 indicates the increase in the rut as the snow depth increases which leads to the increase in the contact area and thus increases in the rolling resistance coefficient.

The parameters of the in-plane rigid ring tire model of the RHD tire running over snow are provided in appendix A.2.1.

6.2.2 Determination of the out-of-plane rigid ring model parameters

In this section the out-of-plane rigid ring model parameters of the truck tire running over snow at different inflation pressure, vertical load and snow depth are computed.

6.2.2.1 lateral tire stiffness

The same lateral stiffness test procedure mentioned in section 6.1.2.1 for truck tire running over flooded surface is used for the snow surface as well. Figure 6.29 shows the variation of the lateral stiffness as a function of the snow depth at several vertical loads and 586 kPa (85 psi) inflation pressure.

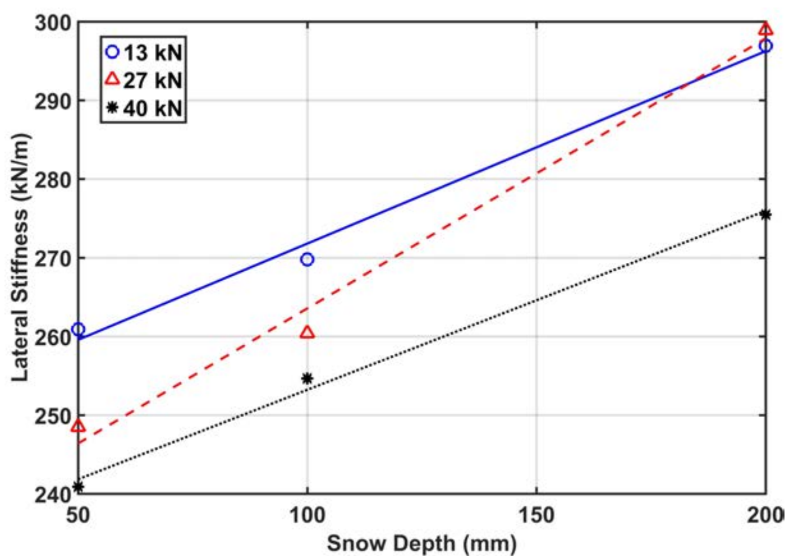

Figure 6.29: Lateral tire stiffness as a function of snow depth at several vertical loads and 586 kPa (85 psi) inflation pressure

It is observed that the lateral stiffness of the tire increases as the snow depth increases at a given vertical load and inflation pressure. The rate of change of the lateral stiffness per snow depth depends on the vertical load, for instance at 27 kN vertical load the rate of change of k_l per 1 mm of snow depth (slope of the lateral stiffness versus snow depth line) is around 0.2 $kN/m.mm$, while for 40 kN vertical load the rate is calculated to be 0.3 $kN/m.mm$. Generally, the lateral stiffness decreases as the vertical load increases at given inflation pressure and snow depth.

It is noted that the lateral stiffness increases as the inflation pressure increase at a given vertical load and snow depth. This conclusion is also observed for the RHD tire running over a flooded surface as well.

6.2.2.2 cornering stiffness

The same cornering test procedure mentioned in section 6.1.2.2 is applied to the truck tire running over snow. Figure 6.30 shows the variation of the cornering tire stiffness as a function of snow depth for several vertical loads and 586 kPa (85 psi) inflation pressure.

The cornering stiffness, k_f, decreases as the snow depth increase at given vertical load and inflation pressure. The reduction in cornering stiffness when the snow depth increases indicate that less lateral force is required to overcome 1 rad of slip angle. Additionally, as the vertical load increase, the cornering stiffness increases as well at given snow depth and inflation pressure. An increase in the vertical load increases the contact area which increases the lateral force as well leading to a higher cornering stiffness.

It is noticed that for higher vertical loads the cornering stiffness exhibits a nonlinear behavior as a function of snow depth. However, it still generally reduce as the snow depth increase. At high snow depth, the recorded cornering stiffness is almost 50 kN/rad for all vertical loads. Furthermore, the cornering stiffness increases as the inflation pressure increase at a given vertical load and snow depth. The increase in cornering stiffness at higher inflation pressures is due to the increase in the contact area, this conclusion is also observed for the RHD tire running over the flooded surface.

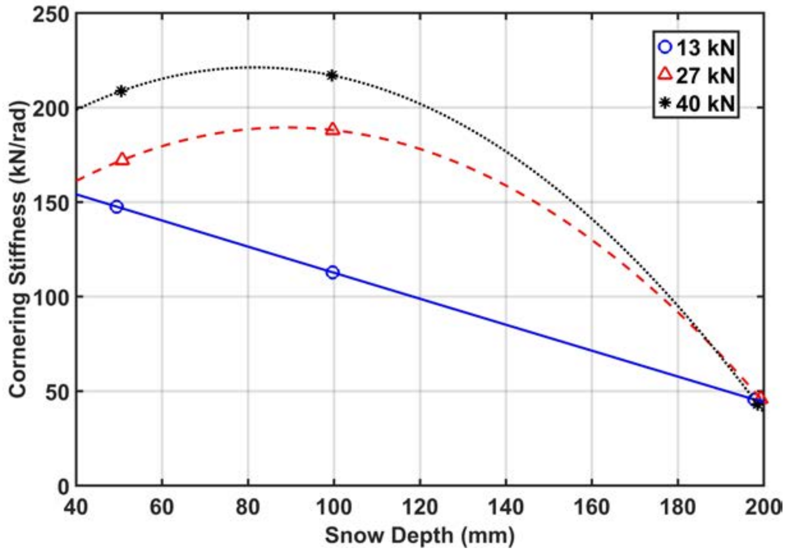

Figure 6.30: Cornering tire stiffness as a function of snow depth for several vertical loads and 586 kPa (85 psi)inflation pressure

6.2.2.3 Selfaligning moment stiffness

Figure 6.31 shows the selfaligning moment stiffness, k_m as a function of snow depth at several vertical loads and 586 kPa (85 psi) inflation pressure. The selfaligning moment stiffness increases as the vertical load increases at given snow depth and inflation pressure. The increase in the selfaligning moment stiffness indicates that more steering is required to return to the right heading. Additionally, the relationship between the selfaligning moment stiffness and the snow depth is not linear at given constant vertical load and inflation pressure. At low vertical loads, the selfaligning moment stiffness reduces as the snow depth increases which is similar to the cornering stiffness behavior. Moreover, at high vertical loads, the selfaligning moment stiffness exhibits a parabolic relationship were it increases with respect to snow depth until 100 mm and then reduces. This observation requires more investigation as 200 mm snow depth is high and the tire-terrain characteristics are closer to the off-road rather than the on-road.

Furthermore, the selfaligning moment stiffness increases as the inflation pressure increase, at given vertical load and snow depth. The increase in selfaligning moment stiffness is due to the increase in the contact area between the tire and snow surface. It is observed that the same relationship is noticed for the RHD tire running over the flooded surface.

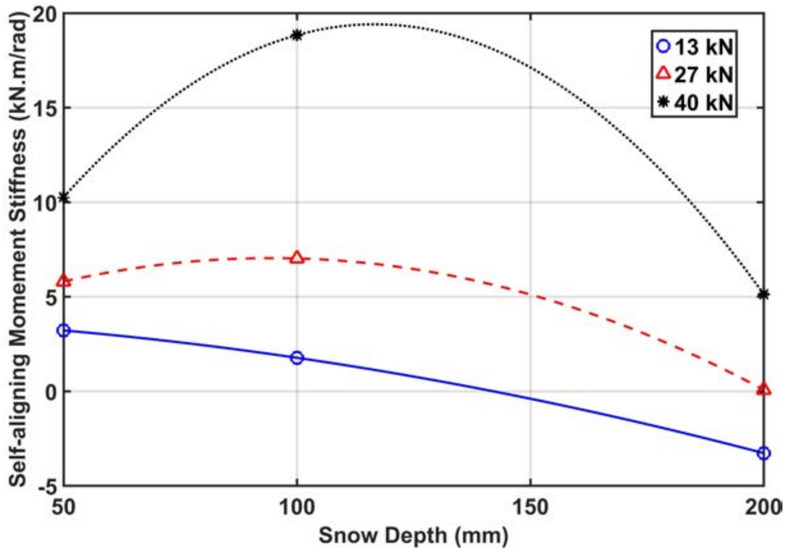

Figure 6.31: Selfaligning moment stiffness as a function of snow depth for several vertical loads and 586 kPa (85 psi) inflation pressure

6.2.2.4 relaxation length

Figure 6.32 shows the variation of the relaxation length as a function of snow depth at several vertical loads and 586 kPa (85 psi) inflation pressure.

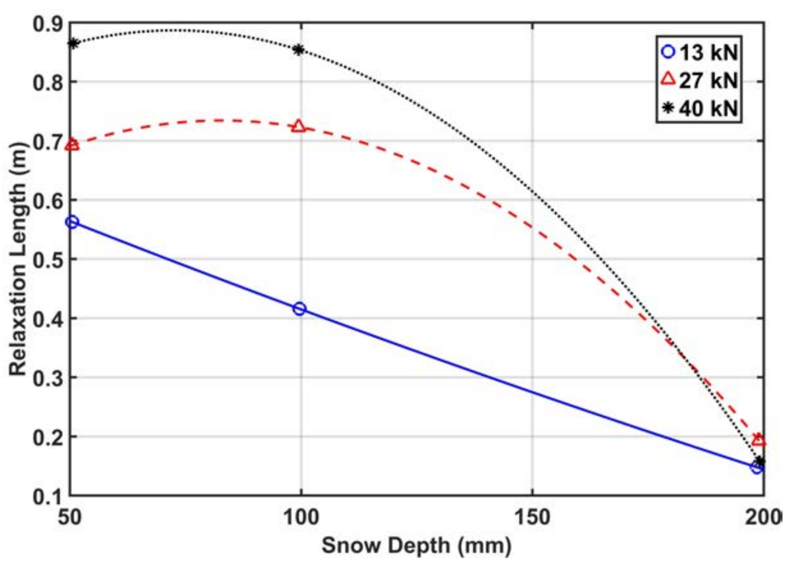

Figure 6.32: Relaxation length as a function of snow depth for several vertical loads and 586 kPa (85 psi) inflation pressure

The relaxation length decreases as the snow depth increases at given vertical load and inflation pressure. The decrease in relaxation length indicates that the tire requires less distance to overcome the steering angle. Additionally, the relaxation length increases as the vertical load increases at given snow depth and inflation pressure. The increase in vertical load increases the cornering stiffness and thus increase the lateral force which requires more distance to overcome the steering.

It is noticed that for higher vertical loads the relationship between the relaxation length and the snow depth becomes nonlinear, however, the relaxation length still decreases as the snow depth increases at given inflation pressure and vertical load.

The parameters of the out-of-plane rigid ring tire model of the RHD tire running over snow are provided in appendix A.2.2.

6.2.3 Verification of tire-snow interaction

In 1981, Harrison [142] conducted experimental testing on a shallow snow model for predicting vehicle performance. The study concluded that the inflation pressure increases the resistance force increases as well, the test was done at Houghton on 30^{th} of January 1975. Additionally, Harrison found a relationship between the drawbar pull and the traffic snow depth, the relationship indicates that as the snow depth increase the drawbar pulls force reduces. Furthermore, Harrison investigated the rut depth as a function of the snow depth as shown in figure 6.33. The results indicate that the rut depth increases as the snow depth increases which leads to a higher rolling resistance coefficient at deeper snow.

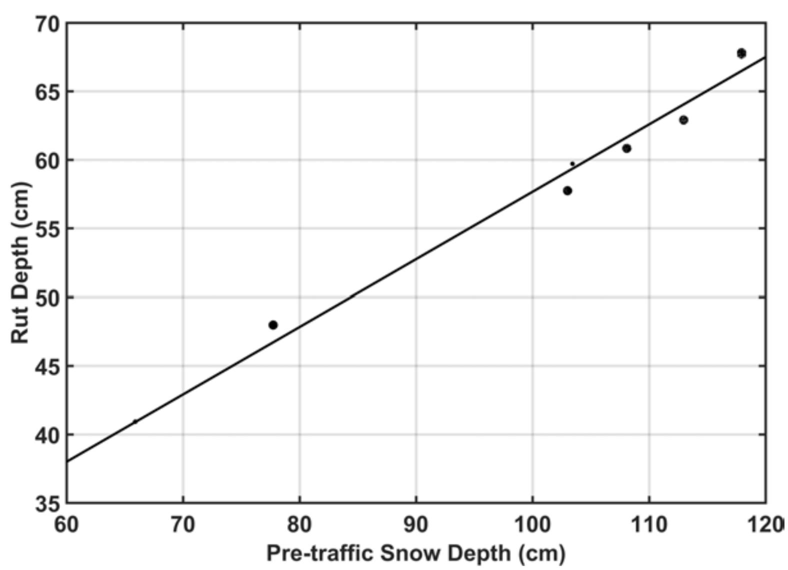

Figure 6.33: Self-propelled test, snow depth versus rut depth [142]

In 2006, Shoop [76] Simulated the relationship between the rolling resistance coefficient and the snow depth using finite element simulations for different tires including the Heavy Extended Mobility Tactical Truck (HEMTT) with 16R20 tire size. Figure 6.34 shows the finite element simulations for the Instrumented Vehicle tire size 235/75 R15 rolling with zero slip, and for unrestricted slip, along with NATO Reference Mobility Model (NRMM) predictions and measured data for rolling resistance in fresh snow (density approximately 200 kg/m^3). This tend is similar to that obtained in this study in section .

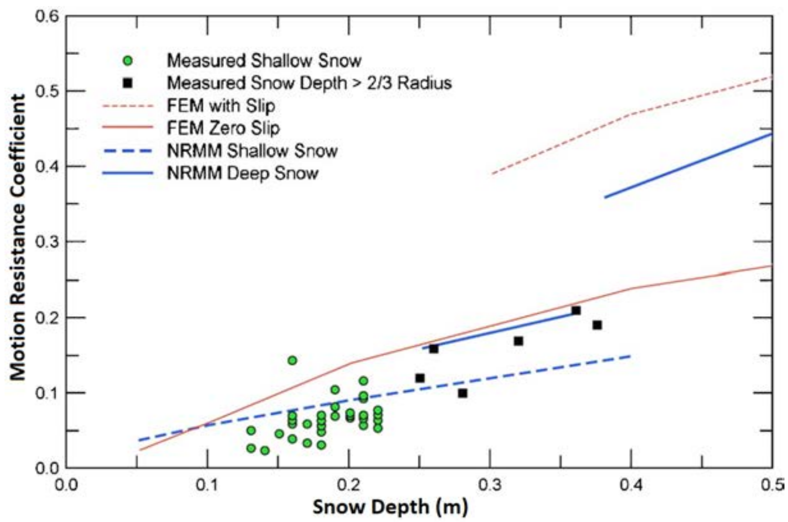

Figure 6.34: Simulations of the instrumented vehicle tire rolling with zero and unrestricted slip, along with NRMM predictions and measured data for rolling resistance in fresh snow [76]

In 1995, Richmond[143] performed rolling resistance experimental research of wheeled vehicles in snow, the study was done by cold regions research and engineering laboratory Hanove. The study concluded that for a driven tire at constant load and inflation pressure the rolling resistance increases as the snow depth increases. This conclusion was observed in this research as well. Richmond also examined the influence of the tire speed on vehicle performance.

Due to the limitations in experimental testing of the rolling resistance coefficient of truck tires over snow, it is difficult to quantify the results obtained, however, the trends and relations are in agreement with previously mentioned published data.

6.3 Summary

The in-plane and out-of-plane rigid ring truck tire-flooded surface model parameters were computed at different operating conditions. It was found that the vertical stiffness is minimally affected by the water depth and that it is majorly affected by the inflation pressure. As the inflation pressure increases the deflection of the tire at a given load decreases. Furthermore, the longitudinal tire stiffness is affected by the applied vertical load, inflation pressure, and water depth. The longitudinal tire stiffness increases as the vertical load increases, however, the longitudinal tire stiffness decreases as the water depth increases. In addition, the longitudinal tire stiffness decreases as the inflation pressure increases. The rolling resistance coefficient is affected by inflation pressure, applied vertical load, and water depth. As the inflation pressure increases the rolling resistance coefficient decreases at given tire speed, water depth, and vertical load. The rolling resistance coefficient decreases as the vertical load increases at given tire speed, inflation pressure, and water depth. In addition, the rolling resistance coefficient increase as the water depth increases at given tire speed, vertical load, and inflation pressure.

Furthermore, the lateral stiffness of the tire increases as the water depth increases at given inflation pressure and vertical load. However, the lateral stiffness increases as the inflation pressure increase at a given vertical load. The cornering stiffness increases as the vertical stiffness increases at given inflation pressure. The cornering stiffness increases as the inflation pressure increases at a given vertical load. However, the cornering stiffness reduces as the water depth increases at a given vertical load and inflation pressure. As for the selfaligning moment stiffness it increases as the water depth increases for a specific load and inflation pressure. And the relaxation length reduces as the water depth increases at given inflation pressure and vertical load. Additionally, the relaxation length increases as the vertical load on the tire increase at given water depth and inflation pressure.

The same analysis of the rigid ring tire model parameter was performed for the same tuck tire running over snow with different depth. It was found that the longitudinal tire stiffness decreases as the inflation pressure increases at given vertical load and snow depth. Additionally, the longitudinal tire stiffness increases as the snow depth on the ground increase at a given vertical load and inflation pressure. Also, the longitudinal tire stiffness decreases as the snow depth increases. As for the vertical stiffness of the tire, it was found that it slightly increases when running at a snow depth between 50 and 100 mm, and decreases as the snow depth increase between 100 and 200 mm. The rolling resistance coefficient of the tire-snow interaction computed for different operating conditions and it was concluded that as the vertical load increases the rolling resistance coefficient of a tire reduces for constant inflation pressure and snow depth. For example if the load is doubles from 13 kN (3000 lbs) to 27 kN (6000 lbs) the rolling resistance coefficient reduces by 57% for an inflation pressure of 758 kPa (110 psi) and 200 mm snow depth. On the other side, the rolling resistance coefficient increases as the inflation pressure increase for given vertical load and snow depth. It is noted that the effect of inflation pressure at high vertical loads becomes negligible. Additionally, the rolling resistance coefficient increases as the snow become deeper on the ground for constant inflation pressure and loading. Generally, the highest rolling resistant coefficient recorded was 0.328 at 13 kN (3000 lbs) loading, 586 kPa (85 psi) inflation pressure and 200 mm snow depth. Finally, as the tire speed increases for given inflation pressure, loading and snow depth the rolling resistance coefficient increases.

The lateral characteristics of the tire running over snow were examined as well. It was concluded that the lateral stiffness of the tire increases as the snow depth increases at given vertical load and inflation pressure The cornering characteristics of the truck tire running over snow were also investigated. It was concluded that the cornering stiffness, k_f, decreases as the snow depth increase for given vertical load and inflation pressure. While the selfaligning moment stiffness increases as the vertical load increases for given snow depth and inflation pressure. Finally, the relaxation length decreases as the snow depth increases at a given vertical load and inflation pressure.

The in-plane and out-of-plane rigid ring tire model parameters for all cases investigated in this chapter are presented in tables in appendix A.

CHAPTER 7

TIRE-MOIST TERRAIN INTERACTION

This chapter focuses on the determination of the terrain dependent in-plane and out-of-plane rigid ring model parameters of the truck tire running over terrains with different moisture content. The terrains include the sandy loam with 25, 50 and 62% moisture content calibrated in section 5.2 and sand with 10, 30 and 50% moisture content calibrated in section 5.3. The in-plane rigid ring model parameters are the longitudinal tire stiffness, vertical stiffness, and rolling resistance coefficient. The out-of-plane rigid-ring model parameters include the lateral stiffness, cornering stiffness, selfaligning moment stiffness, and relaxation length.

7.1 Tire-Sandy Loam Interaction

The in-plane and out-of-plane rigid ring model parameters of the tuck tire running over sandy loam with different moisture content are determined in this section. The effect of several operating conditions including the inflation pressure (379, 586 and 758 kPa), vertical load (13, 27 and 40 kN) and moisture content (25,50 and 62%) on the tire-sandy loam interaction are investigated and discussed.

Figure 7.1 demonstrates the tire-sandy loam interaction at different moisture content. The three simulations are performed at 586 kPa (85 psi) inflation pressure and 27 kN (6000 lbs) vertical load. The contour shown in this figure is for the normal displacement, it is observed that the sandy loam with 62% moisture content had the highest recorded displacement which is 211 mm. This indicates that the soil with higher moisture content has a higher sinkage as well. The soil in the bottom of the box of 25% moisture content shows a very low displacement and is almost not compacted which is opposite of what is seen in the case of 62% moisture where almost all the soil region is compacted.

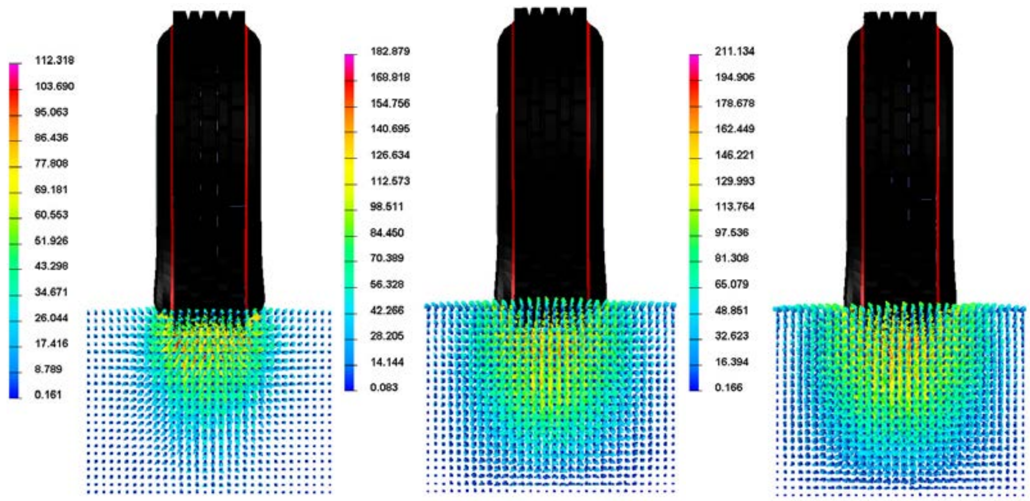

(a) 25% moisture content (b) 50% moisture content (c) 62% moisture content

Figure 7.1: Tire sandy loam interaction at different moisture content and 586 kPa (85 psi) inflation pressure and 27 kN (6000 lbs) vertical load

A similar observation was reported in previous publication [1] for a measured contact area of a tire under different soil conditions. It was reported that the rut becomes deeper with increasing porosity and moisture content of the soil, which is the same observation reported in this research work. Also, it was reported that in soft soil, the pressure over the contact area varies with the depth of the rut, which is also observed in this research.

7.1.1 Determination of the in-plane rigid ring model parameters

The terrain independent in-plane rigid ring model parameters of truck tire running over sandy loam simulation procedures and results are discussed and investigated below.

7.1.1.1 longitudinal tire stiffness

The simulation procedure to determine the longitudinal stiffness is explained in detail in section 6.1.1.1. Figure 7.2a shows that the longitudinal force reaches a maximum value for a longitudinal slip between 15% and 40% depending on the operating conditions. The longitudinal force increases as the applied vertical load increases and the longitudinal force reach its peak earlier for a higher vertical load. On the other side, the peak longitudinal force is slightly affected by the inflation pressure, as the inflation pressure increases the peak longitudinal force decreases.

This is due to the fact that the higher the inflation pressure, the lower the contact area is.

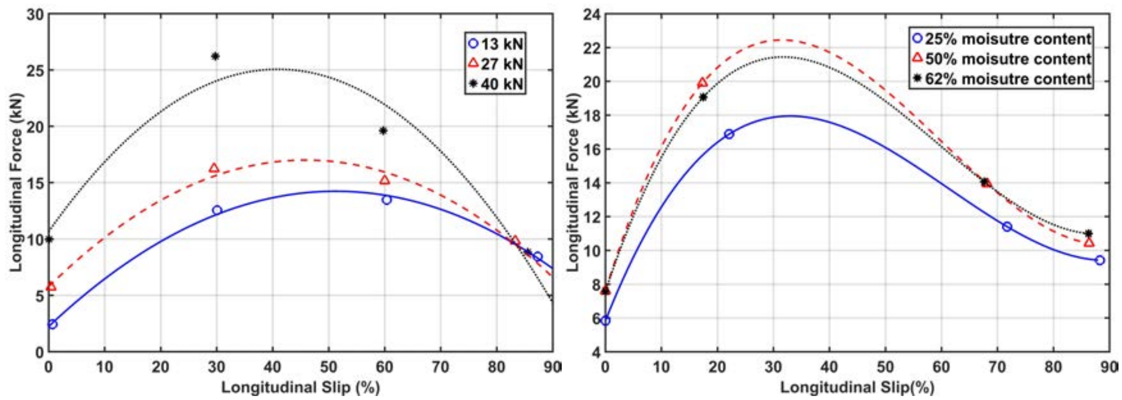

(a) Effect of vertical load at 756 kPa (110 psi) and 50% moisture content

(b) Effect of moisture at 586 kPa (85 psi) and 40 kN (9000 lbs) load

Figure 7.2: Longitudinal force as a function of longitudinal slip for several sandy loam with different moisture content

Furthermore, the effect of the moisture content in sandy loam on the longitudinal force is observed in figure 7.2b. The simulations are done at different moisture content by generating different soils. This figure shows that the 50% and 62% moisture content soil has a similar longitudinal force at 0% slip and the 25% moisture content has less initial longitudinal force. As the longitudinal slip increases the longitudinal force increases for all moisture content. However, the 62% moisture content records a slightly lower force than that of the 50% moist sandy loam.

7.1.1.2 total equivalent vertical stiffness

The total equivalent vertical stiffness, k_{tot}, is calculated based on equation 7.1.

$$\frac{1}{k_{tot}} = \frac{1}{k_{tire}} + \frac{1}{k_{soil}} \tag{7.1}$$

The simulation procedure to determine the tire vertical stiffness previously explained in section 6.1.1.2. The soil vertical stiffness, k_{soil} is determined from the slopes of the curves shown in figure 7.3. It is found that as the moisture content increases the total equivalent vertical stiffness reduces which is due to the reduction of the soil vertical stiffness. Additionally, at given moisture content as the inflation pressure increases the total vertical stiffness increases as well.

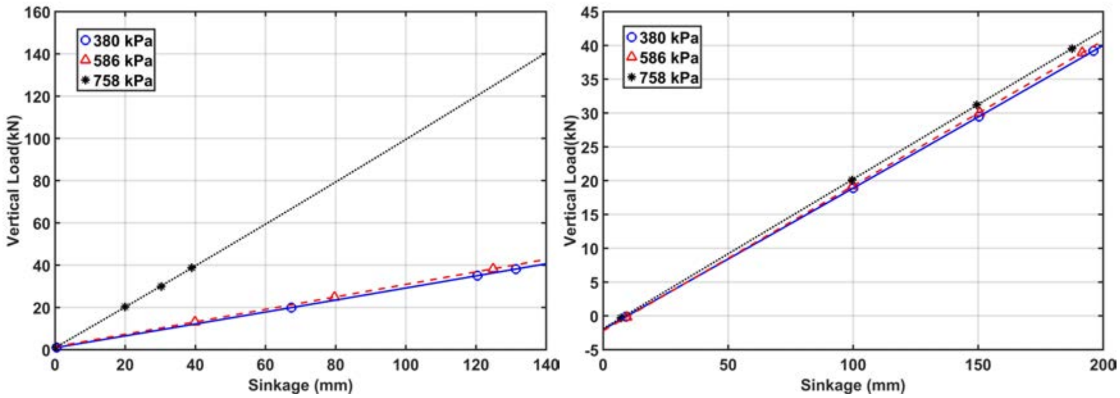

(a) 25 % moisture content (b) 50 % moisture content

Figure 7.3: Vertical load as a function of the tire deflection for several inflation pressure for different moisture sandy loam

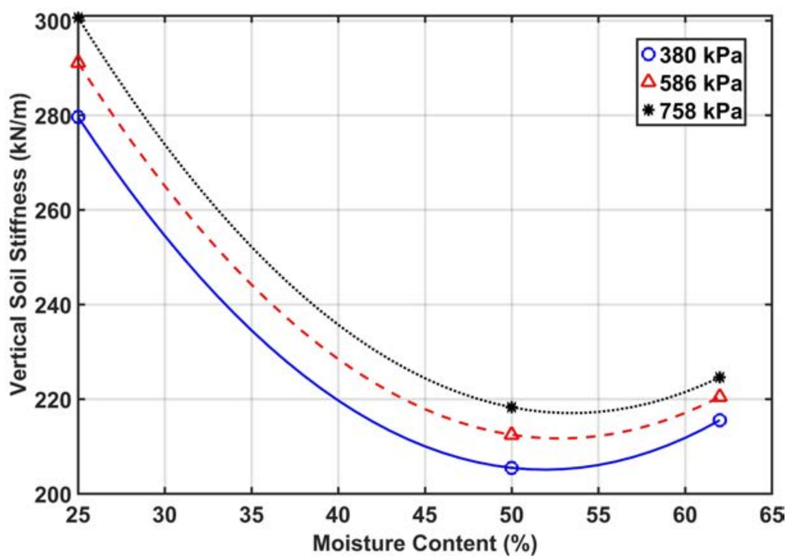

Figure 7.4: Vertical soil stiffness as a function of sandy loam moisture content at different inflation pressures

7.1.1.3 rolling resistance coefficient

The simulation procedure to determine the rolling resistance coefficient is previously explained in section 6.1.1.3. Figure 7.5a shows the variation of the rolling resistance coefficient as a function of the moisture content at 758 kPa (110 psi) inflation pressure and different vertical loads at given speed of 10 km/h. The rolling resistance coefficient increases as the moisture content increases, this is due to the higher tire sinkage at higher moisture content. On the other side, the rolling resistance coefficient increases as the load increases at given inflation pressure and moisture content.

It is noted that the variation of the angular velocity at constant linear longitudinal velocity results in longitudinal slip which indicates that the rolling resistance is not calculated at a freely rolling tire.

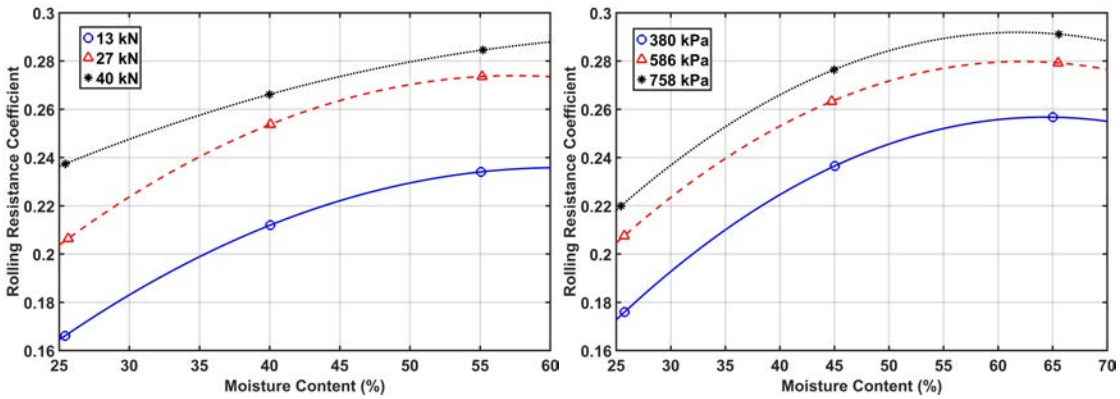

(a) Effect of vertical load at 758 kPa (b) Effect of inflation pressure at 40 kN

Figure 7.5: Rolling resistance coefficient as a function of moisture content at different inflation pressures and vertical loads

To further understand the relationship between the rolling resistance coefficient and the tire operating conditions figure 7.5b is presented. Figure 7.5b shows the variation of the rolling resistance coefficient as a function of the moisture content at a given vertical load of 40 kN (9000 lbs) and different inflation pressures at given longitudinal speed of 10 km/h. It is shown from this figure that as the inflation pressure increases the rolling resistance coefficient increases for constant soil moisture and vertical load.

This result is due to the fact that the increase of the inflation pressure increases the tire sinkage leading to more resistance forces. The same conclusion mentioned in the previous paragraph is also noticed here. The rolling resistance coefficient increases as the moisture content increases at a given vertical load and inflation pressure. This relationship is due to the fact that the contact area between the tire and sandy loam increases as the moisture content increases.

The parameters of the in-plane rigid ring tire model of the RHD tire running over sandy loam are provided in appendix A.3.1

7.1.2 Determination of the out-of-plane rigid ring model parameters

In this section, the terrain dependent out-of-plane rigid ring model parameters of the tire-sandy loam interaction are determined and discussed. The out-of-plane parameters include lateral and cornering characteristics.

7.1.2.1 lateral tire stiffness

The simulation procedure to determine the lateral stiffness is previously explained in section 6.1.2.1. Figure 7.6a shows the variation of the lateral stiffness, k_l, as a function of the vertical load for sandy loam with 25% moisture content and different inflation pressures. As the inflation pressure increases the lateral stiffness increases as well at given moisture content and vertical load, for instance, if the inflation pressure is double the lateral stiffness increases by 45% for a vertical load of 13 kN (3000 lbs). Additionally, as the vertical load increase the lateral stiffness increases as well at given moisture content and inflation pressure, for example if the tire is inflated to 586 kPa (85 psi)and the load is doubled from 27 (6000) to 40 kN (9000 lbs) the lateral stiffness increases by 15%.

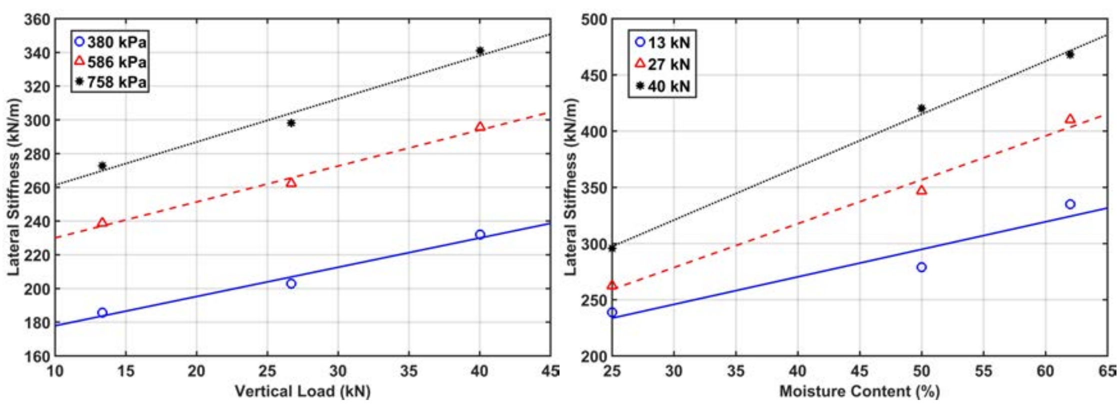

(a) Lateral stiffness as a function of the vertical load

(b) Lateral stiffness as a function of moisture

Figure 7.6: Lateral stiffness as a function of the vertical load and moisture content for tire running over sandy loam

Figure 7.6b shows the variation of the lateral stiffness as a function of the sandy loam moisture content at 586 kPa (85 psi) and different vertical loads. It is observed that as the moisture content in sandy loam increases the lateral stiffness increases at given inflation pressure and vertical load. For instance, if the sandy loam moisture content increased from 10 to 50 % the lateral stiffness increases by around 40% for a vertical load of 40 kN (9000 lbs) and inflation pressure of 586

kPa (85 psi). Generally, the lateral stiffness ranges between 180 and 500 kN/m depending on the moisture content, vertical load and inflation pressure.

7.1.2.2 cornering stiffness

The simulation procedure to determine the cornering stiffness is previously explained in section 6.1.2.2. The cornering stiffness of the tire is determined at several operating conditions. Figure 7.7a shows the variation of the cornering stiffness as a function of vertical load at different inflation pressures of tire running over sandy loam with 25% moisture. It is observed that the cornering stiffness increases as the vertical load increase at given inflation pressure and moisture content. Additionally, the concerning stiffness of the tire also increases as the inflation pressure increases at given vertical load and moisture content. At a high vertical load the contact area between the tire and the soil increases which causes a higher lateral force and thus higher stiffness.

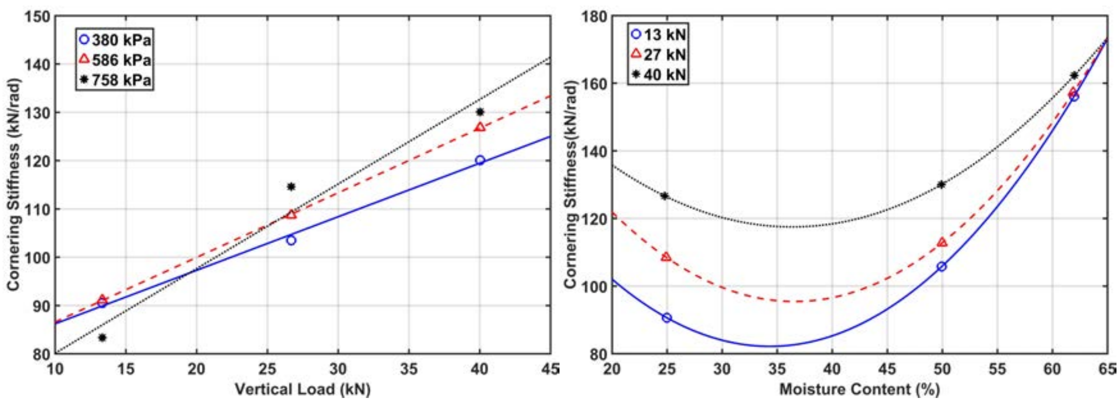

(a) Cornering stiffness as a function of vertical load (b) Cornering stiffness as a function of moisture

Figure 7.7: Cornering stiffness as a function of vertical load and moisture content for tire running over sandy loam

Furthermore, figure 7.7b shows the variation of the cornering stiffness as a function of moisture content at tire inflation pressure of 586 kPa (85 psi) and different vertical loads. The cornering stiffness increases as the moisture content increases at given vertical load and inflation pressure. The increase in moisture content increases the sinkage of the tire in soil and thus increases the contact area which increases the lateral force causing a higher cornering stiffness.

7.1.2.3 selfaligning moment stiffness

The simulation procedure to determine the selfaligning moment stiffness is previously explained in section 6.1.2.3. The selfaligning moment stiffness as a function of vertical load at different inflation pressure for tire running over sandy loam with 25% moisture content is presented in figure 7.8a.

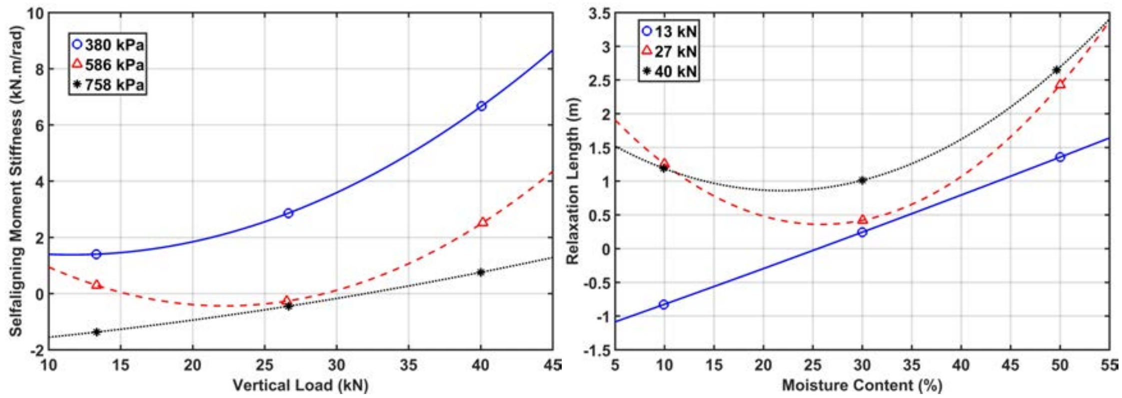

(a) Selfaligning moment stiffness as a function of vertical load

(b) Selfaligning moment stiffness as a function of moisture

Figure 7.8: Selfaligning moment stiffness as a function of vertical load and moisture content for tire running over sandy loam with 25% moisture content

The selfaligning moment stiffness increases as the vertical load increases at given inflation pressure and moisture content. Furthermore, the selfaligning moment stiffness decreases as the inflation pressure increases at given vertical load and moisture content. The increases in inflation pressure reduce the contact area between the tire and soil which reduces the required moment to align the tire.

The variation of the selfaligning moment stiffness as a function of moisture content for an inflation pressure of 586 kPa (85 psi) and different vertical loads is presented in figure 7.8b. The selfaligning moment stiffness has a nonlinear relationship with the moisture content. The selfaligning moment stiffness reduces as the moisture content increases until the moisture content reaches a value between 40 and 45% then the selfaligning moment stiffness starts increasing as the moisture content increases. This nonlinear relationship requires further investigation at low moisture content.

7.1.2.4 relaxation length

The simulation procedure to determine the relaxation length is previously explained in section 6.1.2.4. Figure 7.9a shows the variation of the relaxation length as a function of vertical load at different inflation pressure for tire running over sandy loam with 25% moisture content. The relaxation length increases as the vertical load increases at given inflation pressure and moisture content. Moreover, the relaxation length decreases as the inflation pressure increases at given vertical load and moisture content.

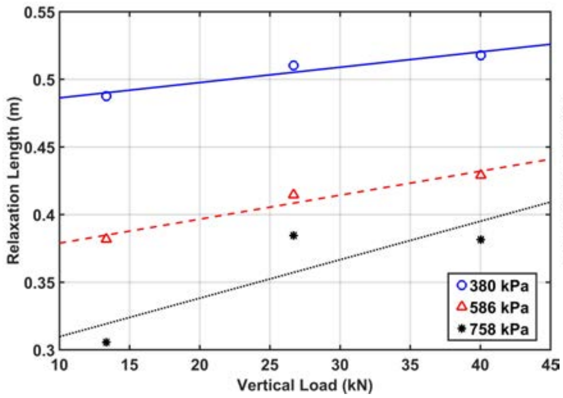

(a) Relaxation length as a function of vertical load

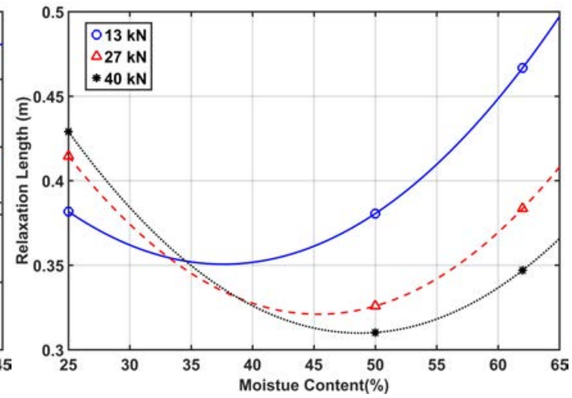

(b) Relaxation length as a function of moisture

Figure 7.9: Relaxation length as a function of vertical load and moisture content for tire running over sandy loam

Figure 7.9b shows the variation of the relaxation length as a function of moisture content for an inflation pressure of 586 kPa (85 psi) and different vertical loads. The relaxation length is observed to have a nonlinear relationship as a function of the moisture content. The relaxation length reduces as the moisture content increases until the moisture content reaches a value between 40 and 45% then the relaxation length increases as the moisture content increases. This observation requires further investigation, especially at low moisture content.

The parameters of the out-of-plane rigid ring tire model of the RHD tire running over sandy loam are provided in appendix A.3.2.

7.2 Tire-Moist Sand Interaction

The terrain dependent in-plane and out-of-plane rigid ring model parameters of the tire running over sand with different moisture content are determined and investigated in this section. The moist sand used in this section is modeled uisng the novel moisturizing technique presented in section 5.3. Figure 7.10 shows the moist sand displacement during a rolling resistance run at 586 kPa (85 psi) inflation pressure and 10% moisture content. The maximum recorded displacement is around 400 mm at 40 kN (9000 lbs) vertical load, while the lowest recorded displacement is around 180 mm at 13 kN (3000 lbs) vertical load. It should be noted that almost all soil boxes have a zero displacement at the bottom of the box to avoid soil penetration.

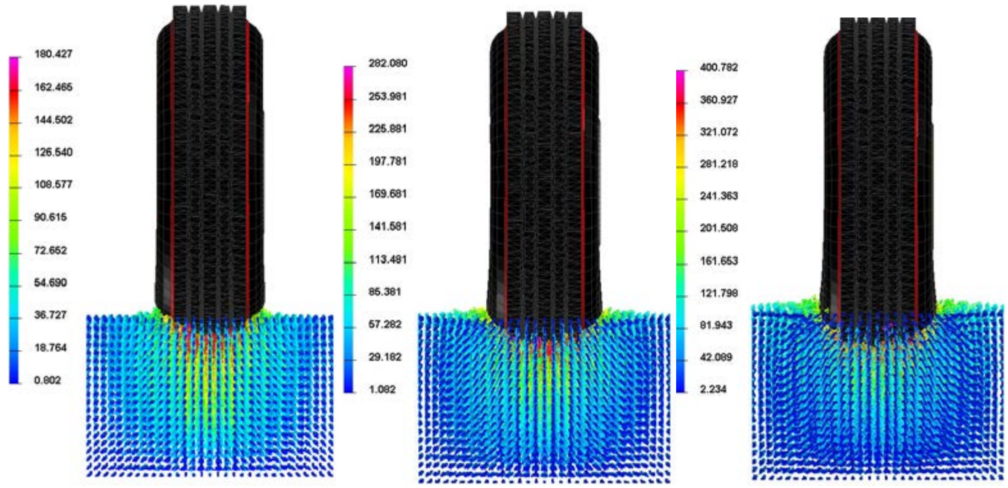

(a) 13 kN vertical load (b) 27 kN vertical load (c) 40 kN vertical load

Figure 7.10: Tire moist soil interaction at different vertical loads and 586 kPa (85 psi) inflation pressure and 10% moisture content

7.2.1 Determination of the in-plane rigid ring model parameters

The terrain dependent in-plane rigid ring model parameters determined are the same as those determined for sandy loam. The simulation procedure for all tests are the same as those mentioned in chapter 6, however, in this case, the terrain consists of two phases as previously discussed in section 5.3.

7.2.1.1 longitudinal tire stiffness

The simulation procedure to determine the longitudinal stiffness is explained in details in section 6.1.1.1. Figure 7.11a shows the variation of longitudinal force as a function of the longitudinal slip for sand with 10% moisture content and 758 kPa (110 psi) inflation pressure at different vertical loads. It is noticed that similar to previous trends as the vertical load increase the peak longitudinal force increase as well. Additionally, at given inflation pressure and moisture content the peak longitudinal force is achieved at a lower longitudinal slip percentage for a higher vertical load.

Figure 7.11b shows the variation of the longitudinal tire stiffness, k_k, as a function of the moisture content in sand at 758 kPa (110 psi) inflation pressure and different vertical loads. The longitudinal tire stiffness is computed in the same method as mentioned before (the slope of the linear portion of longitudinal force vs longitudinal slip). The longitudinal tire stiffness decreases as the moisture content increases at given inflation pressure and vertical load. This indicates that

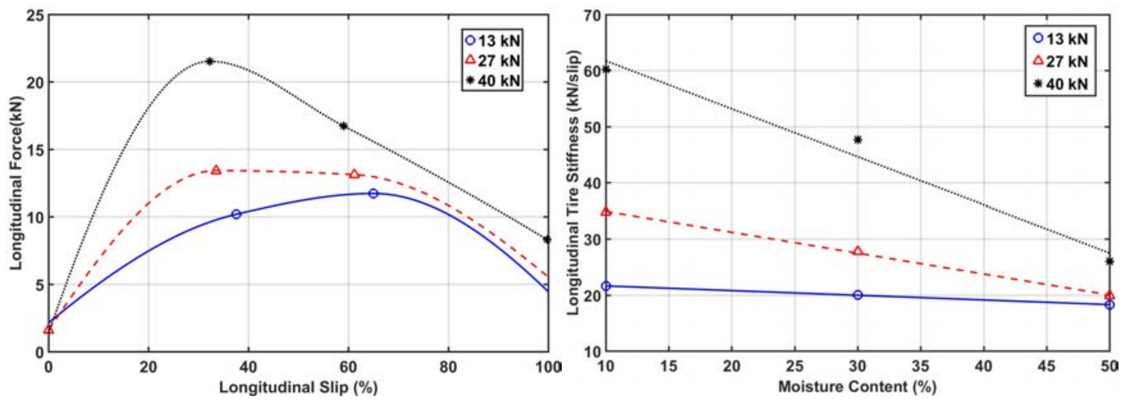

(a) Longitudinal force as a function of the longitudinal slip

(b) Longitudinal tire stiffness as a function of moisture

Figure 7.11: Longitudinal force as a function of the longitudinal slip and moisture content for tire running over moist sand

the longitudinal force required per unit slip reduces when the sand is moister. Additionally, the rate of reduction in longitudinal tire stiffness per rate of increase in moisture content is dependent on the vertical load as well. For example an increase of 20% in moisture content reduces the longitudinal tire stiffness by 1 $kN/slip$ for 13 kN (3000 lbs) vertical load and 11 $kN/slip$ for 40 kN (9000 lbs) vertical load.

7.2.1.2 total equivalent vertical stiffness

The simulation procedure to determine the tire vertical stiffness previously explained in section 6.1.1.2. Figure 7.12 shows the variation of the vertical soil stiffness, k_{soil}, as a function of the moisture content in the sand for different inflation pressure. It is observed that as the moisture content increases the vertical soil stiffness reduces at given inflation pressure, for instance, an increase in the moisture content from 10 to 30% reduces the vertical soil stiffness by around 36%. Additionally, as the inflation pressure increases the vertical stiffness increases as well at given moisture content, for example, for sand with 10% moisture if the inflation pressure is doubled the vertical stiffness increases by around 7%.

At higher moisture content the vertical stiffness varies less, in comparison to lower moisture content. Furthermore, the effect of pressure on vertical soil stiffness is considered minimal, as all three curves are almost parallel to each other.

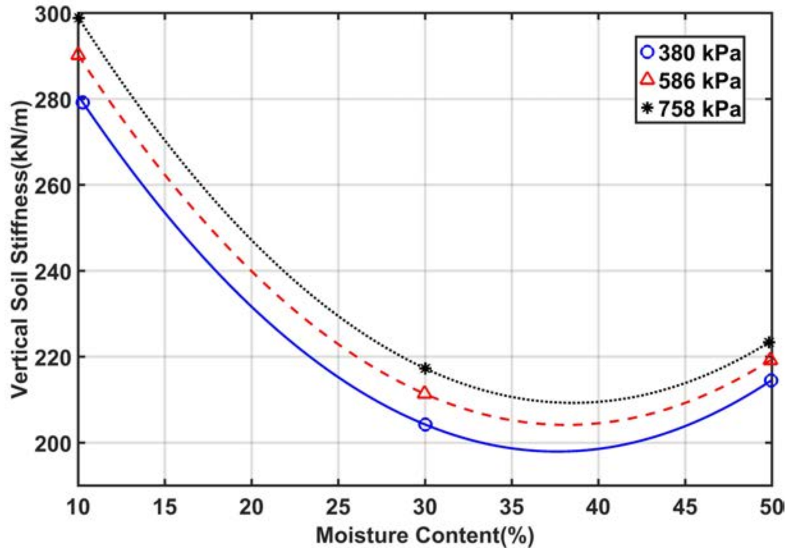

Figure 7.12: Vertical soil stiffness as a function of moisture content at different inflation pressures

7.2.1.3 rolling resistance coefficient

The simulation procedure to determine the rolling resistance coefficient is previously explained in section 6.1.1.3. Figure 7.13a shows the variation of the rolling resistance coefficient as a function of the moisture content in the sand at 586 kPa (85 psi) and different vertical loads. Generally, the rolling resistance coefficient reduces as the moisture content increases at a given vertical load and inflation pressure. For instance, an increase of the moisture content from 10 to 50% reduces the rolling resistance coefficient by around 12% for a vertical load of 40 kN (9000 lbs) and inflation pressure of 586 kPa (85 psi).

Figure 7.13b shows the variation of the rolling resistance coefficient as a function of the inflation pressure at 27 kN (6000 lbs) vertical load and different moisture content. The rolling resistance coefficient increases as the inflation pressure increases at given sand moisture content and vertical load. Additionally, it can be noticed that as the moisture content increase the rolling resistance reduces which is the same observation mentioned above.

The parameters of the out-of-plane rigid ring tire model of the RHD tire running over moist sand are provided in appendix A.4.1.

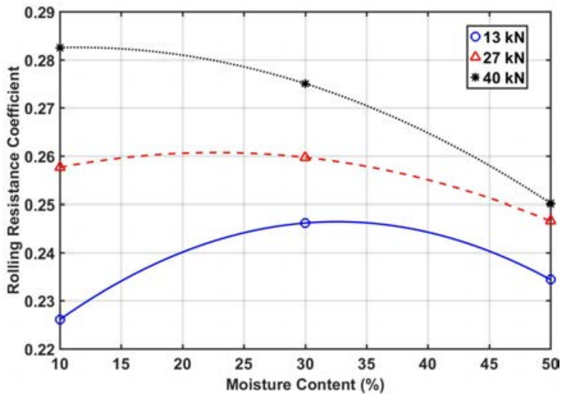

(a) Rolling resistance coefficient as a function of moisture

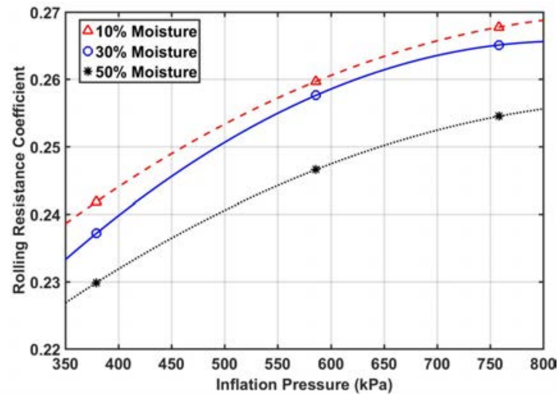

(b) Rolling resistance coefficient versus of inflation pressure

Figure 7.13: Rolling resistance coefficient as a function of inflation pressure and moisture content for tire running over moist sand

7.2.2 Determination of the out-of-plane rigid ring model parameters

The terrain dependent out-of-plane rigid ring tire model parameters are determined for the same conditions mentioned as those for the in-plane rigid ring tire model mentioned in the previous section.

7.2.2.1 lateral tire stiffness

The simulation procedure to determine the lateral stiffness is previously explained in section 6.1.2.1. Figure 7.14a shows the variation of the lateral stiffness as a function of the vertical load for truck tire running over moist sand with 10% moisture content at different inflation pressures. It is observed that the lateral stiffness increases as the vertical load increases at given moisture content and inflation pressure. For a truck tire running over 10% moist sand and 586 kPa (85 psi) inflation pressure the lateral stiffness increases by 24% when the vertical load doubles from 13 kN (3000 lbs) and 27 kN (6000 lbs). The rate of increase of the lateral stiffness as a function of the vertical load depends on the inflation pressure as well as the slope of the curve.

Furthermore, figure 7.14b shows the variation of the lateral stiffness as a function of the moisture content for different vertical loads at 586 kPa inflation pressure. It is observed that the lateral stiffness has a nonlinear relationship with respect to the moisture content. At given inflation pressure and low vertical load, the lateral stiffness reduces as the moisture content increases. Moreover, at given inflation pressure and high vertical load, the effect of the moisture content on the lateral stiffness becomes less in comparison to that at low vertical loads.

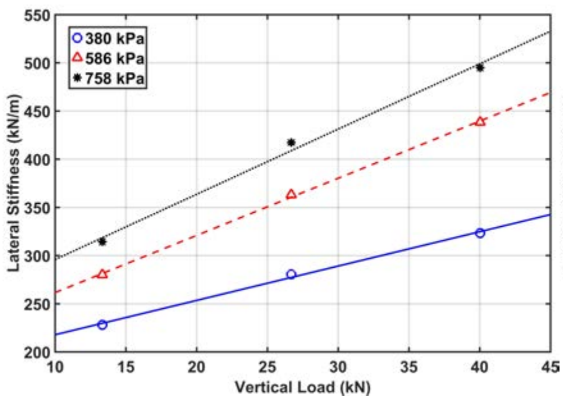

(a) Lateral stiffness as a function of the vertical load

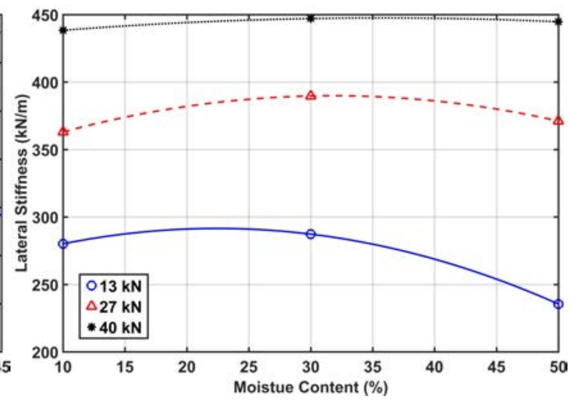

(b) Lateral stiffness as a function of moisture content

Figure 7.14: Lateral stiffness as a function of vertical load and moisture content for tire running over moist sand

7.2.2.2 cornering stiffness

The simulation procedure to determine the cornering stiffness is previously explained in section 6.1.2.2. Figure 7.15a shows the variation of the cornering stiffness as a function of vertical load at different inflation pressures of tire running over moist sand with 30% moisture. It is noticed that the cornering stiffness exhibit a nonlinear behavior as a function of vertical load. As the vertical load at given inflation pressure and moisture content the cornering stiffness increases until 27 kN (6000 lbs) vertical load. Afterward, the cornering stiffness reduces as the vertical load increase. For a tire running over 30% moist sand and 380 kPa (55 kPa) inflation pressure and increase of vertical load from 13 kN (3000 lbs) to 40 kN (9000 lbs) increases the cornering stiffness by 33%.

It is also observed that the rate of increase of the cornering stiffness as a function of vertical load at given moisture content is almost constant regardless of the inflation pressure. Furthermore, the cornering stiffness increases as the inflation pressure increases at a given vertical load and moisture content. The increase in cornering stiffness when the inflation pressure increases are due to the fact that an increase in the inflation pressure increases the contact area between the tire and soil which results in an increase in the cornering force.

Figure 7.15b shows the variation of the cornering stiffness as a function of moisture content for an inflation pressure of 586 kPa (85 psi) and different vertical loads over moist sand. The cornering stiffness increases as the moisture content increases at a given vertical load and inflation pressure. It is also noticed that the cornering stiffness exhibits nonlinear behavior as a function of moisture content.

The increase in moisture content allows for an increase of the tire sinkage in the soil which causes a larger area and thus a larger cornering force. For a moisture

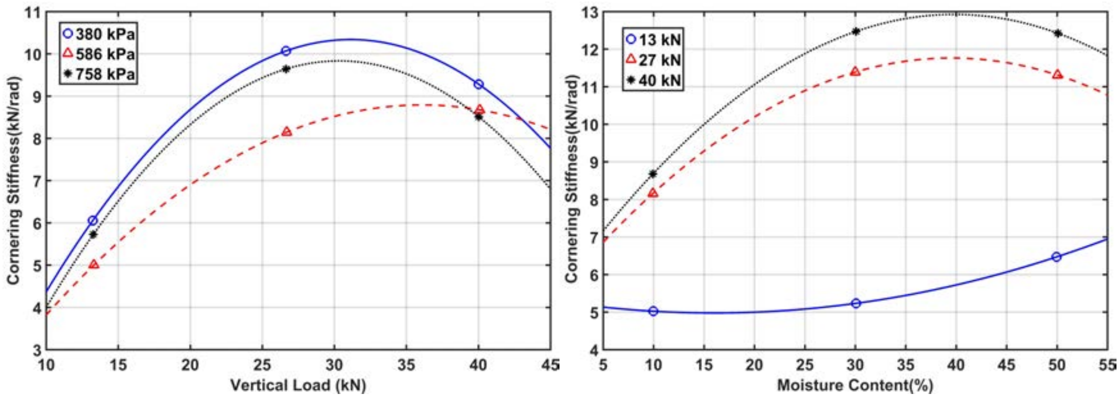

(a) Cornering stiffness as a function of the vertical load

(b) Cornering stiffness as a function of moisture content

Figure 7.15: Cornering stiffness as a function of vertical load and moisture content for tire running over moist sand

content increase from 10% to 50% the cornering stiffness increases by 23% at 13 kN (3000 lbs) vertical load and 586 kPa (85 psi) inflation pressure.Furthermore, as the vertical load increase, the cornering stiffness increases as well at given inflation pressure and moisture content. This is the same conclusion observed from figure 7.15a

7.2.2.3 selfaligning moment stiffness

The simulation procedure to determine the selfaligning moment stiffness is previously explained in section 6.1.2.3. Figure 7.16a shows the variation of the selfaligning moment stiffness as a function of vertical load at different inflation pressure for tire running over moist sand with 10% moisture content. The selfaligning moment stiffness increases the vertical load increase at given inflation pressure and moisture content. The increase in vertical load causes the tire to sink more in soil and thus increases that contact area which results in an increase in the moment to selfaligning the tire again. For an increase of the vertical load from 13 kN to 27 kN the selfaligning moment stiffness increases by 136% for 586 kPa inflation pressure and 10% moisture content.

Furthermore, as the inflation pressure of the tire increases the selfaligning moment stiffness increases as well at given vertical load and moisture content. For a moisture content of 10% and a vertical load of 40 kN (9000 lbs) the selfaligning moment stiffness increases by 45% for an increase in the inflation pressure from 586 kPa (85 psi) to 758 kPa (110 psi).

Figure 7.16b shows the variation of the selfaligning moment stiffness as a function of moisture content for an inflation pressure of 586 kPa (85 psi) and different vertical loads over moist sand. The selfaligning moment stiffness increases as the

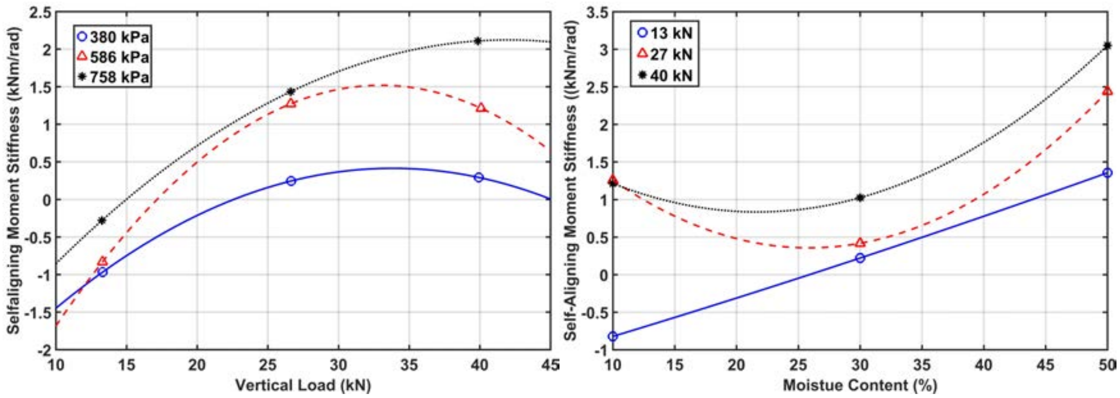

(a) Selfaligning moment stiffness as a function of the vertical load

(b) Selfaligning moment stiffness as a function of moisture content

Figure 7.16: Selfaligning moment stiffness as a function of vertical load and moisture content for tire running over moist sand

moisture content increases at a given vertical load and inflation pressure. As the moisture content increases the tire sinkage in the soil increases as well which causes an increase in the contact area and thus at the moment required to self-align the tire again. For a tire running at 13 kN (3000 lbs) vertical load and 586 kPa (85 psi) inflation pressure, the selfaligning moment stiffness increase by 3 times when the moisture content increase from 10% to 30%.

7.2.2.4 relaxation length

The simulation procedure to determine the lateral stiffness is previously explained in section 6.1.2.1. Figure 7.17 shows the variation of the relaxation length as a function of moisture content for an inflation pressure of 586 kPa (85 psi) and different vertical loads over moist sand. The relaxation length increases non-linearly as the moisture content increases at a given vertical load and inflation pressure. For an inflation pressure of 586 kPa (85 psi) and a vertical load of 27 kN (6000 lbs) the relaxation length increases by 29% when the soil moisture increases from 10% to 30%. The increase in moisture content increases the tire contact area with the soil and thus increases the length required to overcome the cornering force.

Moreover, as the vertical load increases the relaxation length increases as well at given inflation pressure and moisture content. The increase in vertical load increases the tire contact with the soil which increase the length required to overcome the corning force. For instance, if a tire is running over a 10% moist sand with an inflation pressure of 586 kPa (85 psi), an increase in the vertical load from 13kN (3000 lbs) to 27 kN (6000 lbs) increases the relaxation length by 10%.

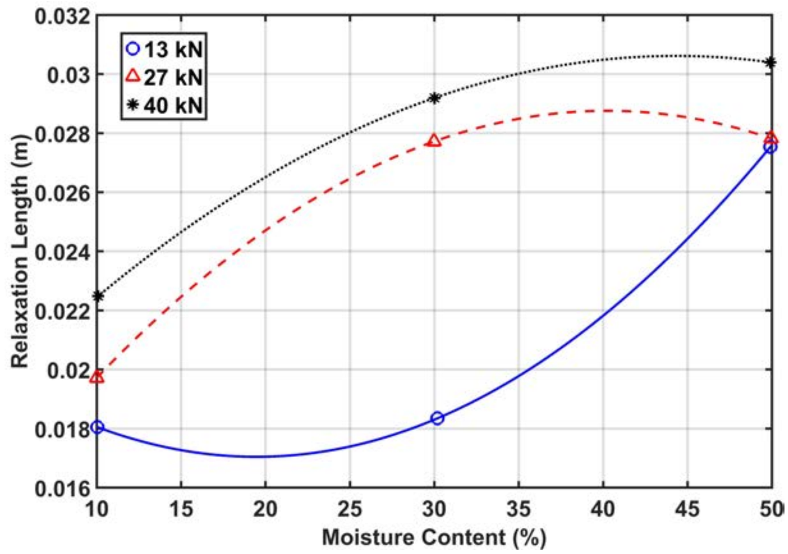

Figure 7.17: Relaxation length as a function of moisture content for an inflation pressure of 586 kPa (85 psi) and different vertical loads over moist sand

The parameters of the out-of-plane rigid ring tire model of the RHD tire running over sandy loam are provided in appendix A.4.2.

7.3 Comparison Between the Two Moisturizing Techniques

Since there is no dry sandy loam, the properties of the sandy loam at 25% are used to apply the layering technique to increase the moisture content to 62%. The predicted rolling resistance coefficient of the tire running over sandy loam modeled using the first (interpolation) and second (moisturizing) techniques, are compared at different inflation pressures and vertical loads.

Figure 7.18a shows the variation of the rolling resistance coefficient as a function of vertical load at 379 kPa (55 psi) inflation pressure for tire running over sandy loam with 62% moisture content using both moisturizing techniques. The rolling resistance coefficient increases as the vertical load increases for both techniques. However, the moisturizing technique tends to give a lower rolling resistance coefficient than that of the interpolation technique at given operating conditions. For instance, for the tire running over 62% sandy loam at 13 kN (3000 lbs) vertical load and 379 kPa (55 psi) inflation pressure the difference between the interpolation and moisturizing technique is around 10%.

Figure 7.18b shows the variation of the rolling resistance coefficient as a function of inflation pressure at 40 kN (9000 lbs) vertical load for a tire running over sandy loam with 62% moisture content using both moisturizing techniques. The rolling

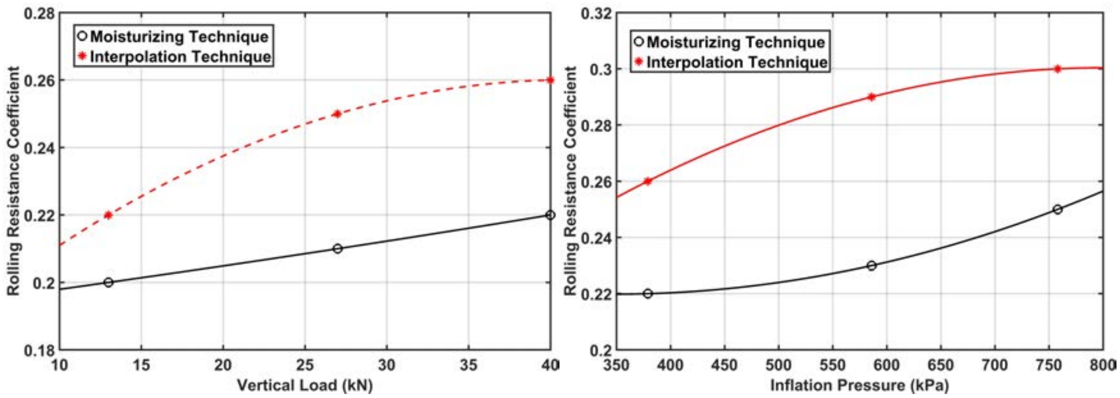

(a) Rolling resistance coefficient as a function of vertical load

(b) Rolling resistance coefficient as a function of inflation pressure

Figure 7.18: Rolling resistance coefficient as a function of vertical load and inflation pressure for both techniques

resistance coefficient increase as the inflation pressure increase for both techniques. However, similar to the results shown in figure 7.18a the moisturizing technique tends to give a lower rolling resistance coefficient than that of the interpolation technique at given operating conditions. For example, for the tire running over sandy loam with 62% moisture content at 40 kN (9000 lbs) vertical load and 379 kPa (55 psi) inflation pressure the difference between the interpolation and moisturizing technique is around 14%.

In general, the difference between the moisturizing and interpolation technique ranges between 10% and 20% depending on the operating conditions.

7.4 Summary

The terrain dependent in-plane and out-of-plane rigid ring tire model parameters were determined for RHD tire running over sandy loam with different moisture content at different operating conditions. The in-plane parameters included longitudinal tire and tread stiffness, the vertical stiffness and the rolling resistance coefficient. The out-of-plane parameters included lateral stiffness, cornering stiffness, selfaligning moment stiffness, and relaxation length. In this case, the sandy loam mechanical properties at different moisture content were based on the terrain interpolation technique explained in section 5.2.

Similarly, the in-plane and out-of-plane terrain dependent parameters of the RHD tire running over sand with different moisture content at different operating conditions were determined. In this analysis, the sand with different moisture content was modeled using the novel moisturizing technique explained in section 5.3.

All the determined terrain dependent and independent in-plane and out-of-plane rigid ring tire model parameters are given in tables in appendix A.

Generally, both sandy loam and moist sand exhibit the same trends for the in-plane and out-of-plane rigid ring tire model parameters, except for the rolling resistance coefficient as a function of moisture content. In the case of sandy loam, the rolling resistance coefficient increases as the moisture content increases at a given speed, vertical load, and inflation pressure, while for the case of moist sand the opposite trend is noticed as the moisture content increases the rolling resistance coefficient reduces. This is due to the angle of shear resistance discussed in chapter 5, were sandy loam and moist sand exhibit opposite trends in terms of the variation of the angle of shear resistance as a function of moisture content.

In addition, a comparison between the predicted rolling resistance coefficient of the RHD tire running over sandy loam with 62% moisture content modeled using the two moisturizing techniques (interpolation and moisturizing) was carried. The analysis was performed at different operating conditions including inflation pressure and vertical load. It was found that both techniques result in similar trends with respect to inflation pressure and vertical load. However, the moisturizing technique predicts 10% to 20% less rolling resistance in comparison to the interpolation technique.

CHAPTER 8

ROLLING RESISTANCE ANALYSIS

This chapter presents a rolling resistance analysis of the RHD tire running over different terrains. The first part of the chapter includes the rolling resistance coefficient prediction for previously terrain. The terrain was modeled and calibrated in chapter 4, including the dry sand, dense sand, and clayey soil. The second part of the chapter includes the development of an Artificial Neural Network (ANN) and Genetic Algorithm (GA) learning algorithms to develop a relationship between the predicted rolling resistance coefficients and the operating conditions. of the truck tire running over different terrains. The operating conditions include tire inflation pressure, vertical load, tire speed, terrain cohesion, terrain shear resistance, and terrain depth. Finally, the results obtained from ANN, GA, and simulations are compared and discussed.

The rolling resistance simulation of each terrain (dry sand, dense sand, and clayey soil) is repeated for several tire operating parameters such as; inflation pressures to model under-inflation of 379 kPa (55 psi), nominal inflation of 586 kPa (85 psi) and over inflation of 758 kPa (110 psi) conditions; and applied vertical loads of 13 kN (3000 lbs), 27 kN (6000 lbs), and 40 kN (9000 lbs). The contact forces in the x and z directions are extracted from the simulations, and the rolling resistance coefficient is computed as a function of time. The reported rolling resistance coefficient is calculated as a mean value when the tire settles, and forces become steady. The results of the dry sand, dense sand, and clayey soil are presented below, while the results of flooded surface and snow are presented in chapter 5 and the results of sandy loam and moist sand are presented in chapter 6. All these results are collected together to form an input/output matrix for the algorithms to compute a relationship.

Figure 8.1 shows a sample of the simulation setup of the tire-soil model (dense sand) to predict the rolling resistance coefficient of the free rolling truck tire at 586 kPa (85 psi) inflation pressure, and 40 kN (9000 lbs) applied vertical load. Figure 8.1a shows the simulation before running the tire over the soil, while figure 8.1b shows the compaction of the soil (residual rut) in the vertical direction due to running the tire over the soil at constant longitudinal speed of 10 km/h.

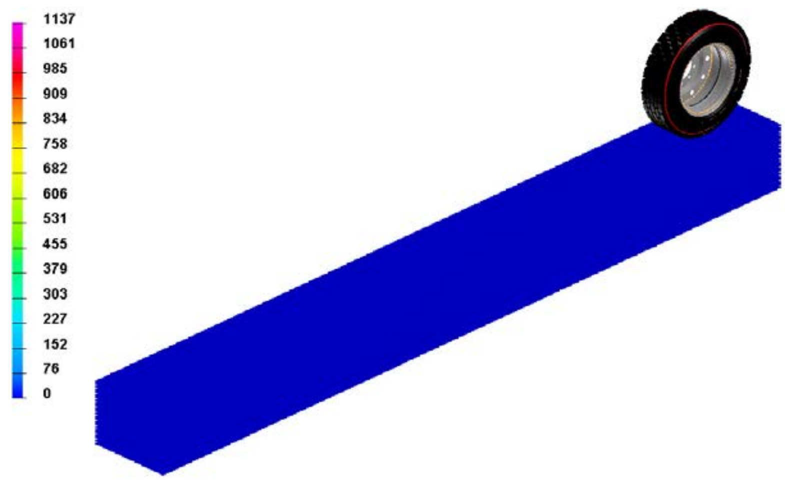

(a) Initial simulation at 0 sec

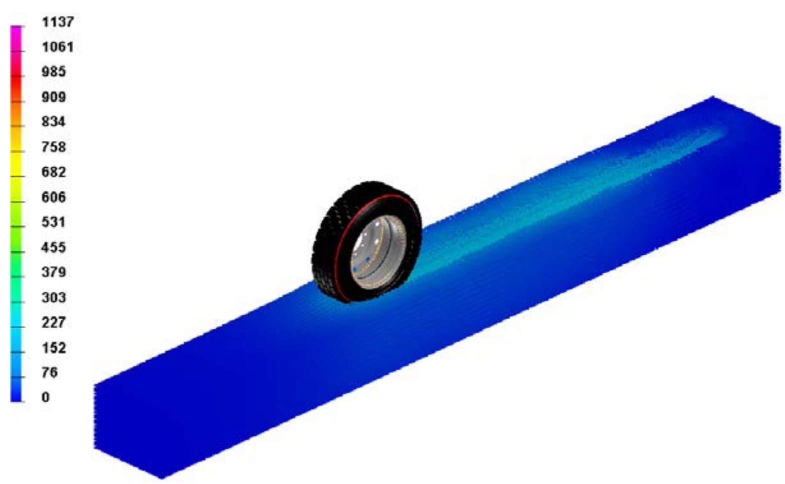

(b) Final simulation at 3 sec

Figure 8.1: Sample of tire soil model setup in Pam-Crash for dense sand at 586 kPa (85 psi) inflation pressure and 40 kN (9000 lbs) applied vertical load

The deformation in the soil after the tire passes is permanent, due to compression. Depending on the soil pressure-sinkage and shear-strength characteristics the tire may sink deeply in the soil and more bulldozing effect is created, which is the case of clayey soil.

Furthermore, the flow patterns and soil wave under a truck tire in different conditions is demonstrated in figure 8.2. Generally, there exist two zones of soil under a rolling tire, in the first zone the soil flows forward and in the second zone, the soil flows backward. Figure 8.2a describes the case when the tire is spinning and the longitudinal velocity is zero (the tire is not moving in the longitudinal direction). In this case, the longitudinal slip is 100% and the soil flows in a single

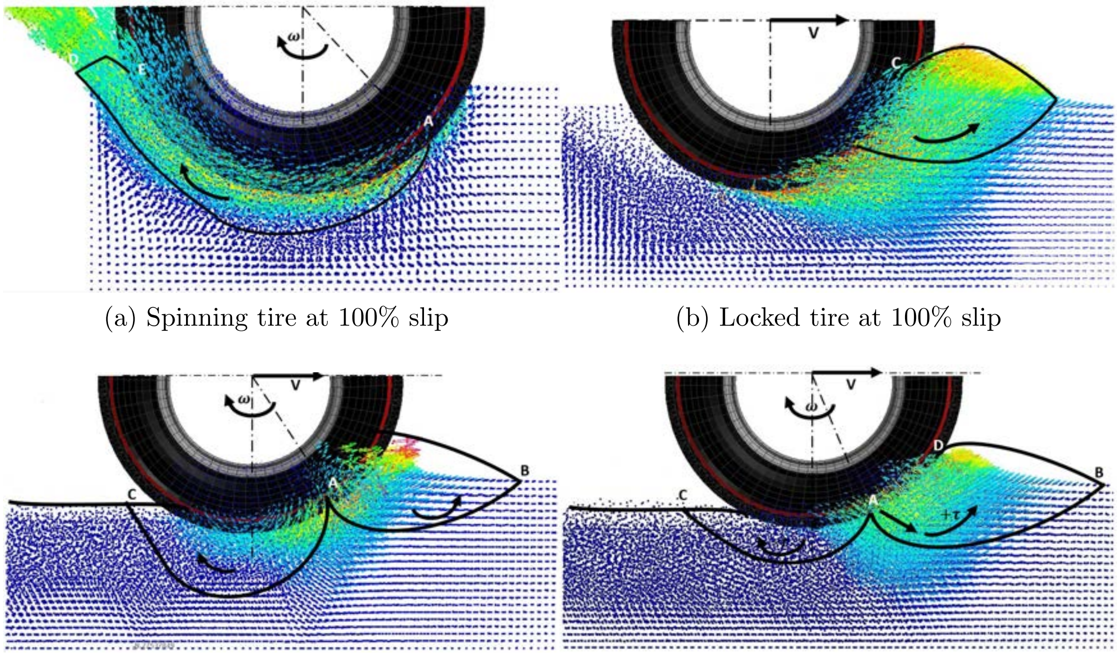

(a) Spinning tire at 100% slip

(b) Locked tire at 100% slip

(c) Driven tire

(d) Towed tire

Figure 8.2: Flow patterns and soil wave for different driving conditions under a tire at 586 kPa (85 psi) inflation pressure and 27 kN (6000 lbs) vertical load

direction backward. Moreover, if the tire is locked as shown in figure 8.2b, where the tire does not rotate but rather moves with a constant longitudinal speed. The soil, in this case, moves in a forward zone only and forms a shape similar to the wedge shape.

Figure 8.2c shows a driven tire over clayey soil at 586 kPa (85 psi) inflation pressure and 27 kN (6000 lbs) vertical load. The logarithmic spiral AB is clearly observed in the zone were the soil moves forward and the logarithmic spiral AC is clear in the backward zone. Moreover, figure 8.2d shows a towed tire over clayey soil at 586 kPa (85 psi) inflation pressure and 27 kN (6000 lbs) vertical load. The shear direction under the tire and in the soil is noticed to have the two flow zones and intersects at point A.

8.1 Validation of Rolling Resistance Model

A series of rolling resistance measurements of the truck tire was performed at Volvo facility in North Carolina [144]. The truck tire tested is the XOne Line Energy T on dry sand. The tire was tested under various loads while fine transducers were assigned to the tire to record three-dimensional forces and moments. The tests were performed with a tractor equipped with the desired tire on the pusher axle (free-rolling tire). The tire was tested under nominal inflation pressure of 758 kPa (110 psi) and constant tractor speed of 8.05 km/h. The truck type reflects the tire loading thus a bobtail truck is an unloaded truck with a vertical load per tire of 8 kN (1774 lbs), a light truck has a load per tire of 12 kN (2680 lbs), Load 2 is 36 kN (8183 lbs) and load 1 is 39 kN (8706 lbs).

Figure 8.3: Tested tire equipped with transducers [144]

Figure 8.3 shows the test tire with the equipped transducers at the Volvo facility in North Carolina, USA. The transducer used is the MSVLW-2T-50K/MSCLW-2T-100K-2 with 6-Axial single or dual wheel load transducer stainless steel. The transducers have a maximum force capacity of 222 kN in the longitudinal and vertical direction and a 111 kN capacity in the lateral direction, the maximum torque capacity in all directions for full-scale output is one mV/V nominal. The transducer is five-arm strain gage bridges and a nonlinearity ogles that 1% of full-scale outputs. Hysteresis and repeatability are also less than 1 % of full-scale output. The zero balance before installation is less than 2% of rated output while the radial sensitivity variation is less than 1% of the radial load. The temperature range is -40 to 125 °C. The excitation voltage is 10 VDC, and the insulation resistance from the bridge case exceeds 1000 M Ω. Finally, the vehicle power input voltage is 10 to 36 VDC [145].

It is noted that the tire tested is a wide base truck tire which is different than the off-road truck tire used in this study. However figure 8.4 compares the measured rolling resistance coefficient of the wide base truck tire freely running over dry sand, and the predicted rolling resistance coefficient of the off-road truck tires at the same operating conditions over the same soil. The purpose of this comparison is to compare the trend of the measured and predicted rolling resistance coefficients not to quantitatively compare the values.

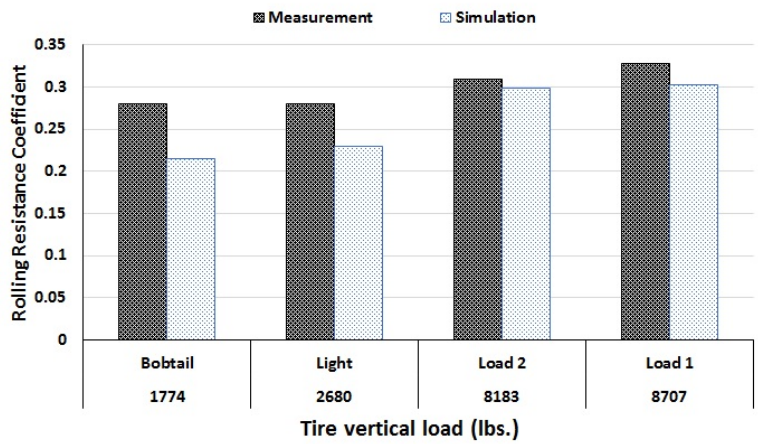

Figure 8.4: Rolling resistance coefficient for measurement and simulation

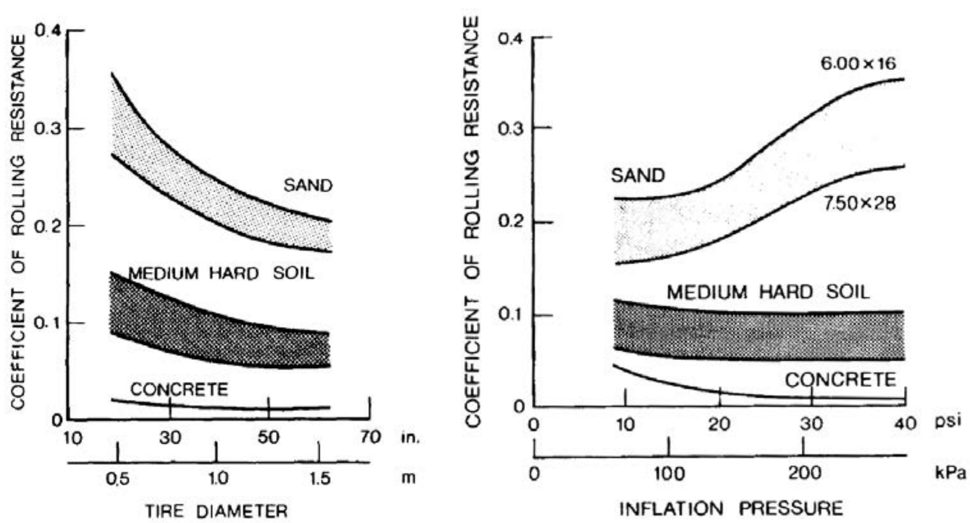

(a) Effect of tire diameter

(b) Effect of inflation pressure

Figure 8.5: Variation of rolling resistance coefficient as a function of different parameters [1]

In addition, according to Wong [1] an off-road truck tire with a diameter of roughly $1m$ running over sand has a rolling resistance coefficient range of 0.2 and 0.3 which is similar to the values obtained from the simulations in case of dry sand. Figure 8.5a shows the variation of the coefficient of rolling resistance as a function of the tire diameter for different terrains. While, figure 8.5b shows the variation of coefficient of rolling resistance as a function of tire inflation pressure for different terrains. In the case of sand the curves indicate that the rolling resistance coefficient increases as the inflation pressure increases.

8.2 Effect of terrain type on rolling resistance coefficient

Figure 8.6a shows the variation of rolling resistance coefficient as a function of applied vertical load for different soils and hard surface at a rated inflation pressure of 586 kPa (85 psi). The clayey soil has the highest rolling resistance coefficient which ranges between 0.30 and 0.64 for a vertical load of 13 kN (3000) to 40 kN (9000 lbs), respectively. While the hard surface had the lowest rolling resistance coefficient which vary between 0.008 and 0.004 for the given vertical load range.

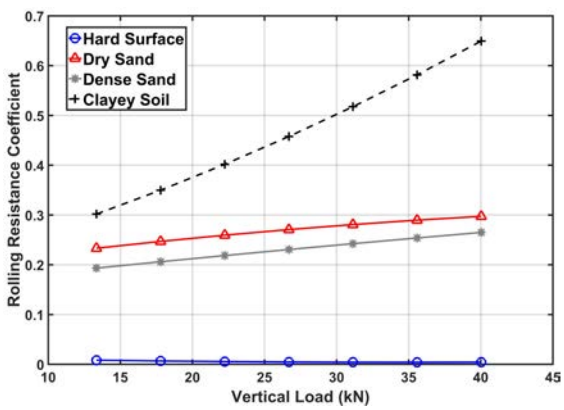

(a) Effect of vertical load

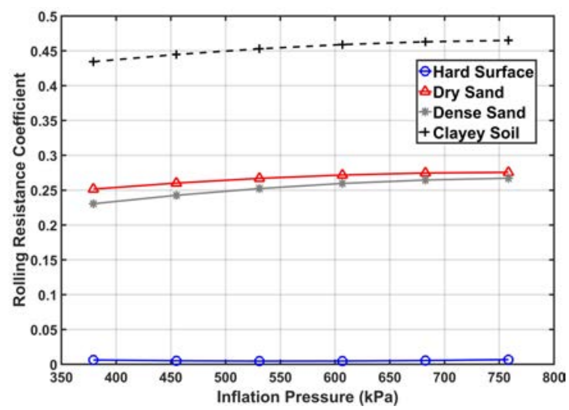

(b) Effect of inflation pressure

Figure 8.6: Rolling resistance coefficient as a function of vertical load and inflation pressure over different soils

The rolling resistance coefficient over soft terrain including dry sand, dense sand, and clayey soil adhere to the same behavior, as the vertical load increase the rolling resistance increase. This is due to the fact that as the vertical load increase the tire tends to sink more into the soil which leads to a larger contact area and thus more forces which increase the rolling resistance coefficient. The rolling resistance coefficient over dry and dense sand is relatively in agreement regarding variation as a function of the vertical load as both adhere to almost parallel behavior.

Figure 8.6a also shows that the rolling resistance coefficient over a hard surface is remarkably lower than that of soft terrains. The rolling resistance coefficient over hard surface increases as the vertical load increases, which is similar to the case of soft terrains. On a hard surface, as the vertical load increase the contact area between the tire and surface increases which lead to an increase in the rolling resistance.

It is concluded that when the truck is driving over clayey soil the rolling resistance is highest and thus fuel consumption is higher than on sand. Moreover, for the case of dry and dense sand, dry sand has higher rolling resistance that the dense one. This is due to the fact that the dry sand has a higher sinkage at the same applied pressure.

Figure 8.6b shows the variation of the rolling resistance coefficient as a function of tire inflation pressure for different soils and hard surface at a vertical load of 27 kN (6000 lbs). Similar to the previous results the clayey soil has the highest rolling resistance coefficient varying between 0.43 and 0.46 for an inflation pressure range of 379 (55 psi) to 758 kPa (110 psi).

In addition, dry and dense sand adhere to similar behavior, and hard surface records the lowest rolling resistance coefficient. Despite the fact that the clayey soil has less sinkage than that of dry sand the resistance force is higher due to the higher density of the clayey soil.

It is noted that in this case, unlike the soft terrains, the hard surface has an opposite behavior. On a hard surface, as the inflation pressure increase, the rolling resistance coefficient reduces. The increase in inflation pressure reduces the contact area between the tire and hard surface which leads to a reduction in the rolling resistance coefficient.

8.3 Effect of vertical load on rolling resistance coefficient

Figures 8.7a, 8.7b, and 8.7c show the variation of tire rolling resistance coefficient as a function of vertical loads at different inflation pressures running over dry sand, dense sand, and clayey soil, respectively.

All soils maintain a general pattern, as the applied vertical load increases the rolling resistance coefficient increases at a given constant inflation pressure. Additionally, as the inflation pressure increases the rolling resistance coefficient also increases at given constant vertical load. The increase in rolling resistance coefficient when the load increase is due to the higher sinkage of the tire in the soil which causes a larger contact area. However, each soil adheres different rate of change with respect to applied vertical load. In the case of dry sand, the rolling resistance coefficient increases in a logarithmic trend with respect to load change. The lowest recorded rolling resistance coefficient was 0.22 at an inflation pressure of 379 kPa (55 psi) and 13 kN (3000 lbs) vertical load, while the highest rolling resistance coefficient was recorded to be 0.31 at an inflation pressure of 758 kPa and 40 kN vertical load. On the other side, the dense sand increases almost in a linear trend as a function of load. The rolling resistance coefficient varied between

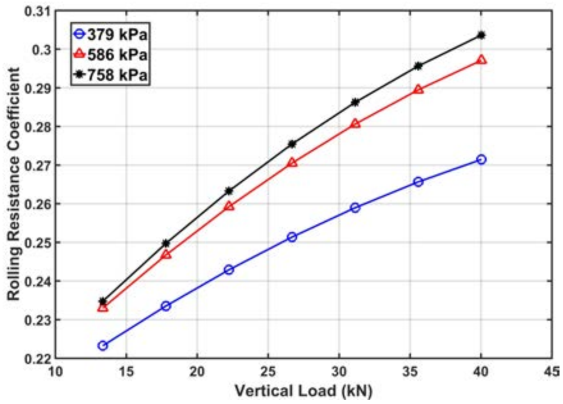

(a) Dry sand

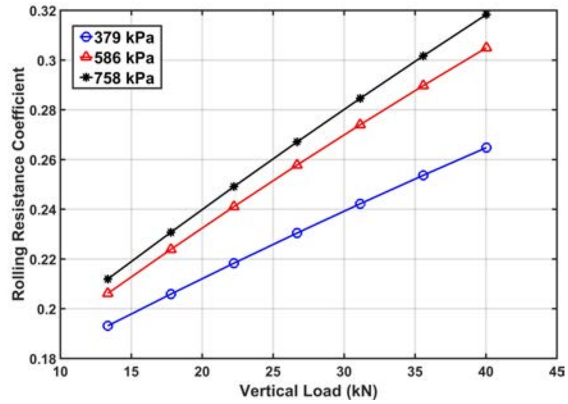

(b) Dense sand

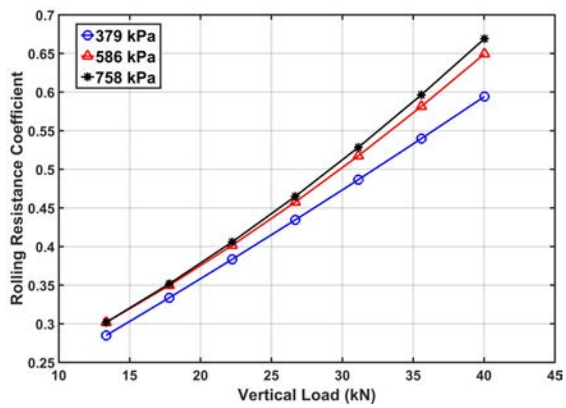

(c) Clayey soil

Figure 8.7: Rolling resistance coefficient as a function of load for different soils

0.1 (for an inflation pressure of 379 kPa (55 psi) an 13 kN (3000 lbs) vertical load) and 0.32 (for an inflation pressure of 758 kPa (110 psi) and vertical load of 40 kN (9000 lbs)). It is noted that the dense sand rolling resistance coefficient range is wide and thus dense sand is more sensitive to loading as compared to dry sand.

The effect of applied vertical load on rolling resistance is shown; an increase of the vertical load of 300% can increase rolling resistance coefficient in soils as high as 213%. Thus, the applied vertical load has a major effect on the truck fuel economy.

8.4 Effect of inflation pressure on rolling resistance coefficient

To demonstrate the relationship between the rolling resistance coefficient and the tire inflation pressure at various applied vertical loads for different soils in a clear way figures 8.8a, 8.8b, and 8.8c are implemented. Figures 8.8a, 8.8b, and 8.8c show the variation of the rolling resistance coefficient as a function of tire inflation pressure for different applied vertical loads for dry sand, dense sand, and clayey soil, respectively.

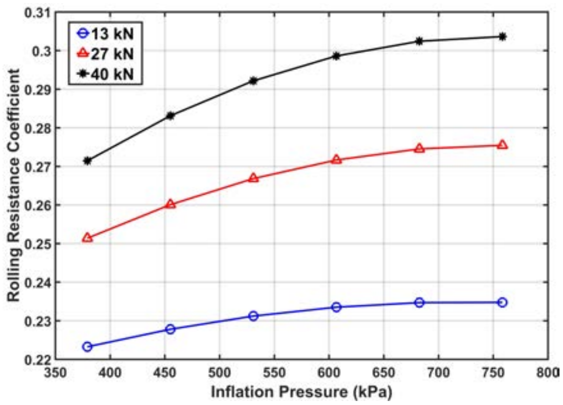

(a) Dry sand

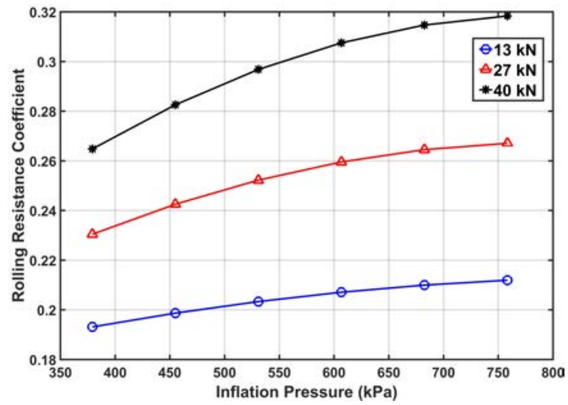

(b) Dense sand

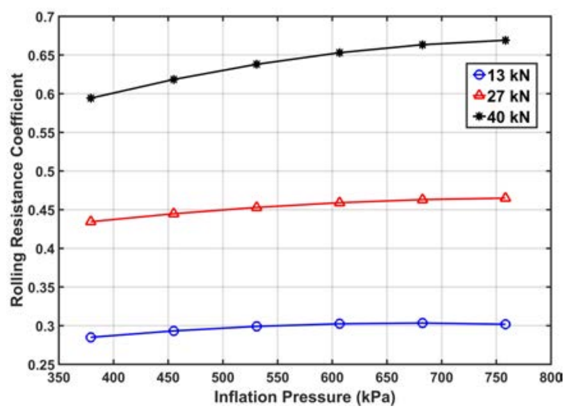

(c) Clayey soil

Figure 8.8: Rolling resistance coefficient as a function of load for different soils

The clayey soil recorded the minimal effect of the inflation pressure on the rolling resistance coefficient. For instance, an increase in inflation pressure of 200% increases the rolling resistance coefficient by 7% for a vertical load of 40 kN (9000 lbs). Additionally, it is noticed that at higher vertical loads the inflation pressure effect becomes higher. Generally, the rolling resistance coefficient varies between 0.25 (for an inflation pressure of 379 kPa (55 psi) an 13 kN (3000 lbs) vertical load) and 0.65 (for an inflation pressure of 758 kPa (110 psi) and vertical load of 40 kN (9000 lbs)). The rolling resistance coefficient range is considered wide and this clayey soil is sensitive to both inflation pressure and load.

On the other side, in the case of dry sand, the rolling resistance coefficient is highly influenced by the tire inflation pressure, an increase of 200% in pressure increases the rolling resistance coefficient by 20%. It is noted that for a low vertical load the inflation pressure has less effect in comparison with that of higher loads.

Dry sand adheres to similar behavior to that of dense sand regarding curves patterns. However, in the case of dense sand, the rate of change of the rolling resistance coefficient as a function of inflation pressure is almost constant and is not affected by the vertical load.

8.5 Development of Analytical Rolling Resistance Relationships

In this section, the ANN and the GA methods are used to develop analytical relationships of the predicted Rolling Resistance Coefficient (RRC) of an RHD tire running over several terrains at different operating conditions. The terrains used include dry sand, dense sand, clayey soil, water, snow, sandy loam with different moisture content and moist sand. The terrains are presented using the cohesion, angle of shear resistance and depth.

The tire operating conditions are presented using the inflation pressure, vertical load, and speed. The data obtained in chapters 5, 6, and 7 are used to train, test and validate the analytical models. Thus, each RRC value is associated with six inputs.

8.5.1 Artificial Neural Network

ANN is an interconnected system of simple processing units. The processing units are referred to as neurons and they work in parallel to achieve a required result. In most applications, the ANN is regarded as a black box that has input and output. One of the first uses of ANN was recorded in 1990 by Dayhoff [146]. Dayhoff used the knowledge of brain function and implemented that into the biochemical reactions.

Figure 8.9 shows the structure of an ANN which is based on the original model developed in 1943 by Mcculloch [147]. The model is an attempt to model the signal processing characteristics of the biological nerve cell in a mathematical approach. It is noted that w_i is the weight of each input channel, p_i, y is the output, and n is the number of neurons. The weight of each channel increases or decreases the incoming signal to the dendritic arms of the biological neuron.

In this research a two-layer fully-interconnected feed-forward ANN is used as shown in figure 8.10. A fully-interconnected ANN means that each input is connected to each neuron and the data is processed from left to right which is the forward direction. The parameter b_i is the bais which is also shown in figure 8.9.

In the case of a single neuron, the relationship between the input and the output is shown in equation 8.1, where f is the activation function performing the

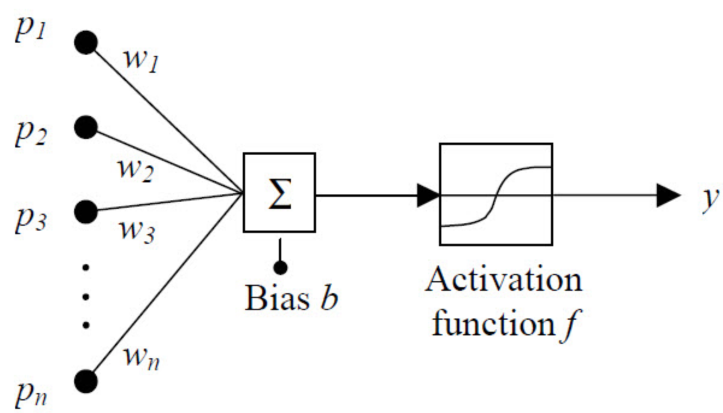

Figure 8.9: A model presenting the artificial neuron [147]

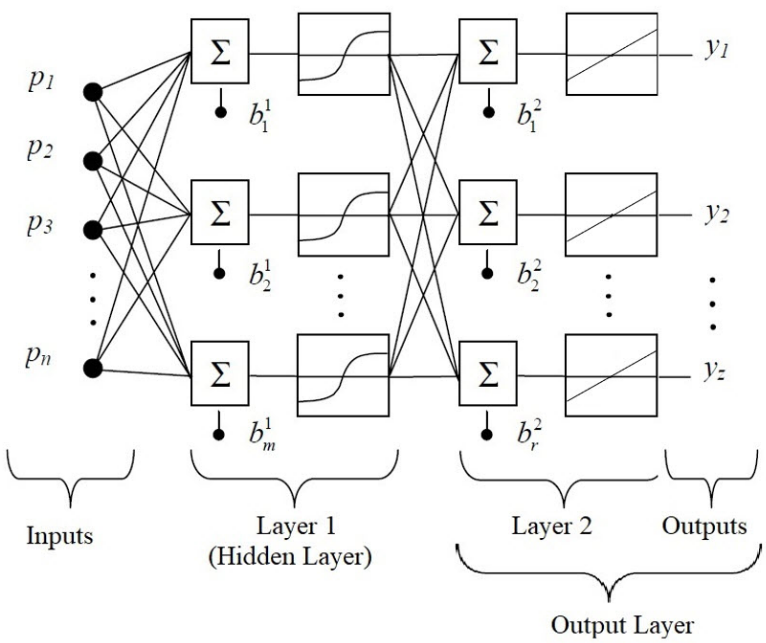

Figure 8.10: Diagram of a two-layer fully-interconnected feed forward ANN

summation of weighted inputs.

$$y = f\left(w_1 p_1 + w_2 p_2 + w_3 p_3 + ... + w_n p_n + b\right) \tag{8.1}$$

Equation 8.1 is expressed in matrix form as shown in equation 8.2. Where W and P are expressed as shown in equation 8.3 and 8.4, respectively.

$$y = f\left(WP + b\right) \tag{8.2}$$

$$W = \begin{bmatrix} w_1 & w_2 & w_3 & ... & w_n \end{bmatrix} \tag{8.3}$$

$$P = [p_1 \quad p_2 \quad p_3 \quad ... \quad p_n]^T \tag{8.4}$$

In a general form for an ANN with k number of layers the desired output is written as shown in equation 8.5 [148].

$$\begin{aligned} Y^k = f^k \big(W^k f^{k-1} \big(W^{k-1} f^{k-2} \big(W^{k-2} f^{k-3} \big(W^{k-3}(...) \\ +B^{k-3}\big) + B^{k-2}\big) + k^{k-1}\big) + B^k\big) \end{aligned} \tag{8.5}$$

Where the matrix Y^K, B^k, and W^k are defined in equations 8.6, 8.7, and 8.8, respectively.

$$Y^k = \begin{bmatrix} y_1^k & y_2^k & y_3^k & ... & y_z^k \end{bmatrix}^T \tag{8.6}$$

$$B^k = \begin{bmatrix} b_1^k & b_2^k & b_3^k ... & b_z^k \end{bmatrix}^T \tag{8.7}$$

$$W^k = \begin{bmatrix} w_{1,1}^k & w_{1,2}^k & w_{1,3}^k & ... & w_{1,n}^k \\ w_{2,1}^k & w_{2,2}^k & w_{2,3}^k & ... & w_{2,n}^k \\ w_{3,1}^k & w_{3,2}^k & w_{3,3}^k & ... & w_{3,n}^k \\ w_{m,1}^k & w_{m,2}^k & w_{m,3}^k & ... & w_{m,n}^k \end{bmatrix} \tag{8.8}$$

The ANN was done in Matlab using the “Neural Net Fitting” tool, the number of layers was chosen to be two, with tan-sigmoid activation function in the hidden layer and linear neurons at the output layer which is a commonly used function approximation [149]. The number of neurons in each layer was set to 10. In addition, the validation and test data consists of 75% training, 15% validating, and 15% testing. Generally, the equation that describes the input-output mapping for an ANN with tan-sigmoid neurons derived from equation 8.2 in the hidden layer and linear neurons in the output are shown in equation 8.9. Where Y is the output vector which is, in this case, the RRC [1x1], X is the input vector which is in this case [6x1], W^2 is the first layer weight matrix with size [10x6], W^1 is the second layer weight matrix with size [1x10], B^1 and B^2 are the first and second layer bias vector. It should be noted that since 10 neurons were deployed during the definition process the vector B^1 has the size [10x1] and the vector B^2 is [1x1].

$$Y = W^2 \left(tansig \left(W^1 X + B^1\right)\right) + B^2 \tag{8.9}$$

The input vector X is defined as shown in equation 8.10, where L is the applied vertical load in kN, P is the tire inflation pressure in kPa, V is the tire speed in m/s, C is the terrain cohesion in kPa, ϕ is the terrain angle of shear resistance in degree and D is the terrain depth in m.

$$X^T = \begin{bmatrix} L & P & V & C & \phi & D \end{bmatrix} \tag{8.10}$$

After collecting all the RRC data produced in this research an input of [6x147] and an output of [1x147] were implemented in Matlab. Consequently, an ANN training was performed and the bias vector and weight matrix were determined. Details of the derivation are given in appendix B.

$$
\begin{aligned}
RRC \quad = & \quad \frac{2.1}{exp(2L - 2.9D - 6.3C + 0.041P + 2.4V - 4.4\phi - 3) + 1} \\
- & \quad \frac{0.63}{exp(4.1D - 3.3C + 0.066L + 0.17P + 2.1V + 0.095\phi + 0.72) + 1} \\
- & \quad \frac{2.9}{exp(0.063C + 1.1D + 1.2L - 0.036P - 2.1V + 0.023\phi + 0.93) + 1} \\
+ & \quad \frac{2.4}{exp(1.4C - 3.7D - 1.6L - 0.14P - 4.1V + 2\phi + 2.9) + 1} \\
- & \quad \frac{0.39}{exp(1.5C + 3.7D - 0.39L + 1.2P + 2.2V + 2.3\phi - 1.5) + 1} \\
+ & \quad \frac{1.1}{exp(0.4D - 3.4C + 1.4L + 0.086P + 1.4V + 0.65\phi - 4.1) + 1} \\
+ & \quad \frac{5.2}{exp(0.059P - 1.3D - 0.23L - 3.1C - 1.4V - 4.4phi + 0.21) + 1} \\
+ & \quad \frac{4.1}{exp(3C + 2.3D - 0.12L + 0.047P + 0.021V - 7.9\phi - 6) + 1} \\
+ & \quad \frac{7.7}{exp(2.8C + 3.1D + 0.16L - 5.7e^{-3}P + 3.6V + 7\phi - 0.95) + 1} \\
- & \quad \frac{1.9}{exp(0.047P - 0.96D - 1.7L - 1.3C + 3.7V - 0.86\phi - 1.3) + 1} \\
- & \quad 10.7
\end{aligned}
\tag{8.11}
$$

Equation 8.11 presents the final relationship between the RRC and the operating conditions, the equation can not be simplified anymore and this is the final form that is used to determine the rolling resistance coefficient at different operating conditions.

Figure 8.11 shows the variation of the observed rolling resistance coefficient as a function of the predicted. The Mean Square Error (MSE) was computed to be $5e^{-5}$ and the R-Square goodness of fit is 0.9974. It is clearly observed that the observed and predicted rolling resistance coefficients fall within the same values and are very close to each other over the whole range. The observed and predicted rolling resistance coefficients are in the range of the line with equation $y = x$ which shows the perfect fitting between both values. It is concluded that the ANN equation successfully predicts the rolling resistance coefficient for the range of the 6 inputs (inflation pressure, vertical load, terrain cohesion, terrain shear resistance, terrain depth, and tire speed).

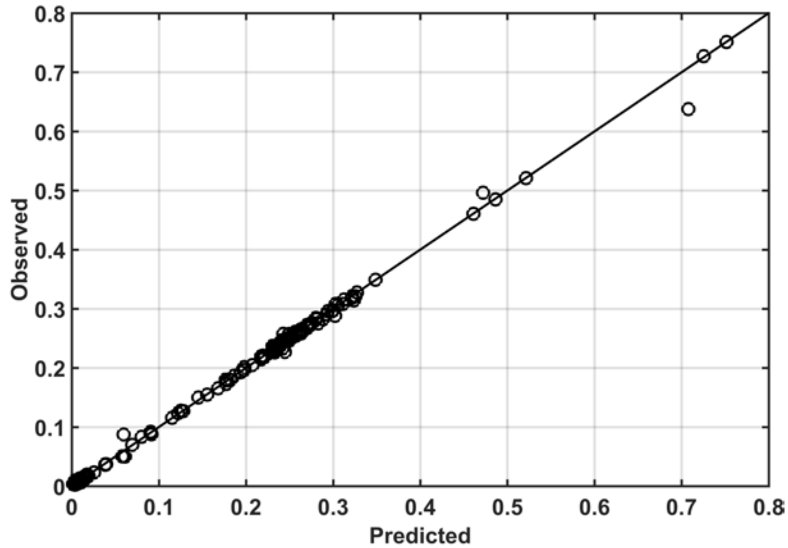

Figure 8.11: Observed rolling resistance coefficient as a function of the predicted one for an R-square fitness

8.5.2 Generic Algorithm

The GA was first introduced by John Holland [150] in the 1970s to make computers do what nature does. Holland was concerned with algorithms that manipulate strings of binary digits. The "chromosome" used in the GA is an artificial one that consists of a number of "genes" and each gene is represented by 0 or 1. It was noticed that nature has the ability to learn and adapt without being told to do that, in other words, nature finds and selects good chromosomes. The GA algorithm was based to duplicate the natural ability, it employees two mechanisms to solve problems, encoding, and evaluation. The GA relies on reproduction, crossover, selection, and mutation which are duplicated by mathematical models. A measure of fitness is used for each individual chromosome to carry out reproduction. While the reproduction takes place, the crossover operator exchanges parts of two single chromosomes and then the mutation operator changes the gene value in some randomly chosen location of the chromosome.

A basic GA has 10 simple steps, first start by representing the problem variable domain as a chromosome of a fixed length and choose the size of the chromosome population, N. Second, define a fitness function to measure the fitness of an individual chromosome. Third, randomly generate an initial population of chromosomes of size N, x_N. Fourth, calculate or compute the fitness of each individual chromosome, $f(x_N)$. Fifth, select a pair of chromosomes for mating from the current population, the selection is based on a probability related to the fitness. Sixth, create a pair of offspring chromosomes by applying the crossover and mutation. Seventh, place the created offspring chromosomes in the new population. Eight, repeat the fifth step until the size of the new chromosome population becomes equal to the size of the initial population, N. Ninth, replace the initial chromosome population with the new offspring one. Finally, repeat all steps from step four until the termination criterion is satisfied.

The fitness functions are known in the optimization process ever since 1992 [151]. The optimization problem is generally defined by equation 8.12, where ϕ_i^t is the penalty function at the i-th string in the t-th generation, X_i^t is the vector of the design variable and N as mentioned before is the population size.

$$\phi_i^t = f\left({X_i}^t\right) + \sum_{j=1}^{m} \beta_j max\left(0, g_i\left({X_i}^t\right)\right) \quad (i = 1...N) \tag{8.12}$$

Using the same inputs and outputs mentioned in section 8.5.1, an equation relating the input parameters to the RRC is generated using GA software called Eureqa. Equation 8.13 describes the output equation, where k_1, k_2, k_3 and k_4 are constant equal to 0.0876, 0.167, 1.08e-5 and 0.001, respectively.

$$RRC = k_1 V * D + k_2 D^2 + k_3 L * P * D^2 + k_4 \frac{L}{\phi - 12.4} + \frac{\phi D}{L * C^2} \tag{8.13}$$

The R-square goodness of fit for the above equation is computed to be 0.94 with an MSE of 0.0012, a maximum error of 0.07, and a mean average error of 0.027. Figure 8.12 shows the observed rolling resistance coefficient as a function of the predicted one.

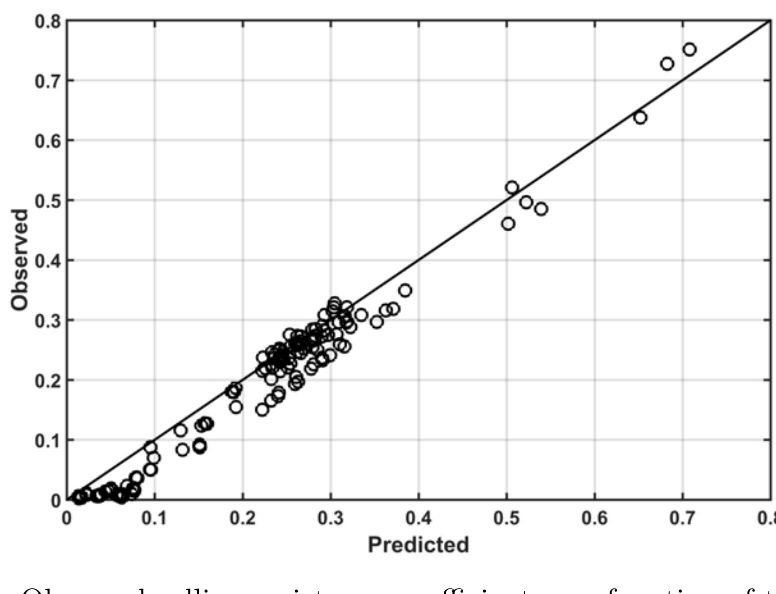

Figure 8.12: Observed rolling resistance coefficient as a function of the predicted one for an R-square fitness

It is noticed that the observed and predicted rolling resistance coefficients fall within a similar range and clearly lies in the range of the straight line with equation $y = x$. However, for a low RRC value, less than 0.1 the results are slightly scattered.

In comparison between figure 8.11 and 8.12 it is concluded that the fitting of the observed versus the predicted rolling resistance coefficient of the ANN is better than that of the GA. However, on the other side, the complexity of the ANN equation mentioned in equation 8.11 is way higher than that of the GA equation mentioned in equation 8.13. Thus a compromise between the complexity of the equation and the fitness should be made depending on the application purpose.

8.6 Summary

The tire-soil interaction for the RHD tire running over different terrains was performed. The terrain models used included dry sand, dense sand, and clayey soil. The terrain was modeled and calibrated using the Smoothed-Particle Hydrodynamics technique, and the results were presented in chapter 4. The analysis focused on determining the rolling resistance coefficient at different operating conditions including tire inflation pressure and vertical loads for various soils. The predicted tire rolling resistance coefficient over dry sand was verified against physical measurements, the results showed a good trend agreement between simulation and measurements.

It was concluded that the rolling resistance coefficient is strongly dependent on the applied vertical load. The rolling resistance coefficient of the truck tire running over dry sand adhere to a logarithmic relation with respect to the vertical load, while it adheres to a linear relation when running over dense sand.

On the other side, the tire inflation pressure has less effect on the rolling resistance coefficient at low vertical loads, but the stronger effect at high vertical loads. For instance, for a truck tire running over clayey soil an increase in inflation pressure of 200% increases the rolling resistance coefficient by 7% for a vertical load of 40 kN (9000 lbs). It is noted that the highest effect of inflation pressure was observed in dense sand for all vertical loads.

In comparison to the truck tire running over different terrains. It was concluded that the truck tire has the highest rolling resistance coefficient over the clayey soil. The behavior of the truck tire over dry sand was similar to that over the dense sand, as they both adhered to similar mechanical properties.

The rolling resistance coefficient data collected from chapter 6, 7 and 8 was used to built a relationship between the rolling resistance coefficient and the operating conditions. The operating conditions included different terrains (dry sand, dense sand, clayey soil, water, snow, sandy loam with moisture, moist sand) presented by cohesion, angle of shear resistance and depth. Additionally, the tire parameters included inflation pressure, vertical load, and speed. Two relationships were built using the Artificial Neural Network and the Genetic Algorithm. The derivation of the Artificial Neural Network was presented in appendix B. The mean standard error of the Artificial Neural Network and Genetic Algorithm was computed to be $5e^{-5}$ and 0.0012, respectively. While the R-square goodness of fit was 0.9974 for the Artificial Neural Network and 0.94 for the Genetic Algorithm. It was concluded that the Artificial Neural Network has a better fitting in regards to the observed versus predicted rolling resistance coefficient data, while the Genetic Algorithm has a better numerical equation in terms of complexity.

CHAPTER 9

HYDROPLANING ANALYSIS

This chapter focuses on building an FEA-SPH model to investigate the hydroplaning phenomenon. Tire-water interaction is modeled and implemented using a node-symmetric node-to-segment contact with edge treatment. The effect of inflation pressure, vertical load, and water depth are investigated. Later, the predicted hydroplaning speed is validated against NASA and Horne's equation. Finally, an empirical equation based on the predicted hydroplaning speed and operating conditions are developed.

The simulation model shown in figure 9.1 consists of a rigid road with sideways, RHD tire, and water. The water is constrained inside the rigid road. The water is in contact with the road and the tire, which is in contact with the water and the road. The tire is constrained in the translational lateral direction and free to translate in the vertical and longitudinal directions. Additionally, the tire is constrained in rotation about the longitudinal and vertical directions and free to rotate about the lateral axes.

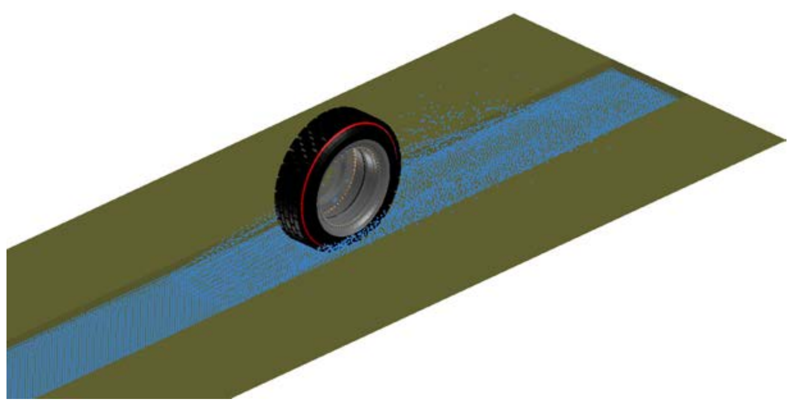

Figure 9.1: Hydroplaning simulation setup using Pam-Crash Model

In this simulation the tire is inflated and then loaded on the ground. Later, longitudinal speed is applied to the center of the tire, the speed is increased gradually from 0 to 200 km/h in a 2 seconds. The tire acceleration is kept constant at 400,000 km/h^2. The contact force in z-direction between the tire and ground is computed and presented as a function of tire speed. Once the contact force reaches zero, the speed is considered as the hydroplaning speed. This simulation test is repeated for various operating conditions including inflation pressure (379 kPa (55 psi); 586 kPa (85 psi) and 758 kPa (110 psi)), vertical load (3 kN (3000 lbs); 27 kN (6000 lbs) and 40 kN (9000 lbs)) and water depth (50 mm; 65 mm and 100 mm).

Figure 9.2 presents a sample of the simulation results at 586 kPa (85 psi) inflation pressure, 13 kN (3000 lbs) load, and a water depth of 50 mm. This figure shows the variation of the contact force in the z-direction as a function of the tire's speed running. The hydroplaning speed of the tire operating under these conditions is found to be 105 km/h.

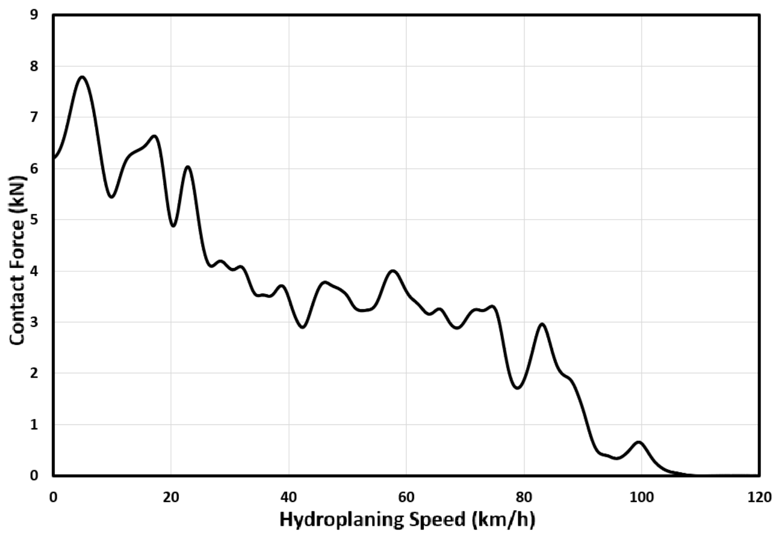

Figure 9.2: Contact force as a function of tire speed at 586 kPa (85 psi) inflation pressure, 13 kN (3000 lbs) load, and a water depth of 50 mm

Figure 9.3 shows the tire-water interaction model at various speeds and at 586 kPa (85 psi) inflation pressure, 13 kN (3000 lbs) load, and a water depth of 50 mm. The tire-water interaction is taken using a bottom view and a pressure distribution contour to visualize the contact pressure. It is clear that at 20 km/h speed the contact area between the tire and ground is highest, in the case of 60 km/h the contact area is still visible as well. While for the case of 105 km/h the contact patch is mostly blue which refers to a minimal pressure.

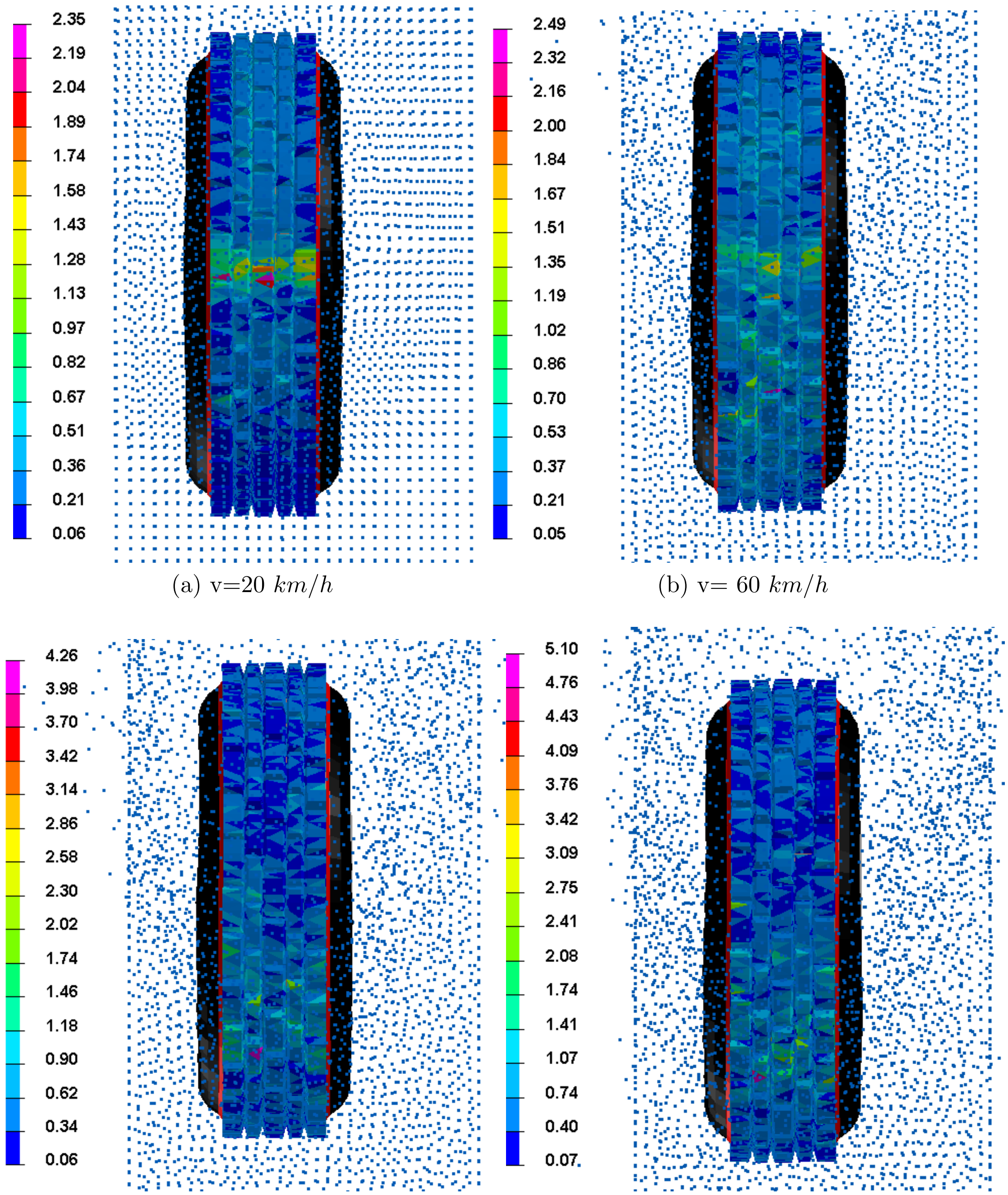

(a) v=20 km/h

(b) v= 60 km/h

(c) v= 80 km/h

(d) v= 105 km/h

Figure 9.3: Truck tire at various speeds at 586 kPa (85 psi) inflation pressure, 13 kN (3000 lbs) load, and a water depth of 50 mm

9.1 Effect of Vertical Load

This section investigates the effect of vertical load on the hydroplaning speed. The simulation test is repeated at different vertical loads of 13 kN (3000 lbs), 27 kN (6000 lbs) and 40 kN (9000 lbs). The variation of the hydroplaning speed as a function of load is shown in figure 9.4 at 100 mm water depth and several inflation pressures. It is observed that the hydroplaning speed increases as the vertical load increases.

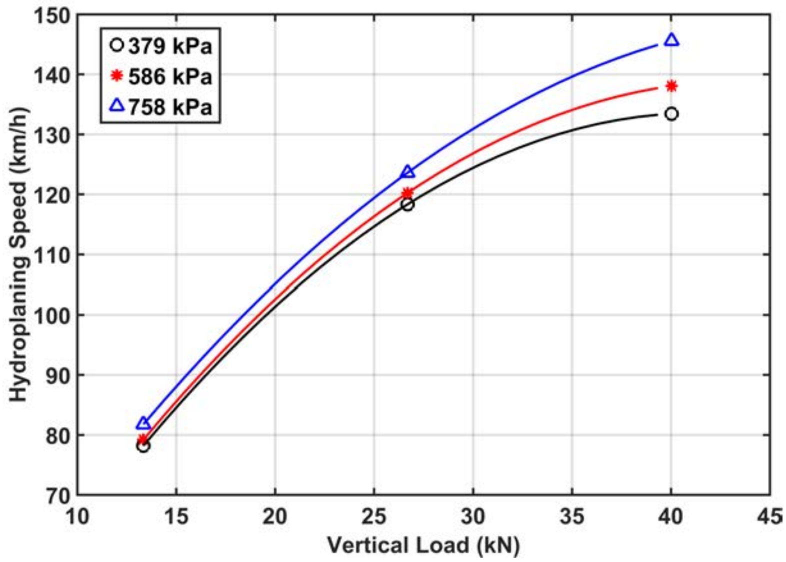

Figure 9.4: Hydroplaning speed as a function of vertical load at 100 mm water depth and several inflation pressures

The increase in vertical load causes the contact area of the tire to produce more pressure, which is a result of higher contact force per unit area. The contact force growth results in greater stability control, and thus a delay to the hydroplaning phenomenon. An increase of 27 kN (6000 lbs) vertical load or in other words tripling the vertical load from 13 kN (3000 lbs) to 40 kN (9000 lbs) causes the hydroplaning speed to double up from 62 km/h to 129 km/h at given inflation pressure of 379 kPa (55 psi) and a static water depth of 100 mm. Thus, the vertical loading has a significant effect on the hydroplaning speed. The tire loading acts as a stabilizer against hydroplaning.

9.2 Effect of Tire Inflation Pressure

This section investigates the effect of tire inflation pressure on the hydroplaning speed. In 2008, Oh [107] concluded that inflation pressure is a key factor affecting the hydroplaning speed. however, later in 2010, Chang [152] reported that the inflation pressure does not have a significant effect when it comes to truck tires. None the less, the increase in inflation pressure causes the hydroplaning speed to increase infinitesimally. A high inflation pressure although leads to a less contact area, however the contact force per unit area increases. The increase in contact force per unit area will require more hydrodynamic pressure from the water to lift the tire which leads to a higher hydroplaning speed.

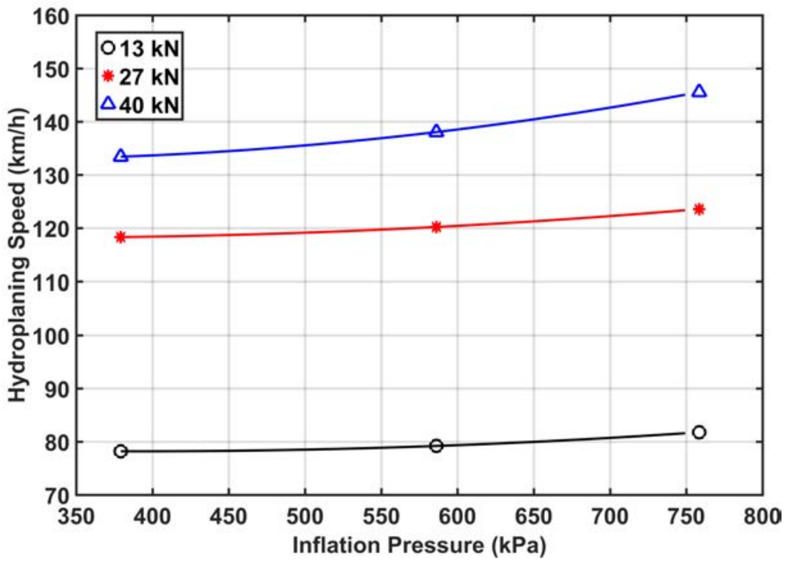

Figure 9.5: Hydroplaning speed as a function of inflation pressure at100 mm water depth and several vertical loads

Figure 9.5 shows the variation of the hydroplaning speed as a function of the tire inflation pressure at a water depth of 100 mm and several vertical loads. It is observed that the hydroplaning speed increases as the inflation pressure increases. An increase of 300% in the inflation pressure from 379 kPa (55 psi) to 758 kPa (110 psi) at a rated vertical load of 27 kN (6000 lbs) and 100 mm static water depth causes the hydroplaning speed to increase by 2%, which is considered significantly minimal.

9.3 Effect of Water Depth

Water depth has a major effect on the hydroplaning speed. This section investigates the effect of water depth on the hydroplaning speed. The tire treads are covered faster when the water is deeper on the ground. It is a well-known fact that in order for a tire to hydroplane the grooves should be filled with water. The tire treads supply stability and control during wet driving conditions, thus the filling of tire treads with water decrease the allocated stability resulting in accelerated hydroplaning. Equations relating the hydroplaning speed to the water depth exists only for car tires, and no previous attempt to numerically evaluate the effect of water depth on truck tire hydroplaning was done. The water depth selected in this study is based on literature and the tread depth of the tire used. The water depth examined are 50 mm, 65 mm and 100 mm. Figure 9.6 shows the variation of the hydroplaning speed as a function of water depth at a nominal inflation pressure of 586 kPa (85 psi) and various vertical loads.

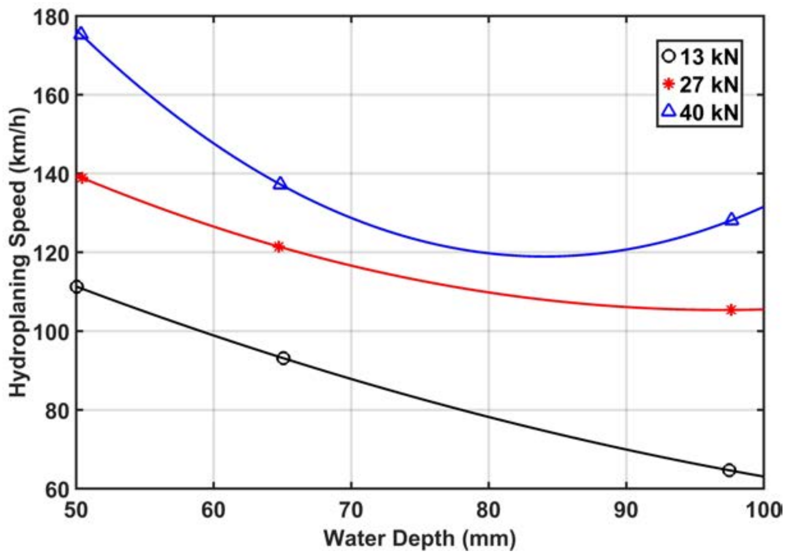

Figure 9.6: Hydroplaning speed as a function of water depth at 586 kPa (85 psi) inflation pressure and several vertical loads

It is observed that the increase in the water depth results in the decrease of the hydroplaning speed at all vertical loads. In other words, driving in deeper water accelerates the tire hydroplaning. For instance, if the truck is driving over a 100 mm static water depth, an inflation pressure of 586 kPa (85 psi) and a vertical load of 13 kN (3000 lbs) the hydroplaning may happen at a speed as low as 65 km/h. Additionally, if the water depth is doubled on the ground the hydroplaning speed may reduce by 25%. Furthermore, at higher vertical loads the effect of water depth becomes less in comparison to that of lower vertical loads.

The summary of the hydroplaning speed at different operating conditions is presented in table 9.1.The table shows that at low water depth such as 20 mm the hydroplaning speed ranges between 160 and 280 km/h depending on the inflation pressure and vertical load. This speed is very high and thus hydroplaning does not happen at low water depth. It should be noted that the tread of the RHD tire is 27 mm in depth and in order to hydroplane the tread should fill with water.

Table 9.1: Summary of hydroplaning speeds at different operating conditions

Hydroplaning Speed (km/h)	Water Depth (mm)	Inflation Pressure (kPa)	Vertical Load (kN)
162	20	379	13
217			27
260			40
168		586	13
209			27
264			40
175		758	13
220			27
275			40
108	50	379	13
145			27
173			40
112		586	13
139			27
176			40
116		758	13
146			27
183			40
90	65	379	13
115			27
134			40
94		586	13
122			27
137			40
95		758	13
123			27
139			40
62	100	379	13
105			27
130			40
66		586	13
106			27
129			40
74		758	13
107			27
136			40

9.4 Validation

NASA hydroplaning equation was previously described in equation 2.20 and it is solely a function of the tire inflation pressure. However, several studies indicated that other operating conditions such as vertical load, tread depth and water depth also have a significant effect on the hydroplaning speed [112]. Furthermore, Horne's equation was also previously described in equation 2.21 is designed for truck tires, and is a function of the inflation pressure and footprint aspect ratio which gives the equation little more complexity in comparison to that of NASA equation.

Figure 9.7 shows a comparison between the simulated results at rated inflation pressure of 586 kPa (85 psi) and vertical load of 27kN (6000 lbs), NASA equation, and Horne's equation. The difference between NASA equation and Horne's equation is considered significant and this is due to the fact that NASA equation was design for aircraft and passenger car tires and is only dependent on inflation pressure. However, it is observed that the simulation results, NASA and Horne's equations have the same trend, as the inflation pressure increases the hydroplaning speed increases as well. It is noted that Horne's equation is compared with the simulation results as Horne's equation was designed for truck tire purpose as well. The simulation results fall in the range of speed as that of Horne's equation, especially at high inflation pressure were the difference between the predicted simulation results and Horne's equation is around 3%.

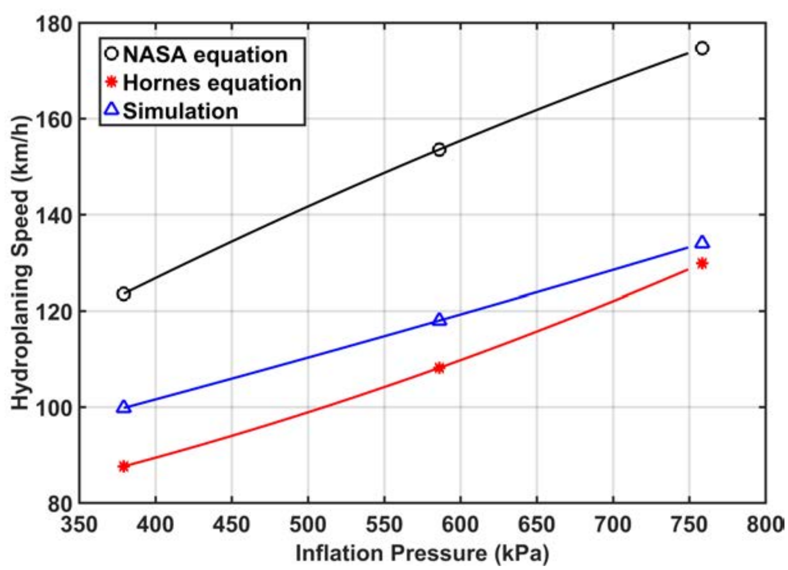

Figure 9.7: Hydroplaning speed as a function of inflation pressure for simulation and different equations

Horne's equations account for the footprint aspect ratio and inflation pressure. Further other operating conditions such as the tire vertical load and water depth are also important and can have a significant effect on the hydroplaning speed as shown in the previous section.

9.5 Hydroplaning Equation Development

A database was developed from the predicted hydroplaning speed using two different types of tires, namely the RHD tire and the widebase tire at different operating conditions. The operating conditions include, the inflation pressure, P, vertical load, L, water depth, t_w, and tread depth, t_d. The database was then used to develop an empirical equation that relates the hydroplaning speed to the above-mentioned conditions.

9.5.1 Data processing platform

In order to generate the hydroplaning equation, a modeling engine called Eureqa [153] was used. Eureqa automates a heavy lifting inherent in analytics and data science. The R^2 goodness fitting was chosen to develop the fitness function. The R^2 goodness is based on linear regression, which calculates an equation based on minimizing the distance between the fitted line and the data points. R^2 goodness measures how close the data are to the fitted regression line as shown in equation 9.1.

$$R^2 = \frac{E}{T} \tag{9.1}$$

Where E is the explained variation and T is the total variation. For example, a value of 0 indicates that the model demonstrates none of the variability of the response data around its means, while a value of 1 indicates that the model demonstrates all the variability of the response data around the mean. Thus, generally the higher the R^2 goodness the better.

The Mean Absolute Error (MAE) is used to minimize the mean of the absolute value of residual errors and is defined in equation 9.2, n is the number of data points, y is the hydroplaning speed input and $f(x)$ is the hydroplaning speed predicted by the equation.

$$MAE = \frac{1}{n}\sum_{i=1}^{n} \mid y - f(x) \mid \tag{9.2}$$

The Mean Squared Error (MSE) is used to minimize the mean of the squared residual errors and is defined in equation 9.3.

$$MSE = \frac{1}{n}\sum_{i=1}^{n} (y - f(x))^2 \tag{9.3}$$

Additionally, the Correlation Coefficient is implemented to normalized covariance and is defined in equation 9.4. The maximum error is an indication of the highest error of the residuals and it is used to minimize the worst case error

$$CC = \frac{1}{n-1}\sum_{i=1}^{n}\left(\frac{f(x_i) - f(\bar{x})}{s_{f(x)}}\right)\left(\frac{y_i - \bar{y}}{s_y}\right) \tag{9.4}$$

9.5.2 Hydroplaning speed equation

Equation 9.5 presents the hydroplaning speed equation as a function of the tire inflation pressure in kPa, vertical load in kN, tread depth in mm, and water depth in mm, k_s are empirical coefficients. The empirical coefficients k_1, k_2, k_3, k_4, k_5, and k_6 are typically 3.3, 9.11, 0.0167, 0.00125, 0.0623 and 0.203, respectively.

$$V = k_1 t_d + k_2 L + k_3 P + {t_w}^2\left(k_4 L - k_5 L^{-1}\right) - k_6 L t_w \tag{9.5}$$

The R^2 goodness of fitness is determined to be 0.9937 which is considered significantly acceptable. The Correlation Coefficient, CC is determined to be 0.9968, while the maximum error is 4.402, the Mean Squared Error, MSE is equal to 5.6 and the Mean Absolute Error, MAE is 1.895, and the complexity is computed to be 32.

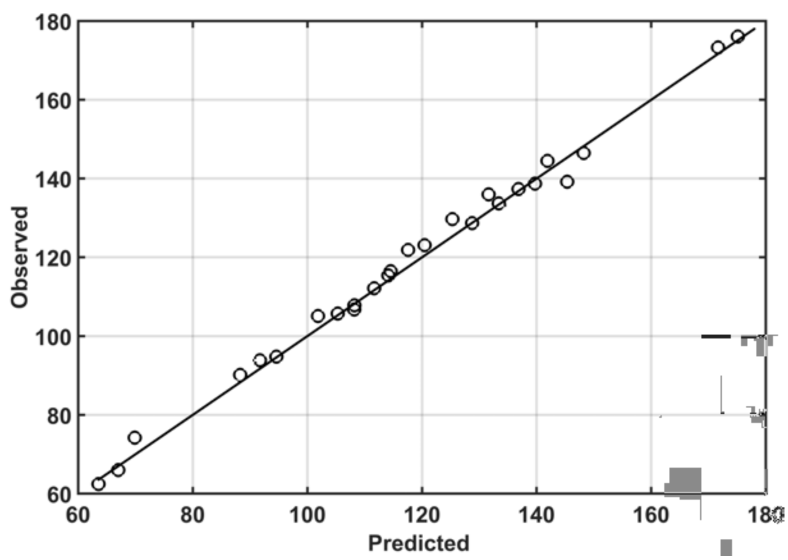

Figure 9.8: Observed versus predicted values of the hydroplaning speed

Figures 9.8 shows the variation of the observed hydroplaning speed from the simulation as a function of the predicted hydroplaning speed from equation 9.5. It is seen that the results are in good agreement and that the data points are well represented.

In order to validate the developed equation figure 9.9 was used to determine the difference between the equation prediction, the simulation prediction, and Horne's equation. It is noted that the simulation and prediction of the equation are both at the same water depth and operating conditions which are not specified in Horne's equation.

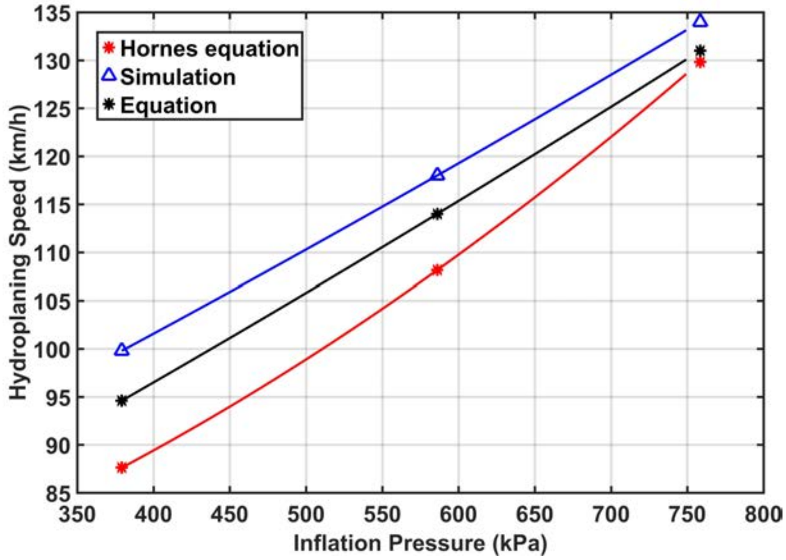

Figure 9.9: Hydroplaning speed versus inflation pressure for the developed equation and Horne's equation

It is concluded that the equation prediction results show a very similar pattern and results as those from Horne's equation for truck tires at the same operating inflation pressures. Thus, the hydroplaning equation developed in this thesis is considered valid.

9.6 Summary

Tire hydroplaning analysis was performed for the RHD tire (size 315/80 R22.5). The hydroplaning test was virtually performed by applying a ramp speed ranging between 0 and 200 km/h to the center of the tire and measuring the contact forces with the ground. The hydroplaning speed was recorded at the time the contact forces reaches zero, which is when the tire loses full contact with the ground. The simulation test procedure was repeated for several operating conditions including inflation pressure, vertical load, and water depth.

The results obtained from simulations were validated against several equations including NASA and Horne's equations. In addition, analysis of the effect of inflation pressure, vertical load, water depth and tread depth on the critical hydroplaning speed was performed. It was concluded that the inflation pressure does not have a significant impact on the hydroplaning speed, however, as the inflation pressure increases the hydroplaning speed increases, which is due to the decrease in the contact area. Furthermore, the load variation effect was also studied, and it was concluded that the hydroplaning speed increases as the vertical load increases at given inflation pressure and static water depth. The water depth effect on hydroplaning speed was also investigated, and it was found that the hydroplaning speed increase as the static water depth decrease at given vertical load and inflation pressure. Thus, a higher risk of hydroplaning exists at deeper water.

The predicted hydroplaning speeds were then used to create an observation data set to develop an empirical equation that relates the hydroplaning speed to the inflation pressure, vertical load, water depth, and tread depth. The equation was developed using R^2 goodness of fit and was then validated against Horne's equation for truck tires. The developed equation has a R^2 goodness of fitness of 0.9937, a Correlation Coefficient of 0.9968, a maximum error of 4.402, a Mean Standard Error of 5.6 and a Mean Average Error of 1.895.

CHAPTER 10

MODELING OF MULTIPLE-TIRE AND GRAVELLY SOIL INTERACTION

This chapter presents a novel modeling technique to compute the interaction between an 8x4 off-road truck and gravelly (sand mixed with gravel) soil. The model setup consists of four tires (RHD tires) presenting the four axles of the truck, the tires on the first axle are steering and free-rolling, the tires on the second and third axles are driven, and the tires on the fourth are free rolling. The truck tires-gravel interaction is computed and validated against physical measurements performed in Göteborg, Sweden. The gravelly soil is modeled using Smoothed-Particle Hydrodynamics (SPH) technique and calibrated against physical measurements using pressure-sinkage and direct shear-strength tests. The tire-gravelly soil interaction is captured using the node symmetric node to segment with edge treatment algorithm deployed for interaction between FEA and SPH elements. The effect of gravelly soil compaction and truck loading on the multi-tires interaction performance are investigated and discussed.

10.1 Gravelly Soil Modeling and Calibration

The material properties of the gravelly soil used in this analysis are characterized and identified by the civil engineering department in Stockholm,Sweden [6]. It was reported that the gravelly soil has a mass density range of 1.9-2.25 ton/m^3 with a typical value of 2.07 ton/m^3, and modulus of elasticity range of 96-192 N/mm^2. The material properties used to model the gravelly soil are shown in table 10.1.

Table 10.1: Material properties of gravelly soil [6]

Material Type	E MPa	K MPa	G MPa	σ MPa	ρ ton/mm^3
gravelly soil	121	80	48	0.048	1.92E-9

Figure 10.1 shows a sample of the gravelly soil used during field testing. The gravelly soil terramechanical characteristics including the angle of shearing resistance and cohesion are also obtained from the civil engineering department in Stockholm [6] and are used to calibrate the SPH gravelly soil model.

Figure 10.1: Sample of the sand with gravel using during testing

The calibration procedure is similar to that performed in chapter 4 and 5; two main tests are performed, namely the pressure-sinkage and the shear-strength. The simulation results are calibrated against the physical measurements.

The pressure-sinkage results obtained from simulations and measurements at different applied pressure are presented in figure 10.2a. The simulation results are considered in good agreement with those obtained from measurements. Both curves exhibits similar trend, at 200 kPa applied load the simulated gravelly soil has a sinkage of 26 mm, while the measurement has 24.3 mm with an error of 6%. It should be noted that gravelly soil is considered a hard soil as it sinks less than dry and dense sand.

The variation of the shear-strength as a function of the applied pressure for results obtained from simulation and measurement is shown in figure 10.2b. The results obtained from simulations are considered in good agreement with those from measurements. Both curves exhibit a similar trend and are almost parallel to each other. As the applied pressure increases the shear-strength increases in an approximately linear trend.

The angle of shearing resistance is calculated from the reverse tangent of the slope of the shear-strength and pressure line; the measured angle of shearing resistance is 39°, while the simulated angle is 34.3°. Thus, the estimated error in the angle of shearing resistance is approximately 8% which is in the acceptable error margin.

Furthermore, the soil cohesion is computed from the intersection of the shear-strength line with the y-axis, meaning at zero applied pressure. The measured cohesion is around 2 kPa, while the simulated on is 2.3 kPa, which is also in the

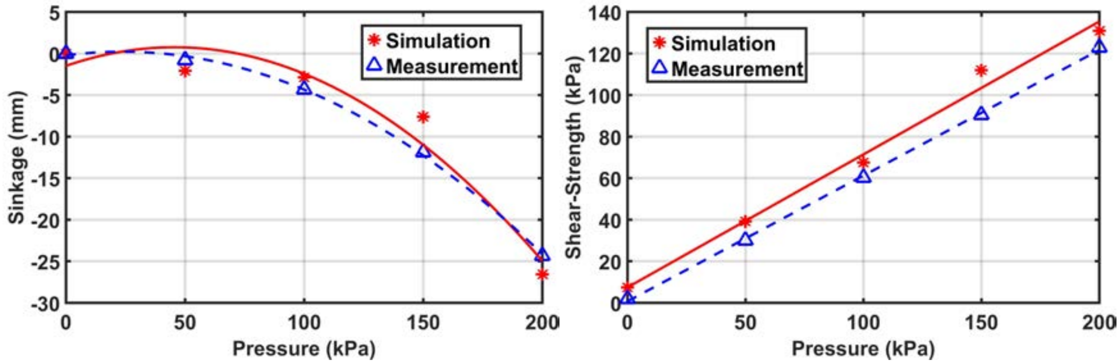

(a) Plate sinkage as a function of pressure (b) Shear-strength as a function of pressure

Figure 10.2: Simulation and measurement results for calibration tests

acceptable error margin. Thus, both pressure-sinkage and shear-strength results obtained from simulated gravelly soil are considered to be in good agreement with the results obtained from measurements.

10.2 Tire-Gravelly Soil Interaction

Figure 10.3a shows the simulation setup of the tire-gravelly soil interaction model. The model consists of a hard surface where the tires are set onto, and a soil box which contains gravelly soil particles. This model is considered to be a bicycle model that has four tires set at a distance similar to that of the four axles of the tested truck. Each of these tires is subjected to a vertical load equivalent to half of the axle load. The first and fourth tires are free rolling non-driven tires, and the second and third tires are driven and are representing the first-second drive axles. The distance between the four tires is similar to the distance between truck axles as shown in figure 10.3b.

Each tire is constraint from translational movement in the lateral direction and from rotational movement along the longitudinal and vertical axis. The tires are first inflated to a rated inflation pressure of 896 kPa (130 psi). Then, the desired vertical load is applied to the center of each tire. The vertical load on each tire is determined based on the actual axles load of the test truck. The tires are then allowed to settle on the hard surface, afterward, the required motion type is applied to the center of each tire; given longitudinal velocity is applied to the center of tire-1 and tire-4; while a constant angular velocity is applied to the center of tire-2 and tire-3. The tires are then allowed to move on top of the hard surface and reaching the gravelly soil box. The simulation continues until all four tires reach steady-state motion on top of the gravelly soil.

The model setup requires 9 different contacts, a contact of each tire with the

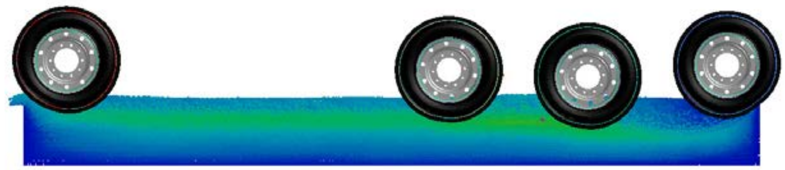

(a) Truck tires model setup over sand with gravel soil

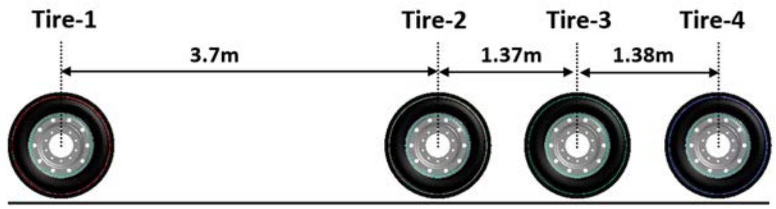

(b) Schematic of the multi-tire locations

Figure 10.3: Truck tires model setup running over gravelly soil with normal displacement contour

ground, a contact of each tire with the gravelly soil, and contact between the gravelly soil and the box holding it. Each contact has a defined thickness and friction coefficient. The forces and moments in all directions, in addition to the longitudinal and angular velocities and vertical displacement, are computed for all four tires. The longitudinal slip percentage, the rolling resistance coefficient, and other performance parameters are computed and validated against physical measurements performed at similar operating conditions. The simulations are repeated for different testing conditions to study the effect of soil compaction and loading on the tire performance.

10.3 Truck-Gravelly Soil Physical Testing

In order to evaluate and validate the results obtained from simulation model, physical testing was carried out at Volvo Groups Truck Technology facility in Göteborg, Sweden. The physical testings were performed and repeated at several operating conditions. The traction performance and soil compaction were analyzed.

The truck used in this testing is a Volvo F-series medium 8x4 tag rigid as shown in figure 10.4a. The lead is mechanical with front suspension and the rear suspension is air. The truck is generally used for very badly maintained roads or off-road less than 5%. The truck can carry up to 44 tonnes of gross combined weight, out of which the front axle carries 8 tonnes and the rear axles carry 27 tonnes. The driving grades are 98% of drive distance with a maximum grade of 16%.

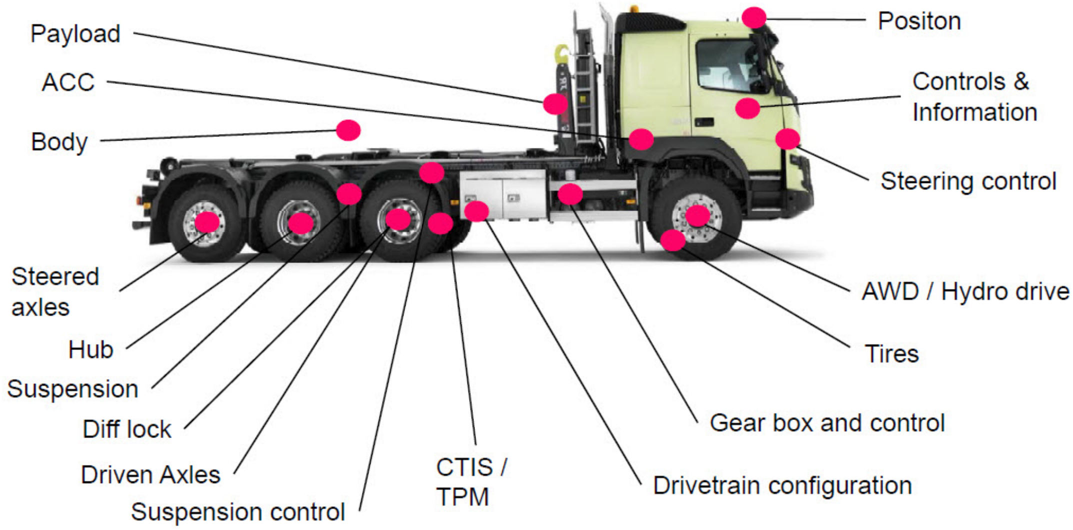

(a) Truck used during testing with part labels

(b) Testing zones available in the site

Figure 10.4: Testing area and truck in Fjärås, Göteborg

Furthermore, figure 10.4b shows the testing area which consists of two zones A1 and A2. Zone A1 has a soft terrain with 110-150 mm depth, while zone A2 is also soft terrain but with 150-250 mm depth. The soft terrain is identified as gravelly soil and the material properties along with the geomechanical properties were provided by [6]. The inclination of both zones ranges between 2-4% and for the purpose of this research is considered minimal.

The traction tests were performed at two different settings; setting one traction control system was off and the truck was loaded; while setting two the traction control system was off and the truck was unloaded. The measurements were performed for reaction and acceleration from terrain and through-axle in addition to the terrain compaction and change of characteristics of the terrain after multiple compactions. It should be noted, however, that due to limitations of sensors and equipment only the driven axles (axles two and three) were equipped with transducers. Both driven axles were equipped with transducers to measure all 6 motions of the tire; longitudinal, lateral and vertical forces; overturning moment, driving torque and selfaligning moment; in addition to the truck forward speed and the angular velocity of each drive tire.

10.4 Results and Discussions

The results obtained from simulations are presented and analyzed. The effect of soil compaction and truck loading on the tire operational performance is presented and discussed. The results obtained from simulations are then validated against physical measurements obtained from testing.

10.4.1 Effect of soil compaction

The effect of soil compaction can be well seen in the rolling resistance coefficient of the two drive axles during a given inflation pressure, load and speed. In order to further investigate the effect of soil compaction on tire rolling resistance figure 10.5a and 10.5b are presented.

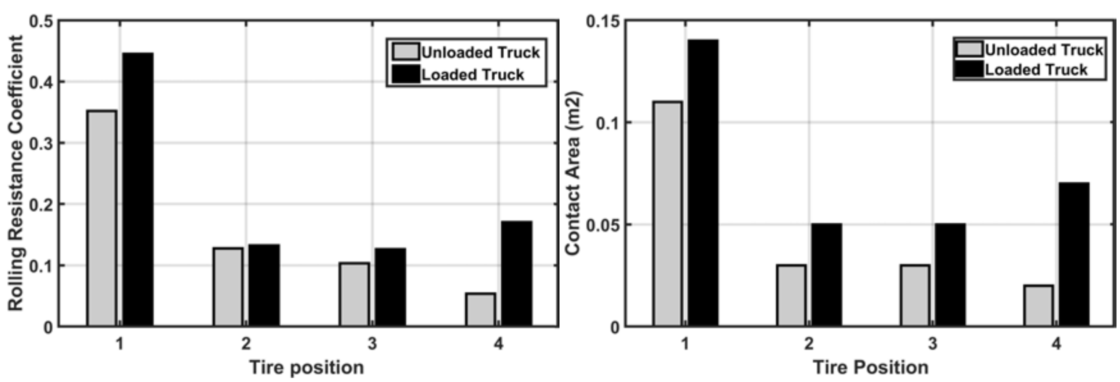

(a) Rolling resistance coefficient

(b) Contact Area

Figure 10.5: Interaction parameters as a function of tire position for unloaded and loaded truck running over gravelly soil

Figure 10.5a shows the variation of the rolling resistance coefficient as a function of the tire position for an unloaded and loaded truck. The effect of soil compaction on the tire rolling resistance is noticed when comparing the first and second drive axles. The second drive axle has a lower rolling resistance coefficient in comparison to that of the first drive axle for both loaded and unloaded truck cases. The difference in the rolling resistance coefficient between the first and second driving axles varies between 8% and 17% for a loaded and unloaded truck, respectively. It is observed that for an unloaded truck the effect of soil compaction is higher than that of a loaded truck, this is due to the fact that at low vertical load the tire sinks less in the soil and thus does not displace the soil particles as much as in the case of a fully loaded.

Figure 10.5b shows the contact area between the tire and the gravelly soil as a function of the tire position for the unloaded and loaded truck. It is observed that tire-1 has the highest contact area leading to the highest rolling resistance coefficient. This is due to the fact that the soil was fresh before the truck run over, also tire-1 has more load than that of the drive tires. Furthermore, the first and second drive tires have similar contact areas leading to a similar rolling resistance coefficient, which further explains the results from figure 10.5a. The fourth tire which is tire-4 has a lower contact area than that of the drive tires due to the hardness of the soil (compaction), thus leading to a lower rolling resistance coefficient.

10.4.2 Effect of truck loading

Figure 10.6 shows the variation of the rolling resistance force as a function of time at different tire position during an unloaded truck running over gravelly soil. In the case of an unloaded truck, tire-1 experiences the highest rolling resistance force as it also experiences the highest loading force. The high rolling resistance

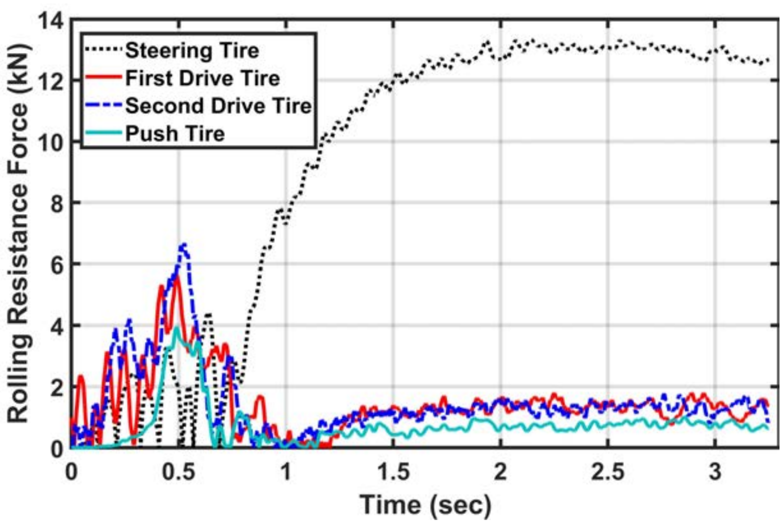

Figure 10.6: Rolling resistance force as a function of time for different tire positions during an unloaded truck running over gravelly soil

force is due to multiple factors including that the soil is fresh and higher sinkage is observed. The two drive tires (tire-2 and tire-3) experience almost a similar rolling resistance force as they have equally distributed load. However, the second drive tire experiences a slightly less rolling resistance force as the soil is further compacted by the first drive tire. In the case of unloaded truck tire-4 experiences less rolling resistance force than all of the other tires due to less loading and repetitive soil compaction.

Furthermore, as the vertical load increases the rolling resistance coefficient increases as well. This is observed when comparing the loaded and unloaded rolling resistance coefficient at the same drive axle. The increase of load on tire causes the tire to sink more in the soil increasing the contact area and thus increasing the rolling resistance.

A further observation is seen when comparing the rolling resistance coefficient of the different tires during a loaded truck running over gravelly soil. For example, tire-1 has a rolling resistance coefficient of 0.44, tire-2 has a coefficient of 0.14, the tire-3 has a coefficient of 0.12 and tire-4 has a coefficient of 0.17. The first tire (tire-1) has the highest rolling resistance coefficient as it is the first tire to resist the soil and to start the process of compaction, however, the steering tire also has the highest vertical load of almost double that of the drive tire. The first and second drive tires have a similar coefficient, however, the first drive has a slightly higher coefficient than the second drive. Finally, the tire-4 has a higher resistance due to the higher loading applied.

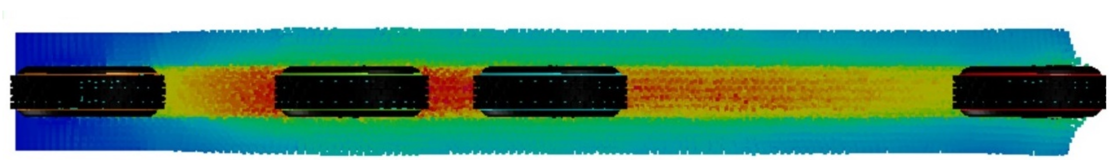

(a) Loaded truck

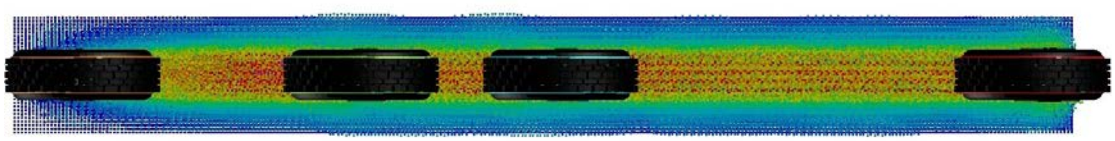

(b) Unloaded truck

Figure 10.7: Normal displacement in gravelly soil for loaded and unloaded truck

Figure 10.7 shows the soil displacement for all four tires when running during a loaded and unloaded truck case. Figure 10.7a shows the displacement in the soil for the case of a loaded truck, it is observed that the maximum displacement in the soil is recorded to be around 475 mm. Furthermore, tire-1 is noticed to further push the soil outside the box domain and the boundaries of the box also show some displacement. Figure 10.7b shows the displacement in the soil for the unloaded truck case, the maximum recorded displacement is around 246 mm which is roughly around 50% of that of the loaded case. It is also observed that tire-1 in the case of unloaded is not pushing the soil outside the box domain as seen in the case of a loaded truck. Furthermore, the boundaries of the box domain show no displacement at all in the case of an unloaded truck, which is opposite to the case of a loaded truck.

10.4.3 Validation of results

Figure 10.8 shows the rolling resistance and vertical forces obtained from simulations and measurements on the first and second drive axles for a loaded truck running at a speed of 2 m/s. A fully loaded truck indicates that the load on the first axle is 45 kN per tire, the load in the first and second drive axle is 20 kN per tire, and the load on the push axle is 35 kN per tire.

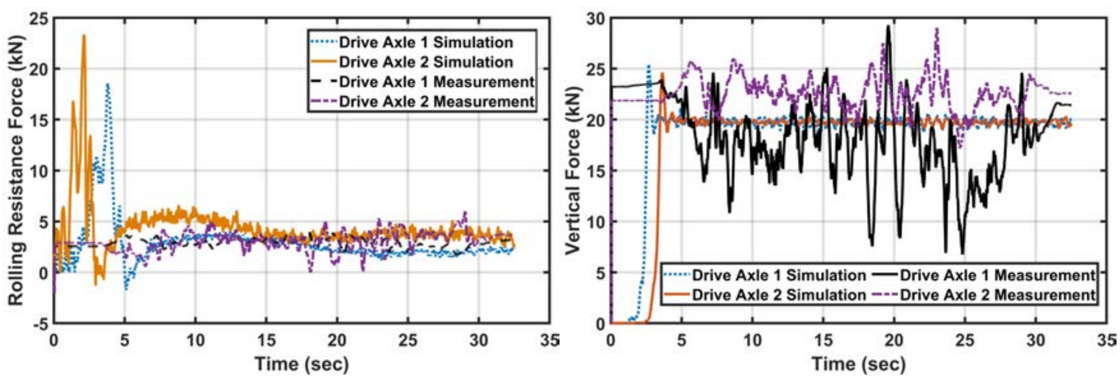

(a) Rolling resistance force (b) Vertical force

Figure 10.8: Forces obtained from simulation and measurements for a loaded truck

Figure 10.8a shows the variation of the rolling resistance force per tire as a function of time for simulations and measurements on the first and second drive axles. The rolling resistance force is computed by subtracting the longitudinal force from the force generated by the torque. It is shown that at steady state both the simulation and measurement results are in good agreement, and reach a similar value. In the case of the first drive axle, the simulated steady-state rolling resistance force is 2.75 kN per tire, while the measured one is 3.6 kN per tire. In the case of the second drive axle, the simulated steady-state rolling resistance force is 2.61 kN per tire, while the measured one is 2.59 kN per tire. Thus, the simulated and measured steady-state rolling resistance forces are considered in good agreement. Furthermore, it is noticed that the second drive axle has a lower rolling resistance force in comparison to the first drive axle at the same vertical load, this is due to the soil compaction caused by the rolling of the first drive axle.

Figure 10.8b shows the variation of the vertical force per tire as a function of time for simulations and measurements on the first and second drive axles. It is noticed that the results obtained from measurement are disturbed and this is due to the vibration and extraneous factors during testing. However, the average of the vertical force during the steady-state section is considered to be the steady-state vertical load. In the case of the first drive axle, the steady-state simulated vertical load is 20.7 kN, while the measured on is 19.4 kN. In the case of the second drive axle, the steady-state simulated vertical load is 20.7 kN, while the measured on is 20.4 kN. Thus, the simulated and measured steady-state rolling resistance forces are considered in good agreement.

Table 10.2: Sample of tire parameters obtained from simulation and measurement for loaded truck

	Simulation		Measurement		Error	
	Drive 1	Drive 2	Drive 1	Drive 2	Drive 1	Drive 2
F_z	20.71	20.71	19.4	20.4	1.4%	6.2%
F_{rr}	2.74	2.61	3.67	2.59	25%	0.77%
RRC	0.14	0.12	0.16	0.12	13%	0.8%
Torque (kNm)	1.56	1.49	1.67	1.66	6.5%	6.6 %
Slip (%)	45.15	45.04	47.57	48.91	5.3%	7.9%

Table 10.2 shows sample of other tire parameters that are used to validated the simulation model including the rolling resistance coefficient, the torque and the longitudinal slip. It is concluded that the simulation model is able to well predict the rolling resistance coefficient at the second drive axle with an error less than 1% and for the first drive axle with a error exceeding 20%. However, the model is well able to predict both the torque and the longitudinal slip with an error margin less than 8% for all cases. Thus, the simulated model demonstrates good agreement in comparison to measurements.

Table 10.3 shows the simulation and measurement results for the case of an unloaded truck for the first and second drive tires. It is noticed that the simulation and measurement results are in good agreement and that the error in predicting the rolling resistance coefficient is less than 3% for both drive tires.

Furthermore, Figure 10.9 shows the variation of the rolling resistance coefficient for both simulation and measurement at the first and second drive axles as a function of the vertical load applied. It is noticed that both drive axles have a similar trend, as the vertical load increase the rolling resistance coefficient increases at given tire conditions. A low vertical load such as 12 kN indicates that the truck is unloaded, while a high vertical load such as 20 kN indicates that the truck is loaded. It is observed that the simulation and measurement results are considered in good agreement for both drive axles. The largest difference between simulation

Table 10.3: Sample of tire parameters obtained from simulation and measurement for unloaded truck

	Simulation		Measurement		Error	
	Drive 1	Drive 2	Drive 1	Drive 2	Drive 1	Drive 2
F_z	12.91	12.89	11.42	11.85	11.48%	8.07%
F_{rr}	1.65	1.33	1.41	1.21	14.38%	9.5%
RRC	0.13	0.103	0.12	0.101	3.28%	1.55%
Torque (kNm)	0.94	0.8	0.53	1.2	42.1%	37.5 %
Slip (%)	446.11	45.20	45.47	48.61	1.39%	7.6%

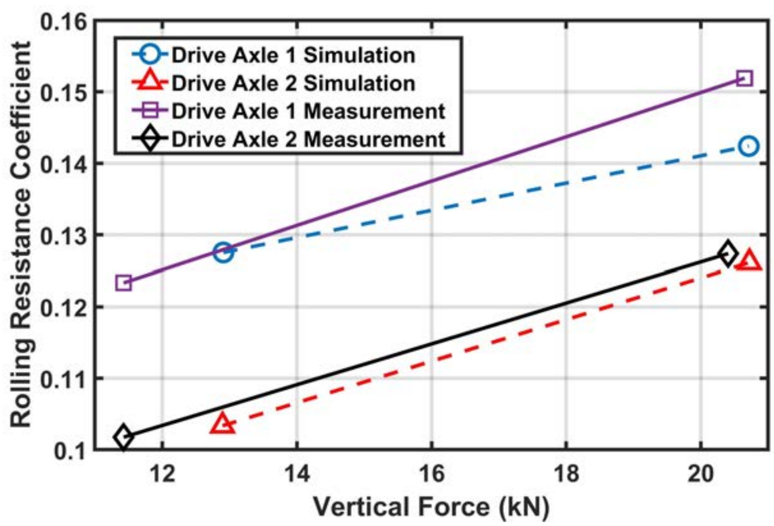

Figure 10.9: Rolling resistance coefficient as a function of vertical load for simulations and measurements

and measurement is recorded at a loaded truck on the front-drive axle, this is possible due to the vertical displacement of the tire in the soil during measurement.

10.5 Summary

A novel off-road truck tire-gravelly soil (sand mixed with gravel) interaction model was presented and validated. The model consists of four RHD tires cossetted to present a four-axle truck running over gravelly soil domain. The gravelly soil was modeled using Smoothed-Particle Hydrodynamics technique and calibrated using physical measurements obtained from the civil engineering department in Stockholm, Sweden [6]

The simulation model setup including the contact algorithm and test procedure were described in detail. The model setup consisted of the tires, soil domain, and a hard surface to carry the tires before reaching the soil domain. The distance between the tires was selected to match that of the axles on the truck. The selected inflation pressure and speed match those from testing site data. Furthermore, the test is repeated for two cases loaded and unloaded cases to mimic a loaded and unloaded truck, respectively.

Moreover, the truck physical testing performed in Göteborg, Sweden were presented and described. The truck specification along with the tire was described in details and the list of measured parameters was specified. The test was repeated several times under different conditions to investigate the effect of soil compaction and truck loading on interaction performance.

Furthermore, it was observed that the rolling resistance coefficient decreases as the soil is compacted due to the hardness of the soil when compacted at given inflation pressure and driving conditions. Moreover, the rolling resistance coefficient increases as the vertical load increases at given inflation pressure and driving conditions. The increase of the rolling resistance coefficient as the vertical load increase was associated with the increase in the contact area between the tire and the gravelly soil. It was also noticed that the soil compaction is almost 50% less in the case of the unloaded truck in comparison to that of a loaded truck.

The driven tires traction performance characteristics obtained from simulation were then validated against physical measurements at different operating conditions. It was concluded that the simulations and measurements are in good agreement in predicting the tires rolling resistance and traction characteristics. A summary of the primary tire characteristics was presented in table 10.2 and table 10.3 for the case of a loaded and unloaded truck, respectively. The error percentage demonstrated to be within an acceptable frame of correlation between measurements and simulations.

CHAPTER 11

FULL VEHICLE ANALYTICAL MODEL

The full vehicle model is also known as Volvo Transportation Model (VTM) is a Matlab/Simulink code that is used to predict the full vehicle motions on-road and off-road during different maneuvers. In VTM the tires are modeled as the rigid ring and utilize in-plane and out-of-plane rigid ring model parameters obtained in chapters 6 and 7. The rigid ring model is validated against the simulation results obtained in this research. In this chapter the rigid ring model is described and investigated, the output of the Matlab code and a sample of the validation against simulation is presented.

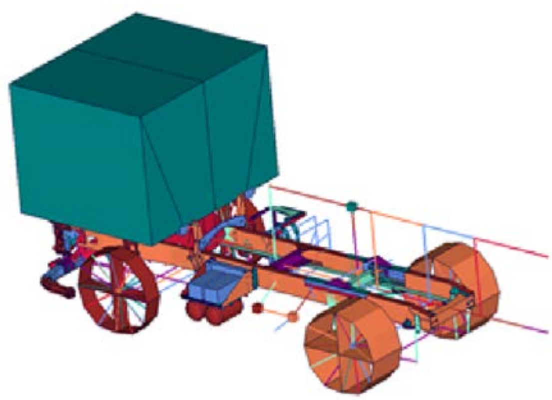

Figure 11.1: Implementation of full vehicle model [154]

The VTM, in addition to the rigid ring tire model, has five other modules, cab, chassis frame, load carrier, steered axles, and non-steered axles as shown in figure 11.1. The inputs of the rigid ring tire model are the tire rim's three translational velocities, the driving torque, the road vertical position, and the road slopes in case of pitch or roll. While the output of the tire model is the axle forces in all three directions, the moments around all axles, the tire rotational speed, the longitudinal slip, the slip angle, and the effective tire radius.

11.1 Rigid Ring Model Over Hard Surface

The rigid ring model consists of two parts, the in-plane and the out-of-plane that are connected together by springs and dampers. Figure 11.2 represents the in-plane and out-of-plane rigid ring model parameters on a hard surface.

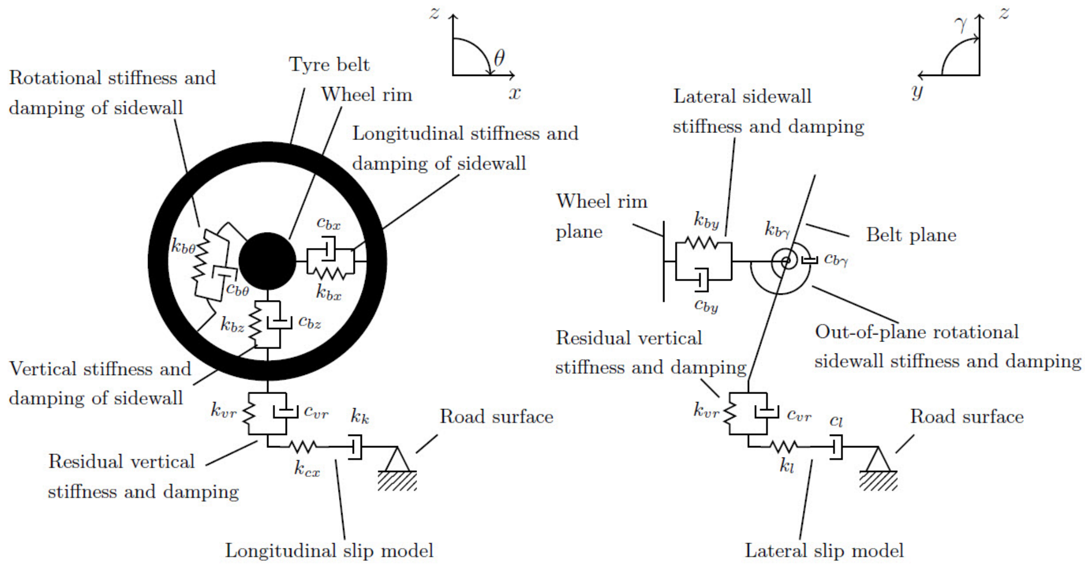

Figure 11.2: In-plane and out-of-plane rigid ring model on hard surface [154]

The in-plane rigid ring consists of the rim mass and inertia in addition to the inner part of the sidewall, while the out-of-plane ring consists of the tire belt mass and the mass of the outer part of the sidewall.

11.1.1 In-plane rigid ring model

The in-plane rigid ring tire model over hard surface consists of the tire reaction in rotation, vertical and longitudinal models.

11.1.1.1 in-plane rotational tire model

Figure 11.3 present the rigid ring model of the in-plane rotational moment, the model has two degrees of freedom. The rim rotation is denoted by θ_1, and the belt rotation is denoted by θ_2. The rim and belt rotations are connected by the spring representing the in-plane rotational belt stiffness, $k_{b,\theta}$, and damping, $c_{b,\theta}$.

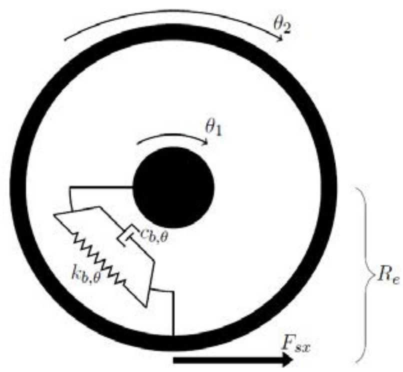

Figure 11.3: Description of the tire in-plane rotation moment model on hard surface [154]

Equation 11.1 show the equation of motion derived from figure 11.3.

$$\begin{bmatrix} M \\ -F_{sx}R_e \end{bmatrix} = k_{b\theta} \begin{bmatrix} 1 & -1 \\ -1 & 1 \end{bmatrix} \begin{bmatrix} \theta_1 \\ \theta_2 \end{bmatrix} + c_{b\theta} \begin{bmatrix} 1 & -1 \\ -1 & 1 \end{bmatrix} \begin{bmatrix} \dot{\theta}_1 \\ \dot{\theta}_2 \end{bmatrix} + \begin{bmatrix} I_{1y} & 0 \\ 0 & I_{2y} \end{bmatrix} \begin{bmatrix} \ddot{\theta}_1 \\ \ddot{\theta}_2 \end{bmatrix} \tag{11.1}$$

M is the driving torque, I_{1y} and I_{2y} are the in-plane moment of inertia of the rim and belt, respectively. The moments acting on the rim, and belt are noted as M_{yr} and M_{yb}, respectively are defined in equations 11.2 and 11.3.

$$M_{yr} = I_{1y}\ddot{\theta}_1 \tag{11.2}$$

$$M_{yb} = I_{2y}\ddot{\theta}_2 \tag{11.3}$$

Using the equations of motions derived in equation 11.1 the moments M_{yr} and M_{yb} are further expanded as shown in equations 11.4 and 11.5.

$$M_{yr} = k_{b\theta}(\theta_2 - \theta_1) + c_{b\theta}(\dot{\theta}_2 - \dot{\theta}_1) + M \tag{11.4}$$

$$M_{ub} = k_{b\theta}(\theta_1 - \theta_2) + c_{b\theta}(\dot{\theta}_1 - \dot{\theta}_2) - F_{sx}R_e \tag{11.5}$$

11.1.1.2 tire vertical model

Figure 11.4 shows the tire vertical model used to calculate the total vertical stiffness, k_{tot}, and two sets of springs and dampers as shown in figure . The vertical tire model consists of the vertical stiffness and damping of the tire, k_{bz} and c_{bz}, respectively, connected in parallel to the residual stiffness and damping, k_{vr} and c_{vr}, respectively. The rim mass and position are represented by, m_1, z_1, respectively, and the belt mass and position are represented by, m_2 and z_2, respectively, and z_r represents the position of the hard surface.

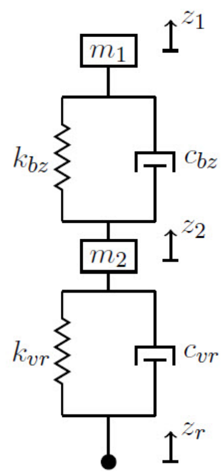

Figure 11.4: Description of the tire vertical model on hard surface [154]

The system shown in figure 11.4 is solved to develop the matrix shown in equation 11.6.

$$
\begin{aligned}
\begin{bmatrix} m_1 & 0 & 0 \\ 0 & m_2 & 0 \\ 0 & 0 & 0 \end{bmatrix} \begin{bmatrix} \ddot{z}_1 \\ \ddot{z}_2 \\ \ddot{z}_r \end{bmatrix} &= \begin{bmatrix} -k_{bz} & k_{bz} & 0 \\ k_{bz} & -k_{bz} - k_{vr} & k_{vr} \\ 0 & k_{vr} & -k_{vr} \end{bmatrix} \begin{bmatrix} z_1 \\ z_2 \\ z_r \end{bmatrix} \\
&+ \begin{bmatrix} -c_{bz} & c_{bz} & 0 \\ c_{bz} & -c_{bz} - c_{vr} & c_{vr} \\ 0 & c_{vr} & -c_{vr} \end{bmatrix} \begin{bmatrix} \dot{z}_1 \\ \dot{z}_2 \\ \dot{z}_r \end{bmatrix}
\end{aligned} \tag{11.6}
$$

Solving equation 11.6 for the vertical acceleration of where the sidewall meets the tire tread, equation 11.8 is developed.

$$m_2\ddot{z}_2 = k_{bz}z_1 + (-k_{bz} - k_{vr})z_2 + k_{vr}z_r + c_{bz}\dot{z}_1 - (c_{bz} + c_{vr})\dot{z}_2 + c_{vr}\dot{z}_r \tag{11.7}$$

$$\ddot{z}_2 = \frac{k_{bz}z_1 - (k_{bz}k_{vr})z_2 + k_{vr}z_r + c_{bz}\dot{z}_1 - (c_{bz} + c_{vr})\dot{z}_2 + c_{vr}\dot{z}_r}{m_2} \tag{11.8}$$

11.1.1.3 tire longitudinal slip model

Figure 11.5 shows the description of the longitudinal slip model that is used to determine the longitudinal force as a function of the longitudinal slip on hard surface during acceleration or braking. The longitudinal tread and tire stiffness are described as, k_{cx} and k_k, respectively, and u_x is the tire tread deformation.

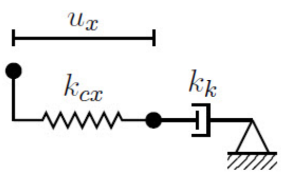

Figure 11.5: Description of the tire longitudinal slip model on hard surface [154]

The longitudinal slip, i_s, of a tire is defined in equation 11.20, ω is the tire angular velocity and R_e is known as the effective rolling radius and R_o is the unloaded tire radius. The relationship between the effecting and unloaded tire radius is described as $R_e = R_o - z_r + z_1$.

$$i_s = \frac{R_e\omega}{v_x} + \frac{\dot{u}_x}{v_x} - 1 \tag{11.9}$$

Where u_x is the tire tread deformation, and the value of $\dot{u}_x$ is zero when steady state condition is applied. Referring to figure 11.5 the force produced from the slip model at steady state is defined in equations 11.10 and 11.11.

$$\begin{aligned} F_{cx} &= -k_k i_s && (11.10)\\ F_{cx} &= k_{cx} u_x && (11.11) \end{aligned}$$

Using equation 11.20 and equating equations 11.10 and 11.11 the relationship between $\dot{u}_x$ and u_x is developed and presented in equation 11.16.

$$\begin{aligned} -k_k i_s &= k_{cx} u_x && (11.12)\\ -k_k\left(\frac{R_e\omega}{v_x} + \frac{\dot{u}_x}{v_x} + -1\right) &= k_{cx} u_x && (11.13)\\ \frac{R_e\omega}{v_x} + \frac{\dot{u}_x}{v_x} - 1 &= \frac{-k_{cx}}{k_k} u_x && (11.14)\\ \frac{\dot{u}_x}{v_x} &= \frac{-k_{cx}}{k_k} u_x - \frac{R_e\omega}{v_x} + 1 && (11.15)\\ \dot{u}_x &= \frac{-k_{cx}}{k_k} u_x v_x - R_e\omega + v_x && (11.16) \end{aligned}$$

In this case, the longitudinal force is saturated since the nonlinear behavior can not be captured by this model. The saturation criteria are defined using the simulation model by taking the mean force after the point where the tire stiffness is no longer considered linear which is around 15% slip.

11.1.2 Out-of-plane rigid ring model

The out-of-plane rigid ring tire model over hard surface consists of the tire reaction in rotational and lateral models.

11.1.2.1 out-of-plane rotational tire model

The out-of-plane rotational tire model is described in figure 11.6. The out-of-plane rotational moment is similar to that of the in-plane with out-plane rotational belt stiffness, $k_{b,\gamma}$, parallel to the damper representing the out-plane rotational belt damping, $c_{b,\gamma}$.

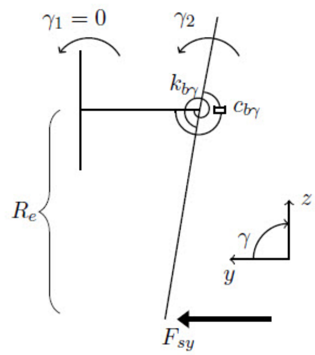

Figure 11.6: Description of the tire out-of-plane rotational tire model on hard surface [154]

Applying equilibrium in the moment equation, the angular acceleration $\ddot{\gamma}_2$ is derived and expressed in equation 11.19.

$$-F_{sy}R_e = k_{b\gamma}\gamma_2 + c_{b\gamma}\dot{\gamma}_2 + I_{2x}\ddot{\gamma}_2 \quad (11.17)$$

$$I_{2x}\ddot{\gamma}_2 = -F_{sy}R_e - k_{b\gamma}\gamma_2 - c_{b\gamma}\dot{\gamma}_2 \quad (11.18)$$

$$\ddot{\gamma}_2 = \frac{-F_{sy}R_e - k_{b\gamma}\gamma_2 - c_{b\gamma}\dot{\gamma}_2}{I_{2x}} \quad (11.19)$$

11.1.2.2 tire cornering model

The lateral force generated from the slip model, F_{sy} is calculated directly from the lateral slip angle, α using equation 11.20.

$$F_{sy} = k_f\alpha \quad (11.20)$$

Where k_f is the cornering stiffness of the tire, the slip angle α is defined as the lateral velocity divide by the longitudinal velocity. In dynamic motion, the relaxation length of the tire, σ should be taken into consideration as shown in equation 11.21.

$$\alpha + \frac{\sigma}{v_x}\dot{\alpha} = -\frac{v_y}{v_x} \quad (11.21)$$

In this case, the lateral force is saturated since the nonlinear behavior can not be captured by this model. The saturation criteria are defined using the simulation model by taking the mean force after the point where the tire stiffness is no longer considered linear which is around 5°slip angle.

11.1.2.3 tire lateral model

Figure 11.7 described the tire lateral model on a hard surface. The model consists of the translational belt stiffness, k_{by} connected in parallel with the translational belt damping, c_{by} .

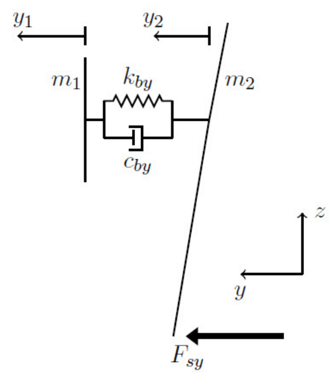

Figure 11.7: Description of the tire lateral model on hard surface [154]

The free body diagram shown in figure 11.7 are used to develop the equations of motions presented in equation 11.22.

$$\begin{bmatrix} 0 \\ f_{sy} \end{bmatrix} = k_{by} \begin{bmatrix} 1 & -1 \\ -1 & 1 \end{bmatrix} \begin{bmatrix} y_1 \\ y_2 \end{bmatrix} + c_{by} \begin{bmatrix} 1 & -1 \\ -1 & 1 \end{bmatrix} \begin{bmatrix} \dot{y}_1 \\ \dot{y}_2 \end{bmatrix} + \begin{bmatrix} m_1 & 0 \\ 0 & m_2 \end{bmatrix} \begin{bmatrix} \ddot{y}_1 \\ \ddot{y}_2 \end{bmatrix} \tag{11.22}$$

The term F_{sy} is the force generated in the slip model due to the slip angle and is calculated as $F_{sy} = k_f \alpha$. The lateral force acting on the rim defined as F_y is derived based on the acceleration, $\ddot{y}_1$ and shown in equation 11.24.

$$\begin{aligned} F_y &= m_1 \ddot{y}_1 && (11.23) \\ &= k_{by}(y_2 - y_1) + c_{by}(\dot{y}_2 - \dot{y}_1) && (11.24) \end{aligned}$$

The lateral force generated in the tire sidewall defined as F_{wy} is based on the acceleration $\ddot{y}_2$ and shown in equation 11.26.

$$\begin{aligned} F_{wy} &= m_2 \ddot{y}_2 && (11.25) \\ &= F_{sy} - F_y && (11.26) \end{aligned}$$

11.2 Rigid Ring Model Over Soft Terrain

The rigid ring tire model parameters over soft terrain are presented in figure 11.8. The rigid ring tire model on soft terrain includes an additional set of springs and dampers to represent the soft terrain that is added to the rigid ring tire model over hard surface.

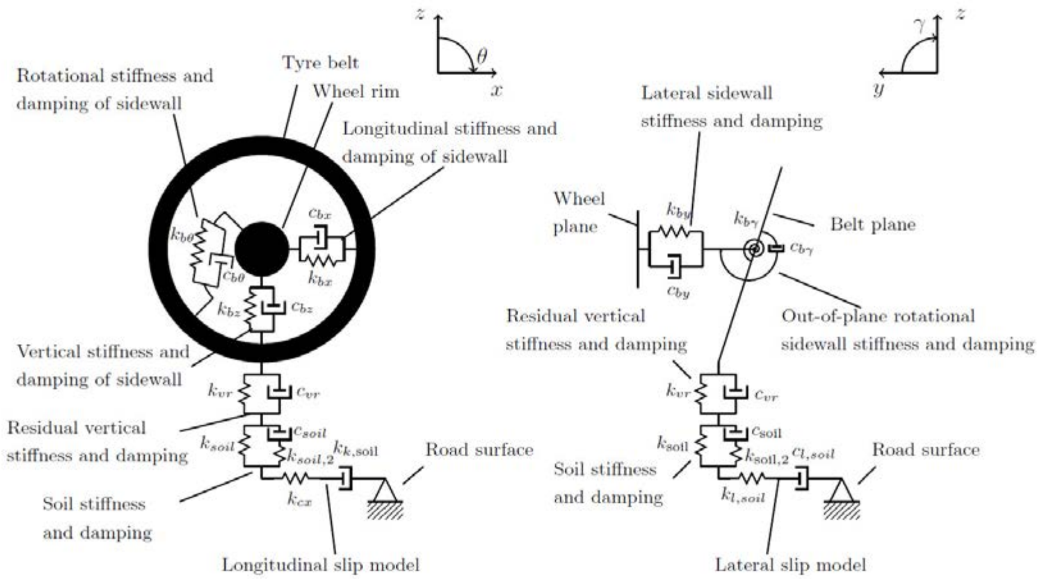

Figure 11.8: In-plane and out-of-plane rigid ring model on soft terrain [154]

11.2.1 In-plane rigid ring model

The in-plane rigid ring tire model over soft terrain is presented by vertical and longitudinal sub-models. The rotational model is considered a tire characteristic and is independent of the terrain characteristics. The model and its sub-models are explained in this section.

11.2.1.1 tire vertical model

The vertical rigid ring model over soft terrain is shown in figure 11.9. The model includes an additional fictive mass, m_{soil}, and a spring representing the stiffness constant in equivalent damping, $k_{soil,2}$ connected in series to a damper representing the damping constant in equivalent damping, c_{soil}, which are both then connected in parallel to another spring representing the vertical stiffness of the soil, k_{soil}.

The equations derived for the the soil stiffness and damping are defined as shown in equations 11.27 and 11.28.

$$k_{\prime soil}(\omega) = \frac{k_{soil,2}}{1 + \left(\frac{k_{soil,2}}{\omega c_{soil}}\right)^2} \tag{11.27}$$

$$c_{\prime soil}(\omega) = \frac{c_{soil,2}}{1 + \left(\frac{\omega c_{soil}}{k_{soil,2}}\right)^2} \tag{11.28}$$

The equations of motions are then derived and presented in matrix form in equation 11.29.

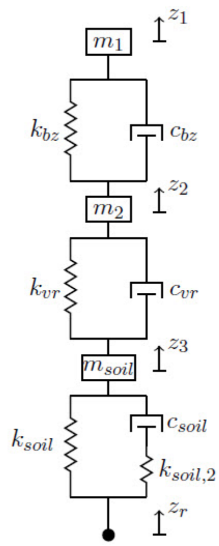

Figure 11.9: Description of the tire vertical model on soft terrain [154]

$$\begin{bmatrix} m_1 & 0 & 0 & 0 \\ 0 & m_2 & 0 & 0 \\ 0 & 0 & m_{soil} & 0 \\ 0 & 0 & 0 & 0 \end{bmatrix} \begin{bmatrix} \ddot{z}_1 \\ \ddot{z}_2 \\ \ddot{z}_3 \\ \ddot{z}_r \end{bmatrix} = \begin{bmatrix} -k_{bz} & k_{bz} & 0 & 0 \\ k_{bz} & -k_{bz} - k_{vr} & k_{vr} & 0 \\ 0 & k_{vr} & -k_{vr} - k_{soil} & k_{soil} \\ 0 & 0 & k_{soil} & -k_{soil} \end{bmatrix} \begin{bmatrix} z_1 \\ z_2 \\ z_3 \\ z_r \end{bmatrix}$$
$$+ \begin{bmatrix} -c_{bz} & c_{bz} & 0 & 0 \\ c_{bz} & -c_{bz} - c_{vr} & c_{vr} & 0 \\ 0 & c_{vr} & -c_{vr} - c\prime_{soil} & c\prime_{soil} \\ 0 & 0 & c\prime_{soil} & -c\prime_{soil} \end{bmatrix} \begin{bmatrix} \dot{z}_1 \\ \dot{z}_2 \\ \dot{z}_3 \\ \dot{z}_r \end{bmatrix} \quad (11.29)$$

Solving equation 11.29 to derive the three equations of motions of the acceleration at the rim, sidewall and and interaction point as shown in equation 11.30, 11.31 and 11.32, respectively.

$$\ddot{z}_1 = \frac{k_{vz}(z_2 - z_1) + c_{bz}(\dot{z}_2 - \dot{z}_1)}{m_1} \quad (11.30)$$
$$\ddot{z}_2 = \frac{k_{vz}(z_1 - z_2) + k_{vr}(z_3 - z_2) + c_{bz}(\dot{z}_1 - \dot{z}_2) + c_{vr}(\dot{z}_3 - \dot{z}_2)}{m_2} \quad (11.31)$$
$$\ddot{z}_3 = \frac{k_{vr}(z_2 - z_3) + k_{soil}(z_r - z_3) + c_{vr}(\dot{z}_2 - \dot{z}_3) + c\prime_{soil}(\dot{z}_r - \dot{z}_3)}{m_{soil}} \quad (11.32)$$

The vertical force F_z is calculated from the equation of motion of the rim and is derived as sown in equation 11.34.

$$F_z = m_1 \ddot{z}_1 \quad (11.33)$$
$$= k_{vz}(z_2 - z_1) + c_{bz}(\dot{z}_2 - \dot{z}_1) \quad (11.34)$$

11.2.1.2 tire longitudinal slip model

The tire longitudinal slip model over soft terrain is similar to that over hard surface the only different is the equation of the effective radius which is shown in equation 11.35 for tire model over soft terrain.

$$R_e = R_o - (z_3 - z_1) \tag{11.35}$$

11.2.2 Out-of-plane rigid ring model

The out-of-plane rigid ring tire model over soft terrain is similar to that of the rigid ring tire model over hard surface.

11.2.2.1 tire cornering model

The same tire cornering model used on hard surface is used on soft terrain. In the case of soft terrain there is no saturation limit as the lateral force has no maximum value due to resistance force from the terrain.

11.2.2.2 tire lateral model

The same tire lateral model used on hard surface is used on soft terrain. Figure 11.7 is still used to compute the lateral force as well.

11.3 Rigid Ring Tire Model Validation

The Matlab rigid ring tire model is validated against results obtained from FEA simulations under similar conditions. A sample of the rigid ring tire model versus simulations is presented at nominal inflation pressure of 586 kPa (85 psi) and three vertical loads of 13 kN (3000 lbs), 27 kN (6000 lbs), and 40 kN (9000 lbs). However, the validation was performed at all three inflation pressure and vertical loads and given in appendix C.

11.3.1 Tire-hard surface characteristics

Figure 11.10 shows the three terrain independent tests of the truck tire running over a hard surface. Figure 11.10a shows the in-plane rotational model characteristics of the rigid ring tire model and the simulations. The angular displacement as a function of time for the rigid ring model and the simulations are considered to be in good agreement in terms of amplitude and phase, the angular displacement at 586 kPa (85 psi) inflation pressure and 27 kN (6000 lbs) vertical load ranges between -0.015 rad and 0.015 rad.

Figure 11.10b shows the out-of-plane rotational model characteristics of the rigid ring tire model and the simulations. The angular displacement as a function of time for the rigid ring model and the simulations are considered in good agreement in terms of amplitude and phase, the angular displacement at 586 kPa (85 psi) inflation pressure and 27 kN (6000 lbs) vertical load ranges between -0.008 rad and 0.008 rad.

Figure 11.10c shows the translational model characteristics of the rigid ring tire model and the simulations. The translational displacement as a function of time for the rigid ring model and the simulations are considered in good agreement in terms of amplitude and phase, the translational displacement at 586 kPa (85 psi) inflation pressure and 27 kN (6000 lbs) vertical load ranges between -5 mm and 5 mm.

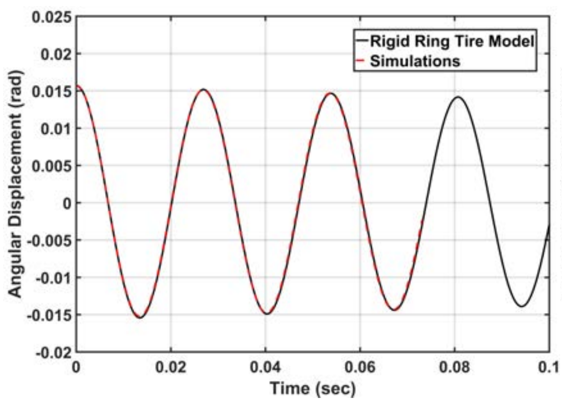

(a) In-plane rotational model

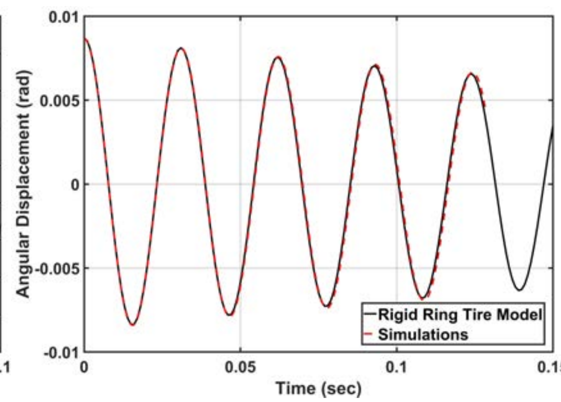

(b) Out-of-plane rotational model

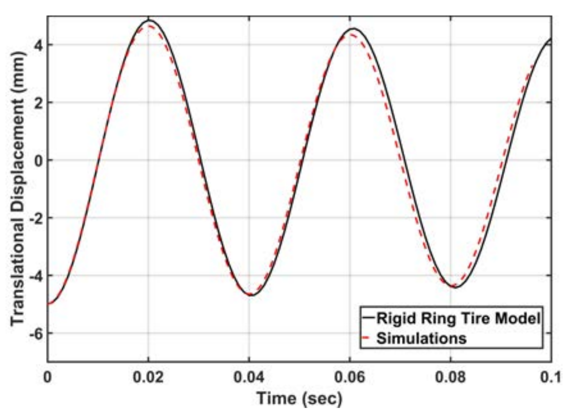

(c) Translational model

Figure 11.10: Rigid ring tire model versus simulations at 586 kPa (85 psi) inflation pressure and 27 kN (6000 lbs) vertical load for terrain independent in-plane and out-of-plane model over hard surface

Figure 11.11 shows the terrain dependent results of the rigid ring tire model and simulations of a tire running over hard surface at 586 kPa (85 psi) inflation pressure and different vertical loads. Figure 11.11a shows the longitudinal force as a function of longitudinal slip predicted from the rigid ring tire model and simulations. The linear part of the longitudinal force is well captured by the rigid ring tire model in comparison to the simulations at small longitudinal slip. At large longitudinal slip the predicted longitudinal force by the rigid ring tire model and simulations are also in good agreement.

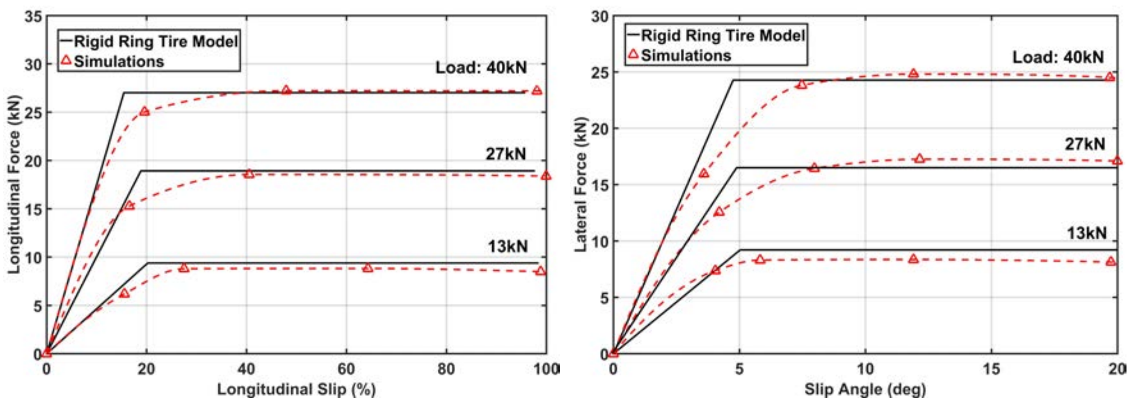

(a) Longitudinal model (b) Lateral model

Figure 11.11: Rigid ring tire model versus simulations at 586 kPa (85 psi) inflation pressure and different vertical load for terrain dependent in-plane and out-of-plane results over hard surface

At the end of the linear part of the longitudinal force predicted by the rigid ring tire model saturates at a value equal to μF_z, while the simulations show non-linear behavior of the longitudinal force. It can be seen from figure 11.11a that the rigid ring tire model saturates at a longitudinal slip of approximately 20%, 18%, and 15% at vertical loads of 13 kN (3000 lbs), 27 kN (6000 lbs), and 40 kN (9000 lbs), respectively. The results of the rigid ring tire model are considered in good agreement with the simulations at all vertical loads and longitudinal slip.

Figure 11.11b shows the lateral (cornering) force as a function of slip angle predicted from the rigid ring tire model and the simulations. The lateral force as a function of the slip angle is considered in good agreement between the rigid ring tire model and the simulations at small slip angles. As the slip angle increase, the simulations capture the non linear behavior of the lateral force as a function of the slip angle, while the rigid ring tire model saturates. Furthermore, as the vertical load increase the lateral force saturates at a smaller slip angle. It can be seen from figure 11.11b that the lateral force predicted by the rigid ring tire model saturates at a slip angle of 5°, 4.8°and 4.5°at a vertical load of 13 kN (3000 lbs), 27 kN (6000 lbs), and 40 kN (9000 lbs), respectively. The results of the rigid ring tire model are considered in good agreement with the simulations, in particular at at vertical loads and slip angles.

Table 11.1: Vertical steady state displacement at 586 kPa (85 psi) inflation pressure and different vertical loads over hard surface

Vertical Load (kN)	Rigid Ring Tire Model	Simulations
13	20	18
27	34	36
40	51	53

Table 11.1 shows the vertical steady-state displacement of the truck tire running over the hard surface at 586 kPa (85 psi) inflation pressure and different vertical loads for both rigid ring tire model and simulations. The results show that as the vertical load increases the vertical displacement increase for both rigid ring tire model and simulations. The predicted vertical displacement obtained from the rigid ring tire model is considered in good agreement with that obtained from the simulations at all vertical loads.

The validation results of the rigid ring tire model versus simulations for a truck tire running over hard surface at inflation pressures of 380 kPa (55 psi), and 758 kPa (110 psi) and vertical loads of 13 kN (3000 lbs), 27 kN (6000 lbs), and 40 kN (9000 lbs) are given in appendix C.1. The results shown in appendix C.1 are following approximately the same trend as that shown in figure 11.11 and table 11.1.

11.3.2 Tire-wet surface characteristics

Figure 11.12a shows the longitudinal force as a function of longitudinal slip predicted from the rigid ring tire model and the simulations over wet surface. The linear part of the longitudinal force is well captured by the rigid ring tire model in comparison to the simulations at small longitudinal slip. At the end of the linear part the rigid ring tire model saturates, while the simulations shows the non-linear behavior.

It can be seen from figure 11.12a that the rigid ring tire model saturates at a longitudinal slip around 20%, 17%, and 15% at vertical loads of 13 kN (3000 lbs), 27 kN (6000 lbs) and 40 kN (9000 lbs) vertical load, respectively. It should be noted that the peak longitudinal force occurs at different longitudinal slip depending on the vertical load, as the vertical load increase the peak value occurs at a higher longitudinal slip. For example, the peak longitudinal force captured by the simulations is around 15 kN (3150 lbs) at 20% longitudinal slip for a truck tire running over the wet surface at 27 kN (6000 lbs) vertical load. The maximum recorded longitudinal force is around 22 kN (4950 kN) at 25% longitudinal slip,

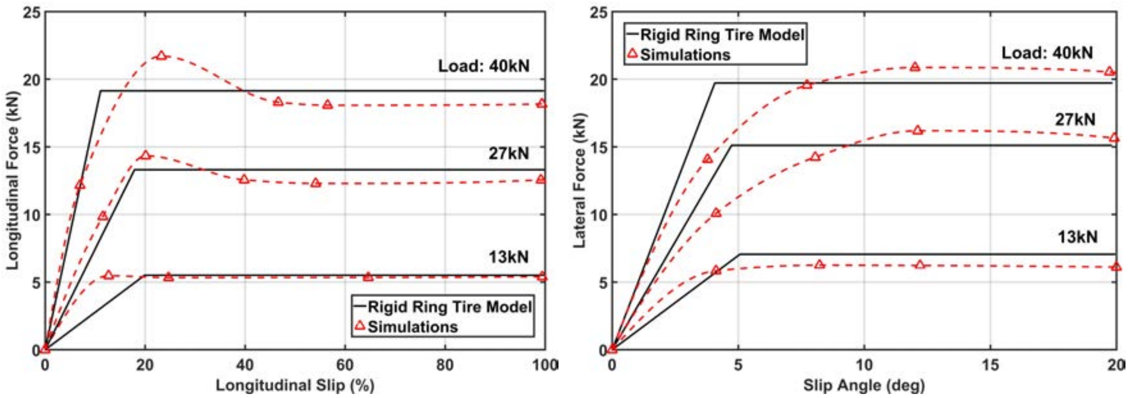

(a) Longitudinal model (b) Lateral model

Figure 11.12: Rigid ring tire model versus simulations at 586 kPa (85 psi) inflation pressure and different vertical load for all in-plane and out-of-plane results over wet surface

and 40 kN (9000 lbs) vertical load. The rigid ring tire model is considered in good agreement with the simulations results, especially at high vertical loads.

Figure 11.14b shows the lateral (cornering) force as a function of slip angle predicted from the rigid ring tire model and the simulations for a tire running over wet surface. The lateral force as a function of the slip angle is considered in good agreement between the rigid ring tire model and the simulations at small slip angles. As the slip angle increase, the simulations capture the nonlinear behavior of the lateral force as a function of the slip angle, while the rigid ring tire model saturates. At large slip angle, the predicted lateral force from the rigid ring tire model is considered in good agreement with the simulations as well. The predicted lateral force from the rigid ring tire model saturates at 5°, 4.6°and 3.9°at vertical loads of 13 kN (3000 lbs), 27 kN (6000 lbs) and 40 kN (9000 lbs), respectively. In general, the lateral characteristics predicted by the rigid ring tire model and the simulations are considered in good agreement, at all vertical loads and slip angles.

Table 11.2: Vertical steady state displacement at 586 kPa (85 psi) inflation pressure and different vertical loads over wet surface

Vertical Load (kN)	Rigid Ring Tire Model	Simulations
13	34	49
27	67	65
40	95	81

Table 11.2 shows the vertical steady-state displacement of the truck tire running

over the wet surface at 586 kPa (85 psi) inflation pressure and different vertical loads for both rigid ring tire model and simulations. The results show that as the vertical load increase the vertical displacement increase for both rigid ring tire model and simulations. The predicted vertical displacement obtained from the rigid ring tire model is considered in good agreement with that obtained from the simulations at all vertical loads.

Generally, the hard surface and the wet surface exhibits similar characteristics in steering, braking, and accelerating. However, the difference in peak values is due to the difference in coefficient of friction. The wet surface has a lower coefficient of friction and thus the peak values of the longitudinal force and lateral force are less than that of the hard surface. In regards to the vertical characteristics both hard and wet surfaces exhibit similar characteristics.

The validation results of the rigid ring tire model versus simulations for a truck tire running over wet surface at inflation pressures of 380 kPa (55 psi), and 758 kPa (110 psi) and vertical loads of 13 kN (3000 lbs), 27 kN (6000 lbs), and 40 kN (9000 lbs) are given in appendix C.2. The results shown in appendix C.2 are following approximately the same trend as that shown in figure 11.12 and table 11.2.

11.3.3 Tire-snow characteristics

Figure 11.13a shows the longitudinal force as a function of longitudinal slip predicted from the rigid ring tire model and simulations for a truck tire running over 50 mm snow. The linear part of the longitudinal force as a function of the longitudinal slip is well captured by the rigid ring tire model in comparison to the simulations at small longitudinal slip, especially at low vertical loads. At large longitudinal slip, the predicted longitudinal force by the rigid ring tire model and simulations are also in good agreement at all vertical loads.

At the end of the linear part, the longitudinal force predicted by the rigid ring tire model saturates, while the simulations show the non-linear behavior. The rigid ring tire model saturates at a longitudinal slip around 20%, 18%, and 14% at vertical loads of 13 kN (3000 lbs), 27 kN (6000 lbs), and 40 kN (9000 lbs), respectively. It should be noted that the peak longitudinal force occurs at different longitudinal slip depending on the vertical load, as the vertical load increase the peak value occurs at a higher longitudinal slip. It is noticed that the longitudinal force in the simulation model reduces after 65% longitudinal slip reaching 6 kN (1350 lbs) at 100% slip for a vertical load of 13 kN (3000 lbs), this part is not captured by the rigid ring model. The predicted results from the rigid ring tire model are considered in good agreements with the simulation results for all vertical load and longitudinal slips.

Figure 11.13b shows the lateral (cornering) force as a function of slip angle predicted from the rigid ring tire model and the simulations for a tire running over

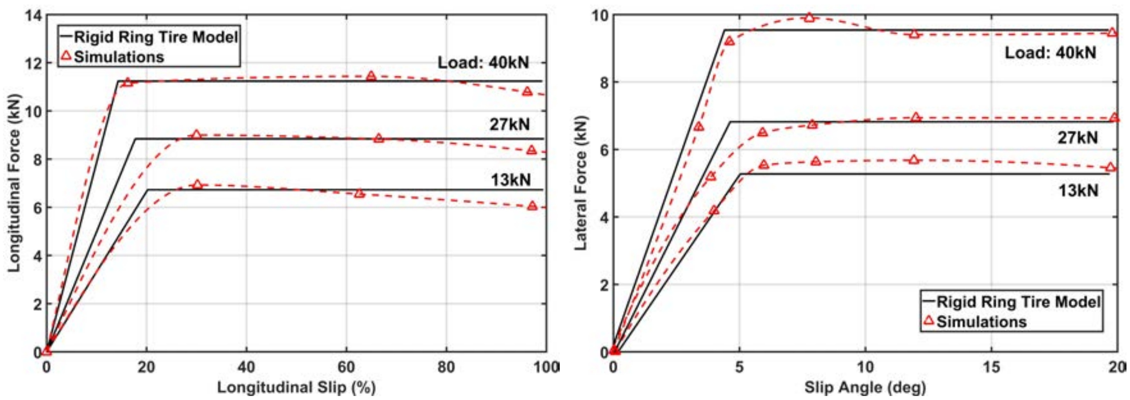

(a) Longitudinal model (b) Lateral model

Figure 11.13: Rigid ring tire model versus simulations at 586 kPa (85 psi) inflation pressure and different vertical load for all in-plane and out-of-plane reactions over 50 mm snow

50mm snow. The lateral force as a function of the slip angle is considered in good agreement between the rigid ring tire model and the simulations, especially for high vertical loads and large slip angles. The predicted lateral force from the rigid ring tire model saturates at a slip angle around 5°, 4.5°and 4°at vertical loads of 13 kN (3000 lbs), 27 kN (6000 lbs) and 40 kN (9000 lbs), respectively. In general, the lateral characteristics predicted by the rigid ring tire model and the simulations are considered in good agreement, at all vertical loads and slip angles.

Table 11.3: Vertical steady state displacement values at 586 kPa (85 psi) inflation pressure and different vertical loads over snow

Vertical Load (kN)	Rigid Ring Tire Model	Simulations
13	34	39
27	52	48
40	69	65

Table 11.3 shows the vertical steady-state displacement of the truck tire running over 50 mm snow at 586 kPa (85 psi) inflation pressure and different vertical loads for both rigid ring tire model and simulations. The results show that as the vertical load increase the vertical steady-state displacement increase for both rigid ring tire model and simulations. The predicted vertical displacement obtained from the rigid ring tire model is considered in good agreement with that obtained from the simulations at all vertical loads.

Generally, the hard surface, wet surface and snow exhibit similar characteristics in steering, braking, and accelerating. However, the difference in peak values is due to the difference in coefficient of friction. In regards to the vertical characteristics, all three models exhibit similar characteristics.

The validation results of the rigid ring tire model versus simulations for a truck tire running over 50 mm snow at inflation pressures of 380 kPa (55 psi), and 758 kPa (110 psi) and vertical loads of 13 kN (3000 lbs), 27 kN (6000 lbs), and 40 kN (9000 lbs) are given in appendix C.3. The results shown in appendix C.3 are following approximately the same trend as that shown in figure 11.13 and table 11.3.

11.3.4 Tire-soft terrain characteristics

Figure 11.14 shows the terrain dependent results of the rigid ring tire model and simulations of a tire running over dry sand, the results include the longitudinal force versus slip, lateral force versus slip angle.

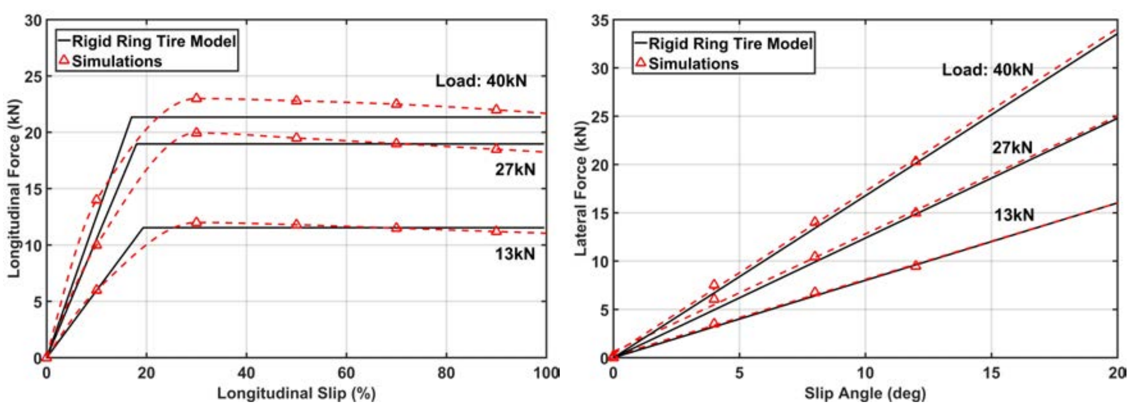

(a) Longitudinal model

(b) Lateral model

Figure 11.14: Rigid ring tire model versus simulations at 586 kPa (85 psi) inflation pressure and different vertical load for all in-plane and out-of-plane reactions over dry sand

Figure 11.14a shows the longitudinal force as a function of longitudinal slip predicted from the rigid ring tire model and the simulations over dry sand. The linear part of the longitudinal force as a function of the longitudinal slip is well captured by the rigid ring tire model in comparison to the simulations at small longitudinal slip. As the longitudinal slip increases the predicted longitudinal force from the rigid ring tire model saturates at a longitudinal slip of approximately 20%, 18% and 15% at vertical loads of 13 kN (3000 lbs), 27 kN (6000 lbs) and 40 kN (9000 lbs), respectively. The predicted longitudinal force from the rigid ring model over soft terrain is captured weakly, as the longitudinal tire reaction over soft terrain is highly nonlinear and does not saturate as a function of longitudinal slip. The peak longitudinal force predicted by the rigid ring tire model at 40 kN (9000 *lbs*) vertical load is almost equal to that of the simulation which is around 21 kN (4720 lbs) longitudinal force.

The reduction in longitudinal force in the nonlinear part was also noticed during field testing [155] for a dual tires size 20.8R42 running over three different soft soils at an axle load of 81 kN (18210 lbs) and tire pressure pressure of 83 kPa (12 psi). The study reported a reduction of roughly 25% in longitudinal force between 40% and 80% longitudinal slip. It was also concluded that as soils become softer the tire demonstrated a greater different in tractive efficiency (longitudinal force divided by vertical load).

Figure 11.14b shows the lateral (cornering) force as a function of slip angle predicted from the rigid ring tire model and the simulations for the truck tire running over dry sand at 586 kPa (85 psi) inflation pressure and different vertical load. The lateral force as a function of the slip angle is considered in good agreement between the rigid ring tire model and the simulations at all vertical loads and slip angles. It should be noted that unlike the hard surface the lateral force over soft terrain does not saturate and this behavior has been deployed in the rigid ring tire model. The maximum lateral force recorded is around 15 kN (3375 lbs), 25 kN (5620 lbs) and 35 kN (7868 lbs) at a slip angle of 20°and vertical loads of 13 kN (3000 lbs), 27 kN (6000 lbs) and 40 kN (9000 lbs), respectively. In general, the lateral characteristics predicted by the rigid ring tire model and the simulations are considered in good agreement, at all vertical loads and slip angles.

Table 11.4: Vertical steady state displacement values at 586 kPa (85 psi) inflation pressure and different vertical loads over dry sand

Vertical Load (kN)	Rigid Ring Tire Model	Simulations
13	106	112
27	135	143
40	169	165

Table 11.4 shows the vertical steady-state displacement of the truck tire running over dry sand at 586 kPa (85 psi) inflation pressure and different vertical loads for both rigid ring tire model and simulations. The results show that as the vertical load increase the vertical steady-state displacement increase for both rigid ring tire model and simulations. The predicted vertical displacement obtained from the rigid ring tire model is considered in good agreement with that obtained from the simulations at all vertical loads.

The validation results of the rigid ring tire model versus simulations for a truck tire running over dry sand at inflation pressures of 380 kPa (55 psi), and 758 kPa (110 psi) and vertical loads of 13 kN (3000 lbs), 27 kN (6000 lbs), and 40 kN (9000 lbs) are given in appendix C.4. The results shown in appendix C.4 are following approximately the same trend as that shown in figure 11.14 and table

11.4. Figure 11.15 shows the results of the rigid ring tire model and the simulations for the truck tire running over sandy loam with 25% moisture at 586 kPa (85 psi) inflation pressure and different vertical loads.

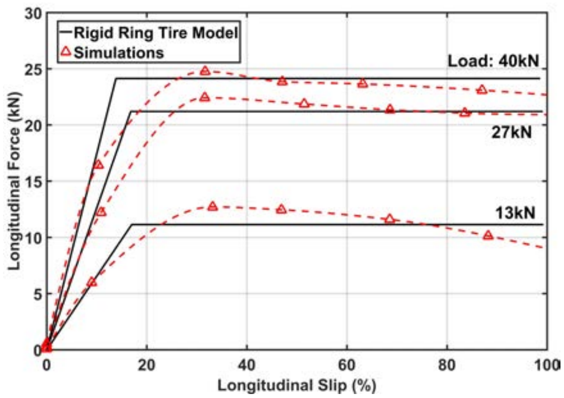

(a) Longitudinal model

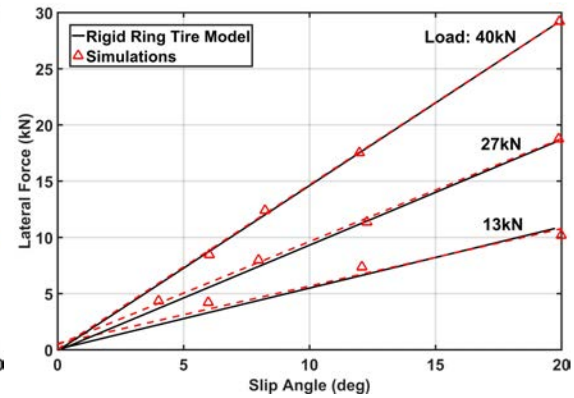

(b) Lateral model

Figure 11.15: Rigid ring tire model versus simulations at 586 kPa (85 psi) inflation pressure and different vertical loads for all in-plane and out-of-plane reactions over sandy loam with 25% moisture

Figure 11.15a shows the longitudinal force as a function of longitudinal slip predicted by the rigid ring tire model and the simulations over sandy loam with 25% moisture content. The linear part of the longitudinal force as a function of the longitudinal slip is well captured by the rigid ring tire model in comparison to the simulations at small longitudinal slip. As the longitudinal slip increase after the linear part the longitudinal force predicted from the rigid ring tire model saturates at a longitudinal slip of 17%, 16% and 14% at vertical loads of 13 kN (3000 lbs), 27 kN (6000 lbs), and 40 kN (9000 lbs), respectively. The peak longitudinal force predicted from simulations is around 25 kN (5620 lbs) at 30% slip and 24 kN (5400 lbs) vertical load, which is around 4% different from that predicted by the rigid ring tire model. The longitudinal force as a function of the longitudinal slip is considered nonlinear after the peak value which is not captured by the rigid ring model. In general, the rigid ring tire model well predicts the longitudinal force and longitudinal stiffness during the linear part of the longitudinal force versus slip curve for all vertical loads.

Figure 11.15b shows the lateral (cornering) force as a function of slip angle predicted from rigid ring tire model and the simulations over sandy loam with 25% moisture. The lateral force as a function of the slip angle is considered in good agreement between the rigid ring tire model and the simulations, at all vertical loads and slip angles. It should be noted that unlike the hard surface the lateral force over soft terrain does not saturate and this behavior has been deployed in the rigid ring tire model. The lateral forces predicted by the rigid ring tire model at

20°slip angle are 7 kN (1575 lbs), 19 kN (4270 lbs) and 30 kN (6745 lbs) at vertical loads 13 kN (3000 lbs), 27 kN (6000 lbs), and 40 kN (9000 lbs), respectively. In general, the lateral characteristics predicted by the rigid ring tire model and the simulations are considered in good agreement, at all vertical loads and slip angles.

Table 11.5: Vertical steady state displacement values at 586 kPa (85 psi) inflation pressure and different vertical loads over sandy loam

Vertical Load (kN)	Rigid Ring Tire Model	Simulations
13	79	76
27	107	112
40	123	138

Table 11.5 shows the vertical steady-state displacement of the truck tire running over dry sand at 586 kPa (85 psi) inflation pressure and different vertical loads for both rigid ring tire model and simulations. The results show that as the vertical load increase the vertical steady-state displacement increase for both rigid ring tire model and simulations. In general, the predicted vertical displacement obtained from the rigid ring tire model is in good agreement with that obtained from the simulations at all vertical loads.

The validation results of the rigid ring tire model versus simulations for a truck tire running over sandy loam at inflation pressures of 380 kPa (55 psi), and 758 kPa (110 psi) and vertical loads of 13 kN (3000 lbs), 27 kN (6000 lbs), and 40 kN (9000 lbs) are given in appendix C.5. The results shown in appendix C.5 are following approximately the same trend as that shown in figure 11.15 and table 11.5.

Figure 11.16 shows the predicted results obtained from the rigid ring tire model and simulations for the truck tire running over 10% moist sand at 586 kPa (85 psi) inflation pressure and different vertical loads.

Figure 11.16a shows the longitudinal force as a function of longitudinal slip predicted by the rigid ring tire model and the simulations over moist sand with 10% moisture content. The linear part of the longitudinal force as a function of the longitudinal slip is well captured by the rigid ring tire model in comparison to the simulations at small longitudinal slip. As the longitudinal slip increases the longitudinal force predicted from the rigid ring tire model saturates at a longitudinal slip of 20%, 18%, and 16% at vertical loads of 13 kN (3000 lbs), 27 kN (6000 lbs), and 40 kN (9000 lbs), respectively. The longitudinal force as a function of the longitudinal slip is considered nonlinear after the peak value which is not captured by the rigid ring model. In general, the rigid ring tire model well predicts the longitudinal force at all vertical loads in the linear part of the longitudinal force versus slip curve.

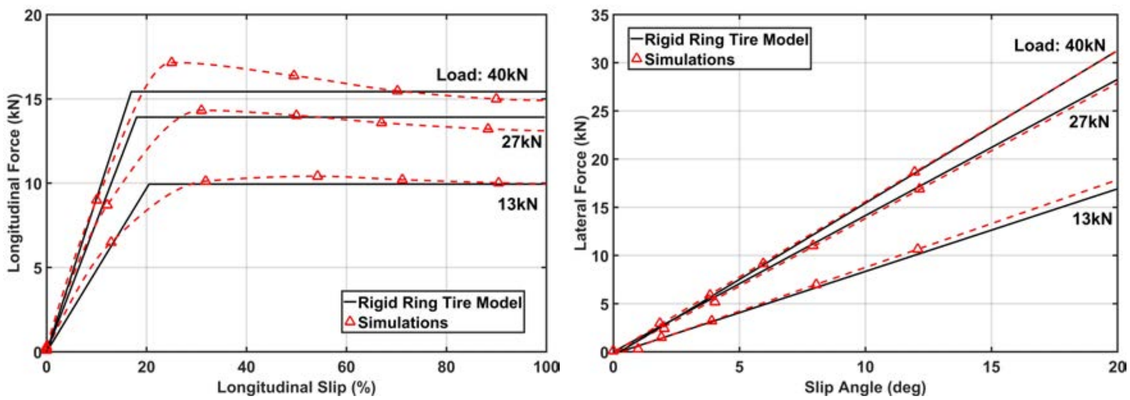

(a) Longitudinal model (b) Lateral model

Figure 11.16: Rigid ring tire model versus simulations at 586 kPa (85 psi) inflation pressure and different vertical loads for all in-plane and out-of-plane reactions over 10% moist sand

Figure 11.16b shows the lateral (cornering) force as a function of slip angle predicted from the rigid ring tire model and the simulations over moist sand with 10% moisture. The lateral force as a function of the slip angle is considered in good agreement between the rigid ring tire model and the simulations over 10% moist sand especially at all vertical loads and all slip angles. The lateral forces predicted form the rigid ring tire model at 20°slip angle are 14 kN (3150 lbs), 25 kN (5620 lbs) and 32 kN (7195 lbs) at 13 kN (3000 lbs), 27 kN (6000 lbs), and 40 kN (9000 lbs), respectively. In general, the lateral characteristics predicted by the rigid ring tire model and the simulations are considered in good agreement, at all vertical loads and slip angles.

Table 11.6: Vertical steady state displacement values at 586 kPa (85 psi) inflation pressure and different vertical loads over 10% moist sand

Vertical Load (kN)	Rigid Ring Tire Model	Simulations
13	145	165
27	178	196
40	193	222

Table 11.4 shows the vertical steady-state displacement of the truck tire running over dry sand at 586 kPa (85 psi) inflation pressure and different vertical loads for both rigid ring tire model and simulations. The results show that as the vertical load increase the vertical steady-state displacement increase for both rigid ring tire model and simulations. In general, the predicted vertical displacement obtained from the rigid ring tire model is in good agreement with that obtained from the

simulations at all vertical loads.

The validation results of the rigid ring tire model versus simulations for a truck tire running over 10% moist sand at inflation pressures of 380 kPa (55 psi), and 758 kPa (110 psi) and vertical loads of 13 kN (3000 lbs), 27 kN (6000 lbs), and 40 kN (9000 lbs) are given in appendix C.6. The results shown in appendix C.6 are following approximately the same trend as that shown in figure 11.16 and table 11.6.

11.4 Summary

The development of a rigid ring tire model was performed using Matlab/Simulink. The model included both in-plane and out-of-plane rigid ring tire models. The in-plane models include the in-plane rotational tire reaction, the vertical tire reaction, and the longitudinal tire reaction. The out-of-plane models include the out-of-plane rotational tire reaction and the lateral tire reaction. The effect of several operating conditions was investigated including the tire inflation pressure, the vertical load, and different terrains. The terrains examined included dry and wet hard surfaces, snow, dry and moist sand.

Over a hard surface, the rigid ring tire model showed a good agreement with the simulations for the in-plane rotational model, vertical model, out-of-plane rotational model, and translational model. While the longitudinal and lateral models showed a similar trend for a longitudinal slip in comparison to the simulations results. For the rigid ring tire model running over the wet surface and hard surface covered with snow, a similar trend to that of the hard surface is noticed. Generally, the rigid ring tire model over wet surface and snow is in good agreement with that of simulation results.

The off-road terrains examined included dry sand, sandy loam, and moist sand. In the case of the rigid ring tire model running over dry sand, it was concluded that the rigid ring tire model is in good agreement with the simulation results for the vertical and lateral model. However, the longitudinal tire reaction determined using the rigid ring tire model saturates at a certain force based on the coefficient of friction, while the simulation curve continues to show a nonlinear behavior. In the case of the tire running over sandy loam and moist sand, a similar conclusion to that of the dry sand was observed.

The validation results of the rigid ring tire model running over different terrain at several inflation pressures and vertical loads are provided in appendix C. The results show a good agreement between the rigid ring tire model and the simulation results.

CHAPTER 12

CONCLUSIONS AND FUTURE WORK

In this chapter, the conclusions emerged from this study are described. In addition, the major contributions, future work, and recommendations are then presented. At the end of this chapter, the refereed journals and conferences publications are listed.

12.1 Conclusions

This study dealt with modeling and analysis of a truck tire-terrain interaction. The tire used in this research is the off-road RHD tire size 315/80R22.5, which was modeled using Finite Element Analysis (FEA) technique. The hard surface terrain was also modeled using the FEA technique while the soft terrains were modeled using the meshless technique called Smoothed-Particle Hydrodynamics (SPH). The most important conclusions emerged from this research work are listed below:

1. Based on the literature review of the published research in the field of this study, it was concluded that there are incomplete or no publications in regards to the modeling of moist soils, investigating truck hydroplaning, a rigid ring tire model that can be integrated into a full vehicle model.

2. The FEA RHD 315/80R22.5 drive tire was validated in static and dynamic domain against measured data, the results showed a good agreement.

3. Calibration was performed to model several terrains using Smoothed-Particle Hydrodynamics techniques (SPH). The calibration was performed using pressure sinkage and direct shear-strength tests, and results were calibrated against published terramechanics data. The effect of various parameters, such as terrain material properties and shear box displacement speed on the terrain behavior were investigated. It was concluded that the shear box displacement speed has minimal effect on shearing characteristics if kept between 1 and 10 mm/s. Furthermore, the yield strength has a minimal

effect on the shearing characteristics, however, it has a high impact on the pressure-sinkage relationship.

4. Two novel soil moisturizing techniques were proposed and investigated. The first technique relies on linear interpolation between published terramechanics data of sandy loam. The second technique pressurizes water particles into sand particles to model moist sand with different moisture content based on a percentage of the wet volume. The first (interpolation) technique was successfully used to model sandy loam with different soul moisture content. The second (moisturizing) technique was successfully used to model moist sand with different moisture content. The moisturizing technique was validated against laboratory testing performed at similar conditions. It was concluded that the results obtained from the proposed technique and those obtained from testing are in good agreement.

5. The tire-terrain interaction was performed to compute the in-plane and out-of-plane rigid ring model parameters of the truck tire running over flooded surface and snow at different operating conditions. It was concluded that the developed tire-terrain interaction model was successful in predicting the in-plane and out-of-plane rigid ring tire model parameters and fall within previously published data.

6. The calibrated moist soils were further used to investigate the effect of operating conditions (inflation pressure, vertical load) and moisture content on tire-terrain interaction. The in-plane and out-of-plane rigid ring tire model parameters were successfully computed for both sandy loam and moist sand with different moisture content. It was concluded that both techniques were in good agreement.

7. An extensive analytical analysis of the rolling resistance coefficient of the RHD truck tire running over different terrains was conducted using Artificial Neural Network and Genetic Algorithm. The relationship between the rolling resistance coefficient and the operating conditions was developed and presented for both algorithms. It was concluded that the Artificial Neural Network has a better fitting in regards to the observed versus predicted rolling resistance in comparison to that of the Genetic Algorithm. While the Genetic Algorithm has a better numerical equation in terms of complexity in comparison to that of the Artificial Neural Network.

8. The hydroplaning phenomenon of the truck tire was explored and investigated. A tire-road model was designed to simulate the hydroplaning phenomenon using a combination of Finite Element Analysis and Smoothed-Particle Hydrodynamics techniques. The model was simulated under different operating conditions (inflation pressure, vertical load, water depth,

and tread depth). The results obtained from simulations were then validated against the NASA equation and Horne's equation for truck tires. The operating conditions were then used as input data (input array) and the associated hydroplaning speed was used as an output for a Genetic Algorithm to formulate an equation that relates the inputs to the output. It was concluded that the developed equation well predicts the hydroplaning speed with respect to various operating conditions.

9. The simulated results of the multi-truck tire-gravelly soil interaction obtained were validated against physical testing performed in Gothenburg, Sweden by Volvo Groups Truck Technology. It was concluded that the simulation results and the physical measurements were in good agreement.

10. The results of the rigid ring tire model were validated against simulations for different terrains and operating conditions. It was concluded that the rigid ring model is in good agreement with the simulation results.

12.2 Major Contributions

The major contributions achieved thorough out this study are as follows:

1. A novel virtual soil moisturizing technique to better model the real-life soil environments. The technique presented pressurizes water particles into sand particles to produce moist sand. The moisture content can be controlled by the volume of water pressurized into the sand. The moist sand generated included a range of moisture content ranging from 10 to 50% moisture.

2. A novel tire-flooded surface interaction model was presented for the first time to model truck tire running over a thick layers of water.

3. Development of a new virtual off-road in-plane and out-of-plane rigid ring truck tire model for tire-moist soil interaction. The developed model uses moist soil generated to determine the rigid ring model parameters over these soil and examines the effect of the moisture content in soils on the tire operational performance and characteristics.

4. Evaluation of soil moisturizing effect on tire operational performance as compared to that of the simple soil model. The effect of moisture content on tire-terrain interaction using hybrid FEA-SPH models was examined for the first time.

5. A novel equation to predict the rolling resistance coefficient of a truck tire running over different terrains and operating conditions using Artificial Neural Network and Genetic Algorithm. The developed equations proved to successfully predict the rolling resistance coefficient.

6. A novel equation to predict truck tire hydroplaning speed as a function of different operating conditions was developed. The developed equation was proven to successfully predict the hydroplaning speed under different conditions.

7. The integration of the developed rigid ring tire model with the Volvo transportation model was performed for the first time to enhance the simulation performance of the full vehicle model.

8. Virtual multi-tire terrain interaction was introduced for the first time and validated against actual physical testing in the fields at Volvo Facility in Sweden.

12.3 Future Work and Recommendations

The future work and recommendations include a list of research ideas that are helpful for a better understanding of tire-terrain interaction:

1. Perform physical measurements of pressure-sinkage and shear-strength tests for moist sand at different moisture content. The measurements will help to better understand the effect of soil moisture on soil terramechanics characteristics, and to validate the presented models.

2. Perform further physical testing of the truck tire over different terrains including snow and flooded surface. The measurements will quantitatively validate the results obtained in this research work and will help tune the full vehicle model.

3. Further, investigate operating conditions on tire hydroplaning speed, the operating conditions can further include tread depth and tread design. This will produce a new set of data that should be added to the data obtained in chapter 9 and into the equation developed to produce a more generalized equation for different types of tires.

4. Optimize the soil calibration techniques by using Pam-Opt to generate better-calibrated soil. The optimized soil calibration will lead to better soil characteristics and to a less compromise between pressure-sinkage and shear-strength.

5. Further, examine the particle layering technique to include a wider range of terrains, for example, clayey soil topped with sand. The particles pressurizing technique can be further used to wider terrains that are more realistic. These terrains can also include compacted sand topped with loose sand.

6. Optimize tire design parameters leading to the best possible rolling/motion resistances and thereby enhanced the energy efficiency, and improved cornering characteristics.

7. Investigate the terramechanics characteristics of mud in terms of pressure-sinkage and shear-strength using the Smoothed-Particle Hydrodynamics technique. The mud can be further implemented as several layers of SPH on top of saturated soil.

12.4 Publications

The publications completed during the course of PhD are listed below:

Referred journal papers

1. El-Sayegh, Zeinab, Moustafa El-Gindy, Inge Johansson, and Fredrik Oijer. "Truck tyre-terrain interaction modelling and testing: literature survey." International Journal of Vehicle Systems Modelling and Testing 12, no. 3-4 (2017): 163-216.

2. El-Sayegh, Zeinab, and Moustafa El-Gindy. "Sensitivity analysis of truck tyre hydroplaning speed using FEA-SPH model." International Journal of Vehicle Systems Modelling and Testing 12, no. 1-2 (2017): 143-161.

3. El-Sayegh, Zeinab, Moustafa El-Gindy, Inge Johansson, and Fredrik Oijer. "Improved tire-soil interaction model using FEA-SPH simulation." Journal of Terramechanics 78 (2018): 53-62.

4. El-Sayegh, Zeinab, Moustafa El-Gindy. "Cornering characteristics of a truck tire on wet surface using finite element analysis and smoothed-particle hydrodynamics". International Journal of Dynamics and Control 6.4 (2018): 1567-1576.

5. El-Sayegh, Zeinab, Moustafa El-Gindy, Inge Johansson, and Fredrik Oijer. "Development and validation of an off-road rigid ring truck tyre model." International Journal of Vehicle Systems Modelling and Testing 13, no. 3 (2019): 275-294.

6. El-Sayegh, Zeinab, Moustafa El-Gindy, Inge Johansson, and Fredrik Oijer. " Modelling Tire-Moist Terrain Interaction Using Advanced Computational Techniques". Journal of Terramechanics (under review), 2020.

7. El-Sayegh, Zeinab, Moustafa El-Gindy, Inge Johansson, and Fredrik Oijer. "Development and validation of off-road tire-gravel interaction using

advanced computational techniques". Journal of Terramechanics (under review), 2019.

8. El-Sayegh, Zeinab and Moustafa El-Gindy. "Modelling and prediction of tyre-snow interaction using finite element analysis and smoothed particle hydrodynamics techniques". Proceedings of the Institution of Mechanical Engineers, Part D: Journal of Automobile Engineering, 233(7):1783-1792, 2019.

9. El-Sayegh, Zeinab, Mirwais Sharifi, Fatemeh Gheshlaghi, and Aref Mardani. "Development of an HLFS agricultural tire model using FEA technique." SN Applied Sciences 1, no. 11 (2019): 1454.

10. El-Sayegh, Zeinab, Moustafa El-Gindy,." Rolling resistance prediction of off-road tire using advanced simulation and analytical techniques. Proceedings of the Institution of Mechanical Engineers", SN Applied Sciences (under review).

11. Gheshlaghi, Fatemeh, El-Sayegh Zeinab, Sharifi Mirwais, and Moustafa El-Gindy. "'Prediction and validation of terramechanics models for estimation of tyre rolling resistance coefficient". Int. J. Vehicle Systems Modelling and Testing, 14, no. 3-4 (2020) 1-12.

12. Gheshlaghi, Fatemeh, El-Sayegh Zeinab, and Aref Mardani. "Prediction of Energy Dissipation of Wheeled Agricultural Vehicles Using Smoothed-Particle Hydrodynamics Techniques". Int. J. Vehicle Systems Modelling and Testing, 14, no. 3-4 (2020) 1-12.

Referred conference papers

1. El-Sayegh, Zeinab, Moustafa El-Gindy, Inge Johansson, and Fredrik Oijer. "Modeling of interaction between tire and wet surface using finite element analysis and smoothed-particle hydrodynamics techniques." SAE Technical Paper 2018-01 (2018): 1118.

2. El-Sayegh, Zeinab, Moustafa El-Gindy, Inge Johansson, and Fredrik Oijer. "Off-road soft terrain modeling using smoothed particle hydrodynamics technique". 15th International Conference on Design Education, International Design Engineering Technical Conferences, IDETC 2018-85005, Quebec City, Quebec, Canada. August 26-29, 2018.

3. El-Sayegh, Zeinab, Moustafa El-Gindy, Inge Johansson, and Fredrik Oijer. "development of in-plane rigid ring truck tire model over flooded surface using sph technique". 15th International Conference on Design Education,

International Design Engineering Technical Conferences, IDETC 2018-85006, Quebec City, Quebec, Canada, August 26-29,2018.

4. Sharifi, Mirwais, Zeinab El-Sayegh, and Moustafa El-Gindy. "Sensitivity Analysis of Tire-Soil Interaction Using Finite Element Analysis and Smoothed Particle Hydrodynamics Techniques". No. 2019-01-0174. SAE Technical Paper, 2019.

5. El-Sayegh, Zeinab, Moustafa El-Gindy, Inge Johansson, and Fredrik Oijer. "development of out-of-plane rigid ring truck tire model parameters over flooded surface using fea-sph techniques". 16th International Conference on Design Education, International Design Engineering Technical Conferences, IDETC 2019- 97036, Anahiem, California, USA. August 18-21, 2019.

6. El-Sayegh, Zeinab, Gheshlaghi Fatemeh, Sharifi Mirwais, Moustafa El-Gindy. "Prediction and Validation of an Agricultural Tire-Soil Interaction Using Advanced Modelling Techniques". Tire Science and Technology, TST-19-212, 2019.

LIST OF REFERENCES

[1] Jo Yung Wong. *Theory of ground vehicles.* John Wiley & Sons, 2008.

[2] Jeffrey L Slade. Development of a new off-road rigid ring model for truck tires using finite element analysis techniques. Master's thesis, The Pennsylvania State University, 2009.

[3] PAM System International. Pam-crash user manual version 2014. *ESI Group*, 2014.

[4] Geoengineering Research Group. Shear strength properties of a construction sand under different water contents. Technical report, Carleton University, 2019.

[5] Seokyong Chae. *Nonlinear finite element modeling and analysis of a truck tire.* PhD thesis, The Pennsylvania State University, 2006.

[6] Shruthi Prakash. Nonlinear finite element analysis of shrinking reinforced concrete slabs-on-ground, 2018.

[7] The evolution of the wheel. https://www.historyanswers.co.uk/ inventions/ how-was-stained-glass-made/. Accessed: 2017-06-12.

[8] David W Anthony. *The horse, the wheel, and language: how Bronze-Age riders from the Eurasian steppes shaped the modern world.* Princeton University Press, 2010.

[9] Charles Goodyear. *Gum-elastic and its Varieties: With a Detailed Account of its Applications and Uses, and of the Discovery of Vulcanization*, volume 2. Published for the author, 1853.

[10] The history of pneumatic devices; pneumatic devices - pneumatic tube. http://inventors.about.com/library/inventors/blpneumatic.htm. Accessed: 2017-06-12.

[11] Stephen L Harp. *Marketing Michelin: Advertising and cultural identity in twentieth-century France.* JHU Press, 2001.

[12] Samuel Mercer. Locked wheel skid performance of various tires on clean, dry road surfaces. *Highway Research Board Bulletin*, 186:8–25, 1958.

[13] Walter B Horne and Trafford JW Leland. Influence of tire tread pattern and runway surface condition on braking friction and rolling resistance of a modern aircraft tire. 1962.

[14] W Gengenbach. Experimantelle untersuchung von reifen auf nasser fahrbahn (experimental investigation of tires on wet tracks). *Automobiltechnische Zeitschrift, Yol*, 70:310–316, 1968.

[15] KA Grosch and G Maycock. Influence of test conditions on wet skid resistance of tire tread compounds. *Rubber Chemistry and Technology*, 41(2):477–494, 1968.

[16] KE Holmes. Braking force/braking slip: Measurements over a range of conditions between 0 and 100 per cent slip. *Transportation Research Board*, 1970.

[17] Samuel K Clark. *Mechanics of pneumatic tires*. US Government Printing Office, 1981.

[18] Hans Pacejka. *Tire and vehicle dynamics*. Elsevier, 2005.

[19] William F Milliken, Douglas L Milliken, et al. *Race car vehicle dynamics*, volume 400. Society of Automotive Engineers Warrendale, 1995.

[20] K Anupam, S Srirangam, A Scarpas, C Kasbergen, and M Kane. Study of cornering maneuvers of a pneumatic tire on asphalt pavement surfaces using the finite element method. *Transportation Research Record: Journal of the Transportation Research Board*, (2457):129–139, 2014.

[21] Paul Haney. Rubber friction. *The Racing & High-Performance Tire, Sports Car Magazine, January*, 2004.

[22] Thomas D Gillespie. Fundamentals of vehicle dynamics. Technical report, SAE Technical Paper, 1992.

[23] Evgeny Barkanov. Introduction to the finite element method. *Institute of Materials and Structures Faculty of Civil Engineering Riga Technical University*, 2001.

[24] Jun Sui and John Hirshey. Evaluation on analytical tire models for vehicle vertical vibration simulation using virtual tire testing method. Technical report, SAE Technical Paper, 1999.

[25] Egbert Bakker, Lars Nyborg, and Hans B Pacejka. Tyre modelling for use in vehicle dynamics studies. Technical report, SAE Technical Paper, 1987.

[26] HB Pacejka and IJM Besselink. Magic formula tyre model with transient properties. *Vehicle system dynamics*, 27(S1):234–249, 1997.

[27] Peter WA Zegelaar and Hans B Pacejka. Dynamic tyre responses to brake torque variations. *Vehicle System Dynamics*, 27(S1):65–79, 1997.

[28] PWA Zegelaar and HB Pacejka. The in-plane dynamics of tyres on uneven roads. *Vehicle System Dynamics*, 25(S1):714–730, 1996.

[29] Son-Joo Kim and Arvin R Savkoor. The contact problem of in-plane rolling of tires on a flat road. *Vehicle System Dynamics*, 27(S1):189–206, 1997.

[30] Kazuya Yoshida and Genya Ishigami. Steering characteristics of a rigid wheel for exploration on loose soil. In *2004 IEEE/RSJ International Conference on Intelligent Robots and Systems (IROS)(IEEE Cat. No. 04CH37566)*, volume 4, pages 3995–4000. IEEE, 2004.

[31] Norm Frey. Development of a rigid ring tire model and comparison among various tire models for ride comfort simulations. 2009.

[32] Ari J Tuononen, Lassi Hartikainen, Frank Petry, and Stephan Westermann. Parameterization of in-plane rigid ring tire model from instrumented vehicle measurements. In *Proceedings of the 11th International Symposium on Advanced Vehicle Control (AVEC '12)*, pages 9–12, 2012.

[33] Brendan J Chan and Corina Sandu. Development of a 3-d quasi-static tyre model for on-road and off-road vehicle dynamics simulations: Part i–on-road flexible tyre model. *International Journal of Vehicle Systems Modelling and Testing*, 9(1):77–105, 2014.

[34] Brendan J Chan and Corina Sandu. Development of a 3-d quasi-static tyre model for on-road and off-road vehicle dynamics simulations: Part ii–off-road rigid wheel model. *International Journal of Vehicle Systems Modelling and Testing*, 9(2):107–136, 2014.

[35] Brendan J Chan and Corina Sandu. Development of a 3-d quasi-static tyre model for on-road and off-road vehicle dynamics simulations: Part iii–off-road flexible wheel model. *International Journal of Vehicle Systems Modelling and Testing*, 9(2):151–176, 2014.

[36] Corina Sandu, Shahyar Taheri, Saied Taheri, and David Gorsich. Hybrid soft soil tire model (hsstm). part i: Tire material and structure modeling. *Journal of Terramechanics*, 86:1–13, 2019.

[37] C Sandu, Sh Taheri, S Taheri, and D Gorsich. Hybrid soft soil tire model (hsstm). part ii: Tire-terrain interaction. *Journal of Terramechanics*, 86:15–29, 2019.

[38] C Sandu, Sh Taheri, S Taheri, S Els, and E Jimenez. Hybrid soft soil tire model (hsstm). part iii: Model parameterization and validation. *Journal of Terramechanics*, 88:1–15, 2020.

[39] Walter Ritz. Über eine neue methode zur lösung gewisser variationsprobleme der mathematischen physik. *Journal für die reine und angewandte Mathematik*, 135:1–61, 1909.

[40] Richard Courant. Variational methods for the solution of problems of equilibrium and vibrations. *Lecture Notes in Pure and Applied Mathematics*, pages 1–1, 1943.

[41] Donald S Dugdale. Yielding of steel sheets containing slits. *Journal of the Mechanics and Physics of Solids*, 8(2):100–104, 1960.

[42] John H Argyris. Energy theorems and structural analysis: a generalized discourse with applications on energy principles of structural analysis including the effects of temperature and non-linear stress-strain relations part i. general theory. *Aircraft Engineering and Aerospace Technology*, 27(2):42–58, 1955.

[43] M Jon Turner. Stiffness and deflection analysis of complex structures. *journal of the Aeronautical Sciences*, 2012.

[44] Alexander Hrennikoff. Solution of problems of elasticity by the framework method. *Journal of applied mechanics*, 8(4):169–175, 1941.

[45] RN Yong, EA Fattah, and P Boonsinsuk. Analysis and prediction of tyre-soil interaction and performance using finite elements. *Journal of Terramechanics*, 15(1):43–63, 1978.

[46] Muhammad Aslam Noor. An iterative scheme for a class of quasi variational inequalities. *Journal of Mathematical Analysis and Applications*, 110(2):463–468, 1985.

[47] J De Eskinazi, K Ishihara, H Volk, and TC Warholic. Towards predicting relative belt edge endurance with the finite element method. *Tire Science and Technology*, 18(4):216–235, 1990.

[48] T Hiroma, S Wanjii, T Kataoka, and Y Ota. Stress analysis using fem on stress distribution under a wheel considering friction with adhesion between a wheel and soil. *Journal of terramechanics*, 34(4):225–233, 1997.

[49] M Koishi, K Kabe, and M Shiratori. Tire cornering simulation using an explicit finite element analysis code. *Tire Science and Technology*, 26(2):109–119, 1998.

[50] Melvin Mooney. A theory of large elastic deformation. *Journal of applied physics*, 11(9):582–592, 1940.

[51] OH Yeoh. Characterization of elastic properties of carbon-black-filled rubber vulcanizates. *Rubber chemistry and technology*, 63(5):792–805, 1990.

[52] Thomas L Ford and Fred S Charles. Heavy duty truck tire engineering. Technical report, SAE Technical Paper, 1988.

[53] Yin-Ping Chang. *Nonlinear FEA rotating tire modeling for transient response simulations*. PhD thesis, Pennsylvania State University, 2002.

[54] Pedro Yap. Measurement of radial truck tire dry cornering characteristics. Technical report, SAE Technical Paper, 1991.

[55] P Davis, V Martinson, T Yager, and S Stubbs. 26x6. 6 radial-belted aircraft tire performance. *Progress in Technology*, 66:251–260, 1997.

[56] Kristian Lee Lardner. Prediction of the off-road rigid-ring model parameters for truck tire and soft soil interactions. Master's thesis, University of Ontario Institute of Technology, Canada, 2017.

[57] O Onafeko. Instrumentation for measuring radial and tangential stresses beneath rigid wheels. *Journal of Terramechanics*, 1(3):61–68, 1964.

[58] O Onafeko and AR Reece. Soil stresses and deformations beneath rigid wheels. *Journal of Terramechanics*, 4(1):59–80, 1967.

[59] Jo-Yung Wong and AR Reece. Prediction of rigid wheel performance based on the analysis of soil-wheel stresses part i. performance of driven rigid wheels. *Journal of Terramechanics*, 4(1):81–98, 1967.

[60] Jo-Yung Wong and AR Reece. Prediction of rigid wheel performance based on the analysis of soil-wheel stresses: Part ii. performance of towed rigid wheels. *Journal of Terramechanics*, 4(2):7–25, 1967.

[61] Lok-Man Chu and Jian-Hua Yin. Comparison of interface shear strength of soil nails measured by both direct shear box tests and pullout tests. *Journal of geotechnical and geoenvironmental engineering*, 131(9):1097–1107, 2005.

[62] Jo Yung Wong. *Terramechanics and off-road vehicle engineering: terrain behaviour, off-road vehicle performance and design*. Butterworth-heinemann, 2009.

[63] Shahram Shokouhfar. *A Virtual Test Platform for Analyses of Rolling Tyres on Rigid and Deformable Terrains*. PhD thesis, Concordia University, 2017.

[64] Hamed Niroumand. *Soil Reinforcement for Anchor Plates and Uplift Response*. Butterworth-Heinemann, 2017.

[65] Rui He, Corina Sandu, Aamir K Khan, A Glenn Guthrie, P Schalk Els, and Herman A Hamersma. Review of terramechanics models and their applicability to real-time applications. *Journal of Terramechanics*, 81:3–22, 2019.

[66] Corina Sandu, Adrian Sandu, and L Li. Stochastic modeling of terrain profiles and soil parameters. *SAE transactions*, pages 211–220, 2005.

[67] L Li and C Sandu. Modeling and simulation of 2d arma terrain models for vehicle dynamics applications. *SAE 2007 Transactions*, 116(6), 2007.

[68] Scott David Naranjo, Corina Sandu, Saied Taheri, and Shahyar Taheri. Experimental testing of an off-road instrumented tire on soft soil. *Journal of Terramechanics*, 56:119–137, 2014.

[69] HyunWook Lee, Corina Sandu, and Carvel Holton. Dynamic model for the wheel–rail contact friction. *Vehicle system dynamics: Int. J. of Vehicle Mechanics and Mobility*, 50(2):299–321, 2012.

[70] Lin Li and Corina Sandu. Stochastic modelling of 1-d and 2-d terrain profiles using a polynomial chaos approach. *International Journal of Vehicle Design*, 63(2-3):305–326, 2013.

[71] Lin Li and Corina Sandu. Stochastic vehicle handling prediction using a polynomial chaos approach. *International journal of vehicle design*, 63(4):327–363, 2013.

[72] Mehran Motamedi, Saied Taheri, and Corina Sandu. Rubber–road contact: Comparison of physics-based theory and indoor experiments. *Tire Science And Technology*, 44(3):150–173, 2016.

[73] Mehran Motamedi, Saied Taheri, Corina Sandu, and Pierrick Legrand. Characterization of road profiles based on fractal properties and contact mechanics. *Rubber Chemistry and Technology*, 90(2):405–427, 2017.

[74] Rui He, Corina Sandu, and Javier E Osorio. Systematic tests for study of tire tractive performance on soft soil: Part i–experimental data collection. *Journal of Terramechanics*, 85:59–76, 2019.

[75] Rui He, Corina Sandu, and Javier E Osorio. Systematic tests for study of tire tractive performance on soft soil: Part ii–parameterization of terramechanics model and tire model. *Journal of Terramechanics*, 85:77–88, 2019.

[76] S Shoop, K Kestler, and R Haehnel. Finite element modeling of tires on snow. *Tire science and technology*, 34(1):2–37, 2006.

[77] J Hambleton and Andrew Drescher. Development of improved test rolling methods for roadway. 2008.

[78] Ryan Lescoe. Improvement of soil modeling in a tire-soil interaction using finite element analysis and smooth particle hydrodynamics. Master's thesis, The Pennsylvania State University, 2010.

[79] Soil traingle, the idaho association of soil conservation districts. http://www.oneplan.org/Water/soil-triangle.asp. Accessed: 2017-06-11.

[80] Ranvir Singh Dhillon. Development of truck tire-terrain finite element analysis models. Master's thesis, University of Ontario Institute of Technology, Canada, 2013.

[81] Mehrsa Marjani. Development of fea wide-base truck tire and soil interaction models. Master's thesis, University of Ontario Institute of Technology, Canada, 2016.

[82] Richard E Goodman, Robert L Taylor, and Tor L Brekke. A model for the mechanics of jointed rocks. *Journal of Soil Mechanics & Foundations Div*, 94:637–659, 1968.

[83] EA Wilson and B Parsons. Finite element analysis of elastic contact problems using differential displacements. *International Journal for Numerical Methods in Engineering*, 2(3):387–395, 1970.

[84] SK Chan and IS Tuba. A finite element method for contact problems of solid bodies—part i. theory and validation. *International Journal of Mechanical Sciences*, 13(7):615–625, 1971.

[85] Sh Taheri, C Sandu, S Taheri, E Pinto, and D Gorsich. A technical survey on terramechanics models for tire–terrain interaction used in modeling and simulation of wheeled vehicles. *Journal of Terramechanics*, 57:1–22, 2015.

[86] David J Benson and John O Hallquist. A single surface contact algorithm for the post-buckling analysis of shell structures. *Computer Methods in Applied Mechanics and Engineering*, 78(2):141–163, 1990.

[87] JO Hallquist, GL Goudreau, and DJ Benson. Sliding interfaces with contact-impact in large-scale lagrangian computations. *Computer methods in applied mechanics and engineering*, 51(1-3):107–137, 1985.

[88] Gentaro Hirota, Susan Fisher, A State, Chris Lee, and Henry Fuchs. An implicit finite element method for elastic solids in contact. In *Computer Animation, 2001. The Fourteenth Conference on Computer Animation. Proceedings*, pages 136–254. IEEE, 2001.

[89] Timon Rabczuk, Shao Ping Xiao, and M Sauer. Coupling of mesh-free methods with finite elements: basic concepts and test results. *International Journal for Numerical Methods in Biomedical Engineering*, 22(10):1031–1065, 2006.

[90] MI Thiyahuddin, YuanTong Gu, RB Gover, and DP Thambiratnam. Fluid–structure interaction analysis of full scale vehicle-barrier impact using coupled sph–fea. *Engineering Analysis with Boundary Elements*, 42:26–36, 2014.

[91] C Hermange, G Oger, and David Le Touzé. Development of a coupling strategy between smoothed particle hydrodynamics and finite element method for violent fluid-structure interaction problems. In *3rd International Conference on Violent Flows 2016*, 2016.

[92] Aimin Yang, Jinze Li, Hengheng Qu, Yuhang Pan, Yanhong Kang, and Yuzhu Zhang. Numerical simulation of hypervelocity impact fem-sph algorithm based on large deformation of material. 2016.

[93] Syh-Tsang Jenq, Yuen-Sheng Chiu, et al. Hydroplaning analysis for tire rolling over water film with various thicknesses using the ls-dyna fluid-structure interactive scheme. *Computers, Materials & Continua (CMC)*, 11(1):33, 2009.

[94] E Seta, Y Nakajima, T Kamegawa, and H Ogawa. Hydroplaning analysis by fem and fvm: effect of tire rolling and tire pattern on hydroplaning. *Tire Science and Technology*, 28(3):140–156, 2000.

[95] Walter B Horne and Robert C Dreher. Phenomena of pneumatic tire hydroplaning. 1963.

[96] CS Martin. Hydroplaning of tire hydroplaning final report. *Project B-608, Georgia Institute of Technology*, 1966.

[97] CG Moore and M Porter. Structural characterization of vulcanizates. part vi. the 2-mercaptobenzothiazole-accelerated natural rubber–sulfur system. *Journal of Applied Polymer Science*, 11(11):2227–2253, 1967.

[98] A Eshel. A study of tires on a wet runway. *Ampex Corp., RR*, pages 67–24, 1967.

[99] A Browne, H Cheng, and A Kistler. Dynamic hydroplaning of pneumatic tires. *Wear*, 20(1):1–28, 1972.

[100] Trafford JW Leland. An evaluation of some unbraked tire cornering force characteristics. 1972.

[101] James F Sinnamon. Hydroplaning and tread pattern hydrodynamics. 1974.

[102] H Grogger and M Weiss. Calculation of the three-dimensional free surface flow around an automobile tire. *Tire Science and Technology*, 24(1):39–49, 1996.

[103] OK Panagouli and AG Kokkalis. Skid resistance and fractal structure of pavement surface. *Chaos, Solitons & Fractals*, 9(3):493–505, 1998.

[104] Ibrahim Mustafa Janajreh. Tire having a groove wall lining for reducing formation of anomalies causing subjective user dissatisfaction, April 10 2001. US Patent 6,213,181.

[105] Longjia Chu and TF Fwa. Incorporating pavement skid resistance and hydroplaning risk considerations in asphalt mix design. *Journal of Transportation Engineering*, 142(10):04016039, 2016.

[106] Ghim Ping Ong and TF Fwa. Wet-pavement hydroplaning risk and skid resistance: modeling. *Journal of Transportation Engineering*, 133(10):590–598, 2007.

[107] C-W Oh, T-W Kim, H-Y Jeong, K-S Park, and S-N Kim. Hydroplaning simulation for a straight-grooved tire by using fdm, fem and an asymptotic method. *Journal of Mechanical Science and Technology*, 22(1):34–40, 2008.

[108] JH Choi, JR Cho, JS Woo, and KW Kim. Numerical investigation of snow traction characteristics of 3-d patterned tire. *Journal of Terramechanics*, 49(2):81–93, 2012.

[109] VE Gough. Cornering characteristics of tyres. *Automobile Engineer*, 44:137, 1954.

[110] Walter B Horne and Upshur T Joyner. Pneumatic tire hydroplaning and some effects on vehicle performance. Technical report, SAE Technical Paper, 1965.

[111] Walter B Horne, Thomas J Yager, and Don L Ivey. Recent studies to investigate effects of tire footprint aspect ratio on dynamic hydroplaning speed. In *The Tire Pavement Interface*. ASTM International, 1986.

[112] BM Gallaway, DL Ivey, G Hayes, WB Ledbetter, RM Olson, DL Woods, and RF Schiller Jr. Pavement and geometric design criteria for minimizing hydroplaning. Technical report, Federal Highway Administration, 1979.

[113] James C Wambold, EC Yeh, and John Jewett Henry. Methodology for analyzing pavement condition data (mapcon). Technical report, Maintenance and Operations Manuals for the IBM 370 Version, 1984. Volume II.

[114] L Liver Norman et al. Development and applications of intrusion grout mixed-in-place piles. *Civil Engineering, March*, pages 56–57, 1954.

[115] R Christopher and Brian H Jasperse. Deep soil mixing at the jackson lake dam. In *ASCE Geotechnical and Construction Divisions Special Conference*, volume 5, pages 25–29, 1989.

[116] Kenneth B Andromalos, Yasser A Hegazy, and Brian H Jasperse. Stabilization of soft soils by soil mixing. In *Soft ground technology*, pages 194–205. 2001.

[117] CW Fervers. Improved fem simulation model for tire–soil interaction. *Journal of Terramechanics*, 41(2):87–100, 2004.

[118] Ha H Bui, K Sako, and R Fukagawa. Numerical simulation of soil–water interaction using smoothed particle hydrodynamics (sph) method. *Journal of Terramechanics*, 44(5):339–346, 2007.

[119] H Nakashima, H Fujii, A Oida, M Momozu, H Kanamori, S Aoki, T Yokoyama, H Shimizu, J Miyasaka, and K Ohdoi. Discrete element method analysis of single wheel performance for a small lunar rover on sloped terrain. *Journal of Terramechanics*, 47(5):307–321, 2010.

[120] Kaiming Xia. Finite element modeling of tire/terrain interaction: Application to predicting soil compaction and tire mobility. *Journal of Terramechanics*, 48(2):113–123, 2011.

[121] Tadaomi Eguchi and Tatsuro Muro. Measurement of compacted soil density in a compaction of thick finishing layer. *Journal of Terramechanics*, 44(5):347–353, 2007.

[122] VN Nguyen, T Matsuo, S Inaba, and T Koumoto. Experimental analysis of vertical soil reaction and soil stress distribution under off-road tires. *Journal of Terramechanics*, 45(1):25–44, 2008.

[123] Tire and Rim Association Inc. Tire and rim association year book. 1996.

[124] M Joachim Stallmann, P Schalk Els, and Carl M Bekker. Parameterization and modelling of large off-road tyres for ride analyses: Part 1–obtaining parameterization data. *Journal of terramechanics*, 55:73–84, 2014.

[125] Hossam Ragheb. *Torque control strategy for off-road vehicle mobility.* PhD thesis, 2014.

[126] Paris Altidis. Analyzing hyperelastic materials with some practical considerations. *Midwest ANSYS Users Group*, 18, 2005.

[127] MG Bekker. Introduction to terrain-vehicle systems. part i: The terrain. part ii: The vehicle. Technical report, DTIC Document, 1969.

[128] Robert A Gingold and Joseph J Monaghan. Smoothed particle hydrodynamics: theory and application to non-spherical stars. *Monthly notices of the royal astronomical society*, 181(3):375–389, 1977.

[129] Larry D Libersky, Albert G Petschek, Theodore C Carney, Jim R Hipp, and Firooz A Allahdadi. High strain lagrangian hydrodynamics: a three-dimensional sph code for dynamic material response. *Journal of computational physics*, 109(1):67–75, 1993.

[130] Joe J Monaghan. Simulating free surface flows with sph. *Journal of computational physics*, 110(2):399–406, 1994.

[131] Joseph J Monaghan and John C Lattanzio. A refined particle method for astrophysical problems. *Astronomy and astrophysics*, 149:135–143, 1985.

[132] Joe J Monaghan. Smoothed particle hydrodynamics. *Annual review of astronomy and astrophysics*, 30(1):543–574, 1992.

[133] Maurice A Biot. Theory of propagation of elastic waves in a fluid-saturated porous solid. ii. higher frequency range. *The Journal of the acoustical Society of america*, 28(2):179–191, 1956.

[134] Ralph Brazelton Peck, Walter Edmund Hanson, and Thomas Hampton Thornburn. *Foundation engineering*, volume 10. Wiley New York, 1974.

[135] David A Robinson. Field estimation of soil water content: A practical guide to methods, instrumentation and sensor technology. *Soil Science Society of America Journal*, 73(4):1437, 2009.

[136] AS ASTM. Standard practice for classification of soils for engineering purposes, 2011.

[137] ASTM Committee D-18 on Soil, Plasticity Rock. Subcommittee D18. 03 on Texture, and Density Characteristics of Soils. *Standard test method for particle-size analysis of soils.* ASTM International, 2007.

[138] Murad Abu-Farsakh, Julian Coronel, and Mingjiang Tao. Effect of soil moisture content and dry density on cohesive soil–geosynthetic interactions using large direct shear tests. *Journal of Materials in Civil Engineering*, 19(7):540–549, 2007.

[139] Jeff S Loeb, Dennis A Guenther, Hung-Hsu Fred Chen, and John R Ellis. Lateral stiffness, cornering stiffness and relaxation length of the pneumatic tire. *SAE transactions*, pages 147–155, 1990.

[140] Jerzy Ejsmont, Leif Sjögren, Beata Świeczko-Żurek, and Grzegorz Ronowski. Influence of road wetness on tire-pavement rolling resistance. *Journal of Civil Engineering and Architecture*, 9(11):96, 2015.

[141] Raymond Brach and Matthew Brach. The tire-force ellipse (friction ellipse) and tire characteristics. Technical report, SAE Technical Paper, No 2011-01-0094, 2011.

[142] William L Harrison. Shallow snow model for predicting vehicle performance. Technical report, Cold Regions Research and Engineering Lab Hanover NH, 1981.

[143] Paul W Richmond. Motion resistance of wheeled vehicles in snow. Technical report, Cold Regions Research and Engineering Lab Hanover NH, 1995.

[144] Mehrsa Marjani, Moustafa El-Gindy, David Philipps, Fredrik Öijer, and Inge Johansson. Development of fea tyre/soil interaction model using sph and hybrid sph/fea technique. *International Journal of Vehicle Performance*, 3(3):199–223, 2017.

[145] Corporation, wheel load measurement system. milford, mi. http://www.michsci.com/. Accessed: 2017-07-30.

[146] Judith E Dayhoff. *Neural network architectures: an introduction.* Van Nostrand Reinhold Co., 1990.

[147] Warren S McCulloch and Walter Pitts. A logical calculus of the ideas immanent in nervous activity. *The bulletin of mathematical biophysics*, 5(4):115–133, 1943.

[148] Robert W Goldman. Development of a rollover-warning device for road vehicles. 2001.

[149] Martin T Hagan, Howard B Demuth, Mark H Beale, and Orlando De Jesús. *Neural network design*, volume 20. Pws Pub. Boston, 1996.

[150] John H Holland. Genetic algorithms. *Scientific american*, 267(1):66–73, 1992.

[151] S Rajeev and CS Krishnamoorthy. Discrete optimization of structures using genetic algorithms. *Journal of structural engineering*, 118(5):1233–1250, 1992.

[152] Cao Changyong. *Skid resistance and hydroplaning analysis of rib truck tire*. PhD thesis, National University of Singapore, 2010.

[153] Eureqa : The a.i. powered modeling engine. https://www.nutonian.com/products/eureqa/. Accessed: 2017-09-30.

[154] Albin Brantin and Oscar Grundén. Implementation of the rigid ring tyre model and accompanying soil model in a complete vehicle simulation tool for trucks. Master's thesis, Chalmers University of Technology, 2016.

[155] Frank Michael Zoz and Robert Dwight Grisso. *Traction and tractor performance*. ASAE St. Joseph, 2003.

APPENDIX A

IN-PLANE AND OUT-OF-PLANE RIGID RING TIRE MODEL PARAMETERS

This appendix presents a summary of the tire-terrain and tire-moist terrain interaction presented in chapter 6 and 7, respectively.

A.1 Tire-Flooded Surface Interaction Parameters

A.1.1 Summary of in-plane off-road rigid ring model parameters

Table A.1: In-plane off-road rigid ring model parameters at 13 kN (3000 lbs)

In-Plane Parameters	Symbol	380 kPa 55 psi	586 kPa 85psi	758 kPa 110 psi	Units
Total Vertical Stiffness	k_{tot}	575.450	817.910	993.650	kN/m
Sidewall Stiffness	k_{bz}	2912.050	3458.950	4170.420	kN/m
Residual Vertical Stiffness	k_{vr}	717.170	1071.210	1034.450	kN/m
Vertical Damping	c_{bz}	0.506	0.487	0.532	kN.s/m
Residual Damping	c_{vr}	0.75	0.915	1.01	kNs/m
Tire Damping	c_{tot}	0.302	0.318	0.3484	kN.s/m
Rotational Stiffness	$k_{b\theta}$	405.341	467.507	516.719	kN.m/rad
Rotational Damping	$c_{b\theta}$	0.030	0.031	0.031	kN.m.s/rad
Longitudinal Tire Stiffness					
Water depth – 0%	k_k	60.57	51.48	80.63	kN/unit slip
Water depth – 25%		11.94	21.28	31.84	
Water depth – 50%		14.66	13.45	17.20	
Water depth – 75%		7.72	6.91	8.39	
Longitudinal Tread Stiffness					
Water depth – 0%	k_{cx}	969.15	823.76	1290.07	kN/m
Water depth – 25%		191.02	340.46	509.41	
Water depth – 50%		234.69	215.26	275.24	
Water depth – 75%		123.65	110.52	134.32	
Total Equivalent Vertical Stiffness					
Water depth – 0%	k_z	570.67	820.32	1017.80	kN/m
Water depth – 25%		570.80	821.51	1010.20	
Water depth – 50%		574.24	834.74	1006.20	
Water depth – 75%		584.62	834.79	1016.20	
Rolling Resistance Coefficient at 10km/h					
Water depth – 0%	RRC	0.0083	0.0071	0.0089	-
Water depth – 25%		0.0096	0.0082	0.011	
Water depth – 50%		50.015	0.015	0.014	
Water depth – 75%		0.0095	0.017	0.019	
Longitudinal Slip at Pure Rolling					
Water depth – 0%	i_s	8.31	8.28	7.74	%
Water depth – 25%		7.87	7.62	7.07	
Water depth – 50%		5.42	5.74	4.95	
Water depth – 75%		4.01	3.82	4.23	

Table A.2: In-plane off-road rigid ring model parameters at 27 kN (6000 lbs)

In-Plane Parameters	Symbol	380 kPa 55 psi	586 kPa 85psi	758 kPa 110 psi	Units
Total Vertical Stiffness	k_{tot}	575.450	817.910	993.650	kN/m
Sidewall Stiffness	k_{bz}	2996.260	3773.410	4170.420	kN/m
Residual Vertical Stiffness	k_{vr}	712.240	1044.260	1304.450	kN/m
Vertical Damping	c_{bz}	0.523	0.543	0.532	kN.s/m
Residual Damping	c_{vr}	0.746	0.904	1.01	kNs/m
Tire Damping	c_{tot}	0.307	0.340	0.348	kN.s/m
Rotational Stiffness	$k_{b\theta}$	4405.341	467.507	516.719	kN.m/rad
Rotational Damping	$c_{b\theta}$	0.030	0.031	0.031	kN.m.s/rad
Longitudinal Tire Stiffness					
Water depth – 0%	k_k	110.74	166.57	79.22	kN/unit slip
Water depth – 25%		28.86	47.96	44.670	
Water depth – 50%		27.20	46.75	24.61	
Water depth – 75%		55.03	31.48	25.11	
Longitudinal Tread Stiffness					
Water depth – 0%	k_{cx}	1771.89	2665.11	1267.51	kN/m
Water depth – 25%		461.78	767.33	714.73	
Water depth – 50%		435.26	747.94	393.78	
Water depth – 75%		880.48	503.83	401.68	
Total Equivalent Vertical Stiffness					
Water depth – 0%	k_z	570.67	820.32	1017.80	kN/m
Water depth – 25%		570.80	821.51	1010.20	
Water depth – 50%		574.24	834.74	1006.20	
Water depth – 75%		584.62	834.79	1016.20	
Rolling Resistance Coefficient at 10km/h					
Water depth – 0%	RRC	0.0045	0.0038	0.0026	-
Water depth – 25%		0.0054	0.0048	0.0034	
Water depth – 50%		0.0086	0.0073	0.0087	
Water depth – 75%		0.0096	0.0038	0.0089	
Longitudinal Slip at Pure Rolling					
Water depth – 0%	i_s	10.74	9.17	7.93	%
Water depth – 25%		9.23	8.00024	7.33	
Water depth – 50%		6.086	5.23	4.77	
Water depth – 75%		4.62	9.51	3.99	

Table A.3: In-plane off-road rigid ring model parameters at 40 kN (9000 lbs)

In-Plane Parameters	Symbol	380 kPa 55 psi	586 kPa 85psi	758 kPa 110 psi	Units
Total Vertical Stiffness	k_{tot}	575.450	817.910	993.650	kN/m
Sidewall Stiffness	k_{bz}	3166.121	3871.686	4277.627	kN/m
Residual Vertical Stiffness	k_{vr}	703.270	1036.975	1294.302	kN/m
Vertical Damping	c_{bz}	0.560	0.560	0.550	kN.s/m
Residual Damping	c_{vr}	0.742	0.901	1.006	kNs/m
Tire Damping	c_{tot}	0.189	0.345	0.355	kN.s/m
Rotational Stiffness	$k_{b\theta}$	405.341	467.507	516.719	kN.m/rad
Rotational Damping	$c_{b\theta}$	0.030	0.031	0.031	kN.m.s/rad
Longitudinal Tire Stiffness					
Water depth – 0%	k_k	191.46	189.37	98.73	kN/unit slip
Water depth – 25%		129.66	60.30	130.01	
Water depth – 50%		61.52	59.40	50.78	
Water depth – 75%		39.92	50.94	38.62	
Longitudinal Tread Stiffness					
Water depth – 0%	k_{cx}	3063.43	3029.94	1579.78	kN/m
Water depth – 25%		2074.66	964.80	2080.09	
Water depth – 50%		984.38	950.48	812.52	
Water depth – 75%		638.65	815.01	617.96	
Total Equivalent Vertical Stiffness					
Water depth – 0%	k_z	570.67	820.32	1017.80	kN/m
Water depth – 25%		570.80	821.51	1010.20	
Water depth – 50%		574.24	834.74	1006.20	
Water depth – 75%		584.62	834.79	1016.20	
Rolling Resistance Coefficient at 10km/h					
Water depth – 0%	RRC	0.0055	0.0022	0.0029	-
Water depth – 25%		0.00602	0.0025	0.0033	
Water depth – 50%		0.0062	0.0059	0.0059	
Water depth – 75%		0.0081	0.0063	0.0064	
Longitudinal Slip at Pure Rolling					
Water depth – 0%	i_s	14.11	10.66	13.02	%
Water depth – 25%		11.45	9.68	11.27	
Water depth – 50%		5.9	9 4.57	6.51	
Water depth – 75%		5.05	4.39	6.0078	

A.1.2 Summary of out-of-plane off-road rigid ring model parameters

Table A.4: Out-of-plane off-road rigid ring model parameters at 13 kN (3000 lbs)

Out-Plane Parameters	Symbol	380 kPa 55 psi	586 kPa 85psi	758 kPa 110 psi	Units
Translational Stiffness	k_{by}	742.93	911.208	1017.61	kN/m
Translational Damping	c_{by}	0.24	0.24	0.25	kN.s/m
Rotational Stiffness	$k_{b\gamma}$	163.71	200.09	227.92	kN.m/rad
Rotational Damping	$c_{b\gamma}$	0.029	0.030	0.029	kN.m.s/rad
Lateral Tire Stiffness On Hard Surface	k_l	222.63	270.35	309.62	kN/m
Lateral Damping On Hard Surface	c_l	0.57	0.57	0.59	kN.s/m
Lateral Slip Stiffness					
Water depth – 0%	k_l	212.84	262.14	306.83	kN/m
Water depth – 25%		221.13	274.92	229.06	
Water depth – 50%		216.97	188.89	469.08	
Water depth – 75%		267.2	599.1	474.52	
Lateral Damping					
Water depth – 0%	c_l	0.90	0.56	0.64	kN.s/m
Water depth – 25%		0.46	0.71	0.96	
Water depth – 50%		0.68	0.68	0.92	
Water depth – 75%		0.53	0.47	0.81	
Cornering Stiffness					
Water depth – 0%	k_f	154.34	151.89	143.48	kN/rad
Water depth – 25%		154.09	150.47	154.34	
Water depth – 50%		153.88	149.45	142.56	
Water depth – 75%		125.25	118.2	114.1	
Self-Aligning Moment Stiffness					
Water depth – 0%	k_M	2.39	2.27	1.22	kN.m/rad
Water depth – 25%		2.33	2.33	1.49	
Water depth – 50%		2.86	3.48	2.63	
Water depth – 75%		2.66	2.19	1.82	
Relaxation Length					
Water depth – 0%	σ	0.73	0.58	0.47	m
Water depth – 25%		0.69	0.55	0.67	
Water depth – 50%		0.71	0.79	0.31	
Water depth – 75%		0.47	0.19	0.24	

Table A.5: Out-of-plane off-road rigid ring model parameters at 27 kN (6000 lbs)

Out-Plane Parameters	Symbol	380 kPa 55 psi	586 kPa 85psi	758 kPa 110 psi	Units
Translational Stiffness	k_{by}	742.93	911.21	1017.6	kN/m
Translational Damping	c_{by}	0.24	0.24	0.25	kN.s/m
Rotational Stiffness	$k_{b\gamma}$	163.71	200.09	227.92	kN.m/rad
Rotational Damping	$c_{b\gamma}$	0.029	0.029	0.03	kN.m.s/rad
Lateral Tire Stiffness On Hard Surface	k_l	212.39	265.42	302.20	kN/m
Lateral Damping On Hard Surface	c_l	0.59	0.590	0.591	kN.s/m
Lateral Slip Stiffness					
Water depth – 0%	k_l	206.94	260.42	305.81	kN/m
Water depth – 25%		216.84	271.06	299.68	
Water depth – 50%		290.55	904.89	348.92	
Water depth – 75%		438.06	254.14	1409.31	
Lateral Damping					
Water depth – 0%	c_l	0.26	0.51	0.62	kN.s/m
Water depth – 25%		0.56	0.59	0.87	
Water depth – 50%		1.95	1.01	1.77	
Water depth – 75%		0.71	0.55	0.97	
Cornering Stiffness					
Water depth – 0%	k_f	166.29	204.21	203.77	kN/rad
Water depth – 25%		179.47	201.91	205.24	
Water depth – 50%		178.41	212.02	212.99	
Water depth – 75%		180.11	207.89	208.92	
Self-Aligning Moment Stiffness					
Water depth – 0%	k_M	5.61	5.67	5.81	kN.m/rad
Water depth – 25%		10.87	5.61	5.56	
Water depth – 50%		11.9	6.96	6.51	
Water depth – 75%		11.18	6.3	6.375	
Relaxation Length					
Water depth – 0%	σ	0.80	0.78	0.67	m
Water depth – 25%		0.83	0.74	0.68	
Water depth – 50%		0.61	0.23	0.61	
Water depth – 75%		0.41	0.82	0.15	

Table A.6: Out-of-plane off-road rigid ring model parameters at 40 kN (9000 lbs)

Out-Plane Parameters	Symbol	380 kPa 55 psi	586 kPa 85psi	758 kPa 110 psi	Units
Translational Stiffness	k_{by}	742.93	911.21	1017.6	kN/m
Translational Damping	c_{by}	0.24	0.24	0.25	kN.s/m
Rotational Stiffness	$k_{b\gamma}$	163.71	200.1	227.92	kN.m/rad
Rotational Damping	$c_{b\gamma}$	0.029	0.03	0.03	kN.m.s/rad
Lateral Tire Stiffness On Hard Surface	k_l	211.67	320.23	439.58	kN/m
Lateral Damping On Hard Surface	c_l	0.59	0.58	0.62	kN.s/m
Lateral Slip Stiffness					
Water depth – 0%	k_l	202.23	246.75	294.5	kN/m
Water depth – 25%		3186.3	239.168	283.063	
Water depth – 50%		190.5	236.13	290.8	
Water depth – 75%		189.5	236.38	288.61	
Lateral Damping					
Water depth – 0%	c_l	0.23	0.48	0.58	kN.s/m
Water depth – 25%		0.64	0.48	0.73	
Water depth – 50%		0.63	0.58	0.73	
Water depth – 75%		0.69	0.51	0.86	
Cornering Stiffness					
Water depth – 0%	k_f	177.4	219.06	237.68	kN/rad
Water depth – 25%		184.46	218.38	235.1	
Water depth – 50%		175.98	214.68	238.76	
Water depth – 75%		178.1	214.17	238.93	
Self-Aligning Moment Stiffness					
Water depth – 0%	k_M	21.08	13.35	-1.27	kN.m/rad
Water depth – 25%		18.505	12.22	7.42	
Water depth – 50%		19.76	13.97	12.2	
Water depth – 75%		17.16	14.15	9.92	
Relaxation Length					
Water depth – 0%	σ	0.72	0.58	0.47	m
Water depth – 25%		0.058	0.91	0.83	
Water depth – 50%		0.92	0.91	0.82	
Water depth – 75%		0.94	0.91	0.83	

A.2 Tire-Snow Interaction Parameters

A.2.1 Summary of in-plane off-road rigid ring model parameters

Table A.7: In-plane off-road rigid ring model parameters at 13 kN (3000 lbs)

In-Plane Parameters	Symbol	380 kPa 55 psi	586 kPa 85psi	758 kPa 110 psi	Units
Total Vertical Stiffness	k_{tot}	575.45	817.91	993.65	kN/m
Sidewall Stiffness	k_{bz}	2912.05	3458.95	4170.42	kN/m
Residual Vertical Stiffness	k_{vr}	717.17	1071.21	1034.45	kN/m
Vertical Damping	c_{bz}	0.51	0.49	0.53	kN.s/m
Residual Damping	c_{vr}	0.75	0.92	1.01	kNs/m
Tire Damping	c_{tot}	0.30	0.32	0.35	kN.s/m
Rotational Stiffness	$k_{b\theta}$	405.34	467.51	516.72	kN.m/rad
Rotational Damping	$c_{b\theta}$	0.030	0.031	0.031	kN.m.s/rad
Longitudinal Tire Stiffness					
Snow depth –50 mm	k_k	30.35	29.65	29.11	kN/unit slip
Snow depth –100 mm		25.89	25.47	24.03	
Snow depth –200 mm		14.46	16.84	23.88	
Longitudinal Tread Stiffness					
Snow depth –50 mm	k_{cx}	94.11	91.95	90.25	kN/m
Snow depth –100 mm		80.29	78.98	74.52	
Snow depth –200 mm		44.83	52.22	74.06	
Total Equivalent Vertical Stiffness					
Snow depth –50 mm	k_z	586.75	805.03	976.96	kN/m
Snow depth –100 mm		611.04	882.7	1055.6	
Snow depth –200 mm		432.25	504.77	646.52	
Rolling Resistance Coefficient at 10 km/h					
Snow depth –50 mm	RRC	0.015	0.016	0.016	-
Snow depth –100 mm		0.089	0.092	0.088	
Snow depth –200 mm		0.314	0.321	0.328	

Table A.8: In-plane off-road rigid ring model parameters at 27 kN (6000 lbs)

In-Plane Parameters	Symbol	380 kPa 55 psi	586 kPa 85psi	758 kPa 110 psi	Units
Total Vertical Stiffness	k_{tot}	575.45	817.91	993.65	kN/m
Sidewall Stiffness	k_{bz}	2996.26	3773.41	4170.42	kN/m
Residual Vertical Stiffness	k_{vr}	712.24	1044.26	1304.45	kN/m
Vertical Damping	c_{bz}	0.52	0.54	0.53	kN.s/m
Residual Damping	c_{vr}	0.75	0.91	1.01	kNs/m
Tire Damping	c_{tot}	0.31	0.34	0.35	kN.s/m
Rotational Stiffness	$k_{b\theta}$	4405.34	467.51	516.72	kN.m/rad
Rotational Damping	$c_{b\theta}$	0.030	0.031	0.031	kN.m.s/rad
Longitudinal Tire Stiffness					
Snow depth –50 mm	k_k	32.31	27.46	26.81	kN/unit slip
Snow depth –100 mm		43.934	37.796	55.73	
Snow depth –200 mm		36.97	35.53	32.55	
Longitudinal Tread Stiffness					
Snow depth –50 mm	k_{cx}	82.54	70.15	68.49	kN/m
Snow depth –100 mm		112.23	96.54	42.36	
Snow depth –200 mm		94.45	90.77	83.16	
Total Equivalent Vertical Stiffness					
Snow depth –50 mm	k_z	586.75	805.03	976.96	kN/m
Snow depth –100 mm		611.04	882.7	1055.6	
Snow depth –200 mm		432.25	504.77	646.52	
Rolling Resistance Coefficient at 10 km/h					
Snow depth –50 mm	RRC	0.017	0.018	0.019	-
Snow depth –100 mm		0.050	0.051	0.050	
Snow depth –200 mm		0.180	0.180	0.187	

Table A.9: In-plane off-road rigid ring model parameters at 40 kN (9000 lbs)

In-Plane Parameters	Symbol	380 kPa 55 psi	586 kPa 85psi	758 kPa 110 psi	Units
Total Vertical Stiffness	k_{tot}	575.45	817.91	993.65	kN/m
Sidewall Stiffness	k_{bz}	3166.12	3871.68	4277.62	kN/m
Residual Vertical Stiffness	k_{vr}	703.27	1036.97	1294.3	kN/m
Vertical Damping	c_{bz}	0.56	0.56	0.55	kN.s/m
Residual Damping	c_{vr}	0.74	0.90	1.01	kNs/m
Tire Damping	c_{tot}	0.19	0.35	0.36	kN.s/m
Rotational Stiffness	$k_{b\theta}$	405.34	467.51	516.72	kN.m/rad
Rotational Damping	$c_{b\theta}$	0.030	0.031	0.031	kN.m.s/rad
Longitudinal Tire Stiffness					
Snow depth –50 mm	k_k	61.18	32.31	37.93	kN/unit slip
Snow depth –100 mm		54.06	64.82	75.72	
Snow depth –200 mm		57.34	60.56	55.63	
Longitudinal Tread Stiffness					
Snow depth –50 mm	k_{cx}	144.12	76.12	89.35	kN/m
Snow depth –100 mm		127.35	152.70	178.38	
Snow depth –200 mm		135.078	142.68	131.06	
Total Equivalent Vertical Stiffness					
Snow depth –50 mm	k_z	586.75	805.03	976.96	kN/m
Snow depth –100 mm		611.04	882.7	1055.6	
Snow depth –200 mm		432.25	504.77	646.52	
Rolling Resistance Coefficient at 10 km/h					
Snow depth –50 mm	RRC	0.014	0.013	0.013	-
Snow depth –100 mm		0.037	0.037	0.036	
Snow depth –200 mm		0.124	0.128	0.127	

A.2.2 summary of out-of-plane off-road rigid ring model parameters

Table A.10: Out-of-plane off-road rigid ring model parameters at 13 kN (3000 lbs)

Out-Plane Parameters	Symbol	380 kPa 55 psi	586 kPa 85psi	758 kPa 110 psi	Units
Translational Stiffness	k_{by}	742.92	911.20	1017.60	kN/m
Translational Damping	c_{by}	0.24	0.244	0.25	kN.s/m
Rotational Stiffness	$k_{b\gamma}$	163.71	200.09	227.92	kN.m/rad
Rotational Damping	$c_{b\gamma}$	0.029	0.030	0.029	kN.m.s/rad
Lateral Tire Stiffness On Hard Surface	k_l	222.63	270.34	309.62	kN/m
Lateral Damping On Hard Surface	c_l	0.57	0.56	0.59	kN.s/m
Lateral Slip Stiffness					
Snow depth – 50 mm	k_l	214.47	260.91	293.36	kN/m
Snow depth – 100 mm		214.94	269.77	302.68	
Snow depth – 200%		231.82	296.92	360.52	
Lateral Damping					
Snow depth – 50 mm	c_l	0.90	0.56	0.64	kN.s/m
Snow depth – 100 mm		0.46	0.71	0.96	
Snow depth – 200 mm		0.68	0.68	3.12	
Cornering Stiffness					
Snow depth – 50 mm	k_f	151.32	148.59	146.59	kN/rad
Snow depth – 100 mm		113.31	113.62	154.34	
Snow depth – 200 mm		25.49	46.72	68.93	
Self-Aligning Moment Stiffness					
Snow depth – 50 mm	k_M	4.07	3.21	2.62	kN.m/rad
Snow depth – 100 mm		3.98	1.77	2.03	
Snow depth –200 mm		-2.59	-3.28	-5.37	
Relaxation Length					
Snow depth –50 mm	σ	0.71	0.57	0.50	m
Snow depth –100 mm		0.53	0.42	0.51	
Snow depth – 200 mm		0.11	0.16	0.19	

Table A.11: Out-of-plane off-road rigid ring model parameters at 27 kN (6000 lbs)

Out-Plane Parameters	Symbol	380 kPa 55 psi	586 kPa 85psi	758 kPa 110 psi	Units
Translational Stiffness	k_{by}	742.93	911.21	1017.6	kN/m
Translational Damping	c_{by}	0.24	0.244	0.25	kN.s/m
Rotational Stiffness	$k_{b\gamma}$	163.71	200.09	227.92	kN.m/rad
Rotational Damping	$c_{b\gamma}$	0.029	0.029	0.029	kN.m.s/rad
Lateral Tire Stiffness On Hard Surface	k_l	212.39	265.42	302.2	kN/m
Lateral Damping On Hard Surface	c_l	0.594	0.590	0.591	kN.s/m
Lateral Slip Stiffness					
Snow depth – 50 mm	k_l	205.90	248.51	297.90	kN/m
Snow depth – 100 mm		210.04	260.39	309.10	
Snow depth – 200%		219.41	298.92	345.97	
Lateral Damping					
Snow depth – 50 mm	c_l	0.26	0.51	0.62	kN.s/m
Snow depth – 100 mm		0.56	0.59	0.87	
Snow depth – 200 mm		1.95	1.01	7.77	
Cornering Stiffness					
Snow depth – 50 mm	k_f	165.65	173.07	161.72	kN/rad
Snow depth – 100 mm		179.30	189.82	191.51	
Snow depth – 200 mm		24.80	46.11	72.50	
Self-Aligning Moment Stiffness					
Snow depth – 50 mm	k_M	6.34	5.80	5.39	kN.m/rad
Snow depth – 100 mm		12.78	7.02	7.55	
Snow depth –200 mm		1.37	0.08	2.25	
Relaxation Length					
Snow depth –50 mm	σ	0.80	0.70	0.54	m
Snow depth –100 mm		0.85	0.73	0.62	
Snow depth – 200 mm		0.11	0.15	0.21	

Table A.12: Out-of-plane off-road rigid ring model parameters at 40 kN (9000 lbs)

Out-Plane Parameters	Symbol	380 kPa 55 psi	586 kPa 85psi	758 kPa 110 psi	Units
Translational Stiffness	k_{by}	742.92	911.21	1017.6	kN/m
Translational Damping	c_{by}	0.24	0.244	0.25	kN.s/m
Rotational Stiffness	$k_{b\gamma}$	163.71	200.09	227.92	kN.m/rad
Rotational Damping	$c_{b\gamma}$	0.029	0.030	0.029	kN.m.s/rad
Lateral Tire Stiffness On Hard Surface	k_l	211.66	320.23	439.57	kN/m
Lateral Damping On Hard Surface	c_l	0.59	0.57	0.62	kN.s/m
Lateral Slip Stiffness					
Snow depth – 50 mm	k_l	196.9	240.89	292.80	kN/m
Snow depth – 100 mm		208.60	254.64	300.24	
Snow depth – 200%		207.0	8 275.48	323.88	
Lateral Damping					
Snow depth – 50 mm	c_l	0.23	0.48	0.58	kN.s/m
Snow depth – 100 mm		0.64	0.48	0.73	
Snow depth – 200 mm		0.63	0.58	0.73	
Cornering Stiffness					
Snow depth – 50 mm	k_f	182.67	208.91	216.01	kN/rad
Snow depth – 100 mm		170.75	218.06	234.67	
Snow depth – 200 mm		18.61	38.97	69.61	
Self-Aligning Moment Stiffness					
Snow depth – 50 mm	k_M	12.09	10.27	9.66	kN.m/rad
Snow depth – 100 mm		28.13	18.84	13.14	
Snow depth –200 mm		6.03	5.13	5.10	
Relaxation Length					
Snow depth –50 mm	σ	0.93	0.87	0.74	m
Snow depth –100 mm		0.82	0.86	0.78	
Snow depth – 200 mm		0.09	0.14	0.21	

A.3 Tire-Sandy Loam Interaction Parameters

A.3.1 Summary of in-plane off-road rigid ring model parameters

Table A.13: In-plane off-road rigid ring model parameters at 13 kN (3000 lbs)

In-Plane Parameters	Symbol	380 kPa 55 psi	586 kPa 85psi	758 kPa 110 psi	Units
Total Vertical Stiffness	k_{tot}	575.450	817.910	993.650	kN/m
Sidewall Stiffness	k_{bz}	2912.050	3458.950	4170.420	kN/m
Residual Vertical Stiffness	k_{vr}	717.170	1071.210	1034.450	kN/m
Vertical Damping	c_{bz}	0.506	0.487	0.532	kN.s/m
Residual Damping	c_{vr}	0.75	0.915	1.01	kNs/m
Tire Damping	c_{tot}	0.302	0.318	0.3484	kN.s/m
Rotational Stiffness	$k_{b\theta}$	405.341	467.507	516.719	kN.m/rad
Rotational Damping	$c_{b\theta}$	0.030	0.031	0.031	kN.m.s/rad
Longitudinal Tire Stiffness					
Moisture Content – 25%	k_k	11.94	21.28	31.84	kN/unit slip
Moisture Content – 50%		14.67	13.45	17.2	
Moisture Content – 62%		7.73	6.91	8.39	
Longitudinal Tread Stiffness					
Moisture Content – 25%	k_{cx}	37.02	65.98	98.72	kN/m
Moisture Content – 50%		45.48	41.72	53.34	
Moisture Content – 62%		23.96	21.42	26.03	
Total Equivalent Vertical Stiffness					
Moisture Content – 25%	k_z	279.6	291.05	300.59	kN/m
Moisture Content – 50%		205.46	212.45	218.26	
Moisture Content – 62%		215.53	220.46	224.6	
Rolling Resistance Coefficient at 10km/h					
Moisture Content – 25%	RRC	0.150	0.166	0.179	-
Moisture Content – 50%		0.220	0.232	0.236	
Moisture Content – 62%		0.219	0.236	0.240	

Table A.14: In-plane off-road rigid ring model parameters at 27 kN (6000 lbs)

In-Plane Parameters	Symbol	380 kPa 55 psi	586 kPa 85psi	758 kPa 110 psi	Units
Total Vertical Stiffness	k_{tot}	575.4	817.91	993.65	kN/m
Sidewall Stiffness	k_{bz}	2996.26	3773.41	4170.42	kN/m
Residual Vertical Stiffness	k_{vr}	712.24	1044.26	1304.45	kN/m
Vertical Damping	c_{bz}	0.52	0.543	0.53	kN.s/m
Residual Damping	c_{vr}	0.75	0.90	1.01	kNs/m
Tire Damping	c_{tot}	0.31	0.34	0.35	kN.s/m
Rotational Stiffness	$k_{b\theta}$	4405.34	467.51	516.72	kN.m/rad
Rotational Damping	$c_{b\theta}$	0.030	0.031	0.031	kN.m.s/rad
Longitudinal Tire Stiffness					
Moisture Content – 25%	k_k	28.86	47.96	44.67	kN/unit slip
Moisture Content – 50%		27.20	46.75	24.61	
Moisture Content – 62%		55.03	31.49	25.11	
Longitudinal Tread Stiffness					
Moisture Content – 25%	k_{cx}	73.72	122.50	114.10	kN/m
Moisture Content – 50%		69.49	119.40	62.86	
Moisture Content – 62%		140.56	80.43	64.13	
Total Equivalent Vertical Stiffness					
Moisture Content – 25%	k_z	279.6	291.05	300.59	kN/m
Moisture Content – 50%		205.46	212.45	218.26	
Moisture Content – 62%		215.53	220.46	224.6	
Rolling Resistance Coefficient at 10km/h					
Moisture Content – 25%	RRC	0.17	0.21	0.22	-
Moisture Content – 50%		0.25	0.27	0.28	
Moisture Content – 62%		0.25	0.27	0.28	

Table A.15: In-plane off-road rigid ring model parameters at 40 kN (9000 lbs)

In-Plane Parameters	Symbol	380 kPa 55 psi	586 kPa 85psi	758 kPa 110 psi	Units
Total Vertical Stiffness	k_{tot}	575.45	817.91	993.65	kN/m
Sidewall Stiffness	k_{bz}	3166.12	3871.66	4277.62	kN/m
Residual Vertical Stiffness	k_{vr}	703.27	1036.97	1294.30	kN/m
Vertical Damping	c_{bz}	0.56	0.56	0.55	kN.s/m
Residual Damping	c_{vr}	0.74	0.90	1.01	kNs/m
Tire Damping	c_{tot}	0.19	0.34	0.35	kN.s/m
Rotational Stiffness	$k_{b\theta}$	405.34	467.51	516.72	kN.m/rad
Rotational Damping	$c_{b\theta}$	0.03	0.031	0.031	kN.m.s/rad
Longitudinal Tire Stiffness					
Moisture Content – 25%	k_k	129.67	60.30	130.01	kN/unit slip
Moisture Content – 50%		61.52	59.41	50.78	
Moisture Content – 62%		39.92	50.94	38.62	
Longitudinal Tread Stiffness					
Moisture Content – 25%	k_{cx}	305.46	142.05	306.26	kN/m
Moisture Content – 50%		144.93	139.94	119.63	
Moisture Content – 62%		94.03	119.99	90.98	
Total Equivalent Vertical Stiffness					
Moisture Content – 25%	k_z	279.6	291.05	300.59	kN/m
Moisture Content – 50%		205.46	212.45	218.26	
Moisture Content – 62%		215.53	220.46	224.6	
Rolling Resistance Coefficient at 10km/h					
Moisture Content – 25%	RRC	0.193	0.237	0.256	-
Moisture Content – 50%		0.261	0.282	0.298	
Moisture Content – 62%		0.261	0.290	0.306	

A.3.2 Summary of out-of-plane off-road rigid ring model parameters

Table A.16: Out-of-plane off-road rigid ring model parameters at 13 kN (3000 lbs)

Out-Plane Parameters	Symbol	380 kPa 55 psi	586 kPa 85psi	758 kPa 110 psi	Units
Translational Stiffness	k_{by}	742.92	911.21	1017.6	kN/m
Translational Damping	c_{by}	0.24	0.24	0.25	kN.s/m
Rotational Stiffness	$k_{b\gamma}$	163.71	200.09	227.92	kN.m/rad
Rotational Damping	$c_{b\gamma}$	0.029	0.030	0.029	kN.m.s/rad
Lateral Tire Stiffness On Hard Surface	k_l	222.63	270.34	309.62	kN/m
Lateral Damping On Hard Surface	c_l	0.57	0.56	0.59	kN.s/m
Lateral Slip Stiffness					
Moisture Content – 25%	k_l	185.64	238.73	272.73	kN/m
Moisture Content – 50%		227.34	278.83	323.07	
Moisture Content – 62%		265.60	334.94	389.72	
Lateral Damping					
Moisture Content – 25%	c_l	0.90	0.56	0.64	kN.s/m
Moisture Content – 50%		0.46	0.71	0.96	
Moisture Content – 62%		0.68	0.68	3.12	
Cornering Stiffness					
Moisture Content – 25%	k_f	90.51	91.13	83.33	kN/rad
Moisture Content – 50%		111.15	106.11	154.34	
Moisture Content – 62%		152.20	156.34	122.15	
Self-Aligning Moment Stiffness					
Moisture Content – 25%	k_M	1.38	0.35	1.26	kN.m/rad
Moisture Content – 50%		-0.15	-1.64	-1.34	
Moisture Content – 62%		3.81	1.36	-2.57	
Relaxation Length					
Moisture Content – 25%	σ	0.49	0.38	0.31	m
Moisture Content – 50%		0.49	0.38	0.48	
Moisture Content – 62%		0.57	0.47	0.31	

Table A.17: Out-of-plane off-road rigid ring model parameters at 27 kN (6000 lbs)

Out-Plane Parameters	Symbol	380 kPa 55 psi	586 kPa 85psi	758 kPa 110 psi	Units
Translational Stiffness	k_{by}	742.93	911.21	1017.6	kN/m
Translational Damping	c_{by}	0.24	0.24	0.25	kN.s/m
Rotational Stiffness	$k_{b\gamma}$	163.71	200.09	227.92	kN.m/rad
Rotational Damping	$c_{b\gamma}$	0.029	0.029	0.029	kN.m.s/rad
Lateral Tire Stiffness On Hard Surface	k_l	212.39	265.420	302.20	kN/m
Lateral Damping On Hard Surface	c_l	0.59	0.59	0.59	kN.s/m
Lateral Slip Stiffness					
Moisture Content – 25%	k_l	202.85	262.27	298.14	kN/m
Moisture Content – 50%		269.62	346.71	401.24	
Moisture Content – 62%		318.59	410.17	468.34	
Lateral Damping					
Moisture Content – 25%	c_l	0.26	0.51	0.62	kN.s/m
Moisture Content – 50%		0.56	0.59	0.87	
Moisture Content – 62%		1.95	1.01	7.77	
Cornering Stiffness					
Moisture Content – 25%	k_f	103.49	108.71	114.61	kN/rad
Moisture Content – 50%		90.42	112.99	104.06	
Moisture Content – 62%		100.78	157.30	90.58	
Self-Aligning Moment Stiffness					
Moisture Content – 25%	k_M	2.87	-0.24	-0.40	kN.m/rad
Moisture Content – 50%		2.12	-1.25	-1.31	
Moisture Content – 62%		3.60	2.44	-3.07	
Relaxation Length					
Moisture Content – 25%	σ	0.51	0.41	0.38	m
Moisture Content – 50%		0.34	0.33	0.26	
Moisture Content – 62%		0.32	0.38	0.19	

Table A.18: Out-of-plane off-road rigid ring model parameters at 40 kN (9000 lbs)

Out-Plane Parameters	Symbol	380 kPa 55 psi	586 kPa 85psi	758 kPa 110 psi	Units
Translational Stiffness	k_{by}	742.92	911.21	1017.6	kN/m
Translational Damping	c_{by}	0.24	0.24	0.25	kN.s/m
Rotational Stiffness	$k_{b\gamma}$	163.71	200.09	227.92	kN.m/rad
Rotational Damping	$c_{b\gamma}$	0.029	0.030	0.029	kN.m.s/rad
Lateral Tire Stiffness On Hard Surface	k_l	211.66	320.23	439.58	kN/m
Lateral Damping On Hard Surface	c_l	0.59	0.58	0.62	kN.s/m
Lateral Slip Stiffness					
Moisture Content – 25%	k_l	231.94	295.62	340.99	kN/m
Moisture Content – 50%		331.03	420.21	473.19	
Moisture Content – 62%		349.34	468.03	541.93	
Lateral Damping					
Moisture Content – 25%	c_l	0.23	0.48	0.58	kN.s/m
Moisture Content – 50%		0.64	0.48	0.73	
Moisture Content – 62%		0.63	0.58	0.73	
Cornering Stiffness					
Moisture Content – 25%	k_f	120.09	126.84	130.08	kN/rad
Moisture Content – 50%		98.34	130.35	136.39	
Moisture Content – 62%		147.48	162.42	111.34	
Self-Aligning Moment Stiffness					
Moisture Content – 25%	k_M	6.61	2.53	0.75	kN.m/rad
Moisture Content – 50%		3.18	0.81	-0.88	
Moisture Content – 62%		6.56	3.05	-2.31	
Relaxation Length					
Moisture Content – 25%	σ	0.52	0.43	0.38	m
Moisture Content – 50%		0.30	0.31	0.29	
Moisture Content – 62%		0.42	0.35	0.21	

A.4 Tire-Moist Sand Interaction Parameters

A.4.1 Summary of in-plane off-road rigid ring model parameters

Table A.19: In-plane off-road rigid ring model parameters at 13 kN (3000 lbs)

In-Plane Parameters	Symbol	380 kPa 55 psi	586 kPa 85psi	758 kPa 110 psi	Units
Total Vertical Stiffness	k_{tot}	575.450	817.910	993.650	kN/m
Sidewall Stiffness	k_{bz}	2912.05	3458.95	4170.42	kN/m
Residual Vertical Stiffness	k_{vr}	717.17	1071.21	1034.45	kN/m
Vertical Damping	c_{bz}	0.51	0.49	0.53	kN.s/m
Residual Damping	c_{vr}	0.75	0.92	1.01	kNs/m
Tire Damping	c_{tot}	0.30	0.32	0.349	kN.s/m
Rotational Stiffness	$k_{b\theta}$	405.34	467.51	516.72	kN.m/rad
Rotational Damping	$c_{b\theta}$	0.030	0.031	0.031	kN.m.s/rad
Longitudinal Tire Stiffness					
Moisture Content – 10%	k_k	27.36	24.90	21.60	kN/unit slip
Moisture Content – 30%		19.11	15.16	20	
Moisture Content – 50%		31.28	20.66	18.2	
Longitudinal Tread Stiffness					
Moisture Content – 10%	k_{cx}	84.84	77.20	66.98	kN/m
Moisture Content – 30%		59.27	47.01	62.02	
Moisture Content – 50%		97.01	64.07	56.63	
Total Equivalent Vertical Stiffness					
Moisture Content – 10%	k_z	279.6	291.05	300.59	kN/m
Moisture Content – 30%		205.46	212.45	218.26	
Moisture Content – 50%		215.53	220.46	224.6	
Rolling Resistance Coefficient at 10km/h					
Moisture Content – 10%	RRC	0.22	0.23	0.23	-
Moisture Content – 30%		0.23	0.24	0.25	
Moisture Content – 50%		0.24	0.23	0.26	

Table A.20: In-plane off-road rigid ring model parameters at 27 kN (6000 lbs)

In-Plane Parameters	Symbol	380 kPa 55 psi	586 kPa 85psi	758 kPa 110 psi	Units
Total Vertical Stiffness	k_{tot}	575.45	817.91	993.65	kN/m
Sidewall Stiffness	k_{bz}	2996.26	3773.41	4170.42	kN/m
Residual Vertical Stiffness	k_{vr}	712.24	1044.26	1304.45	kN/m
Vertical Damping	c_{bz}	0.52	0.54	0.53	kN.s/m
Residual Damping	c_{vr}	0.746	0.904	1.01	kNs/m
Tire Damping	c_{tot}	0.31	0.34	0.35	kN.s/m
Rotational Stiffness	$k_{b\theta}$	4405.34	467.51	516.72	kN.m/rad
Rotational Damping	$c_{b\theta}$	0.030	0.031	0.031	kN.m.s/rad
Longitudinal Tire Stiffness					
Moisture Content – 10%	k_k	61.59	61.04	34.80	kN/unit slip
Moisture Content – 30%		31.78	22.10	27.75	
Moisture Content – 50%		56.78	16.24	19.89	
Longitudinal Tread Stiffness					
Moisture Content – 10%	k_{cx}	157.31	155.92	88.89	kN/m
Moisture Content – 30%		81.17	56.46	70.88	
Moisture Content – 50%		145.02	41.47	50.79	
Total Equivalent Vertical Stiffness					
Moisture Content – 10%	k_z	279.6	291.05	300.59	kN/m
Moisture Content – 30%		205.46	212.45	218.26	
Moisture Content – 50%		215.53	220.46	224.6	
Rolling Resistance Coefficient at 10km/h					
Moisture Content – 10%	RRC	0.23	0.26	0.27	-
Moisture Content – 30%		0.24	0.26	0.27	
Moisture Content – 50%		0.23	0.25	0.26	

Table A.21: In-plane off-road rigid ring model parameters at 40 kN (9000 lbs)

In-Plane Parameters	Symbol	380 kPa 55 psi	586 kPa 85psi	758 kPa 110 psi	Units
Total Vertical Stiffness	k_{tot}	575.45	817.91	993.65	kN/m
Sidewall Stiffness	k_{bz}	3166.12	3871.69	4277.62	kN/m
Residual Vertical Stiffness	k_{vr}	703.27	1036.98	1294.30	kN/m
Vertical Damping	c_{bz}	0.56	0.56	0.55	kN.s/m
Residual Damping	c_{vr}	0.74	0.90	1.01	kNs/m
Tire Damping	c_{tot}	0.19	0.34	0.35	kN.s/m
Rotational Stiffness	$k_{b\theta}$	405.34	467.51	516.72	kN.m/rad
Rotational Damping	$c_{b\theta}$	0.03	0.031	0.031	kN.m.s/rad
Longitudinal Tire Stiffness					
Moisture Content – 10%	k_k	38.16	40.72	60.23	kN/unit slip
Moisture Content – 30%		43.17	47.39	47.62	
Moisture Content – 50%		40.24	40.25	25.99	
Longitudinal Tread Stiffness					
Moisture Content – 10%	k_{cx}	89.89	95.93	141.89	kN/m
Moisture Content – 30%		101.70	111.64	112.18	
Moisture Content – 50%		94.79	94.82	61.23	
Total Equivalent Vertical Stiffness					
Moisture Content – 10%	k_z	279.6	291.05	300.59	kN/m
Moisture Content – 30%		205.46	212.45	218.26	
Moisture Content – 50%		215.53	220.46	224.6	
Rolling Resistance Coefficient at 10km/h					
Moisture Content – 10%	RRC	0.26	0.28	0.3	-
Moisture Content – 30%		0.24	0.27	0.28	
Moisture Content – 50%		0.23	0.25	0.26	

A.4.2 Summary of out-of-plane off-road rigid ring model parameters

Table A.22: Out-of-plane off-road rigid ring model parameters at 13 kN (3000 lbs)

Out-Plane Parameters	Symbol	380 kPa 55 psi	586 kPa 85psi	758 kPa 110 psi	Units
Translational Stiffness	k_{by}	742.92	911.21	1017.60	kN/m
Translational Damping	c_{by}	0.23	0.24	0.25	kN.s/m
Rotational Stiffness	$k_{b\gamma}$	163.71	200.09	227.92	kN.m/rad
Rotational Damping	$c_{b\gamma}$	0.029	0.030	0.029	kN.m.s/rad
Lateral Tire Stiffness On Hard Surface	k_l	222.62	270.34	309.62	kN/m
Lateral Damping On Hard Surface	c_l	0.56	0.57	0.59	kN.s/m
Lateral Slip Stiffness					
Moisture Content – 10%	k_l	228.03	280.12	314.27	kN/m
Moisture Content – 30%		226.36	287.27	335.7	
Moisture Content – 50%		212.28	235.46	266.31	
Lateral Damping					
Moisture Content – 10%	c_l	2.28	4.46	3.15	kN.s/m
Moisture Content – 30%		1.85	1.79	17.53	
Moisture Content – 50%		1.08	1.00	3.56	
Cornering Stiffness					
Moisture Content – 10%	k_f	6.14	5.08	5.80	kN/rad
Moisture Content – 30%		5.05	5.29	6.52	
Moisture Content – 50%		6.34	6.48	7.28	
Self-Aligning Moment Stiffness					
Moisture Content – 10%	k_M	-0.96	-0.82	-0.25	kN.m/rad
Moisture Content – 30%		-0.84	0.22	-0.20	
Moisture Content – 50%		-0.47	1.36	-0.40	
Relaxation Length					
Moisture Content – 10%	σ	0.18	0.15	0.13	m
Moisture Content – 30%		0.18	0.14	0.12	
Moisture Content – 50%		0.20	0.18	0.16	

Table A.23: Out-of-plane off-road rigid ring model parameters at 27 kN (6000 lbs)

Out-Plane Parameters	Symbol	380 kPa 55 psi	586 kPa 85psi	758 kPa 110 psi	Units
Translational Stiffness	k_{by}	742.92	911.20	1017.60	kN/m
Translational Damping	c_{by}	0.23	0.24	0.25	kN.s/m
Rotational Stiffness	$k_{b\gamma}$	163.71	200.09	227.92	kN.m/rad
Rotational Damping	$c_{b\gamma}$	0.029	0.029	0.029	kN.m.s/rad
Lateral Tire Stiffness On Hard Surface	k_l	212.39	265.42	302.20	kN/m
Lateral Damping On Hard Surface	c_l	0.59	0.59	0.59	kN.s/m
Lateral Slip Stiffness					
Moisture Content – 10%	k_l	280.57	363.04	417.22	kN/m
Moisture Content – 30%		303.50	389.69	461.73	
Moisture Content – 50%		277.18	371.11	470.94	
Lateral Damping					
Moisture Content – 10%	c_l	1.18	1.25	1.56	kN.s/m
Moisture Content – 30%		1.53	1.46	1.58	
Moisture Content – 50%		2.55	1.96	1.30	
Cornering Stiffness					
Moisture Content – 10%	k_f	10.05	8.20	9.70	kN/rad
Moisture Content – 30%		5.79	11.39	11.52	
Moisture Content – 50%		8.08	11.30	9.97	
Self-Aligning Moment Stiffness					
Moisture Content – 10%	k_M	0.25	1.26	1.42	kN.m/rad
Moisture Content – 30%		0.32	0.42	0.43	
Moisture Content – 50%		-1.21	2.44	0.77	
Relaxation Length					
Moisture Content – 10%	σ	0.15	0.11	0.10	m
Moisture Content – 30%		0.14	0.11	0.09	
Moisture Content – 50%		0.15	0.11	0.09	

Table A.24: Out-of-plane off-road rigid ring model parameters at 40 kN (9000 lbs)

Out-Plane Parameters	Symbol	380 kPa 55 psi	586 kPa 85psi	758 kPa 110 psi	Units
Translational Stiffness	k_{by}	742.92	911.20	1017.60	kN/m
Translational Damping	c_{by}	0.23	0.24	0.25	kN.s/m
Rotational Stiffness	$k_{b\gamma}$	163.71	200.09	227.92	kN.m/rad
Rotational Damping	$c_{b\gamma}$	0.029	0.030	0.029	kN.m.s/rad
Lateral Tire Stiffness On Hard Surface	k_l	211.66	320.22	439.57	kN/m
Lateral Damping On Hard Surface	c_l	0.591	0.576	0.616	kN.s/m
Lateral Slip Stiffness					
Moisture Content – 10%	k_l	323.16	438.42	494.91	kN/m
Moisture Content – 30%		335.44	447.09	533.77	
Moisture Content – 50%		316.17	444.76	601.74	
Lateral Damping					
Moisture Content – 10%	c_l	1.41	2.54	4.05	kN.s/m
Moisture Content – 30%		2.34	3.38	5.09	
Moisture Content – 50%		3.14	1.82	2.04	
Cornering Stiffness					
Moisture Content – 10%	k_f	9.29	8.67	8.52	kN/rad
Moisture Content – 30%		10.29	12.42	12.94	
Moisture Content – 50%		11.55	12.42	12.93	
Self-Aligning Moment Stiffness					
Moisture Content – 10%	k_M	0.30	1.21	2.09	kN.m/rad
Moisture Content – 30%		1.71	1.02	0.91	
Moisture Content – 50%		1.29	3.05	1.83	
Relaxation Length					
Moisture Content – 10%	σ	0.13	0.09	0.08	m
Moisture Content – 30%		0.12	0.09	0.08	
Moisture Content – 50%		0.13	0.09	0.07	

APPENDIX B

ARTIFICIAL NEURAL NETWORK DERIVATION

The bias and weight of the ANN were determined as follows:

$$B^{1T} = \begin{bmatrix} 3.0 & -1.5 & 2.1 & -0.36 & 0.73 & -0.11 & 0.48 & -0.47 & 0.65 & 1.5 \end{bmatrix} \quad (B.1)$$

$$B^2 = -2.3 \quad (B.2)$$

$$W^1 = \begin{bmatrix} 0.058 & -0.023 & -0.011 & -1.5 & 3.9 & -1.2 \\ 0.81 & 0.069 & 2.1 & -0.68 & -1.0, & 1.9 \\ -0.68 & -0.043 & -0.72 & 1.7 & -0.32 & -0.2 \\ -0.033 & -0.085 & -1.1 & 1.6 & -0.048 & -2.0 \\ 0.19 & -0.58 & -1.1 & -0.74 & -1.1 & -1.9 \\ 0.11 & -0.029 & 0.69 & 1.5 & 2.2, & 0.65 \\ -0.079 & 0.003 & -1.8 & -1.4 & -3.5 & -1.5 \\ -0.61 & 0.018 & 1.0 & -0.032 & -0.011 & -0.54 \\ 0.84 & -0.023 & -1.8 & 0.67 & 0.43 & 0.48 \\ -1.0 & -0.02 & -1.2 & 3.2 & 2.2 & 1.4 \end{bmatrix} \quad (B.3)$$

$$W^2 = \begin{bmatrix} 2.1 & 1.2 & 0.55 & -0.31 & -0.19 & 2.6 & 3.8 & -1.4 & -0.94 & 1.0 \end{bmatrix} \quad (B.4)$$

Let M be defined as show in equation B.5, in addition the *tansig* is a ANN transfer function that calculates the layer's output from its net input as defined in equation B.6.

$$M = W^1X + B^1 \quad (B.5)$$

$$tansig(W^1X + B^1) = \frac{2}{1 + e^{-2(W^1X+B^1)}} - 1 \quad (B.6)$$

Substituting W^1, B^1 and the input X equation B.5 is rearranged and presented in B.7.

$$M = W^1X + B^1$$

$$
\begin{aligned}
&= \begin{bmatrix} 0.058 & -0.023 & -0.011 & -1.5 & 3.9 & -1.2 \\ 0.81 & 0.069 & 2.1 & -0.68 & -1.0, & 1.9 \\ -0.68 & -0.043 & -0.72 & 1.7 & -0.32 & -0.2 \\ -0.033 & -0.085 & -1.1 & 1.6 & -0.048 & -2.0 \\ 0.19 & -0.58 & -1.1 & -0.74 & -1.1 & -1.9 \\ 0.11 & -0.029 & 0.69 & 1.5 & 2.2, & 0.65 \\ -0.079 & 2.8e^{-3} & -1.8 & -1.4 & -3.5 & -1.5 \\ -0.61 & 0.018 & 1.0 & -0.032 & -0.011 & -0.54 \\ 0.84 & -0.023 & -1.8 & 0.67 & 0.43 & 0.48 \\ -1.0 & -0.02 & -1.2 & 3.2 & 2.2 & 1.4 \end{bmatrix} \begin{bmatrix} L \\ P \\ V \\ C \\ \phi \\ D \end{bmatrix} + \begin{bmatrix} 3.0 \\ -1.5 \\ 2.1 \\ -0.36 \\ 0.73 \\ -0.11 \\ 0.48 \\ -0.47 \\ 0.65 \\ 1.5 \end{bmatrix} \\
&= \begin{bmatrix} 0.058L - 1.2D - 1.5C - 0.023P - 0.011V + 3.9\phi + 3 \\ 1.9D - 0.68C + 0.81L + 0.07P + 2.1V - \phi - 1.5 \\ 1.7C - 0.2D - 0.68L - 0.043P - 0.72V - 0.32\phi + 2.1 \\ 1.6C - 2D - 0.033L - 0.085P - 1.1V - 0.048\phi - 0.36 \\ 0.19L - 1.9D - 0.74C - 0.58P - 1.1V - 1.1\phi + 0.73 \\ 1.5C + 0.65D + 0.11L - 0.029 * P + 0.69 * V + 2.2 * phi - 0.11 \\ 2.8e^{-3}P - 1.5 - 0.079L - 1.4C - 1.8V - 3.5\phi + 0.48 \\ 0.018P - 0.54D - 0.61L - 0.032C + 1.0V - 0.011\phi - 0.47 \\ 0.67C + 0.48D + 0.84L - 0.023P - 1.8V + 0.43\phi + 0.65 \\ 3.2C + 1.4D - 1L - 0.02P - 1.2V + 2.2\phi + 1.5 \end{bmatrix} \qquad \text{(B.7)}
\end{aligned}
$$

Substituting and simplifying equation B.7 in equation B.6, equation B.8 is obtained.

$$
\begin{aligned}
tansig(M) &= \frac{2}{1+e^{-2(M)}} - 1 \\
&= \begin{bmatrix} \frac{2}{1+exp(3C+2.3D-0.12L+0.047P+0.021V-7.9\phi-6)} - 1 \\ \frac{2}{1+exp(1.4C-3.7D-1.6L-0.14P-4.1V+2.0\phi+2.9)} - 1 \\ \frac{2}{1+exp(0.4D-3.4C+1.4L+0.086P+1.4V+0.65\phi-4.1)} - 1 \\ \frac{2}{1+exp(4.1D-3.3C+0.066L+0.17P+2.1V+0.095\phi+0.72)} - 1 \\ \frac{2}{1+exp(1.5C+3.7D-0.39L+1.2P+2.2V+2.3\phi-1.5)} - 1 \\ \frac{2}{1+exp(0.059P-1.3D-0.23L-3.1C-1.4V-4.4\phi+0.21)} - 1 \\ \frac{2}{1+exp(2.8C+3.1D+0.16L-5.7e^{-3}P+3.6V+7\phi-0.95)} - 1 \\ \frac{2}{1+exp(0.063C+1.1D+1.2L-0.036P-2.1V+0.023\phi+0.93)} - 1 \\ \frac{2}{1+exp(0.047P-0.96D-1.7L-1.3C+3.7V-0.86\phi-1.3)} - 1 \\ \frac{2}{1+exp(2L-2.9D-6.3C+0.041P+2.4V-4.4\phi-3)} - 1 \end{bmatrix} \qquad \text{(B.8)}
\end{aligned}
$$

The Y output in equation 8.9 which is in this case the RRC becomes as shown in equation 8.11 after solving using equation B.8.

$$
\begin{aligned}
Y &= W^2\left(tansig(M)\right) + B^2 \\
RRC &= \begin{bmatrix} 2.05 & 1.19 & 0.54 & -0.31 & -0.19 & 2.61 & 3.84 & -1.42 & -0.94 & 1.04 \end{bmatrix}
\end{aligned}
$$

$$\left[\begin{array}{c} \frac{2}{1+exp(3C+2.3D-0.12L+0.047P+0.021V-7.9\phi-6)}-1 \\ \frac{2}{1+exp(1.4C-3.7D-1.6L-0.14P-4.1V+2.0\phi+2.9)}-1 \\ \frac{2}{1+exp(0.4D-3.4C+1.4L+0.086P+1.4V+0.65\phi-4.1)}-1 \\ \frac{2}{1+exp(4.1D-3.3C+0.066L+0.17P+2.1V+0.095\phi+0.72)}-1 \\ \frac{2}{1+exp(1.5C+3.7D-0.39L+1.2P+2.2V+2.3\phi-1.5)}-1 \\ \frac{2}{1+exp(0.059P-1.3D-0.23L-3.1C-1.4V-4.4\phi+0.21)}-1 \\ \frac{2}{1+exp(2.8C+3.1D+0.16L-5.7e-3P+3.6V+7\phi-0.95)}-1 \\ \frac{2}{1+exp(0.063C+1.1D+1.2L-0.036P-2.1V+0.023\phi+0.93)}-1 \\ \frac{2}{1+exp(0.047P-0.96D-1.7L-1.3C+3.7V-0.86\phi-1.3)}-1 \\ \frac{2}{1+exp(2L-2.9D-6.3C+0.041P+2.4V-4.4\phi-3)}-1 \end{array}\right]-2.3$$

$$\begin{aligned}
= \quad & \frac{2.1}{exp(2L-2.9D-6.3C+0.041P+2.4V-4.4\phi-3)+1} \\
- \quad & \frac{0.63}{exp(4.1D-3.3C+0.066L+0.17P+2.1V+0.095\phi+0.72)+1} \\
- \quad & \frac{2.9}{exp(0.063C+1.1D+1.2L-0.036P-2.1V+0.023\phi+0.93)+1} \\
+ \quad & \frac{2.4}{exp(1.4C-3.7D-1.6L-0.14P-4.1V+2\phi+2.9)+1} \\
- \quad & \frac{0.39}{exp(1.5C+3.7D-0.39L+1.2P+2.2V+2.3\phi-1.5)+1} \\
+ \quad & \frac{1.1}{exp(0.4D-3.4C+1.4L+0.086P+1.4V+0.65\phi-4.1)+1} \\
+ \quad & \frac{5.2}{exp(0.059P-1.3D-0.23L-3.1C-1.4V-4.4phi+0.21)+1} \\
+ \quad & \frac{4.1}{exp(3C+2.3D-0.12L+0.047P+0.021V-7.9\phi-6)+1} \\
+ \quad & \frac{7.7}{exp(2.8C+3.1D+0.16L-5.7e^{-3}P+3.6V+7\phi-0.95)+1} \\
- \quad & \frac{1.9}{exp(0.047P-0.96D-1.7L-1.3C+3.7V-0.86\phi-1.3)+1}
\end{aligned} \tag{B.9}$$

APPENDIX C

FULL VEHICLE ANALYTICAL MODEL RESULTS

C.1 Tire-Hard Surface Characteristics

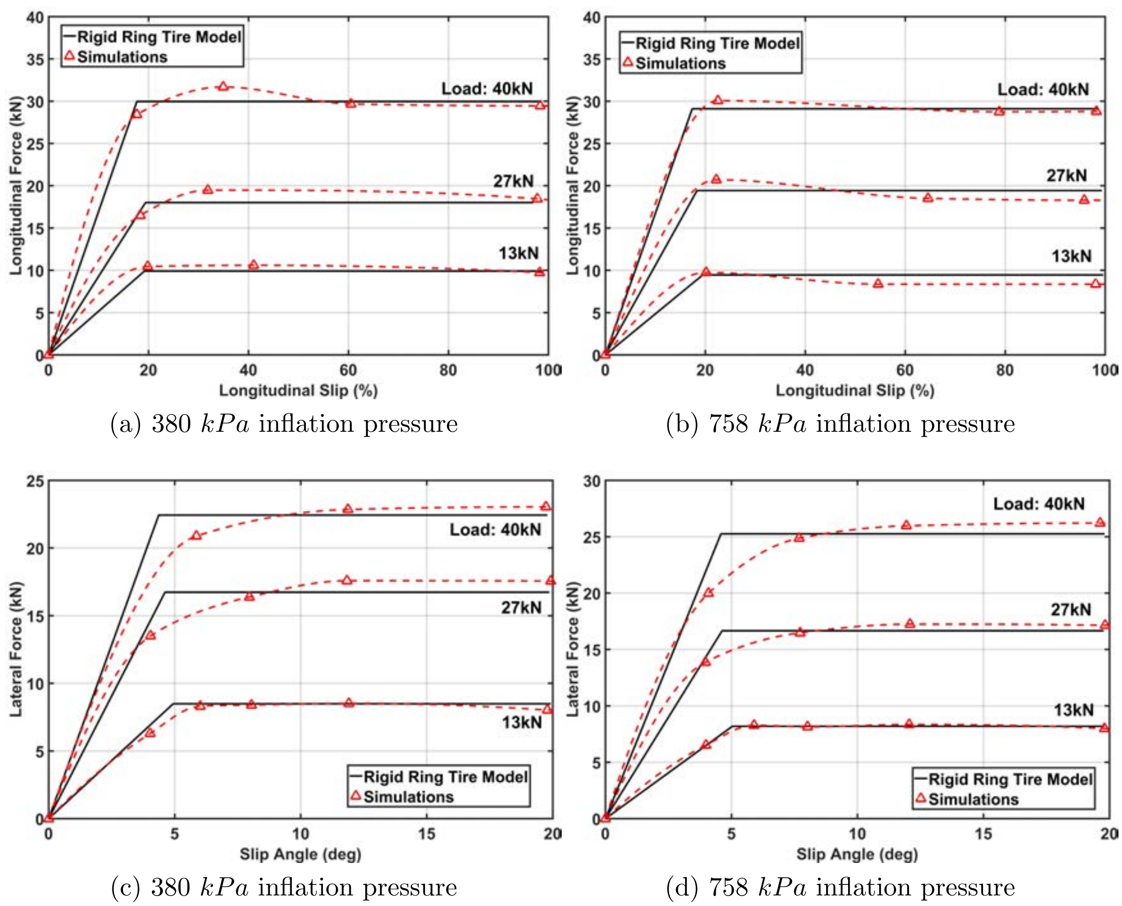

(a) 380 kPa inflation pressure

(b) 758 kPa inflation pressure

(c) 380 kPa inflation pressure

(d) 758 kPa inflation pressure

Figure C.1: Rigid ring tire model and simulation results for truck tire running over hard surface

Table C.1: Vertical steady state displacement of truck tire running over hard surface

Inflation Pressure (kPa)	Vertical Load (kN)	Rigid Ring Tire Model	Simulations
380	13	25	23
	27	46	49
	40	65	75
758	13	17	15
	27	30	30
	40	37	43

C.2 Tire-Wet Surface Characteristics

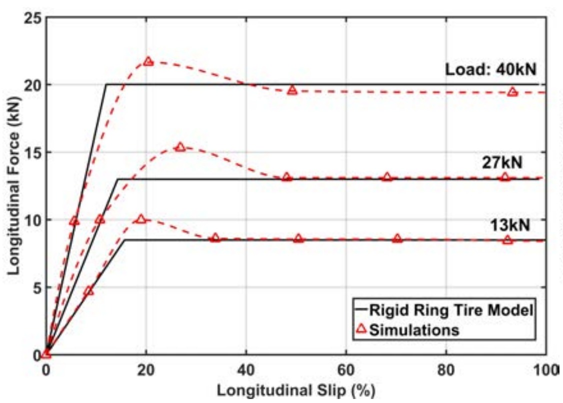

(a) 380 kPa inflation pressure

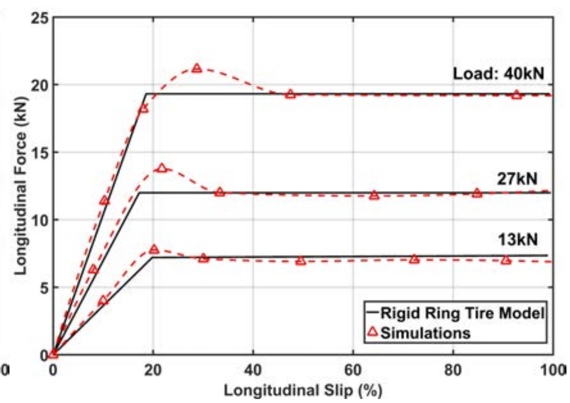

(b) 758 kPa inflation pressure

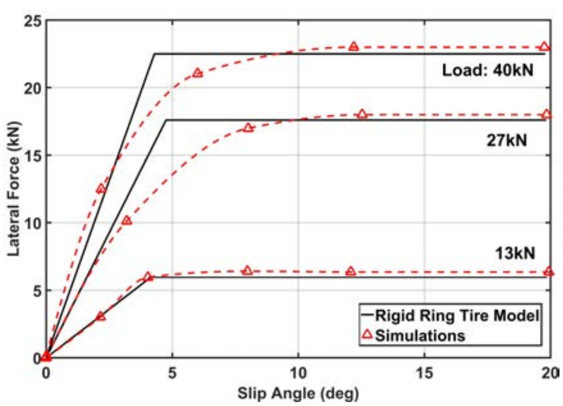

(c) 380 kPa inflation pressure

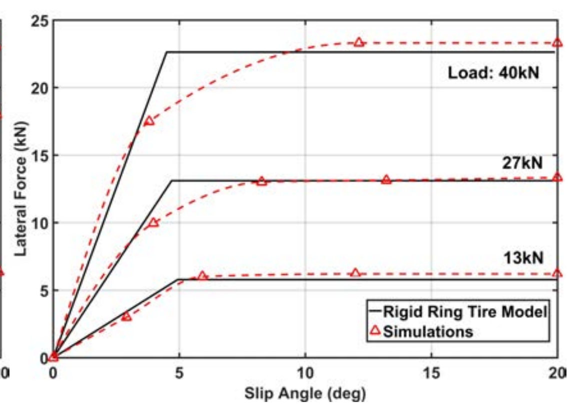

(d) 758 kPa inflation pressure

Figure C.2: Rigid ring tire model and simulation results for truck tire running over wet surface

Table C.2: Vertical steady state displacement of truck tire running over wet surface

Inflation Pressure (kPa)	Vertical Load (kN)	Rigid Ring Tire Model	Simulations
380	13	50	55
	27	87	78
	40	134	102
758	13	32	46
	27	87	59
	40	78	72

C.3 Tire-Snow Characteristics

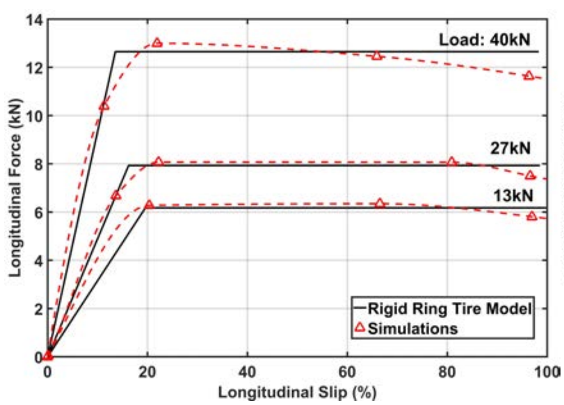

(a) 380 kPa inflation pressure

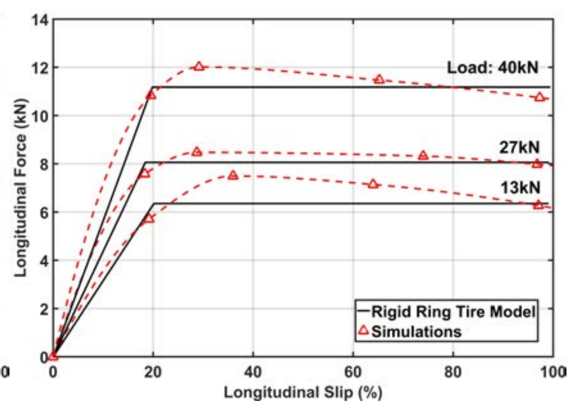

(b) 758 kPa inflation pressure

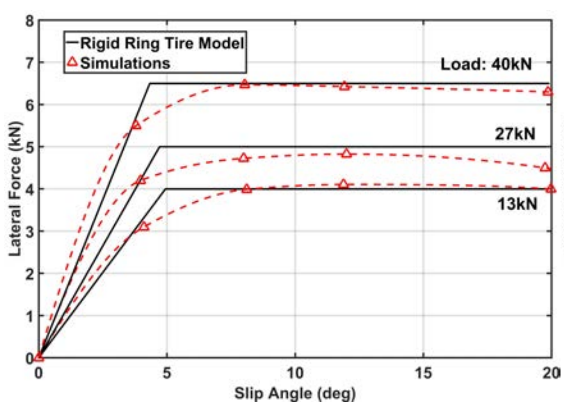

(c) 380 kPa inflation pressure

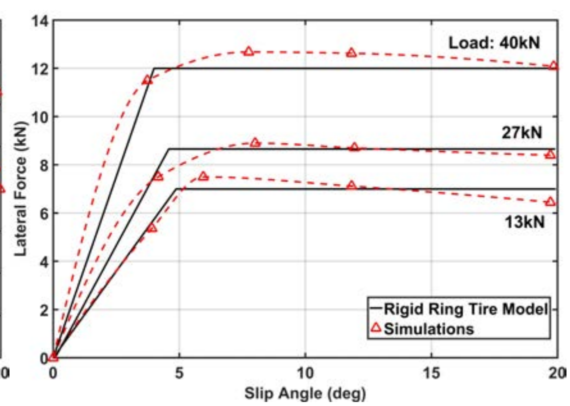

(d) 758 kPa inflation pressure

Figure C.3: Rigid ring tire model and simulation results for truck tire running over 50 mm snow

Table C.3: Vertical steady state displacement of truck tire running over snow

Inflation Pressure (kPa)	Vertical Load (kN)	Rigid Ring Tire Model	Simulations
380	13	49	46
	27	86	61
	40	99	87
758	13	32	36
	27	52	43
	40	70	56

C.4 Tire-Dry Sand Characteristics

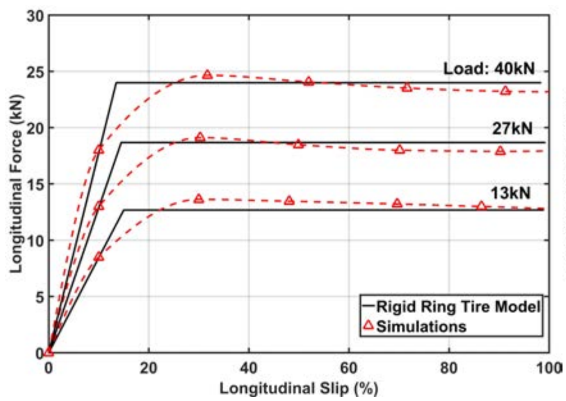

(a) 380 kPa inflation pressure

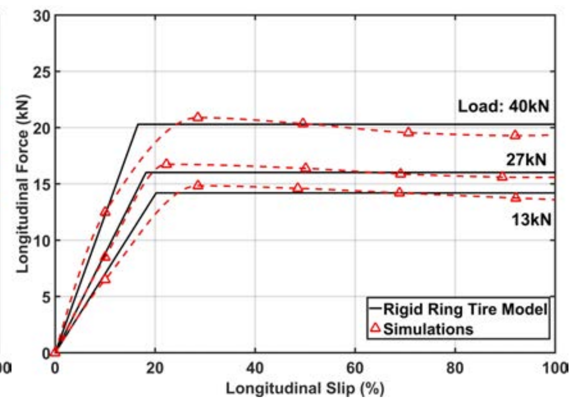

(b) 758 kPa inflation pressure

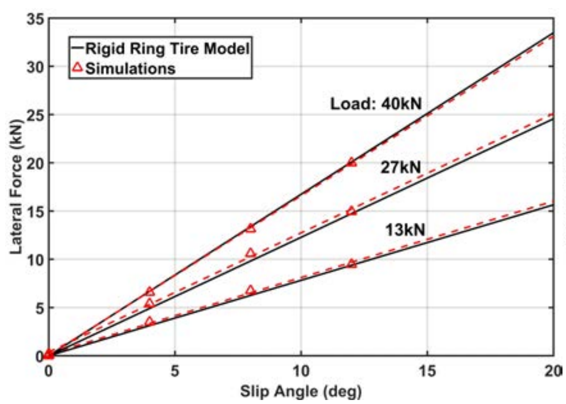

(c) 380 kPa inflation pressure

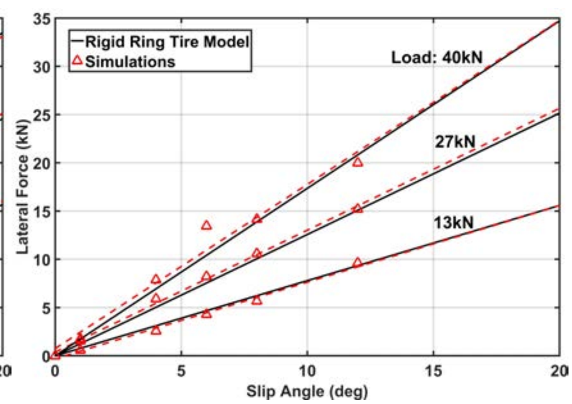

(d) 758 kPa inflation pressure

Figure C.4: Rigid ring tire model and simulation results for truck tire running over dry sand

Table C.4: Vertical steady state displacement of truck tire running over dry sand

Inflation Pressure (kPa)	Vertical Load (kN)	Rigid Ring Tire Model	Simulations
380	13	96	116
	27	144	150
	40	171	175
758	13	112	110
	27	152	139
	40	157	162

C.5 Tire-Sandy Loam Characteristics

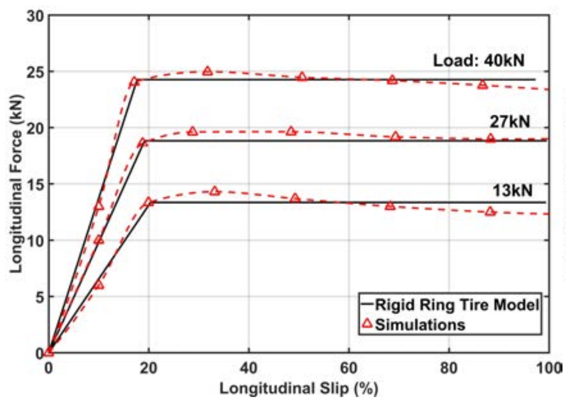

(a) 380 kPa inflation pressure

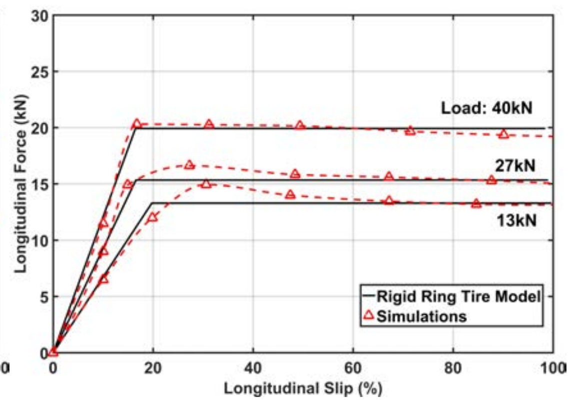

(b) 758 kPa inflation pressure

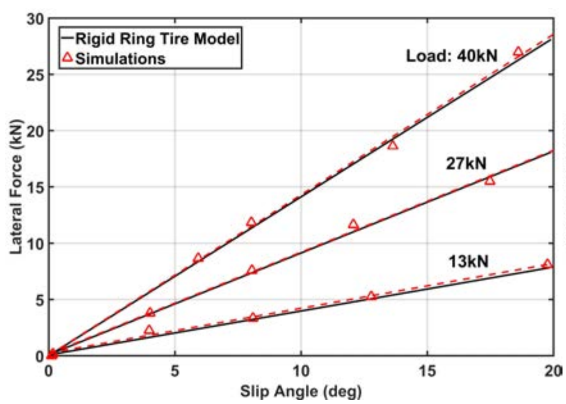

(c) 380 kPa inflation pressure

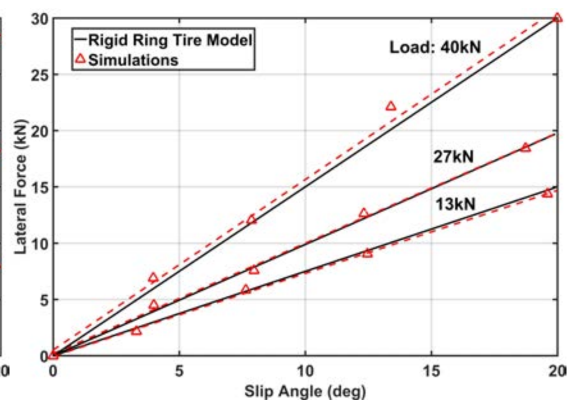

(d) 758 kPa inflation pressure

Figure C.5: Rigid ring tire model and simulation results for truck tire running over sandy loam with 25% moisture content

Table C.5: Vertical steady state displacement of truck tire running over sandy loam

Inflation Pressure (kPa)	Vertical Load (kN)	Rigid Ring Tire Model	Simulations
380	13	87	80
	27	124	117
	40	139	148
758	13	72	75
	27	99	108
	40	87	143

C.6 Tire-Moist Sand Characteristics

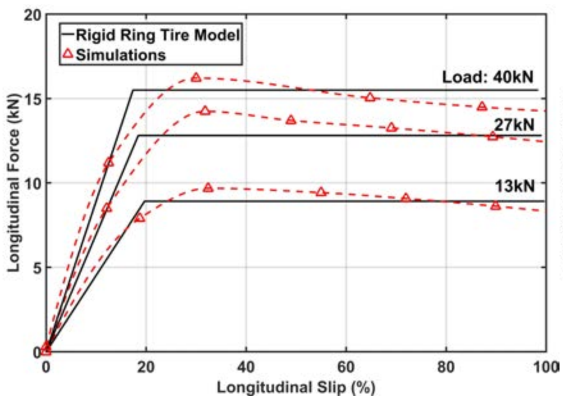

(a) 380 kPa inflation pressure

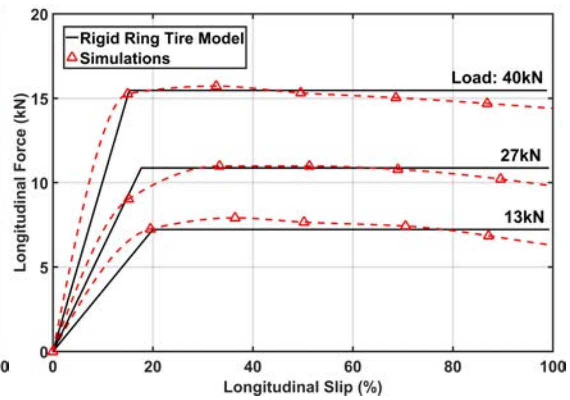

(b) 758 kPa inflation pressure

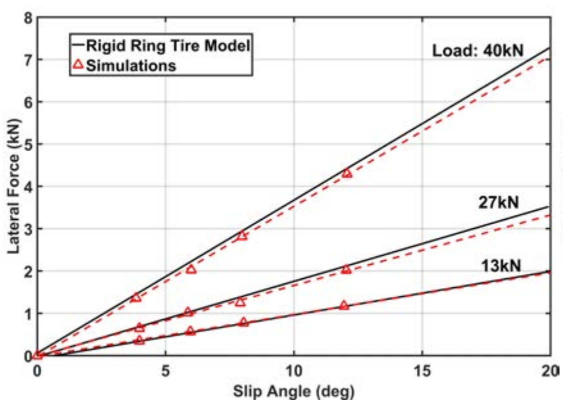

(c) 380 kPa inflation pressure

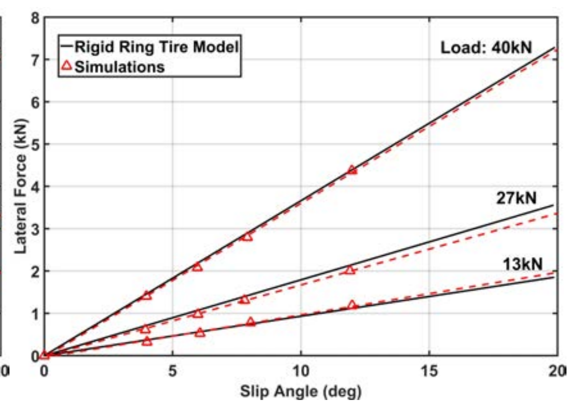

(d) 758 kPa inflation pressure

Figure C.6: Rigid ring tire model and simulation results for truck tire running over 10% moist sand

Table C.6: Vertical steady state displacement of truck tire running over moist sand

Inflation Pressure (kPa)	Vertical Load (kN)	Rigid Ring Tire Model	Simulations
380	13	151	169
	27	186	204
	40	217	230
758	13	136	163
	27	179	194
	40	188	218